HEAT AND MASS TRANSFER – MODELING AND SIMULATION

Edited by **Md Monwar Hossain**

INTECHWEB.ORG

Heat and Mass Transfer – Modeling and Simulation
Edited by Md Monwar Hossain

Published by InTech
Janeza Trdine 9, 51000 Rijeka, Croatia

Publishing Process Manager Alenka Urbancic
Technical Editor Teodora Smiljanic
Cover Designer Jan Hyrat
Image Copyright Nejron Photo, 2010. Used under license from Shutterstock.com

First published September, 2011
Printed in Croatia

A free online edition of this book is available at www.intechopen.com
Additional hard copies can be obtained from orders@intechweb.org

Heat and Mass Transfer – Modeling and Simulation, Edited by Md Monwar Hossain
p. cm.
ISBN 978-953-307-604-1

Contents

Preface

This book covers a number of topics in heat and mass transfer processes for a variety of industrial applications. The research papers provide information and guidelines in terms of theory, mathematical modeling and experimental findings in many research areas relevant to the design of industrial processes and equipment. The equipment includes air heaters, cooling towers, chemical system vaporization, high temperature polymerization and hydrogen production by steam reforming. Nine chapters of the book will serve as an important reference for scientists and academics working in research areas mentioned above, at least in the aspects of heat and/or mass transfer, analytical/numerical solutions and optimization of the processes.

The first chapter deals with the description and mass transfer analysis of fixed-bed chromatographic processes by kinetic adsorption. The second chapter focuses on the effects of gas diffusion layer on the heat transfer process in high temperature polymerization. Chapter 3 is concerned with the description and analysis of heat and mass transfer processes in a fin-and-tube air heater. Hydrogen production by steam reforming and the process intensification strategies are discussed in chapter 4. The effects of external boundary layer in the analysis of heat and mass transfer processes are presented in chapter 5, while optimization of these processes in the design of cooling towers is discussed in chapter 6.

In the seventh chapter certain problems associated with the mathematical modeling of chemical reactor processes are discussed with numerical calculations. Chapter 8 deals with the modeling and simulation of chemical system vaporization with detail description of the transport processes. Chapter 9 introduces the multiphase modeling of complex processes: the effect of non equilibrium fluctuations in electrochemical reactions such as electrodeposition.

Md Monwar Hossain, PhD
Associate professor in Chemical Engineering
Department of Chemical & Petroleum Engineering
United Arab Emirates University
United Arab Emirates

1

Modeling of Batch and Continuous Adsorption Systems by Kinetic Mechanisms

Alice F. Souza[1], Leôncio Diógenes T. Câmara[2] and Antônio J. Silva Neto[2]
[1]*Universidade Federal do Rio de Janeiro-UFRJ, Rio de Janeiro-RJ,*
[2]*Instituto Politécnico da Universidade do Estado do Rio de Janeiro, IPRJ-UERJ*
Dep. Mechanical Eng. Energy - DEMEC, Nova Friburgo-RJ,
Brazil

1. Introduction

This chapter is related to the main aspects of the kinetic adsorption models by heterogeneous mechanisms applied in the studies of mass transfer in chromatography. The kinetic adsorption models are implemented and described according to the adsorption mechanisms as in the next Figure 1. The illustrations as in Fig. 1 are a good way to show the steps in the determination of the final models that represent the mass transfer between the solid and liquid phase.

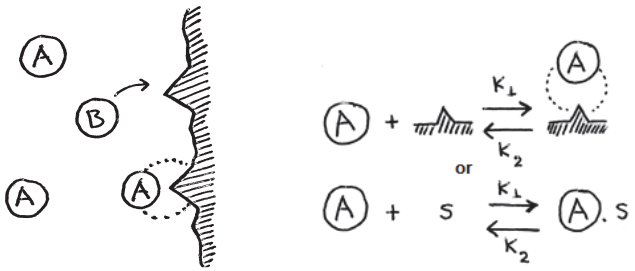

a) b)

Fig. 1. Mechanisms of heterogeneous kinetic adsorption of molecules A on sites s.

From Fig. 1a) can be observed that the mass transfer of molecules A and B between the liquid (left) and solid (right) phase is related to the surface of the solid phase, so it depends on number of active sites on the surface and the number of molecules in the liquid phase. Such surface mechanism is called adsorption and it is represented in the Fig. 1b). In Fig. 1b) the adsorption is related to a kinetic constant k_1 and the desorption is related to a kinetic constant k_2. The adsorption is the main phenomenology present in the chromatography which provides different affinities of the molecules with the adsorbent phase leading to the separation.

The kinetic modeling approach utilized in this work considers the total sum of the adsorption sites which can be located on the internal and external active surface. The

modeling routines were implemented in Fortran 90 and the equations solved numerically applying the 4th order Runge-Kutta method (time step of 10^{-4}).
The rate of consumption of the molecules A ($-r_A$) can be written as follow in terms of the mass balance between the adsorbent solid phase and the liquid phase.

$$(-r_A) = k_1.C_A.C_S - k_2.C_{AS} = k_1.C_A.C_S - k_2.q_A \tag{1}$$

in which C_A, C_S and q_A corresponds, respectively, to the concentration of solute A in the liquid phase, the concentration of active sites on the adsorbent phase and the concentration of solute A in the solid phase.
Different types of adsorption processes can be considered in the separation as can be seen in the Fig. 2. In the batch adsorption process (Fig. 2a) there is no flow entering and exiting the system; In the continuous (Fig. 2b) there is flow entering and exiting and it is considered perfect mixture (CSTR) inside the system in which the concentration inside is the same at the exit; and in the plug flow (PFR) also there is flow entering and exiting and it is considered an axial variation of concentration along the system.

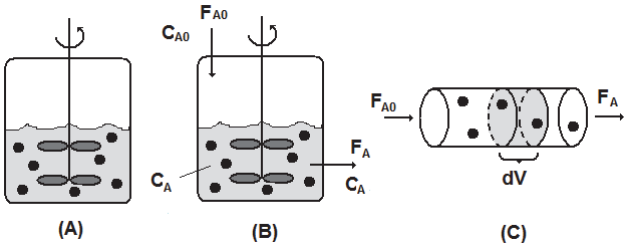

Fig. 2. Types of adsorption processes: a) batch; b) continuous (CSTR) and c) plug flow (PFR).

In the case of batch adsorption process (Fig. 2a) the moles balance (N moles per time) equation is applied without the terms of flow entering and exiting,

$$\frac{dN_j}{dt} = \cancel{F_{J0}} - \cancel{F_{J0}} + r_J.V \qquad \frac{dN_j}{dt} = r_J.V \tag{2}$$

leading to a final expression of rate of adsorption that can be substituted into Eq. 1.

$$r_J = \frac{dN_j}{V.dt} \qquad r_J = \frac{dC_j}{dt} \tag{3}$$

The following final expression (Eq. 4) shows that the concentration of solute A in the liquid phase decreases with the adsorption and increases with the desorption.

$$-\frac{dC_A}{dt} = k_1.C_A.C_S. - k_2.q_A \tag{4}$$

2. Continuous separation by reversible kinetic adsorption models

The chromatographic separation processes, which are involved by the adsorption phenomena, correspond to a very important field for separating substances with high

aggregated value utilized mainly by the chemical and pharmaceutical industry. The application of the modeling and simulation to study such separation mechanisms is a key factor for the comprehension and therefore the improvement of the performance of the chromatographic systems.

The modeling of the chromatographic separation processes can be done applying different mathematical approaches, with advantages and limitations according to the method assumed. A revision of the dynamic and mathematical modeling of the adsorption isotherms and chromatography can be seen in the work of Ruthven, 1984. Among the models of mass transfer kinetics in chromatography, the LDF and the Langmuir, are the most utilized, being both related to a first order kinetic of mass transfer (Guiochon and Lin, 2003). The publication of Thomas (1944) corresponds to a precursor work following the simple adsorption kinetic of Langmuir (kinetic of first order), which derived a solution for the Riemann problem (i.e, for the breakthrough curve) of a model of chromatography combined with the mass balance equation of an ideal model (no axial diffusion). Later, Goldstein (1953) derived a solution of the Thomas model that is valid in the case of a rectangular pulse injection. Wade et al. (1987) obtained a simple solution of the Thomas model that is valid in the case of a Dirac injection. Following the same consideration of adsorption order (kinetic of first order), Chase (1984) derived an analytical form for the breakthrough curve, being it identical to the Thomas's model.

The assumption of LDF or adsorption kinetic of first order is a way to reduce the complexity of the chromatographic systems, being possible through this procedure achieve analytical expressions that can represent the dynamic behavior of these processes as obtained by Thomas (1944) and Chase (1984). The study of the chromatographic continuous systems by the consideration of others adsorption orders is a possibility to understand the separation mechanisms by adsorption, although this procedure can lead to more complex mathematical models. The application of the continuous mass balance models of perfect mixture with the kinetic mechanisms of adsorption with superior orders is an opportunity to analyze the equations terms and parameters that are relevant to the adsorption mechanism involved with the separation processes.

In this work different configurations of adsorption mechanisms combined with mixture mass balance models of the chromatographic columns are analyzed to determine the influence of the equation terms and parameters on the dynamic and equilibrium behavior of the separation processes.

2.1 Modeling approach

The modeling of the chromatographic separation process was based on the adsorption kinetic mechanisms over a solid surface as represented in the Fig. 3.

From the Fig. 3 it can be observed that the adsorption phenomena can follow different mechanisms, as verified from the cases (a) to (c).From it, the rate of consumption of solute A, represented by ($-r_A$), is determined by the following expression

$$(-r_A) = k_1.C_A{}^{\alpha}.C_S{}^{\beta} - k_2.q_A{}^{\gamma} \tag{5}$$

in which C_A, C_S and q_A represent the concentration of solute in the liquid phase, the concentration of active sites of the adsorbent and the concentration of solute A adsorbed in the solid phase, respectively. The parameters α, β and γ represent the stoichiometric coefficients of the adsorption mechanism (See Fig. 3 case (a)).

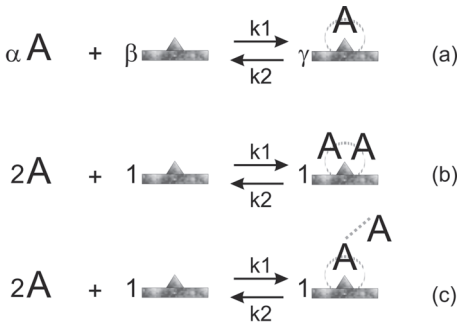

Fig. 3. Mechanisms of adsorption of solute (A) on the adsorbent surface

The active sites concentration are obtained by the mass balance in the adsorbent

$$C_s = (q_m - q_A) \tag{6}$$

with the parameter q_m representing the maximum capacity of adsorption or the maximum concentration of active sites on the surface of the adsorbent.

From the mass transfer of the solute A from the liquid phase to the solid phase can be established that ($-r_A = r_{SA}$), where ($-r_A$) and (r_{SA}), represent the rate of consumption of the solute A in the liquid phase and the rate of adsorption of the solute A on the solid surface, respectively. Figure 4a presents the chromatographic column configuration assumed in the modeling, in which C_{A0} and C_A represent the initial concentration of solute (A) at the entrance of the column and the solute concentration at the column exit, respectively. Figure 4b presents a typical experimental curve of rupture or breakthrough curve for a chromatographic system, which was adapted from the experimental work of Cruz (1997), which studied the adsorption of insulin by the resin Accel Plus QMA.

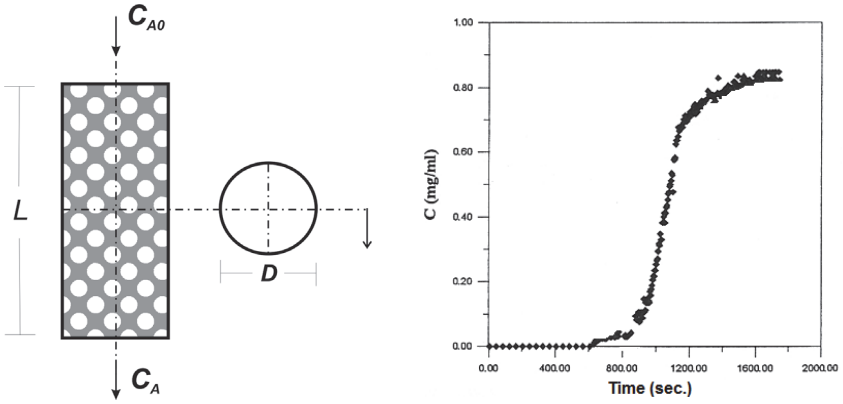

(a) (b)

Fig. 4. (a) Representation of the chromatographic column modeled; (b) typical curve of rupture or breakthrough (adapted from Cruz, 1997).

Applying the mass balances in the chromatography column, according to the column configuration presented in Fig. 4, we obtain the following expressions for the mass balance of the solute in the liquid phase,

$$\varepsilon.V.\frac{dC_A}{dt} = Q.C_{A0} - Q.C_A - r_A.\varepsilon.V \tag{7}$$

and in the solid phase,

$$\varepsilon.V.\frac{dq_A}{dt} = r_{S.A}.\varepsilon.V \tag{8}$$

in which the parameters ε, V and Q correspond to the porosity, the volume and the volumetric flow, respectively. The first term of Eq. 7 corresponds to the accumulation, being the second, third and fourth the terms of solute entering, the solute exiting and the consumption rate, respectively. The accumulation term of the Eq. 7 is proportional to the rate of solute adsorption. These expressions correspond to mass balance models of perfect mixture, in which the solute concentration is the same in all the positions of the system.
Assuming $\varepsilon=1$, for a practical consideration, and substituting the Eqs. 5-6 into the Eqs. 7 and 8 we obtain

$$\frac{dC_A}{dt} = c_1.C_{A0} - c_1.C_A - [k_1.{C_A}^{\alpha}.(q_m - q_A)^{\beta} - k_2.{q_A}^{\gamma}] \tag{9}$$

$$\frac{dq_A}{dt} = k_1.{C_A}^{\alpha}.(q_m - q_A)^{\beta} - k_2.{q_A}^{\gamma} \tag{10}$$

In which the parameter c_1 is equals to Q/V.
The system of Eqs. 9 and 10, which represents, respectively, the mass balance of solute in the liquid and solid phase, was solved numerically, applying a routine according to the 4th order Runge-Kutta method (time step of 10-4) for different considerations of the separation process.

2.2 Results and discussion

2.2.1 Analysis of the separation process only by adsorption

In a first step the calculations were done assuming only the adsorption term of Eqs. 9 and 10, i.e. not considering the desorption term (k_2=0). The stoichiometric coefficients were also considered equal to the unit (α=β=1). For the above considerations Eqs. 9 and 10 are transformed into

$$\frac{dC_A}{dt} = c_1.C_{A0} - c_1.C_A - k_1.C_A.(q_m - q_A) \tag{11}$$

$$\frac{dq_A}{dt} = k_1.C_A.(q_m - q_A) \tag{12}$$

Figure 5 presents the simulation results of the numerical solutions of the previous system of ordinary differential equations (Eqs. 11 and 12). From Fig. 5 it can be observed that the solute concentration in the liquid phase (C_A) presented a different behavior if compared to the concentration of solute adsorbed in the solid phase (q_A). The solute concentration (C_A)

showed a behavior similar to that for the chromatographic systems as can be verified by the typical result of the experimental curve in Fig. 4b. This characteristical aspect ("s" profile) for the chromatographic answer is called the rupture or breakthrough curve. From Fig. 5 it can also be seen that the concentration on the solid surface (q_A) is almost linear, presenting a significant variation at the same time as the inflexion point of the breakthrough curve. Note that the solute adsorption (q_A) is higher at initial times, leading to a high consumption of the solute in the liquid phase (the later appearance of solute at the column exit).

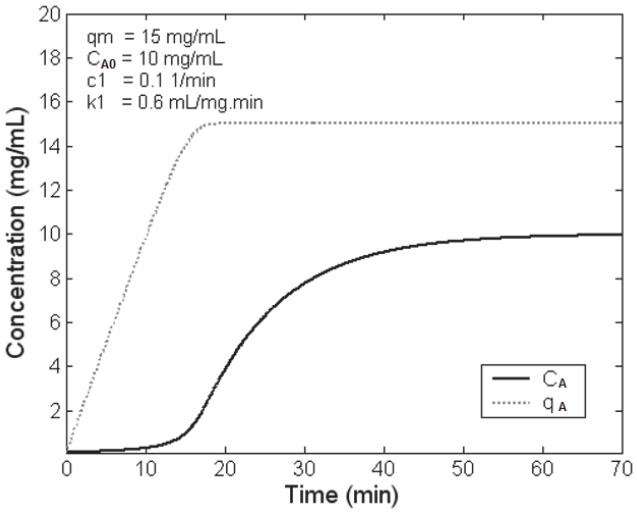

Fig. 5. Profiles of the solute concentration in the liquid (C_A) and solid phase (q_A)

Simulation results with a similar behavior as that obtained in Fig. 4b were obtained from conditions in which either the maximum capacity of adsorption (q_m) was greater than the initial concentration of solute at the entrance (C_{A0}) and the kinetic constant of adsorption was high. These parameters conditions led to higher values of the consumption term of Eq. 11. This observation is coherent with the real processes of chromatographic separation, which in general present high capacity of adsorption.

Figure 6 presents a result with the same behavior as that one observed in Fig. 4b. For this case, the high adsorption rate is attributed to the high kinetic constant of adsorption. From Fig. 6 it can be seen also the great variation of the solute concentration on the solid phase (q_A) at the same time of the inflexion point of the solute concentration in the liquid phase (C_A).

Simulation results showing the increase in the consumption rate of solute due to the increase in the maximum capacity of adsorption (q_m) are presented through the Fig. 7. The rate of adsorption was increased increasing the capacity of adsorption of the adsorbent from q_m=*10* mg/mL (Fig. 7a) to q_m=*40* mg/mL (Fig. 7b). From the case of low adsorption capacity (Fig. 7a) it can be observed that the concentration of solute in the solid phase increases slowly, allowing the appearance of solute in the liquid phase at initial times. For a high capacity of adsorption (Fig. 7b), the concentration of solute in the

solid phase increases fast, allowing a latter appearance of solute at the column exit (around 20 min).

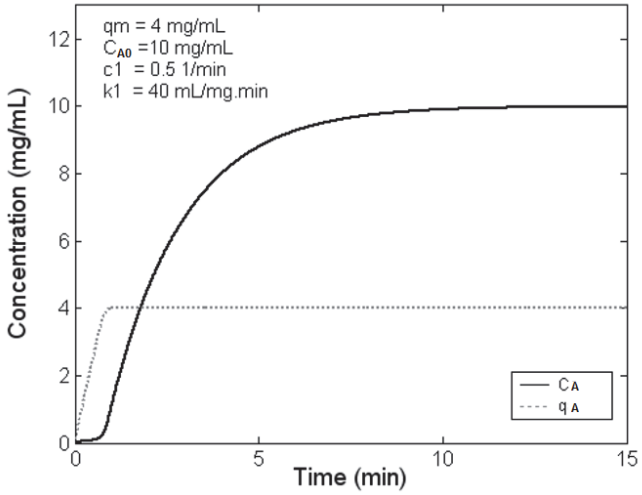

Fig. 6. Profiles of C_A and q_A for a high value of the kinetic constant of adsorption

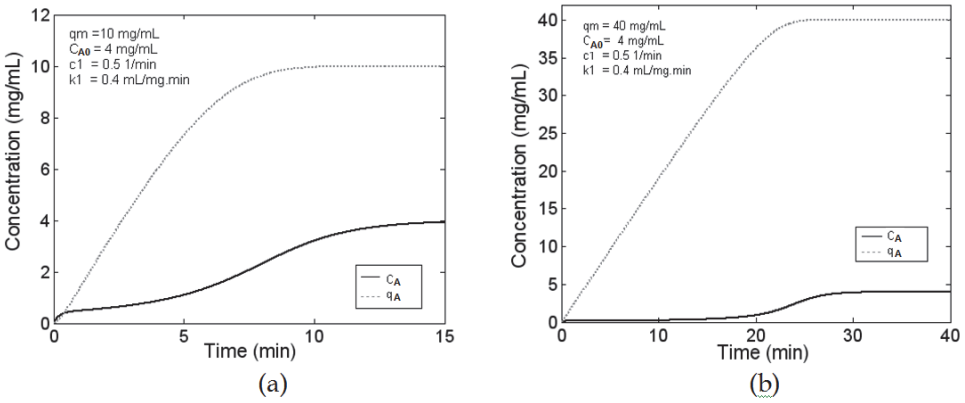

Fig. 7. Influence of q_m in the profile of C_A and q_A

2.2.2 Effects of the adsorption order

In this section, the effects of the stoichiometric coefficients or the order of adsorption on the dynamic behavior were analyzed. From Eqs. 9 and 10 it was assumed, in a first case, only the adsorption term (k_2=0) with the following stoichiometric coefficients (α=1, β=5) which lead to the next expressions

$$\frac{dC_A}{dt} = c_1.C_{A0} - c_1.C_A - k_1.C_A.(q_m - q_A)^5 \tag{13}$$

$$\frac{dq_A}{dt} = k_1.C_A.(q_m - q_A)^5 \tag{14}$$

A comparison is presented through Figs. 8a and 8b, which shows the simulation results from the adsorption kinetic of first (α=1, β=1) and fifth (α=1, β=5) order, respectively, with respect to the active sites concentration (solid phase). As can be seen from Fig. 8 the increase in the adsorption order of the active sites increases the rate of adsorption, leading to a steeper breakthrough curve. Another remark is the decrease in the capacity of adsorption as the final concentration of solute A (q_A) in the solid phase decreases. The decrease in the final amount of solute adsorbed can be attributed to the number of active sites that is necessary for the adsorption. From the adsorption kinetic of fifth order (α=1, β=5) is necessary the presence of 5 (five) adsorption sites to interact and adsorb the solute. At the end of the adsorption process the quantity of available sites is small and they must be close to each other to promote the adsorption of the molecule (for example, by the mechanism of fifth order, for five isolated sites it is not possible to have the adsorption of one solute molecule). The condition of close sites becomes more important as the order of adsorption increases, being necessary a higher quantity of close sites to promote the adsorption of the molecule.

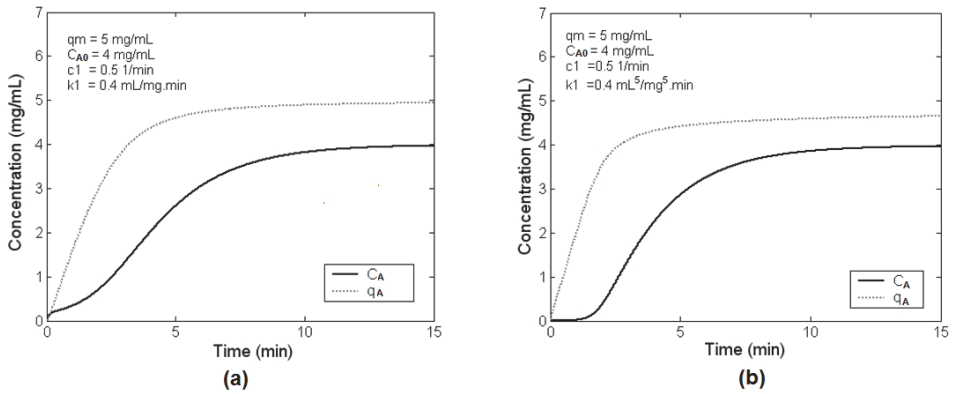

Fig. 8. Influence of the stoichiometric coefficients in the profile of C_A and q_A

2.2.3 Analysis of the separation process by adsorption and desorption

In this part of the work, the desorption term of Eqs. 5 and 6 are considered, with the stoichiometric coefficients equal to the unity (α, β and γ=1) Taking into account these considerations Eqs. 9 and 10 are transformed into

$$\frac{dC_A}{dt} = c_1.C_{A0} - c_1.C_A - k_1.C_A.(q_m - q_A) + k_2.q_A \tag{15}$$

$$\frac{dq_A}{dt} = k_1.C_A.(q_m - q_A) - k_2.q_A \tag{16}$$

The simulations from Eqs. 15 and 16 provided results with behavior equivalent to those obtained by the previous condition without the desorption term.
The Fig. 9 shows the simulation results of the adsorbed phase (q_A) varying the kinetic constant of desorption (k_2). From these results it can be observed that the higher the kinetic constant of desorption the lower the real capacity of adsorption as the final amount of solute adsorbed decreases. This information shows that although the adsorption can reach a maximum capacity (q_m), the real amount adsorbed will be determined by some parameters like the kinetic constant of desorption (k_2).

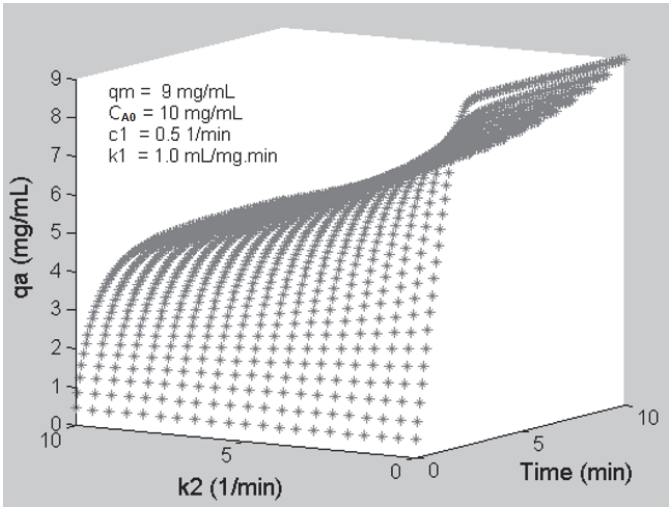

Fig. 9. Effect of the desorption parameter (k_2) over the amount of solute adsorbed (q_A)

Calculations using different adsorption and desorption orders were also performed, showing a great influence of these parameters on the dynamic answer of the chromatographic system. It is important to notice that higher values of the order of desorption (γ>1) significantly decreases the final amount of solute adsorbed with the increase in the kinetic constant of desorption (k_2).

2.2.4 Protein chromatography by steps of adsorption and desorption

Simulations results obtained for a continuous feed for a time period into the protein chromatography are shown in this part of the work. It is considered a flow of solute with a specific concentration being introduced into the column over an initial period of time. Figure 10 presents a typical result obtained with Eqs. 15 and 16, which correspond to a system with a rate of solute adsorption and desorption, for a feed over a time period of 10 min. After the time of feed (10 min), the initial concentration of solute was considered null (C_{A0}=0), which led the system to decrease exponentially the solute concentration of the liquid phase inside the column. Note that the concentration of solute adsorbed starts to

decrease after this point, although the kinetic constant of adsorption is higher than the kinetic constant of desorption (the same parameters for the adsorption and desorption steps). This is attributed to the solute concentration that becomes low, leading to a decrease in the term of adsorption, which is not compensated by the high kinetic constant of adsorption.

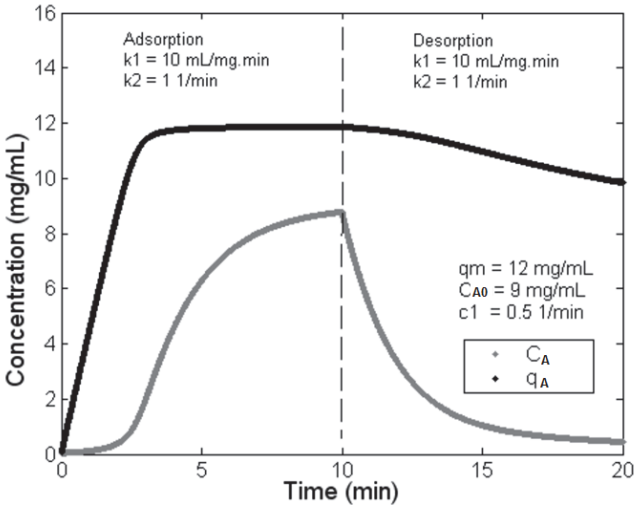

Fig. 10. Influence of feed in the steps of adsorption and desorption

A comparison between the simulation results and the experimental data from a chromatographic procedure of protein separation is presented in Fig. 11. Figures 11a and 11b present the calculations and the experimental data from Silva (2000), respectively.

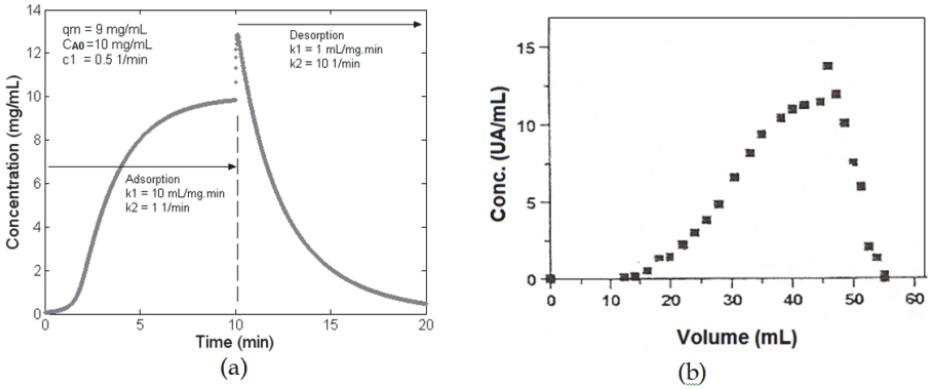

Fig. 11. Adsorption and desorption steps from simulation results (a) and experiments (b)

From the experiments, it can be observed that there is an increase in the solute concentration in the desorption procedure or wash, which corresponds to a volume higher than 45 ml. The wash procedure leads the solute concentration to a value that is higher than the initial concentration (C_{A0}=11.5 UA/mL; UA- enzymatic activity unit). From the simulations (Fig. 11a) it can be seen that an increase in the solute concentration can be reached by the increase in the kinetic parameter of desorption in the step of desorption. This fact is coherent once in the wash procedure the solvent is utilized to promote the desorption of the molecules adsorbed in the solid surface.

3. Irreversible kinetic model with batch adsorption

The agitated batch process of adsorption is an important method used for equilibrium parameters estimation, which are applied in the processes modeling such as chromatography and simulated moving bed (SMB) separation. The hydrodynamic aspects of these processes become the kinetic modeling an interesting tool for the process modeling in obtaining parameters that will be incorporated in the equipment design.
Some contributions in the application of adsorption kinetic models for the liquid phase can be encountered through the following publications: Thomas (1944), Chase (1984), Sarkar and Chattoraj (1993), Hamadi et al. (2001, 2004), Otero et al.(2004), Gulen et al.(2005) and Aroguz (2006). An important contribution comes from the work of Chase (1984), which implemented semi-analytical expressions to model the adsorption phenomenon in agitated tanks and chromatographic columns. He considered the kinetic concepts to model the adsorption process as a reversible system with an overall rate of second-order. In a general point of view, the above publications, with exception of the Chase model (Chase, 1984), use simplified or empiric expressions for the kinetic models. The advantage of utilizing the concepts of kinetic theory to develop new models is that the stoichiometric and order, related to the compounds in the adsorption system considered, can be varied and analyzed independently, leading to a better comprehension of the evolved kinetic phenomenology.
In this work was implemented an irreversible kinetic model of adsorption being it applied in the modeling of salicylic acid adsorption onto different adsorbents as the activated carbon (F400) in three different temperature conditions. The model adjustment through the experimental data is done with the application of an inverse problem approach that minimize the square residues of a cost function.

3.1 Formulation of the adsorption kinetic model

The agitated adsorption techniques to measure adsorption properties are modeled with the following expression for batch processes

$$r_j = \frac{1}{V}\frac{dN_j}{dt} \tag{17}$$

in which r_j, that corresponds to the adsorption rate of component j, is proportional to the variation of the moles number of solute j (N_j) with time. The tank volume (V) is assumed to be constant.
The adsorption stoichiometry considered is represented in Fig. 12. It is related to an irreversible kinetic of adsorption with a kinetic constant k_i. This adsorption mechanism depends both on the solute concentration (liquid phase) and the active surface concentration on the solid phase (site concentration on solid phase).

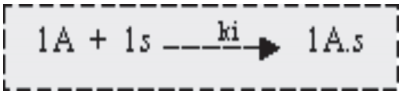

Fig. 12. Representation of the adsorption mechanism assumed.

The adsorption mechanism of Fig. 12 considers the adsorption of 1 (one) mol of solute A on 1 (one) mol of active site (*s*). The kinetic modeling, in terms of consumption rate of solute *j* (r_j), is written in the following form.

$$(-r_j) = k_i C_j{}^n . C_s{}^m \tag{18}$$

where k_i, C_j and C_s represent the kinetic constant, the concentration of solute *j* in the liquid phase and the concentration of sites of adsorption in the solid phase, respectively. For a first order elementary adsorption, the exponents *n* and *m* are equal to 1, which corresponds to an overall rate of second order. The irreversible adsorption is an adequate hypothesis, since in the experimental studies (Pereira, 1999 and Silva, 2000) the desorption procedures are necessary to return the original adsorbent properties, without solute traces. This is done with elution and washing steps.

With the considerations just described, Eq. (18) can be solved analytically through expression (17), applying a balance in the moles number of active sites of adsorption, i.e.

$$C_t = C_s + C_{A.s} \tag{19}$$

in which C_t corresponds to the maximum concentration of adsorption sites, that is the sum between the concentration of vacant sites (C_S) and occupied sites by solute A (C_{AS}). Another important balance is related to the concentration of solute A. In the balance of solute A, the initial concentration in the solution (C_{A0}) corresponds to the sum of the final solute concentration in the solution (C_A) and the adsorbed solute concentration in the solid phase (C_{AS}), i.e.

$$C_{A0} = C_A + C_{A.s} \tag{20}$$

The combination of Eqs. (17-20) leads to

$$\int \frac{dC_A}{C_A(a + C_A)} = \int -k_i dt \tag{21}$$

in which $a = C_t - C_{A0}$. Performing the integrations in Eq. (21) and utilizing the initial and equilibrium conditions lead to the final expressions for the time dependent concentration of solute A (Eq. 22) as a function of C_t, C_{A0} and k_i.

$$\frac{C_A}{a + C_A} = \left(\frac{C_{A0}}{a + C_A} \right) e^{-a.k_i.t} \text{ or } C_A = \frac{a.C_{A0}}{(a + C_{A0})e^{-a.k_i.t} - C_{A0}} \tag{22}$$

Note that the implemented IKM2 (irreversible kinetic model of second order) expression comes from the balance of moles following the moles relation shown in Fig. 12, which can be calculated independently of the volume of each phase. The parameter *a* in the IKM2 (Eq. 22)

can be replaced by the term -C_{eq} (equilibrium concentration of solute A in the liquid phase) becoming the model only dependent on the liquid phase parameters.
The Fig. 13 presents the correlation results between the IKM2 model and the experimental data from Otero *et al.* (2004). As can be observed from the Fig. 13 the IKM2 model showed high fit correlating the experimental points over all temperature conditions.
The IKM2 model was highly satisfactory correlating the experimental data both at the initial period of time and at long times. It provided better correlation results, according to best fits, than those obtained by Otero *et al.*, 2004, which applied a linear driving force (LDF) model for the adsorption kinetic.
An interesting characteristic of the implemented model (IKM2) is the very small computational effort in obtaining the simulation results. It is related to the analytical form of the mathematical expression (Eq. 22). Besides the good agreement with the real experimental data, the kinetic model described (IKM2) requires only two parameters (C_{A0} and C_t or C_{eq}) to obtain the rate kinetic constant (k_i).

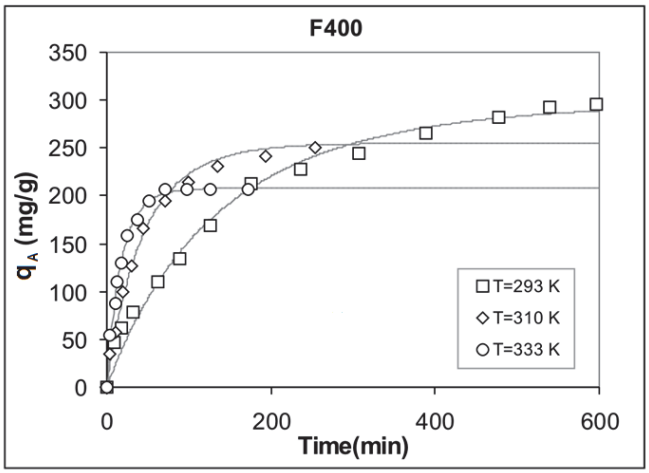

Fig. 13. IKM2 fit with experimental adsorption data of salicylic acid on F400 adsorbent.

4. Acknowledgment

The authors acknowledge the support from the institutions UERJ, UFRJ, Capes, CNPq and Faperj.

5. Conclusions

The kinetic mechanisms presented showed potential in the representation of different adsorption systems involved with mass transfer in the chromatographic separation processes.
The modeling of the chromatographic column by the mass balance models of perfect mixture with the concepts of heterogeneous adsorption mechanisms showed to represent the behavior of the chromatographic processes of adsorption. The simulation results

showed that either the maximum capacity of the adsorbent and the kinetic constant of adsorption and desorption influenced significantly the dynamic behavior of the system. The stoichiometric parameters, related to the order of adsorption and desorption, showed to be also very important for the dynamic of the separation process, being a crucial tool for the comprehension about the dominant mechanism of adsorption. The stoichiometric parameters showed to influence the equilibrium amount of solute adsorbed. This fact was also observed for the reversible mechanism, in which the higher the kinetic constant of desorption the lower the final amount of solute adsorbed. The closer behavior to the chromatographic answer was obtained by the models with higher orders related to the adsorption term. This observation direct to mechanisms of adsorption that the number of sites necessary to promote the solute adsorption is great, which indicate that more than one site participate in the adsorption process.

The analytical kinetic model of adsorption implemented (IKM2) has proved to be satisfactory due to a number of aspects. Firstly, it provided better agreements with experimental data when compared to other kinetic models, such as the kinetic model of linear driving force (Otero *et al*., 2004). Other relevant aspects are related to the necessity of a small number of parameters in the model and the straightforward procedure obtaining the solution. The consideration of an acceptable error domain for the equilibrium concentration (C_{eq}) provided good results by reductions in the residues cost function, which led to a better experimental correlation with an increase in the accuracy of the parameters estimated.

6. Nomenclature

k_1	Kinetic constant of adsorption
k_2	Kinetic constant of desorption
k_i	Irreversible kinetic constant of adsorption
$(-r_A)$	Rate of consumption of molecules A in the liquid phase
(r_{SA})	Rate of adsorption of molecules A in the solid phase
C_A	Solute concentration in the liquid phase
C_s	Vacant active sites of adsorption in the solid phase
q_A	Solute concentration in the solid phase
C_t	Maximum concentration of adsorption sites in a kinetic experiment
q_m	Absolute maximum concentration from isotherm data
F_j	Molar flow of the molecules j
N_j	Number of moles of the molecules j
V	Volume of the column
Q	Volumetric flow
ε	Column bed porosity
α,β,γ	Stoichiometric coefficients of the adsorption

7. References

Aroguz, A.Z., 2006, "Kinetics and Thermodynamics of Adsorption of Azinphosmethyl from Aqueous Solution onto Pyrolyzed (at 600º C) Ocean Peat Moss (Sphagnum sp.)", Journal of Hazardous Materials.

Câmara, L.D.T.; Santana, C.C. & Silva Neto, A.J. (2007). Kinetic Modeling of Protein Adsorption with a Methodology of Error Analysis, *Journal of Separation Science*, ISSN 1615-9306, 30/5, 688-692.

Chase, H.A., 1984, "Prediction of the Performance of Preparative Affinity Chromatography", J. Chromatography, Vol. 297, pp. 179-202.

Cruz, M. C., 1997, Adsorption of insulin on ion exchange resin utilizing fixed and fluidized bed, M. Sc. Thesis, Universidade Estadual de Campinas, Faculdade de Engenharia Química, Campinas-SP, Brazil. (In Portuguese)

Felinger, A., Zhou, D., & Guiochon, G., 2003, "Determination of the Single Component and Competitive Adsorption Isotherms of the 1-Indanol Enantiomers by Inverse Method", Journal of Chromatography A, Vol. 1005, pp. 35-49.

Fogler, H.S. (2006). Elements of Chemical Reaction Engineering. *Prentice Hall,* 4th ed., ISBN 0-13-047394-4

Goldstein, S., 1953, Proc. Roy. Soc.(London), vol. A219, pp. 151.

Guiochon, G. & Lin, B., 2003, Modeling for Preparative Chromatography, Academic Press, San Diego.

Gulen, J., Aroguz, A.Z., & Dalgin, D., 2005, "Adsorption Kinetics of Azinphosmethyl from Aqueous Solution onto Pyrolyzed Horseshoe Sea Crab Shell from the Atlantic Ocean", Bioresource Technology, Vol. 96, pp. 1169-1174.

Hamadi, N.K., Chen, X.D., Farid, M.M.,& Lu, M.G.Q., 2001, "Adsorption Kinetics for the Removal of Chromium(VI) from Aqueous Solution by Adsorbents Derived from Used Tires and Sawdust", Chemical Engineering Journal, Vol. 84, pp. 95-105.

Hamadi, N.K., Swaminathan, S., & Chen, X.D., 2004, "Adsorption of Paraquat Dichloride From Aqueous Solution by Activated Carbon Derived from Used Tires", Journal of Hazardous Materials B, Vol. 112, pp. 133-141.

Otero, M., Grande, C.A., & Rodrigues, A.E., 2004, Adsorption of Salicylic Acid onto Polymeric Adsorbents and Activated Charcoal, Reactive & Func. Polymers, vol. 60, pp. 203-213.

Pais, L.S., & Rodriguez, A.E., 2003, Design of Simulated Moving Bed and Varicol Processes for Preparative Separations with a Low Number of Columns, J. Chrom. A, v.1006, pp. 33.

Pereira, J.A.M., 1999, "Adsorption of β-Galactosidase from Scopulariopsis sp in Ion Exchange Resin with Purification and Scaling-up objective", D.Sc. Thesis, Universidade Estadual de Campinas, São Paulo, Brazil. (In Portuguese)

Ruthven, D.M., 1984, Principles of adsorption and adsorption process simulation, Wiley, New York.

Rodriguez, A.E., & Minceva, M., 2005, Modelling and simulation in chemical engineering: Tools for process inovation, Comp. Chem. Eng., vol. 29, pp. 1167-1183.

Sarkar, D., & Chattoraj, D.K., 1993, "Activation Parameters for Kinetics of Protein Adsorption at Silica-Water Interface", Journal of Colloid and Interface Science, Vol. 157, pp. 219-226.

Silva, F.R.C., 2000, "Study of Inulinases Adsorption in Columns with Ion Exchange Resin: Experimental Parameters and Modeling", D.Sc. Thesis, Universidade Estadual de Campinas, São Paulo, Brazil. (In Portuguese)

Thomas, H., 1944, "Heterogeneous Ion Exchange in Flowing System", J. Am. Chem. Soc., Vol. 66, pp. 1664-1668.
Wade, J.L., Bergold, A.F. & Carr, P.W., 1987, Anal. Chem., vol. 59, pp. 1286.

2

The Gas Diffusion Layer in High Temperature Polymer Electrolyte Membrane Fuel Cells

Justo Lobato, Pablo Cañizares, Manuel A. Rodrigo and José J. Linares
Chemical Engineering Department, University of Castilla-La Mancha
Spain

1. Introduction

1.1 Polymer electrolyte membrane fuel cells. Operation at high temperature (120-200ºC)

1.1.1 General overview

Polymer Electrolyte Membrane Fuel Cells (PEMFC) can be considered as one of the most attractive type of fuel cells. They are able to produce efficiently high power densities. In addition, the use of a polymer electrolyte implies several advantages (Fuel Cell Handbook, 2004), such as low problems of sealing, assembling and handling. No corrosive acids, compared to Phosphoric Acid Fuel Cells (PAFC) are used, and the low temperature of the cell allows faster responses to changes in load demands. The characteristics of these cells make them especially suitable for automotive applications, even though they are also used for stationary generation, and currently, there is a great research effort for its application on portable devices (laptops, mobile phones, cameras, etc.).

PEMFC are composed of the following basic elements:

- Ionic exchange membrane (PEM).
- Gas diffusion layer (GDL).
- Catalytic layer (CL).
- Monopolar/bipolar (in case of a stack) plates.

The combination of the GDL+CL+PEM forms the *membrane-electrode-assembly (MEA)*, which is the real heart of a PEMFC. This MEA can be formed by applying pressure and temperature to the (GDL+CL) in the anode side/PEM/(GDL+CL) in the cathode side (hot pressing procedure), or by directly depositing the CL onto the PEM, and subsequent hot pressing with the GDL.

Ionic exchange membrane fulfils the role of allowing the transient of ionic charges from the anode to the cathode, closing the electrical circuit. It also possesses a low permeability to the gases, in order to avoid the depolarization of the electrode (Savadogo, 2004). A high mechanical and chemical stability is also required for these materials, due to the harsh operational conditions (oxidant and reducing gases in an acid medium). The most extended PEM material is Nafion®, a perflurosulphonated material, whose structure consists of a perfluorocarbon skeleton (Teflon-like), onto which, branch chains with pendant sulphonic acid groups are located, allowing the transient of ionic charges (see Figure 1).

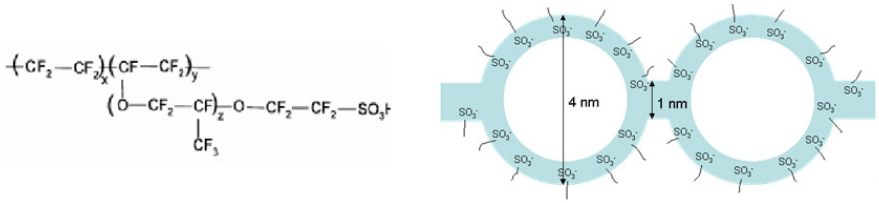

(a) (b)

Fig. 1. (a) Nafion structure, (b) organization within the Nafion membranes of the hydrophilic domains (blue) allowing the transient of protons

The gas diffusion layer (GDL) is placed between the catalytic layer and the bipolar plates (Cindrella et al., 2009). It will be later explained in more detail, but its basic function is to manage the access of the reactants, and the exit of the products (Benziger et al., 2005; Mathias et al., 2003; Williams et al., 2004). This layer is made of a carbonaceous support, onto which it can be deposited another layer, the microporous layer (MPL), formed by carbon black and a certain amount of a polymer binder. In traditional low temperature, this GDL also playes the role of an effective removal of the liquid water is produced in the cathode, in order to avoid the flooding of the electrode (Benziger et al., 2005; Mathias et al., 2003; Prasanna et al., 2004a).

The catalytic layer is the part of the cell where the electrochemical reactions take place. It is placed between the electrolyte and the gas diffusion layer (Mathias et al., 2003). This layer is generally formed by the own catalyst deposited on a porous carbon support. The most widely used catalyst for the reactions that take place in the cell (hydrogen oxidation and oxygen reduction) is platinum. A second element of this layer is the own carbon support, which acts as electronic conductor, and allows the dispersion of the platinum catalyst on its surface. The role of binder between the catalyst particle is performed by the own polymeric electrolyte. This also presents an additional advantage, since the catalyst active sites are in intimate contact with an ionic carrier, increasing its activity (Carrete et al., 2001). This apparent network is widespread all over the catalyst layer structure, forming the so-called three phase boundary.

Monopolar/Bipolar plates are the last element of a fuel cell. They act as support of the previous described elements, allow the access and exit of the reactants and products, respectively, and must allow an uniform current distribution/collection. At laboratory scale, the most widely used material is graphite. However, its high cost and fragility make it relatively unviable for practical applications. Instead stainless steel or titanium plates are proposed, even though platinum, gold or silver plating are recommended in order to alleviate the corrosion problems of those raw materials.

1.1.2 Increasing the operating temperature

Operating at temperatures above 100ºC possesses some advantages (Li et al., 2003a; Li et al., 2004; Savadogo, 2004; Wainright et al., 2003):

- Faster kinetic of the electrochemical reactions.
- Easier water management and cooling system
- Possibility of co-generation.
- Higher tolerance to fuel impurities (e.g., CO) (Li et al., 2003b).

This implies the use of a thermal resistant material, which, at the same time, has to be a proton conductor. A large number of option have been researched and developed in order to increase the operational temperature (Bose et al., 2011). However, among the different options, phosphoric acid impregnated polybenzimidazole (PBI) has emerged as the most interesting and well-established one.

Firstly discover for fuel cell applications by Prof. Savinell's group in Case Western Research University (Wainright et al., 2003), PBI is an aromatic heterocyclic polymer with two benzimidazolic ring linked by a phenyl group. It possesses a high thermal and chemical resistance, with a glass transition temperature of approx. 450ºC (Wainright et al., 2003), as corresponds to a thermoplastic amorphous polymer with a high degree of aromaticy. Benzimidazole groups of PBI provide certain basicity, allowing the impregnation with phosphoric acid. Some advantages of the use of this material are next listed:

- Good conductivity up to 200ºC (Li et al., 2004, Lobato et al., 2006).
- Low methanol permeability (Wang et al., 1996, Lobato et al., 2008a).
- Excellent thermal stability, up to 500ºC in air (Samms et al., 1996).
- Almost zero electro-osmotic drag coefficient (Weng et al., 1996), making unnecessary the pre-humidification of the reactant streams.
- Enhancement of the kinetic of the oxygen reduction reaction compared to PAFC (Qingfeng et al., 2000).

2. Mass transport in polymer electrolyte membranes fuel cells

As previously described, a fuel cell is an electrochemical reactor, in which reactants are consumed, and consequently, new products are generated. This evidently leads to the appearance of concentration gradients, giving rise to mass transport phenomena. In addition, the complex design of the electrodes, with several layers sandwiched together, and the convoluted architecture of each one make it even more difficult the transport of the different species from/to the electrode, leading to the appearance of mass transport limitations if the system design is not the appropriate one.

Mass transport processes already start in the flow fields of the monopolar/bipolar plates. In them, the reactant gases access to the fuel cell system, whereas the products have to leave it. Due to the dimensions of the flow fields, in the scale of millimeters, mass transport is dominated by convection and the corresponding laws of fluid dynamics. In the case of the electrode (GDL+CL), the tiny pore sizes make diffusion to govern the mass transport. The tortuous geometry of the GDL+CL isolates the gas molecules from the convective forces present in the flow channels. Gas transport inside the electrode is a complex processes. The gas must diffuse within the gas diffusion layer, to achieve the catalytic layer, and then, inside this, the gas must access to the active catalyst sites. These catalyst sites are usually covered by a certain amount of electrolyte (Lai et al., 2008; Lobato et al., 2010a), and hence, the reactant gases and the products must also diffuse through it, complicating, even more, the mass transfer processes. Figure 2 shows a typical concentration/partial pressure profile of a PEMFC.

Mass transfer processes have implications in practically all the elements of the fuel cell. In the case of the flow field channels, they should provide an homogeneous distribution across the electrode external surface, minimize the pressure drop, and efficiently remove the product reactions. In the case of the GDL, the requirements are almost the same, even though the inexistence of convection forces makes more difficult the access of the reactants,

and the removal of the products. Thereby, this elements is notoriously more critical in this sense. The catalytic layer also requires an optimum design in order to facilitate all the mass transfer processes. In fact, an excessive amount of polymeric electrolyte causes the appearance of significance mass transfer limitations in the catalytic layer (Song et al., 2001). Finally, the own polymeric electrolyte has got also an important role, since the solubility of the gas in it is highly dependant on the cell operation conditions (Liu et al., 2006).

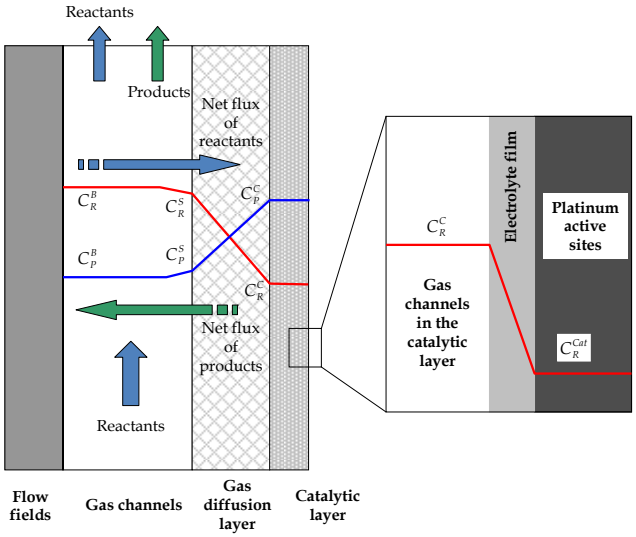

Fig. 2. Typical concentration profile inside a fuel cell

In the case of H_3PO_4 doped PBI-based high temperature PEMFC, compared to traditional Nafion®-based PEMFC, mass transport becomes slightly simpler since all the species are in vapour state, and therefore, flooding problems do not appear (Lobato et al., 2008b). However, this does not imply that mass transport processes are not important in terms of cell performance. Indeed, as previously commented, it is necessary an optimum transport of hydrogen and oxygen gas across the gas diffusion layer. Moreover, the removal of the water vapour generated in the cathode must be effective. In the catalytic layer of this type of fuel cells, phosphoric acid is present in order to provide a protons pathway for their migration, and hence, oxygen and hydrogen must diffuse through this thin electrolyte layer. Oxygen solubility in phosphoric acid has been reported to be low, compared to, for example, Nafion® (Mamlouk et al., 2010), which also results in an extra-limitation in terms of mass transfer within the catalytic layer.

3. The role of the gas diffusion layer in high temperature PEMFC

The membrane-electrode-assembly of a phosphoric acid doped PBI-based PEMFC is similar to traditional low temperature Nafion®-based PEMFC, i.e., is formed by the membrane, and the electrodes. The electrodes, at the same time, are divided into two layers, the catalytic one, and the gas diffusion layer. The gas diffusion layer in high temperature PEM fuel cells must fulfil the following purposes (Benziger et al., 2005; Mathias et al., 2003; Williams et al., 2004):

- Good transport properties, for a uniform distribution of the reactants across the electrode surface.
- High electronic conductivity to allow the transient of electrons between the catalytic layer and the bipolar/monopolar plate.
- Good mechanical resistance, since this layer is the support of the catalytic one.
- Good removal capacity of the water vapour produced in the cathode.

The GDL is formed by a carbonaceous support, generally carbon cloth or carbon fibre paper (Han et al., 2008), relatively rigid, macroporous, and highly conductive (Cindrella et al., 2009). Generally, this carbon support is wet-proofed with a certain amount of Teflon, which assists in an effective water management, and provides a pathway for the access of the reactant gases when massive amounts of water are being generated in the cathode (Park et al., 2004). Also, this amount of Teflon helps to keep the mechanical integrity of the gas diffusion layer during the hot pressing procedure used to prepare the membrane-electrode-assembly (MEA) (Lobato et al., 2008b).

In some cases, a second layer is incorporated to the GDL design, the microporous layer. As previously commented, this layer is formed by carbon black (Vulcan XC-72R, Ketjen Black, Acetylene Black...) (Antolini et al., 2002), and a certain amount of a polymeric binder (generally Teflon) (Carrete el al., 2001; Mathias et al., 2003). Both components, along with an appropriate solvent (generally non-toxic, e.g., isopropyl alcohol, water, ethylene glycol...) (Carrete et al., 2001) is generally deposited by forming a thick ink, and applied by different techniques, filtration, with the aid of an aerograph, tape-casting, etc. The properties of the ink and deposition method influence on the final mass transport properties of this layer (Cindrella et al., 2009; Mathias et al., 2003). The composition of this layer makes it have a microporous nature, with the following advantages:

- Uniform current distribution between the catalyst layer and the carbonaceous support, due to a more intimate contact between the layers.
- Avoid the penetration of catalyst particles in the carbon support, which would be located too far away from the membrane-electrode boundary, where most efficiently evolve the electrochemical reactions (Seland et al., 2006).

Figure 3 shows a schematic structure of a general electrode (including MPL) for a high temperature phosphoric acid doped PBI-based PEMFC.

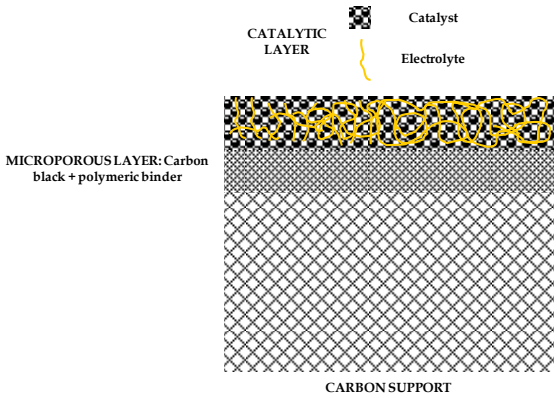

Fig. 3. Schematic general structure of an electrode with microporous layer

Therefore, in order to maximize the cell performance not only in terms of mass transfer, but in global terms, it is logically necessary to have an optimum gas diffusion layer structure, both in terms of the carbon support, and microporous layer. For this purpose, physical and electrochemical characterisation of the gas diffusion layer is performed, as it will be shown in the following sections.

3.1 The carbon support. Influence of the Teflon percentage

Carbon cloth, carbon fibre papers, or carbon felt are different options to be used as carbonaceous support in PEM Fuel Cells. Although any of them presents different advantages and disadvantages, carbon fibre papers is interesting in terms of robustness and mechanical reliability. This carbon paper is supplied by the Japanese company *Toray Industries Inc.*, with different thickness 90, 170, 260 and 350 μm), and also with the possibility of different levels of wet-proofing (Teflon percentage on the basis of the carbon paper weight). If the MEA is prepared by hot pressing, thick carbon supports are more suitable in terms of mechanical integrity. For this material, a very interesting parameter to be analyzed is the influence of the Teflon on its physical properties, and on the electrochemical performance of the subsequent prepared electrode.

3.1.1 Physical characterisation

Next, some results of useful physical characterization techniques are presented. The physical parameters next evaluated have got a strong influence on the mass transport properties of the GDL, and therefore, on the cell performance in terms of mass transfer parameters (limiting current density).

A typical *pore size distribution* of the carbon fibre paper (Toray Graphite Paper, TGPH-120, 350 μm) obtained from *Hg porosimetry* for the different Teflon percentage is shown in Figure 4.

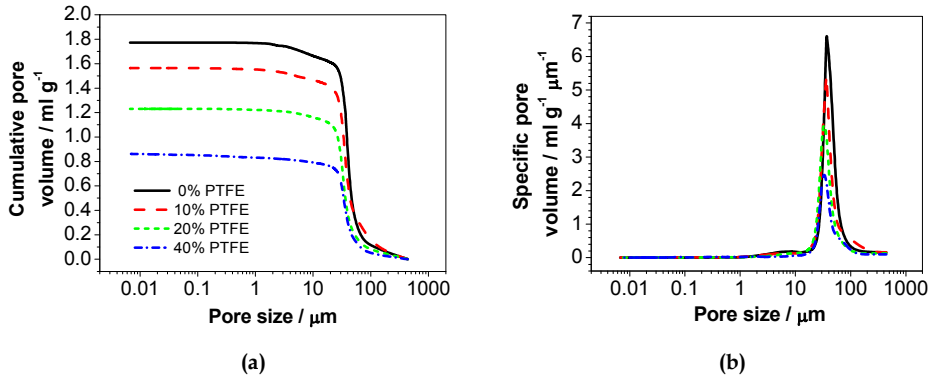

Fig. 4. (a) Cumulative, and (b) Specifical pore size volume for the differente Teflon percentage in the carbon fibre paper (TGPH-120) (Lobato et al., 2008b, with permission of Kluwer Academics)

As it can be seen, the carbon support present a macroporous structure, with most of the pores in the range of 30-70 μm. Moreover, Teflon content reduces the macroporosity of the carbon paper. From the pore size distribution, other interesting parameters can be

evaluated, such as the *overall porosity, the mean pore size, and the tortuosity*. Table 1 collects the corresponding values.

PTFE content / %	Porosity / %	Mean pore diameter / μm	Tortuosity
0	76.3	39.4	2.932
10	73.9	36.7	3.363
20	69.6	33.9	3.582
40	61.6	31.6	4.377

Table 1. Overall porosity, mean pore size and tortuosity of the carbon support for the different Teflon loading percentage (Lobato et al., 2008b, with permission of Kluwer Academics)

As expected from the pore size distribution curves, porosity and mean pore size diminishes with the increase in the Teflon content, whereas the tortuosity increases with the Teflon content. Porosity and tortuosity are important parameters, since they directly influence on the effective diffusion coefficient (Williams et al., 2004), according to Equation 1.

$$D_{eff} = D \cdot \frac{\varepsilon}{\tau} \tag{1}$$

Scanning electron microscopy is also a very useful tool in order to visualize the microstructure of the gas diffusion layer. Figure 5 displays the micrographs of the Toray Graphite Papers for the different Teflon percentage.

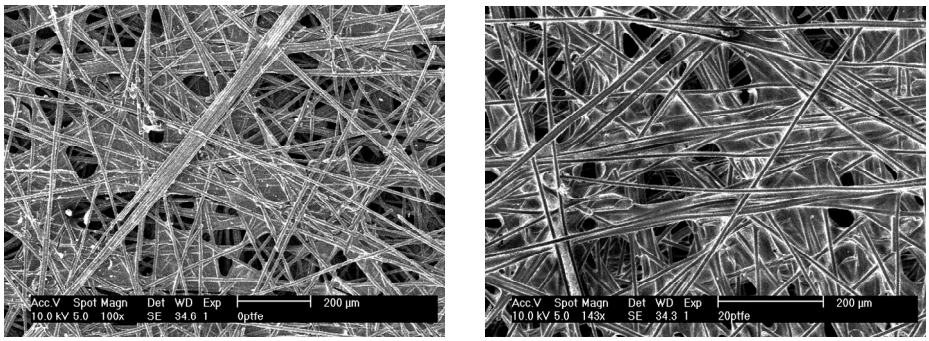

(a) (b)

Fig. 5. SEM micrographs of (a) Plain carbon fibre paper, (b) 20% wet-proofed carbon paper (Lobato et al., 2008b, with permission of Kluwer Academics)

As it can be seen, appreciable differences appear between both carbon papers. When Teflon is applied, a large number of macropores are closed by the presence of the polymer binder, reflecting the previous results obtained by Hg porosimetry. Teflon occupies parts of the macropores between the carbon fibres.

Gas diffusion layer *permeability* is another interesting parameter. Although this parameter is related with convectional processes, it can give us a rough idea about the transport properties of the gas diffusion layer. Figure 6 shows the gases (H_2, O_2, air and water vapour) permeability of the different carbon support. For its calculation, Equation 2 must be used.

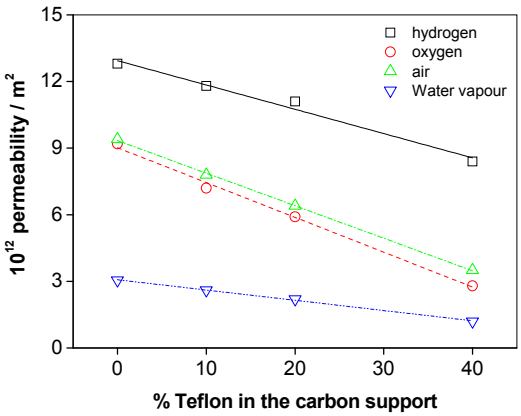

Fig. 6. Gases permeability of the carbon support for different Teflon contents

$$K = \frac{Q \cdot \mu \cdot L}{S \cdot \Delta P} \tag{2}$$

As expected, gas (or water vapour) permeability reduces with the Teflon content due to the blockage of part of the macroporosity by the Teflon (Prasanna et al., 2004a; Prasanna et al., 2004b; Soler et al., 2003; Williams et al., 2004). It is especially significant the value of the water vapour permeability, since in this type of fuel cell, water product will be in this state.

Gases permeability follows the expected trend according to their molecular size. Hydrogen permeates easily through the carbon support, whereas oxygen and air have got a more limited access. This, as will be later shown, reflects on the fuel cell performance, where hydrogen mass transport limitations are less noticeable than in the case of oxygen. In the case of water vapour, the fashion is broken, but this might be due to the vapour nature compared to gases.

3.1.2 Electrochemical behaviour

The electrochemical behaviour of a fuel cell is mainly defined by the polarization curves. As it was previously described, three main regions appear, each one related to different processes governing the performance. In this particular case, mass transport properties of the carbon support will mainly influence the cell performance at the highest current densities, where large amounts of gas reactants are claimed, and massive amounts of water vapour have to be released from the cell. In order to assist for the interpretation of the fuel cell results, a semi-empirical model (Linares, 2010) was developed, which includes kinetic, ohmic, and mass transport parameters (Equation 3).

$$E = E_0' - b \log j - R_e j + b \ln\left(1 - \frac{j}{j_{OL}}\right) - R_{pol} \cdot j \cdot \left(\frac{j_{HL}}{j_{HL} - j}\right)^{1/2} \tag{3}$$

Parameter E is the cell voltage, E_0 is the open circuit voltage, b is the Tafel slope, being these two latter related to the mechanism of the oxygen reduction reaction, R_e is the ohmic resistance of the system, j is the experimental current density, j_{OL} is the limiting cathode current density, R_{pol} is the lineal polarization resistance of the hydrogen oxidation reaction, and j_{HL} is the limiting anode current density.

Impedance can be also an interesting tool to identify the appearance of mass transfer limitations associated with the gas diffusion layer (Bultel et al., 2005; Ciurenau et al., 2001; Ciurenau et al., 2003; Springer et al., 1996; Paganin et al., 1998). In general, it is admitted that the appearance at low cell voltage (high current densities) of a second loop in the typical one-loop spectrum of a fuel cell (Yuan et al., 2007) is due to mass transfer limitations in the gas diffusion layer.

Influence of the percentage of Teflon in the carbon support was studied for both the anode and the cathode. In the case of the cathode, results for reduced stoichometries and air were subjected to study, along with the impedance response of the cell when air was used. In the case of hydrogen, it was analyzed the performance under a limited H_2 stoichometry.

i) The carbon support in the cathode

Figure 7 shows the cell performance for the 10-20-40% Teflon in the carbon support. Points represent the experimental data, whilst lines represent the fitting to the semi-empirical model.

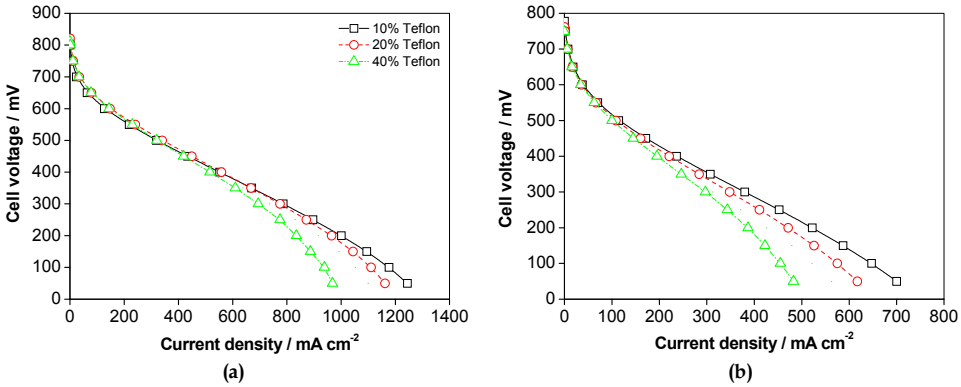

Fig. 7. Fuel Cell performance for the different Teflon percentage in the carbon support: (a) Oxygen stoichometry at 1 A cm^{-2} = 1,5, (b) Air stoichometry at 1 A cm^{-2} = 4

As it can be seen, the presence of a large amount of Teflon in the carbon support diminishes the cell performance, especially at the highest current densities. The corresponding values of the limiting current density are collected in Table 2. They resemble to the fashion of a more limited transport properties of the carbon support the higher is the Teflon percentage. On the other hand, it can be seen the detrimental effect of substituting oxygen by air. Reduction of the oxygen partial pressure dramatically influences the cell performance.

Figure 8 shows the impedance spectra of the cell under air operation, at a cell voltage of 300 mV. Points represent the experimental data, whereas lines show the fitting to the equivalent circuit. In order to help to split the contribution of each process, a equivalent circuit (Boukamp, 1986) consisting of a series association of one ohmic resistance, one parallel mini-

circuit constant phase element and resistance, related to the charge transfer processes (kinetic), and another parallel mini-circuit constant phase element and resistance, associated to mass transfer, is proposed [see Fig. 7(a)]. Table 2 also collects the values of the corresponding mass transfer resistances.

As it can be seen, and concomitantly to fuel cell results, impedance spectra show how the total resistance of the system increases the higher is the Teflon percentage. More concretely, mass transfer resistance calculated from the fitting of the experimental data to the equivalent circuit confirms this notorious increase in R_{mt}. In consequence, a low Teflon percentage in the carbon support is desirable in order to favour the mass transport processes. A non wet-proofed carbon paper may be utilized; however, mechanical integrity of the electrode may be risked, due to the weakness of this particular carbon paper (Lobato et al., 2008b).

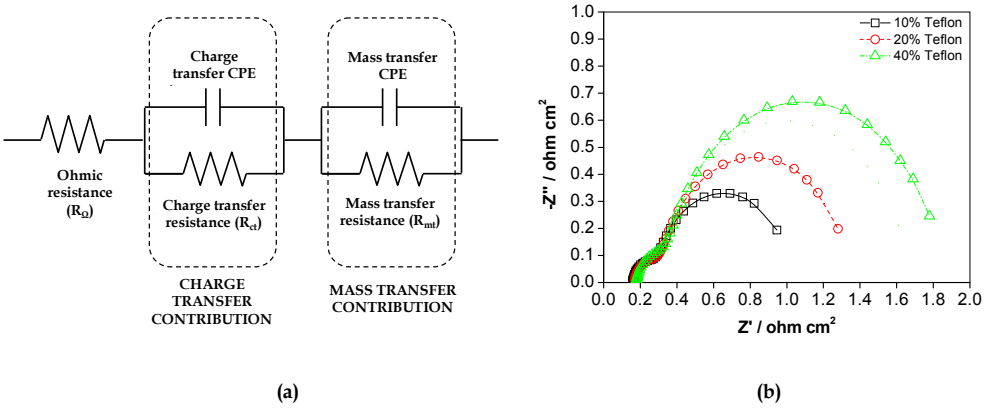

Fig. 8. (a) Equivalent circuit for the fitting of the experimental impedance data, (b) Impedance spectra of the electrodes with different Teflon percentages

PTFE content / %	$j_{OL,oxygen}$ / mA cm^{-2}	$j_{OL,air}$ / mA cm^{-2}	R_{mt} / ohm cm^2
10	1,418.9	952.8	0.744
20	1,272.1	786.6	1.041
40	1,029.8	562.2	1.502

Table 2. Limiting current densities for oxygen and air operation, and the mass transfer resistance for the different Teflon percentage in the carbon support.

ii) The carbon support in the anode

Figure 9 shows the fuel cell performance for the different Teflon loaded carbon supports.

As it can be seen for all the Teflon percentages in the carbon support, the cell performances are almost equal, and just tiny differences are observed when achieving the limiting current density conditions. This demonstrates that the controlling reaction in high temperature PBI-based PEMFC is the cathodic one (Jalani et al., 2006). Differences just appear at limiting conditions, as it was also observed by Pan et al. (Pan et al., 2007). Table 3 collects the corresponding values for the hydrogen mass transfer.

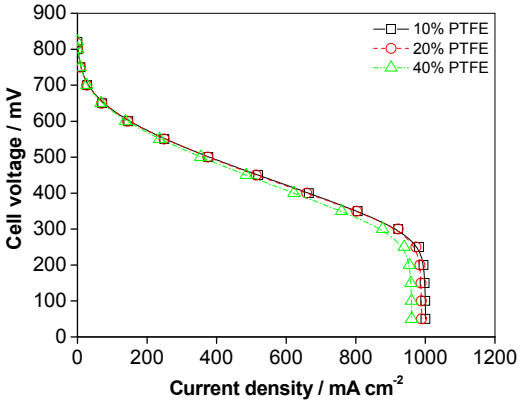

Fig. 9. Influence of the Teflon percentage on the cell performance. Hydrogen stoichometry at 1 A cm^{-2} = 1 (Points: experimental data; lines: fitting to the model)

Values in Table 3 confirm the expected reduction in the limiting current density due to the most limited hydrogen transport from the gas channels to the catalytic layer. However, it is noticeable that these values are very close to the stoichometric ones, so that, in principle, hydrogen transport in the carbon support, unless very limited hydrogen flow, is not a limiting factor in the performance of a High Temperature PEMFC.

PTFE content / %	$j_{HL,hydrogen}$ / mA cm^{-2}
10	1,000.9
20	990.1
40	961.9

Table 3. Limiting current density for the hydrogen oxidation for the different Teflon percentages of the carbon support

3.2 The microporous layer

As it was previously commented, the microporous layer is deposited on the carbon support, and is formed by carbon black and a polymer binder, in this case, Teflon. As in the case of the carbon support, two types of studies were carried out:

- Physical characterisation. Measurements of the pore size distribution, overall porosity, mean pore size, tortuosity, and finally, the permeability to the different reactants and water vapour product.
- Electrochemical behaviour. Evaluation of the cell performance under restricted stoichometries. Impedance spectra are also used in order to assist for the interpretation of the mass transfer influence on the fuel cell results.

Physical characterisation was carried out on the complete gas diffusion layer, i.e., the sum of the carbon support (*10% Teflon loaded TGPH-120*) and the microporous layer. In the case of the electrochemical studies, actual electrodes were tested in the fuel cell. Beneficial effects of the microporous layer are shown in the following results.

3.2.1 Influence of the Teflon percentage in the microporous layer

For this study, microporous layers with a carbon content of 1 mg cm^{-2} were prepared, varying, on a total weight base, the percentage of Teflon (10, 20, 40 and 60%). Lower Teflon percentage could not be used, because they attempted against the integrity of the MPL.

a) Physical characterisation

Figure 10 displays the *pore size distribution* for the gas diffusion layer with different Teflon percentage in the microporous layer. Specific pore size distribution is shown in the macroporous and microporous region, for a better visualization of the effect of the inclusion of the microporous layer in the carbon support, and the effect of the Teflon percentage in the MPL.

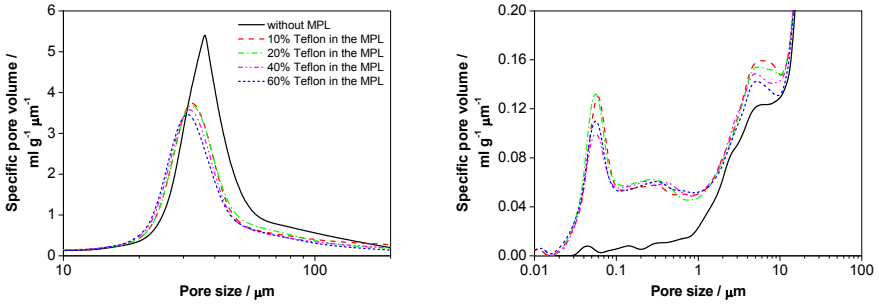

Fig. 10. Specific pore volume for the GDLs with different Teflon percentage in the MPL in: (a) the macroporous region, and (b) in the microporous layer.

As it can be seen, the presence of the MPL reduces the amount of macropores in the carbon support. Part of the microporous layer penetrates inside the carbon support, partially closing its macroporous structure. On the other hand, the increase in the Teflon percentage in the MPL hardly affects the macroporous structure. In the case of the microporous, the presence of the MPL generates microporosity in the GDL. This result diminished with the increase in the binder percentage. The Teflon occupies part of the microporous structure of the MPL. Table 4 displays the values of the *overall porosity, mean pore size, and tortuosity* of the GDL, extracted from the pore size distribution, for the different Teflon-loaded MPL.
As it can be seen, the overall porosity and mean pore size decrease with the Teflon content in the MPL, and further does with the inclusion of the MPL. Comparing with the Teflon percentage in the carbon support, the diminution is lower, since in this case the microporous structure is only affected, which has a lower weight on the global structure of the complete GDL. In the case of the tortuosity, it can be seen a noticeable increase with the inclusion of the MPL, making more difficult the fluid transit.

PTFE content / %	Porosity / %	Mean pore diameter / µm	Tortuosity
Without MPL	73.9	36.69	3.363
0	70.6	34.23	3.795
10	70.2	34.02	3.871
20	69.4	33.81	3.940
40	68.9	33.63	4.130

Table 4. Values of the overall porosity, mean pore size diameter and tortuosity for the GDLs with different Teflon loaded MPL

Gases/water vapour permeability is shown in Figure 11 for the GDL with different Teflon percentage of the MPL.

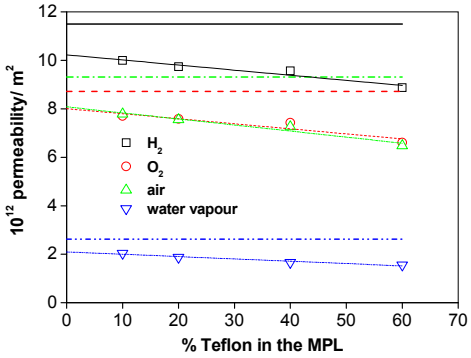

Fig. 11. Gases and water vapour permeability of the GDLs with different Teflon percentage in the MPL (horizontal lines represent the carbon support permeability)

As it can be observed, the gases/water vapour permeability diminishes with the Teflon content in the MPL. Logically, the occlusion of part of the microporous makes more difficult the transient of the gases through the GDL, and therefore, mass transfer becomes more impeded for high Teflon percentages in the MPL. As in the case of the carbon support, the values of the gases permeability for each gas are in the line of its molecular size, except for the case of water vapour.

Therefore, in terms of mass transfer physical related properties, the use of a low percentage of Teflon in the MPL appeared to be beneficial. High porosity and permeability, and low tortuosity can be achieved under these conditions. On the other hand, these results also suggest the suitability of uniquely the carbon support in the MPL, even though these preliminary results must be confirmed by the fuel cells one.

b) Electrochemical behaviour

b.i) The Teflon percentage in the cathodic MPL

Figure 12 shows the variation of the cell performance for the GDLs with different Teflon percentage in the MPL. Points correspond to the experimental data, whereas lines show the fitting of these data to the semi-empirical model.

First of all, it is important to mention the positive effect that has got the inclusion of the MPL in the cell performance. This result can be explained taking into account one of the missions of the MPL: avoid the penetration of the catalyst particle in the carbon support. In the pore size distribution, it has been observed that part of the MPL penetrates into the carbon support, blocking part of the macroporosity. MPL and catalytic layer have a similar pore size distribution (same carbon black support), and therefore this latter penetrates into the carbon support if no MPL is used (Lobato et al., 2010b). Secondly, cell performance clearly worsens with an increase of the Teflon content. Unlike the carbon support, in this case the overall cell performance seems to result affected by an excess of Teflon binder, as Prasanna et al. (Prasanna et al., 2004a) also observed for Nafion®-based PEMFC. Therefore, the MPL

does not only have influence in terms of mass transfer limitations, but in kinetic and ohmic ones due to an excess of insulator material. Table 5 collects the values arisen from the fitting of the experimental data to the semi-empirical model.

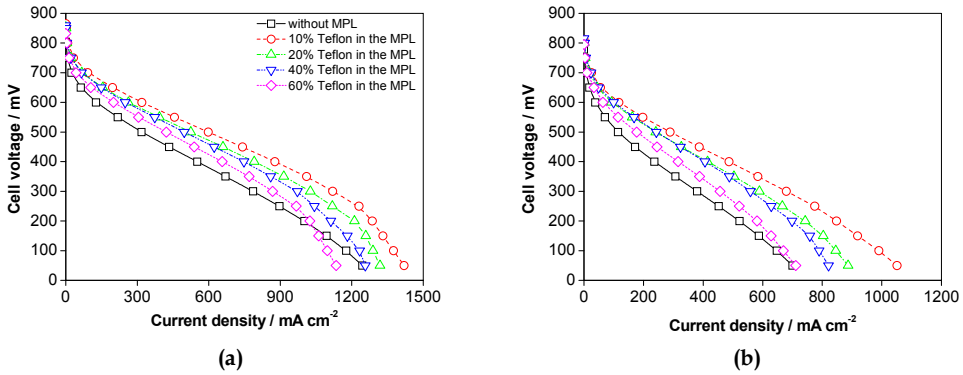

Fig. 12. Cell performance of the electrodes prepared with different Teflon percentage in the MPL, (a) Oxygen stoichometry at 1 A cm^{-2} = 1,5, (b) Air stoichometry at 1 A cm^{-2} = 4

PTFE content / %	$j_{OL,oxygen}$ / mA cm^{-2}	$j_{OL,air}$ / mA cm^{-2}	R_{mt} / ohm cm^2
Without MPL	1,418.9	952.8	0.744
10	1,477.6	1,115.4	0.430
20	1,400.5	1,005.1	0.622
40	1,320.7	922.5	0.761
60	1,240.2	790.3	0.995

Table 5. Limiting current densities for oxygen and air operation, and the mass transfer resistance for the different Teflon percentage in the MPL

Model values confirm the experimental results and show how the 10% Teflon loaded MPL presents the maximum value of the limiting current density, both in the case of oxygen with a reduced stoichometry, and air. Figure 13 shows the corresponding impedance spectra at 300 mV when the cell was operated with air. Values of the mass transfer resistance after fitting the experimental data to the equivalent circuit are collected in Table 5.

Impedance spectra show the benefits of the inclusion of the MPL in the electrode design by the reduction of the global resistance of the cell. Moreover, this resistance attains its lowest values when the MPL is loaded with 10% Teflon. Higher loadings reflect higher mass transfer limitations, as the values of the R_{mt} displays. Consequently, the MPL must be included for high temperature PEMFC electrodes, since all the cell processes are enhanced, despite the decrease in the mass transfer parameters when added. On the other hand, a low Teflon percentage must be used in terms of global performance.

b.ii) The Teflon percentage in the anodic MPL

Figure 14 shows the influence of the Teflon percentage of the MPL in different GDLs.

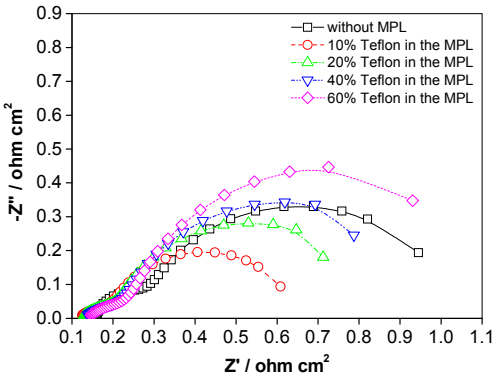

Fig. 13. Impedance spectra of the cell when electrodes with different Teflon percentage in the MPL were used

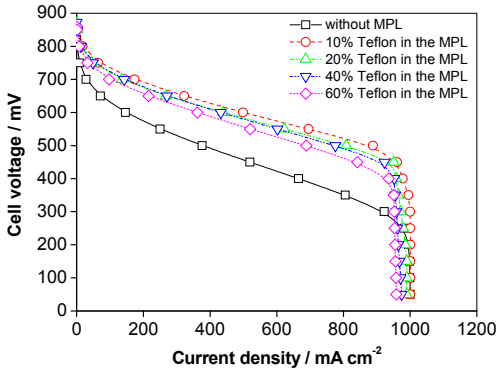

Fig. 14. Influence of the Teflon percentage in the MPL on the cell performance. Hydrogen stoichometry at 1 A cm^{-2} = 1 (Points: experimental data; lines: fitting to the model)

As it can be observed, the influence of the Teflon percentage in the MPL on the cell performance, as in the case of the carbon support, appears almost at the values corresponding to the limiting current density. However, a close look at the curves shows that the limiting current densities slightly diminishes as the Teflon percentage in the MPL increases, reflecting the higher limitation of the mass transport when a less porous or permeable GDL is used. In order to assist for interpretation of the fuel cell results, values of the hydrogen limiting current density are collected in Table 6.

Values in Table 6 display the benefits of using an open GDL. In fact, the highest hydrogen limiting current density was obtained for the MPL free GDL, even though the protection of the catalytic layer plays a more important role in terms of global performance (lower performance in almost the whole range of current densities). Therefore, in terms of global performance, it is also advisable to use a MPL with a low Teflon percentage.

PTFE content / %	$j_{HL,hydrogen}$ / mA cm^{-2}
Without MPL	1.000,8
10	1,000.4
20	990.2
40	980.9
60	964.9

Table 6. Limiting current density for the hydrogen oxidation for the different Teflon percentages of the MPL

3.2.2 Influence of the carbon content in the microporous layer

For this study, microporous layers with a Teflon percentage of 10% were prepared, on a total weight base, varying the carbon loading (0.5, 1, 2 and 4 mg cm^{-2}).

a) Physical characterisation

Figure 15 shows the *pore size distribution* of the gas diffusion layer for the different carbon loadings in the MPL, along with the carbon support. Results are shown focusing on the macroporous and microporous regions.

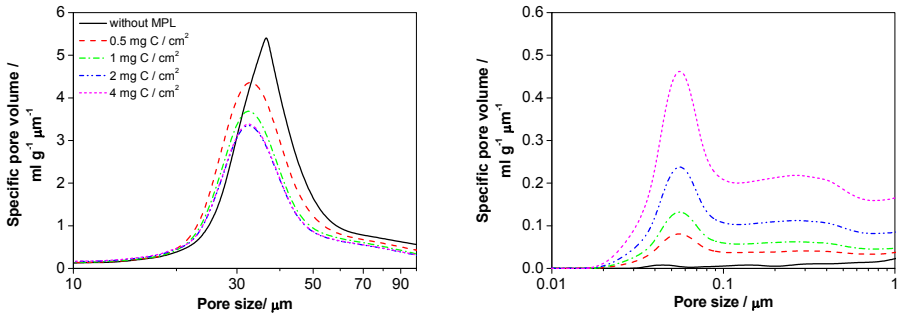

Fig. 15. Specific pore volume for the GDLs with different carbon loadings in the MPL in: (a) the macroporous region, and (b) in the microporous layer (Lobato et al., 2010, with permission of Wiley Interscience)

As it can be observed, the macroporosity of the GDL diminishes with the addition of more carbon to the MPL. As previously commented for the Teflon percentage, part of the MPL will penetrate inside the macroporous carbon support, and therefore, will occlude part of the macropores. Macroporosity decreases until a carbon loading of 2 mg cm^{-2}. Above this value, no more MPL carbon particles seem to penetrate into the carbon support, and therefore, the MPL is fully fulfilling its protective role since it is expected that no catalytic particle will penetrate inside the carbon support. Contrarily, the microporous region increases with the carbon content of the MPL. Logically, more microporosity is introduced in the system the higher is the carbon content (Park et al., 2006).

Overall porosity, mean pore size and tortuosity of the GDL with different carbon loading in the MPL can be estimated from the pore size distribution. The corresponding values are collected in Table 7.

Carbon loading / mg cm^{-2}	Porosity / %	Mean pore diameter / μm	Tortuosity
Without MPL	73.9	36.69	3.363
0.5	72.2	34.32	3.502
1	72.2	33.23	3.717
2	69.2	32.10	4.152
4	67	30.50	4.620

Table 7. Values of the overall porosity, mean pore size diameter and tortuosity for the GDLs with different carbon loadings MPL

As it can be seen, the overall porosity and the mean pore size of the GDL decrease with the carbon loading. The diminution of the macroporosity and the increase of the microporosity of the GDL explain the reduction of the overall porosity and mean pore size. In the case of the tortuosity, the higher is the carbon loading, the thicker the MPL layer becomes, making more difficult the access of the gases to the catalytic layer.
Gases/water vapour permeability for the GDLs with different carbon loading in the MPL are shown in Figure 16.

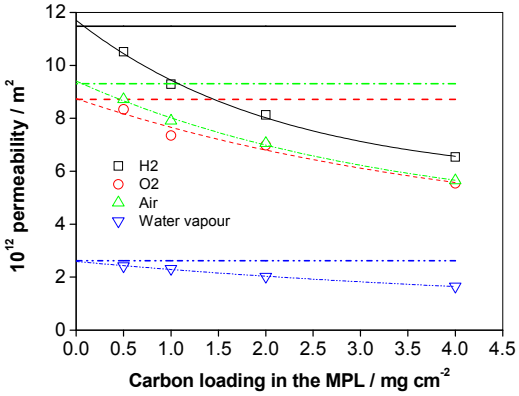

Fig. 16. Gases and water vapour permeability of the GDLs with different carbon loadings in the MPL (horizontal lines represent the carbon support permeability)

As it can be seen, gases/water vapour permeability decreases with the carbon loading in the GDL. This is an effect of the reduction of the macroporosity, and the increase in the microporosity, which makes more difficult the transport of the gases reactant, and the water vapour through the GDL (Wang et al., 2006). On the other hand, the decay in the permeability becomes less noticeable the higher is the carbon loading in the MPL. This agrees with the previously mentioned fact that a lower amount of carbon particles from the MPL penetrates in the carbon support, so that the results reflect the effect of the increase in the microporosity. As in the previous cases, the molecular size of the gases determines the values of the gas permeability, except for the case of the extensively commented water vapour.
As in the case of the influence of the Teflon percentage in the MPL, the simplest GDL, without microporous layer, seems to be the most adequate disposition in terms of mass

transport. However, in terms of fuel cell performance, other factors, as next shown, have to be taken into account. As it has been commented throughout this chapter, the MPL fulfils a very important protective role of the catalytic layer.

b) Electrochemical behaviour

b.i) The carbon loading in the cathodic MPL

Figure 17 shows the variation of the cell performance for the GDLs with different carbon loadings in the MPL. Points correspond to the experimental data, whereas lines show the fitting of these data to the semi-empirical model.

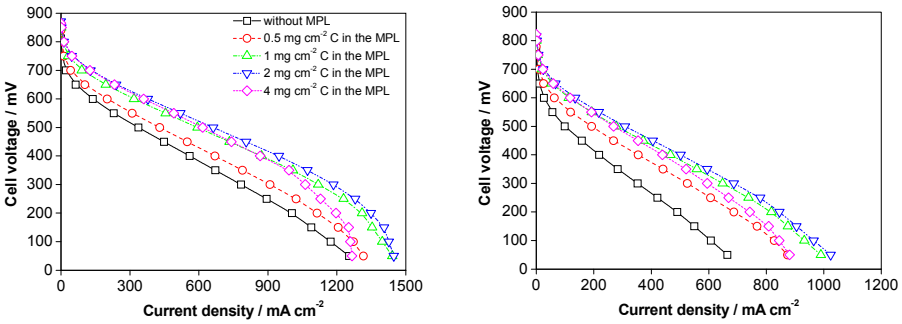

Fig. 17. Cell performance of the electrodes prepared with different carbon loading in the MPL, (a) Oxygen stoichometry at 1 A cm^{-2} = 1,5, (b) Air stoichometry at 1 A cm^{-2} = 4 (Lobato et al., 2010b, with permission of Wiley Interscience)

The beneficial influence of the inclusion of the MPL in the electrode structure can be more clearly seen in these results. Cell performance increases with the addition of a larger carbon amount, due to the greater protection of the MPL, until a value of 2 mg cm^{-2}. At this value, the MPL avoids the complete penetration of catalyst particles inside the carbon support. This results is coincident with the pore size distribution ones, in which macroporosity does not decrease above 2 mg cm^{-2}. On the other hand, when the carbon loading is too excessive, a drop in the cell performance can be observed. This can be ascribed to the increase in the MPL thickness, with the consequent increase in the mass transport limitations. Table 8 collects the values of the limiting current density arisen from the fitting of the experimental data to the semi-empirical model.

Values of the oxygen limiting current densities show the suitability of the 2 mg cm^{-2} carbon loading, despite the most limited mass transport characteristics of this GDL compared to lower carbon loaded ones. This again points up that the important role that plays the microporous layer in terms of protection of the catalytic layer, contributing to a global enhancement of the cell performance. Nonetheless, limiting current density values decreases for the 4 mg cm^{-2} carbon loading, due to more prominent mass transfer limitation when excessively thick GDL are used. Figure 18 shows the corresponding impedance spectra at 300 mV when the cell was operated with air. Values of the mass transfer resistance after fitting the experimental data to the equivalent circuit are collected in Table 8.

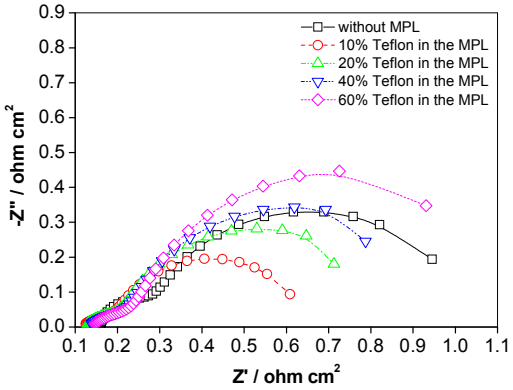

Fig. 18. Impedance spectra of the cell when electrodes with different carbon loading in the MPL were used (Lobato et al., 2010b, with permission of Wiley Interscience)

Carbon loading / mg cm^{-2}	$j_{OL,oxygen}$ / mA cm^{-2}	$j_{OL,air}$ / mA cm^{-2}	R_{mt} / ohm cm^2
Without MPL	1,418.9	952.8	0.744
0.5	1,431.3	1,092.3	0.621
1	1,477.6	1.115.4	0.430
2	1,479.2	1.118.3	0.408
4	1,300.4	980.3	0.565

Table 8. Limiting current densities for oxygen and air operation, and the mass transfer resistance for the different Teflon percentage in the MPL

Impedance spectra confirm the suitability of the inclusion of the MPL, and the particular loading to use in order to obtain a good protection of the catalytic layer. Global cell resistance decreases with the carbon loading until a minimum value corresponding to 2 mg cm^{-2} of carbon. If a higher carbon loading is applied, mass transfer resistance notably increases, showing more limitations in terms of gases/vapour transport, due to the excessive amount of carbon present in the MPL.

The influence of the carbon loading has demonstrated the importance of the addition of the MPL to the electrode design. Protection of the catalytic layer is fundamental in order to maximize the cell performance, and indeed, and according to the experimental results, it plays even a more important role than mass transfer characteristics of the GDL. However, if an excessive amount of carbon is added to the MPL, significant mass transport limitations appear, leading to an optimum carbon loading of 2 mg cm^{-2}.

b.ii) The Teflon percentage in the anodic MPL

Figure 19 shows the influence of the Teflon percentage of the MPL in different GDLs.

As it can be observed, the influence of the carbon loading in the anodic MPL is more notorious than in the case of the cathode. However, it is visible the beneficial effect of the inclusion of the MPL, despite being at the anode. The carbon loading, in this case, slightly improves the global cell performance with an increase of the carbon loading, showing the best performances for 1 and 2 mg cm^{-2}, and a decrease when the carbon loading was

4 mg cm^{-2}. Table 9 collects the values of the hydrogen limiting current density for the different carbon loaded MPL in the gas diffusion layer.

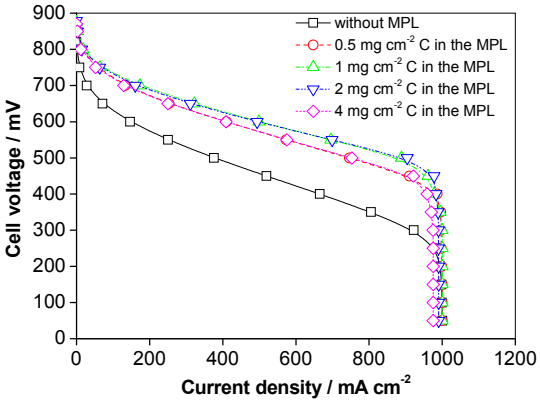

Fig. 19. Influence of the carbon loading in the MPL on the cell performance. Hydrogen stoichometry at 1 A cm^{-2} = 1 (Points: experimental data; lines: fitting to the model) (Lobato et al., 2010b, with permission of Wiley Interscience)

Values of the limiting current density are very similar for GDL without MPL, and with low loadings of carbon, demonstrating the suitability of these gas diffusion layers in terms of mass transport. Nevertheless, in the case of the carbon loading of 2 and 4 mg cm^{-2}, the limiting current density decreases, due to the more impeded access of the hydrogen gas. However, as in the case of the study focused on the cathode, the optimum protective role of the MPL prescribes the use of a carbon loading of 2 mg cm^{-2}, since hydrogen mass transfer limitations will only appear in case of the use of a very restricted stoichometry.

Carbon loading / mg cm^{-2}	$j_{HL,hydrogen}$ / mA cm^{-2}
Without MPL	1.000,8
0.5	1,000.1
1	1,000.4
2	990.2
4	975.3

Table 9. Limiting current density for the hydrogen oxidation for the different carbon loading in the MPL

4. Conclusions

The gas diffusion layer plays an important role for High Temperature PBI-based PEMFC in terms of cell performance. Thus, it is desirable to have a carbonaceous support with a low Teflon content (10% Teflon), in order to guarantee the mechanical stability of the membrane-electrode assembly, and have the maximum porosity and permeability, allowing the reduction of the mass transfer limitations. On the other hand, it is even more important the inclusion of a microporous layer in the design of the electrodes, since this protects the

catalytic layer for penetrating within the macroporous carbon support, maximizing the electrochemically active area of the electrode. For this purpose, a carbon loading of 2 mg cm^{-2} is an optimum value. Besides, with this loading, the electrode presents the best mass transfer characteristics. Finally, the amount of polymer binding (Teflon) to add in this layer must be the minimum possible one (10% Teflon), in order to maximize the cell performance.

5. Acknowledgments

This work was supported by the Ministry of Education and Science of the Spanish Government through project CTM2004-03817, and by the JCCM (Junta de Comunidades de Castilla-La Mancha, Spain) through the project PBI-08-0151-2045.

6. Nomenclature

C_R^B	bulk reactant concentration	S	cross-section
C_P^B	bulk product reactant concentration	ΔP	pressure different observed across the carbon support
C_R^S	reactant concentration at the external surface of the electrode	E	cell voltage
C_P^S	product concentration at the external surface of the electrode	E_0	open circuit voltage
C_R^C	reactant concentration at the catalytic layer	b	Tafel slope
C_P^C	product concentration at the catalytic layer	j	experimental current density
C_R^{cat}	reactant concentration in the platinum active sites	R	ohmic resistance of the system
D_{eff}	effective diffusion coefficient	j_{OL}	limiting cathode current density
D	diffusion coefficient	j_{HL}	limiting anode current density
ε	porosity	R_{pol}	lineal polarization resistance of the hydrogen oxidation reaction
τ	tortuosity	R_Ω	ohmic resistance from impedance measurement
K	permeability	R_{ct}	resistance for the charge transfer process
Q	flow of gas	$(CPE)_{ct}$	constant phase element for the charge transfer process
μ	gas viscosity	R_{mt}	resistance for the mass transfer process
L	thickness of the porous medium	$(CPE)_{mt}$	constant phase element for the mass transfer process

7. References

Antolini, E.; Passos, R.R. & Ticianelli, E.A. (2002). Effects of the cathode gas diffusion layer characteristics on the performance of polymer electrolyte fuel cells. *Journal of The Applied Electrochemistry*, Vol. 32, No. 4, pp. 383-388, ISSN : 0021-891X.

Appleby, A.J. & Foulkes F.R. (1993). *Fuel cell handbook*, Krieger Publishing Company (Ed.), ISBN: 0-89464-733-4, Malabar, Florida, United State.

Benziger, J.; Nehlsen, J.; Blackwell, D.; Brennan, T. & Itescu, J. (2005). Water flow in the gas diffusion layer of PEM fuel cells. *Journal of Membrane Science*, Vol. 261, No. 1-2, (September 2005), pp. 98-106, ISSN: 0376-7388.

Bose, S.; Kuila, T.; Hien Nguyen, T.X.; Kim, N.H; Lau, K.-T. et al. (2011). Polymer membranes for high temperature proton exchange membrane fuel cell: Recent advances and challenges. *Journal of Power Sources*, in press, (January 2011), doi:10.1016/j.progpolymsci.2011.01.003, ISSN: 0378-7753.

Boukamp. B.A. (1986). A package for impedance/admittance data analysis. *Solid State Ionics*, Vol. 18-19, Part 1, (January 1986), pp. 136-140, ISSN: 0167-2738

Bultel, Y.; Wiezell, K.; Jaouen, F.; Ozil, P. & Lindbergh G. (2005). Investigation of mass transport in gas diffusion layer at the air cathode of a PEMFC. *Electrochimica Acta*, Vol. 51, No. 3, (October 2005), pp. 474-488, ISSN: 0013-4686.

Carrete, L.; Friedrich, K.A. & Stimming, U. (2001). Fuel Cells – Fundamentals and Applications. *Fuel Cells*, Vol. 1, No. 1, (May 2001), pp. 5-39, ISSN: 1615-6854.

Cindrella, L. ; Kannan, A.M.; Lin, J.F.; Saminathan K.; Ho Y. et al. (2009). Gas diffusion layer for proton exchange membrane fuel cells—A review. *Journal of Power Sources*, Vol. 194, No. 1, (October 2009), pp. 146-160. ISSN: 0378-7753.

Ciureanu, M. & Roberge R. (2001). Electrochemical Impedance Study of PEM Fuel Cells. Experimental Diagnostics and Modeling of Air Cathodes. Journal of Physical Chemistry B, Vol. 105, No. 17, (April 2001), pp 3531–3539, ISSN: 1089-5647.

Ciureanu, M.; Mikhailenko, S.D.; Kaliaguine, S. (2003). PEM fuel cells as membrane reactors: kinetic analysis by impedance spectroscopy. *Catalysis Today*, Vol. 82, No. 1-4, (July 2003), pp. 105-206, ISSN 0920-5861.

EG&G Technical Services, Inc. (2004). *Fuel Cell Handbook (7th Edition),* U.S. Department of Energy Office of Fossil Energy, Morgantown, West Virginia, United State. Available from http://www.netl.doe.gov/technologies/coalpower/fuelcells/seca/pubs/FCHandbook7.pdf.

Han, M.; Xu, J.H.; Chan, S.H. & Jiang, S.P. (2008). Characterization of gas diffusion layers for PEMFC. *Electrochimica Acta*, Vol. 53, No. 16, (June 2008), pp. 5361-5367, ISSN: 0013-4686.

Jalani, N.H.; Ramani, M.; Ohlsson, K.; Buelte, S.; Pacifico, G. et al. (2006). Performance analysis and impedance spectral signatures of high temperature PBI–phosphoric acid gel membrane fuel cells. *Journal of Power Sources*, Vol. 160, No. 2, (October 2006), pp. 1096-1103, ISSN: 0378-7753.

Lai, C.-M.; Lin, J.-C.; Ting F.-P.; Chyou, S.-D. & Hsueh K.-L. (2008). Contribution of Nafion loading to the activity of catalysts and the performance of PEMFC. *International Journal of Hydrogen Energy*, Vol. 33, No. 15, (August 2008) pp. 4132-4137, ISSN: 0360-3199.

Li, Q.; He, R.; Jensen, J.O. & Bjerrum, N.J. (2003a). Review Approaches and Recent Development of Polymer Electrolyte Membranes for Fuel Cells Operating above 100 °C. *Chemistry of Materials*, Vol. 15, No. 26, (December 2003), pp 4896–4915, ISSN: 0897-4756.

Li, Q.; He, R.; Gao, J.-A.; Jensen, J.O. & Bjerrum, N.J. (2003b). The CO Poisoning Effect in PEMFCs Operational at Temperatures up to 200°C. *Journal of The Electrochemical Society*, Vol. 150, No. 12, (November 2003), pp.A1599-A1605, ISSN: 0013-4651.

Li, Q.; He, R.; Jensen, J.O. & Bjerrum, N.J. (2004). PBI-Based Polymer Membranes for High Temperature Fuel Cells – Preparation, Characterization and Fuel Cell Demonstration. *Fuel Cells*, Vol. 4, No. 3, (August 2004), pp. 147–159, ISSN: 1615-6854.

Linares, J.J. (2010). Celdas de combustible de membrana polimérica de alta temperatura basadas en polibencimidazol impregnado con ácido fosfórico. *PhD Thesis Dissertation*, (January 2010), Ciudad Real, Spain.

Liu, Z.; Wainright, J.S.; Litt, M.H. & Savinell R.F. (2006). Study of the oxygen reduction reaction (ORR) at Pt interfaced with phosphoric acid doped polybenzimidazole at elevated temperature and low relative humidity. *Electrochimica Acta*, Vol. 51, No. 19, (May 2006), pp. 3914-3923, ISSN: 0013-4686.

Lobato, J.; Cañizares, P.; Rodrigo, M.A.; Linares, J.J. & Manjavacas G. (2006). Synthesis and characterisation of poly[2,2-(m-phenylene)-5,5-bibenzimidazole] as polymer electrolyte membrane for high temperature PEMFCs. *Journal of Membrane Science*, Vol. 280, No. 1-2, (September 2006), pp. 351-362, ISSN: 0376-7388.

Lobato, J.; Cañizares, P.; Rodrigo, M.A.; Linares, J.J. & López-Vizcáino, R. (2008a). Performance of a Vapor-Fed Polybenzimidazole (PBI)-Based Direct Methanol Fuel Cell. *Energy&Fuels*, Vol. 22, No. 5, (July 2008), pp 3335–3345, ISSN: 0887-0624.

Lobato, J.; Cañizares, P.; Rodrigo M.A.; Ruíz-López, C. & Linares, J.J. (2008b). Influence of the Teflon loading in the gas diffusion layer of PBI-based PEM fuel cells. *Journal of The Applied Electrochemistry*, Vol. 38, No. 6, pp. 793-802, ISSN: 0021-891X

Lobato, J.; Cañizares, P.; Rodrigo, M.A.; Linares, J.J. & Pinar, F.J. (2010a). Study of the influence of the amount of PBI–H3PO4 in the catalytic layer of a high temperature PEMFC. *International Journal of Hydrogen Energy*, Vol. 35, No. 3, (February 2010), pp. 1347-1355, ISSN: 0360-3199.

Lobato, J.; Cañizares, P.; Rodrigo, M.A; Úbeda, D.; Pinar F.J. et al. (2010b). Optimisation of the Microporous Layer for a Polybenzimidazole-Based High Temperature PEMFC – Effect of Carbon Content. *Fuel Cells*, Vol. Vol. 10, No. 5, (October 2010), pp. 770–777, ISSN: 1615-6854.

Mamlouk, M. & Scott, K. (2010). The effect of electrode parameters on performance of a phosphoric acid-doped PBI membrane fuel cell. *International Journal of Hydrogen Energy*, Vol. 35, No. 2, (January 2010), pp. 784-793, ISSN: 0360-3199.

Mathias, M.; Roth, J.; Fleming, J. & Lehnert W. (2003). Diffusion media materials and characterisation, in: *Handbook of Fuel Cells*, W. Vielstich, A. Lamm, H. A. Gasteiger (Eds.), John Wiley & Sons Ltd, Ch. 46, Chichester, United Kingdom, ISBN: 0-471-49926-9

Paganin, V.A.; Oliveira, C.L.F.; Ticianelli, E.A.; Springer, T.E. & González, E.R. (1998). Modelistic interpretation of the impedance response of a polymer electrolyte fuel cell. *Electrochimica Acta*, Vol. 43, No. 24, (August 1998), pp. 3761-3766, ISSN: 0013-4686.

Pan, C.; Li, Q.; Jensen, J.O.; He, R.; Cleeman, L.N. et al. (2007). Preparation and operation of gas diffusion electrodes for high-temperature proton exchange membrane fuel cells. *Journal of Power Sources*, Vol. 172, No. 1, (October 2007), pp. 278-286, ISSN: 0378-7753.

Park, S.; Lee, J.-W. & Popov, B.N. (2006). Effect of carbon loading in microporous layer on PEM fuel cell performance. *Journal of Power Sources*, Vol. 163, No. 1, (December 2006), pp. 357-363, ISSN: 0378-7753.

Park, G.-G.; Sohn, Y.-J.; Yang T.-H.; Yoon, Y.-G.; Lee, W.-Y. et al. (2004). Effect of PTFE contents in the gas diffusion media on the performance of PEMFC. *Journal of Power Sources*, Vol. 131, No. 1-2, (May 2004), pp. 182-187, ISSN: 0378-7753.

Prasanna, M.; Ha, H.Y. & Cho, E.A. (2004a). Influence of cathode gas diffusion media on the performance of the PEMFCs. *Journal of Power Sources*, Vol. 131, No. 1-2, (May 2004), pp. 147-154, ISSN: 0378-7753.

Prasanna, M.; Ha, H.Y.; Cho, E.A.; Hong, S.-A.; Oh, I.-H. (2004b). Investigation of oxygen gain in polymer electrolyte membrane fuel cells. *Journal of Power Sources*, Vol. 137, No. 1, (October 2004), pp. 1-8, ISSN: 0378-7753.

Quingfeng, L.; Hjuler, H.A. & Bjerrum, N.J. (2000). Oxygen reduction on carbon supported platinum catalysts in high temperature polymer electrolytes. *Electrochimica Acta*, Vol. 45, No. 25-26, (August 2000), pp. 4219-4226, ISSN: 0013-4686.

Samms, S.R.; Wasmus, S.; Savinell, R.F. (1996). Thermal Stability of Proton Conducting Acid Doped Polybenzimidazole in Simulated Fuel Cell Environments. *Journal of The Electrochemical Society*, Vol. 143, No. 4, (April 1996), pp. 1225-1232, ISSN: 0013-4651.

Savadogo, O. (2004). Emerging membranes for electrochemical systems: Part II. High temperature composite membranes for polymer electrolyte fuel cell (PEFC). *Journal of Power Sources*, Vol. 127, No. 1-2, (March 2004), pp. 135-161, ISSN: 0378-7753.

Seland, F.; Berning, T.; Børresen, B. & Tunold R. (2006). Improving the performance of high-temperature PEM fuel cells based on PBI electrolyte. *Journal of Power Sources*, Vol. 160, No. 1, (September 2006), pp. 27-36, ISSN: 0378-7753.

Soler, J.; Hontañón, E. & Daza, L. (2003). Electrode permeability and flow-field configuration: influence on the performance of a PEMFC. *Journal of Power Sources*, Vol. 118, No. 1-2, (May 2003), pp. 172-178, ISSN: 0378-7753.

Song, J.M.; Cha, S.Y. & Lee, W.M. (2001). Optimal composition of polymer electrolyte fuel cell electrodes determined by AC impedance method. *Journal of Power Sources*, Vol. 94, No. 1, (February 2001), pp. 78-84, ISSN: 0378-7753.

Springer, T.E.; Zawodzinski, T.A.; Wilson, M.S.; Gottesfeld, S. (1996). Characterization of Polymer Electrolyte Fuel Cells Using AC Impedance Spectroscopy. *Journal of The Electrochemical Society*, Vol. 143, No. 2, (February 1996), pp. 587-599, ISSN: 0013-4651.

Wainright, J.S.; Litt, M.H. & Savinell R.F. (2003). High Temperatures membranes, in: *Handbook of Fuel Cells*, W. Vielstich, A. Lamm, H. A. Gasteiger (Eds.), John Wiley & Sons Ltd, Vol. 3, Chichester, United Kingdom, ISBN: 0-471-49926-9.

Wang, J.-T.; Wasmus, S. & Savinell, R.F. (1996). Real-Time Mass Spectrometric Study of the Methanol Crossover in a Direct Methanol Fuel Cell. *Journal of The Electrochemical Society*, Vol. 143, No 4, (April 1996), pp. 1233-1239, ISSN: 0013-4651.

Wang, X.L.; Zhang, H.M.; Zhang, J.L.; Xu, H.F.; Tian Z.Q. et al. (2006). Micro-porous layer with composite carbon black for PEM fuel cells. *Journal of Power Sources*, Vol. 51, No. 23, (June 2006), pp. 4909-4915, ISSN: 0378-7753.

Weng, D.; Wainright, J.S.; Landau, U. & Savinell, R.F. (1996). Electro-osmotic Drag Coefficient of Water and Methanol in Polymer Electrolytes at Elevated Temperatures. *Journal of The Electrochemical Society*, Vol. 143, No. 4, (April 1996), pp. 1260-1263, ISSN: 0013-4651.

Williams, M.V.; Begg, E.; Bonville, L.; Kunz H.R. & Fenton, J.M. (2004). Characterization of Gas Diffusion Layers for PEMFC. *Journal of The Electrochemical Society*, Vol. 151, No. 8, (June 2004), pp. A1173-A1180, ISSN: 0013-4651.

Yuan, X.; Wang, H.; Sun, J.C. & Zhang, J. (2007). AC impedance technique in PEM fuel cell diagnosis—A review. *International Journal of Hydrogen Energy*, Vol. 32, No. 17, (December 2007), pp. 4365-4380, ISSN: 0360-3199.

3

Numerical Analysis of Heat and Mass Transfer in a Fin-and-Tube Air Heat Exchanger under Full and Partial Dehumidification Conditions

Riad Benelmir and Junhua Yang
University Henri Poincaré - Nancy I
France

1. Introduction

Heat exchangers are commonly used in industrial fields such as air conditioning, petrochemical and agriculture-food industries. The design and utilization of a heat exchanger should fulfill some conditions of performance, economy and space requirement. The most widely operated heat exchangers make use of fin-and-tube configuration in association with the application of heating, ventilating, air-conditioning and refrigeration systems (Khalfi & Benelmir, 2001). With regard to the fin temperature and dew point temperature of surrounding air, three situations on a fin surface can be distinguished (Lin & Jang, 2002, Benelmir *et al.*, 2009). The fin surface is fully dry if the temperature of the whole fin is higher than the air dew point temperature. It is partially wet when the air dew point temperature is lower than the fin top temperature and is higher than the fin base temperature. Finally, the fully wet surface occurs if the temperature of the whole fin is lower than the dew point temperature. A reliable determination of the fin efficiency must account for the simultaneous heat and mass transfer on the cooling surface. Many experimental, and few numerical, studies have been carried out to study the heat and mass transfer characteristics of the fin-and-tube heat exchangers under dehumidifying conditions. It was stated by Liang *et al.* (2000) that the condensation of the moist air along the fin surface causes reduction of the fin efficiency. They found also that measured fin efficiency was less than the calculated one assuming a uniform heat transfer coefficient. The calculated results of Saboya & Sparrow (1974), Chen *et al.* (2005), Chen & Hsu (2007), and Chen & Chou (2007) concluded that the heat transfer coefficient was non-uniform under dry conditions. Due to the difficulty of considering a variable sensible heat transfer coefficient (Choukairi *et al.*, 2006), this later was often assumed to be uniform by many investigators in the calculation of fin efficiency. Liang *et al.* (2000) used one-dimensional and two-dimensional models to determine the humid fin efficiency of a plate-fin-tube heat exchanger: The results obtained show comparable efficiencies with both 1-D and 2-D models. Chen (1991) analyses the fin performance under dehumidifying conditions and shows, through a 2-D model, that the humid fin efficiency was sensitive to the moist air relative humidity value. As mentioned earlier, the sensible heat transfer coefficient is often assumed uniform. Thus, the wet fin efficiency is usually determined under this assumption and by introducing a functional relation between the relative humidity and the fin temperature [Lin & Jang , 2002, Liang *et*

al., 2000, Chen, 1991, Lin *et al*., 2001, Elmahdy & Biggs, 1983, Coney *et al*., 1989]. The most proposed relation between "the difference of the air humidity ratio and that evaluated at the fin temperature" and "the difference of the ambient temperature and fin temperature" used a factor named the condensation factor. This later was often settled constant. Chen & Wang (2008) proposed one-dimensional and two-dimensional models based on inverse heat conduction method and in conjunction with experimental temperature data for predicting the average overall heat transfer coefficient and wet fin efficiency. In their study the sensible heat transfer coefficient, the functional relation between the relative humidity and fin temperature, and the Lewis number are considered to be unknown. Their results show that the estimated fin efficiency under partially and fully wet conditions is sensitive to the relative humidity. Lin *et al.* (2001) mentioned that the effect of the relative humidity on the fully wet fin efficiency of extended surface was very confused. This work's aims to estimate the overall heat transfer coefficient and the fin efficiency as well as the total heat rate exchanged under partially or fully wet conditions using an appropriate numerical procedure. The airflow pattern is first determined by solving the mass and momentum balance equations. The heat and mass balance equations are then solved by a finite volume method after subdividing the fin in several sub-fin regions. The effect of admission air parameters such as temperature, relative humidity and velocity as well as the fin base temperature mainly on the overall heat transfer coefficient and the fin efficiency are investigated.

2. Mathematical model

2.1 Air dehumidification in contact with a cold wall

Cooling and dehumidifying of moist air by a cold surface involves simultaneous heat and mass transfer (Fig. 1). Within the moist air flow, characterized by the mean dry temperature Ta and absolute humidity W_a, along a cold surface at a fixed temperature T_w, which is lower than the dew point temperature of the air ($T_{dew,a}$), condensation occurs on the wall. At the air-condensate interface, the saturated air is characterized by the condensate-film temperature T_c and the saturated humidity ratio $W_{S,c}$, at T_c. The total wall heat flux includes the sensible part due to convection, spent by cooling air, resulting from the temperature differences between air and condensate-film, and the latent part due to the vapor phase transition heat leading to the partially condensation of the vapor contained in the moist air.

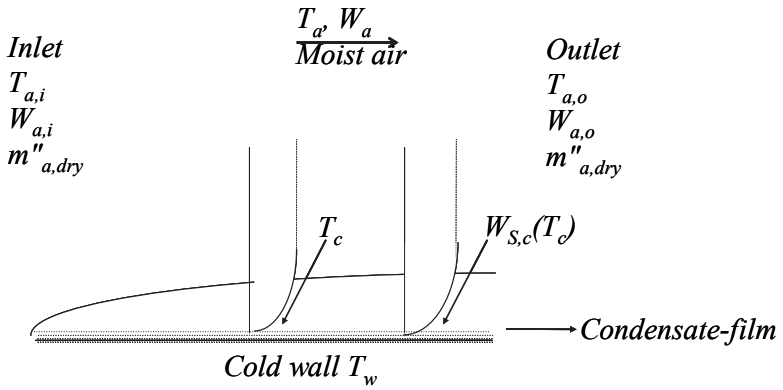

Fig. 1. Air dehumidification by a cold wall

The total heat transfer rate through the wall can be expressed as:

$$q_t'' = m_{a,dry}''\left(i_{a,i} - i_{a,o}\right) - m_c'' i_c \tag{1}$$

Where m''_c is the condensate mass flux.
The error induced by neglecting the sensible heat of the condensate $m''_c i_c$ is in the order of magnitude of 1.3 %. On the other hand, as stated above, the total heat flux results from both sensitive and latent heat components, thus, the following expression of total heat flux density yield:

$$q_t'' = m_{a,dry}''\left(i_{a,i} - i_{a,o}\right) = q_{sen}'' + q_l'' = \alpha_{sen,hum}\left(T_a - T_c\right) + m_c'' L_v \tag{2}$$

According to the mass transfer law, the mass flux of the condensate is expressed as:

$$m_c'' = \alpha_m\left(W_a - W_{S,c}\right) \tag{3}$$

As reported by Lin *et al.* (2001), most of the investigators applied the Chilton-Colburn analogy to set a relationship between the mass transfer coefficient and the sensitive heat transfer coefficient, hence; the following relation is reported and used in our work:

$$\alpha_m = \frac{\alpha_{sen,hum}}{Le^{2/3}.c_{p,a}} \tag{4}$$

Combining equations (2), (3), and (4), the following equation is obtained:

$$q_t'' = \alpha_{sen,hum}\left[\left(T_a - T_c\right) + \frac{Lv}{Le^{2/3}.c_{p,a}}\left(W_a - W_{S,c}\right)\right] \tag{5}$$

Moreover, the total heat flux density is related to the overall heat transfer coefficient by the following relation:

$$q_t'' = \alpha_{O,hum}\left(T_a - T_c\right) \tag{6}$$

Thus, we obtain the expression bellow for the overall heat transfer coefficient:

$$\alpha_{O,hum} = \alpha_{sen,hum}\left[1 + \frac{Lv}{Le^{2/3}.c_{p,a}}\frac{W_a - W_{S,c}}{T_a - T_c}\right] \tag{7}$$

2.2 The physical problem

The schematic diagram of the problem is shown in Fig. 2. The rectangular fins are arranged around tubes lined up or ranked in staggered rows. The refrigerant flows inside tubes and moist air streams outside. The fin temperature is considered lower than the dew point temperature of air, which draws away a condensation on the surface of the tube and the fin. This work will consider the heat and mass transfer for a representative tube and fin elementary unit.

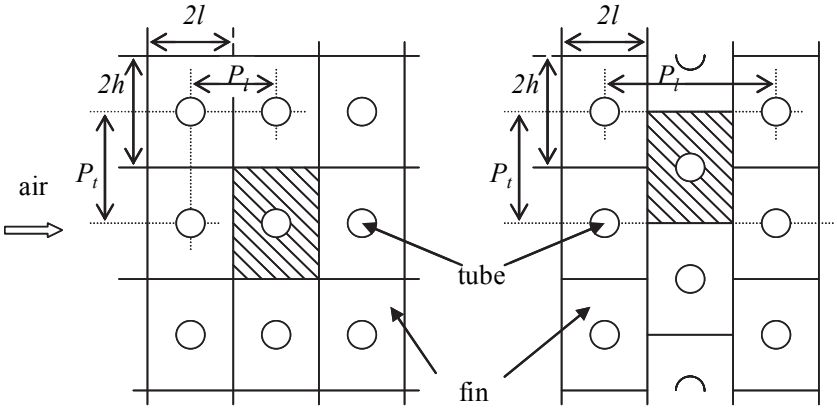

Fig. 2. Schematic of fins arranged around tubes lined up or ranked in staggered rows

The investigation of heat and mass transfer performance during the cooling of moist air through an extended surface, associated with dehumidification, should take into account: the convective heat transfer process between the air-flow and the condensate-film, the conduction inside the fin and the condensate-film, and the mass transfer process between the air-flow and the condensate-film (Fig. 3).

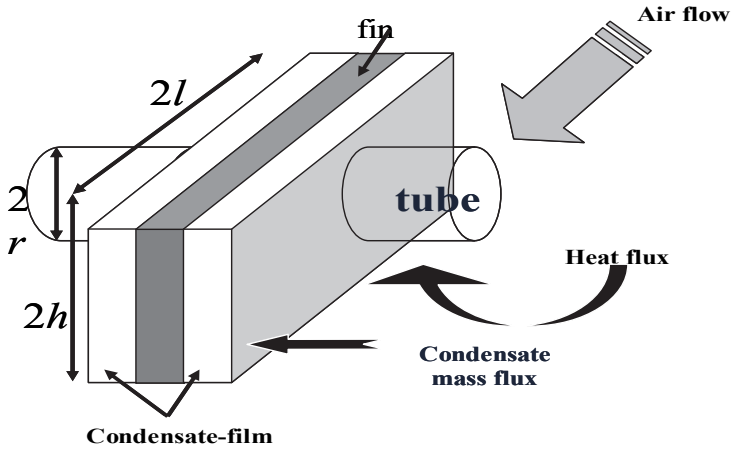

Fig. 3. Heat and mass transfer phenomenon around a fin-tube

As the fins spacing is very weak regarding the fins height and length, heat and mass transfer along with the fin plane's normal direction (z direction) is neglected. The heat flux exchanged by the fin is assumed to be identical on both faces. Hence, only one face is considered in the study of heat and mass transfer by the fin as a result of symmetry condition applied on the fin median plane. Fig. 4 shows the physical domain of the current work.

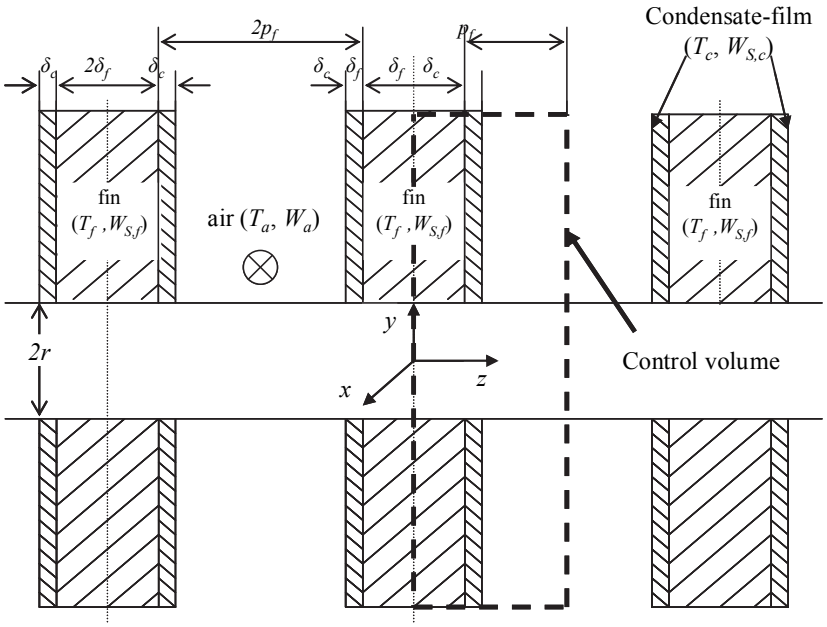

Fig. 4. Physical domain of the present work

The elementary volumes are defined as follow:

$$V_f = \delta_f dxdy\,;\;\; V_c = \delta_c dxdy\,;\;\; V_a = \left(p_f - \delta_c\right)dxdy\,;\;\; V_t = \left(p_f + \delta_f\right)dxdy$$

2.3 Governing equations

In this work, we consider the two-dimensional problem of heat transfer through the fin-surface and condensate-film and the dynamic air-stream according to the (x,y) plane (Fig. 4). The problem of the vapor mass transfer from air to the fin-tube wall occurs according to the direction z. The mathematical formulation is accomplished with respect to some basic assumptions. The air-flow is considered as incompressible and evolving in a laminar steady state. The thermo-physical properties of air, condensate-film and fin-tube are temperature dependant. On the other hand, we consider that heat transfer through the condensate-film is purely conductive and that the radiation transfer mode is always neglected. Furthermore, the condensate-film is assumed to be thin and uniform and, due to the weak thickness of the fin, the adiabatic condition is assumed at the fin-end. For convenience of heat and mass transfer analysis, the following dimensionless parameters are introduced as:

$$T_a^* = \frac{T_a - T_{f,b}}{T_{a,i} - T_{f,b}} \qquad T_f^* = \frac{T_f - T_{f,b}}{T_{a,i} - T_{f,b}} \tag{8}$$

$$W_a^* = \frac{W_a - W_{S,f,b}}{W_{a,i} - W_{S,f,b}} \qquad W_c^* = \frac{W_{S,c} - W_{S,f,b}}{W_{a,i} - W_{S,f,b}} \tag{9}$$

$$x^* = \frac{x}{r} \quad y^* = \frac{y}{r} \quad h^* = \frac{h}{r} \quad l^* = \frac{l}{r} \quad r^* = \frac{r}{r} = 1 \tag{10}$$

$$P^* = \frac{P_f}{r} \quad \delta_c^* = \frac{\delta_c}{r} \quad u_x^* = \frac{u_x}{u_i} \quad u_y^* = \frac{u_y}{u_i} \tag{11}$$

2.3.1 Continuity and momentum equations for air flow

The two-dimensional continuity and momentum equations for air-flow are:

$$\frac{\partial u_x}{\partial x} + \frac{\partial u_y}{\partial y} = 0 \tag{12}$$

$$u_x \frac{\partial u_x}{\partial x} + u_y \frac{\partial u_x}{\partial y} = \nu_a \left(\frac{\partial^2 u_x}{\partial x^2} + \frac{\partial^2 u_x}{\partial y^2} \right) \tag{13}$$

$$u_x \frac{\partial u_y}{\partial x} + u_y \frac{\partial u_y}{\partial y} = \nu_a \left(\frac{\partial^2 u_y}{\partial x^2} + \frac{\partial^2 u_y}{\partial y^2} \right) \tag{14}$$

Introducing the dimensionless variables defined above into Eqs. (12) to (14) leads to the following dimensionless equations:

$$\frac{\partial u_x^*}{\partial x^*} + \frac{\partial u_y^*}{\partial y^*} = 0 \tag{15}$$

$$u_x^* \frac{\partial u_x^*}{\partial x^*} + u_y^* \frac{\partial u_x^*}{\partial y^*} = \frac{2}{\mathrm{Re}_D} \left(\frac{\partial^2 u_x^*}{\partial x^{*2}} + \frac{\partial^2 u_x^*}{\partial y^{*2}} \right) \tag{16}$$

$$u_x^* \frac{\partial u_y^*}{\partial x^*} + u_y^* \frac{\partial u_y^*}{\partial y^*} = \frac{2}{\mathrm{Re}_D} \left(\frac{\partial^2 u_y^*}{\partial x^{*2}} + \frac{\partial^2 u_y^*}{\partial y^{*2}} \right) \tag{17}$$

Where Re_D indicates the Reynolds number based on the internal fin diameter.

$$\mathrm{Re}_D = \frac{\rho_a u_i D}{\mu_a} \tag{18}$$

The air speed at the inlet and outlet is settled uniform and parallel to the x axes, which yields to the following boundary conditions:

$$x^* = \pm l^*, \quad \forall y^*, \quad u_x^* = 1, \quad u_y^* = 0 \tag{19}$$

The upper and lower edges of the fin are subject to the following boundary conditions:

$$y^* = \pm h^*, \quad \forall x^*, \quad u_y^* = 0 \tag{20}$$

Finally, at the fin base, the non-sliding condition is used:

$$\sqrt{x^{*2}+y^{*2}}=1 \quad u_x^*=u_y^*=0 \tag{21}$$

2.3.2 Mass balance equation for vapor in air flow

The vapor flow mass balance equation in the elementary air volume, represented by Fig. 5, is expressed as follow:

$$\Delta \dot{m}_v + m_c{}''dxdy = 0 \tag{22}$$

In this equation, the first term represents the vapor flow rate variation in the air volume, and the second term corresponds to the mass flow rate between the moist air and the condensate-film.

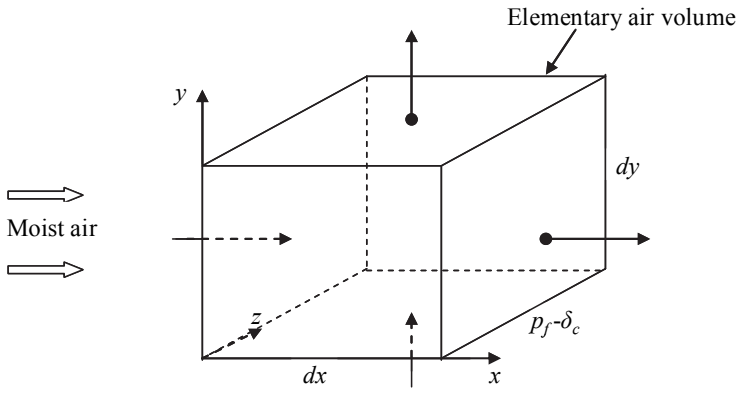

Fig. 5. Vapor flow rate variation in an elementary air volume

According to Fig. 5, the variation of the vapor mass flow is written as:

$$\Delta \dot{m}_v = \left[u_x \frac{\partial W_a}{\partial x} + u_y \frac{\partial W_a}{\partial y} \right] \rho_{a,dry} V_a \tag{23}$$

Using Eqs. (3), (22) and (23) yields to the following equation:

$$u_x \frac{\partial W_a}{\partial x} + u_y \frac{\partial W_a}{\partial y} = -\frac{\alpha_{sen,hum}}{\left(p_f - \delta_c\right).Le^{2/3}.c_{p,a}.\rho_{a,dry}} \left(W_a - W_{S,c}\right) \tag{24}$$

The dimensionless form becomes:

$$u_x^* \frac{\partial W_a^*}{\partial x^*} + u_y^* \frac{\partial W_a^*}{\partial y^*} = -\frac{\alpha_{sen,hum}}{\left(p^* - \delta_c^*\right).Le^{2/3}.c_{p,a}.u_i.\rho_{a,dry}} \left(W_a^* - W_c^*\right) \tag{25}$$

And the corresponding boundary conditions are:

$$x^* = -l^*, \quad \forall y^*, \quad W_a^* = 1$$
$$y^* = \pm h^*, \quad \forall x^*, \quad \frac{\partial W_a^*}{\partial y^*} = 0 \tag{26}$$

2.3.3 Energy balance equation for air flow

Referring to Fig. 5, the energy balance equation held the same form as Eq. (22):

$$\Delta \dot{E}_a + q_{sen}"dxdy = 0 \tag{27}$$

This equation denotes that the most air sensible heat variation of the elementary volume is equilibrated by the sensible heat flow exchanged between air and the condensate-film.
The variation of the sensible heat of the elementary volume can be expressed as:

$$\Delta \dot{E}_a = c_{p,a}\left[u_x \frac{\partial T_a}{\partial x} + u_y \frac{\partial T_a}{\partial y}\right]\rho_{a,dry} V_a \tag{28}$$

Using Eq. (2) and (27), Eq. (28) leads the following form:

$$u_x \frac{\partial T_a}{\partial x} + u_y \frac{\partial T_a}{\partial y} = -\frac{\alpha_{sen,hum}}{\left(p_f - \delta_c\right).Le^{2/3}.c_{p,a}.\rho_a}\left(T_a - T_c\right) \tag{29}$$

After introducing the dimensionless variables, we get :

$$u_x^* \frac{\partial T_a^*}{\partial x^*} + u_y^* \frac{\partial T_a^*}{\partial y^*} = -\frac{\alpha_{sen,hum}}{\left(p^* - \delta_c^*\right).Le^{2/3}.c_{p,a}.u_i.\rho_a}\left(T_a^* - T_c^*\right) \tag{30}$$

The related boundary conditions are:

$$x^* = -l^*, \quad \forall y^*, \quad T_a^* = 1 \tag{31}$$

$$y^* = \pm h^*, \quad \forall x^*, \quad \frac{\partial T_a^*}{\partial y^*} = 0 \tag{32}$$

2.3.4 Energy balance equation for the condensate-film

As mentioned above, heat transfer through the condensate-film is assumed to be purely conductive. Using the fact that the temperature of the condensate-film internal surface is the same as that of the fin surface, the heat flux transferred from the condensate-film to the fin is:

$$q_t'' = \lambda_c \frac{T_c - T_f}{\delta_c} \tag{33}$$

This flux is equal to the convective heat flow transferred by air to the condensate-film, consequently, Eq. (33) can be written:

$$\alpha_{O,hum}\left(T_a - T_c\right) = \lambda_c \frac{T_c - T_f}{\delta_c} \tag{34}$$

From this equation, the condensate-film temperature is deduced:

$$T_c = T_a - \frac{T_a - T_f}{1 + \alpha_{O,hum}\dfrac{\delta_c}{\lambda_c}} \tag{35}$$

2.3.5 Mass balance equation for condensate-film

The film-wise condensation of a stationary saturated vapor on a plane vertical surface has been analyzed by Nusselt (1916) by means of some assumptions. The expression of the condensate-film thickness given by Nusselt is:

$$\delta_c = \left(\frac{4\mu_c \lambda_c (h-y)\left(T_c - T_f\right)}{g L_v \rho_c \left(\rho_c - \rho_v\right)} \right)^{1/4} \tag{36}$$

Where the subscripts c and v refer to condensate-film and water vapor, respectively.
Substituting T_c by its expression (Eq. 35) into Eq. (36) leads to the following relationship:

$$\delta_c = \left(\frac{4\mu_c \lambda_c (h-y)\left(T_a - T_f\right)}{g L_v \rho_c \left(\rho_c - \rho_v\right)} . \frac{\lambda_c}{\lambda_c + \alpha_{O,hum}\delta_c} \right)^{1/4} \tag{37}$$

2.3.6 Energy balance equation for the fin surface

The energy balance equation for the fin is obtained from the heat conduction equation within the fin surface, thus, the subsequent equation is obtained:

$$\lambda_f \left[\frac{\partial^2 T_f}{\partial x^2} + \frac{\partial^2 T_f}{\partial y^2} \right] + \Delta \dot{E}_f = 0 \tag{38}$$

Where, ΔE_f is the thermal energy flow rate received by the fin elementary volume, expressed as:

$$\Delta \dot{E}_f = \frac{q_t'' dx dy}{V_f} = \frac{\alpha_{O,hum}\lambda_c}{\delta_f \left(\lambda_c + \alpha_{O,hum}\delta_C\right)}\left(T_a - T_f\right) \tag{39}$$

Combining these equations yields:

$$\left[\frac{\partial^2 T_f}{\partial x^2} + \frac{\partial^2 T_f}{\partial y^2} \right] + \frac{\alpha_{O,hum}\lambda_c}{\lambda_f \delta_f \left(\lambda_c + \alpha_{O,hum}\delta_C\right)}\left(T_a - T_f\right) = 0 \tag{40}$$

The dimensionless form of Eq. (40) is:

$$\left[\frac{\partial^2 T_f^*}{\partial x^{*2}}+\frac{\partial^2 T_f^*}{\partial y^{*2}}\right]+\frac{r^2\alpha_{O,hum}\lambda_c}{\lambda_f\delta_f\left(\lambda_c+\alpha_{O,hum}\delta_C\right)}\left(T_a^*-T_f^*\right)=0 \tag{41}$$

Using the adiabatic condition in the inlet and the outlet as well as the symmetry condition in both upper and lower, of the fin wall, the following boundary conditions holds:

$$x^*=\pm l^*,\ \ \forall y^*,\ \ \frac{\partial T_f^*}{\partial x^*}=0 \tag{42}$$

$$y^*=\pm h^*,\ \ \forall x^*,\ \ \frac{\partial T_f^*}{\partial y^*}=0 \tag{43}$$

At the fin base surface, the temperature is considered equal to that of the tube:

$$\sqrt{x^{*2}+y^{*2}}=1,\ \ T_f^*=0 \tag{44}$$

2.4 Solving equations

The two-dimensional model developed above is based on the following equations: the continuity and momentum equation (Eqs. 15 to 17), the mass balance equation for water vapor (Eq. 25), the energy balance equation for air stream (Eq. 30), the heat transfer equation in the fin surface (Eq. 41) and the heat and mass transfer equations for the condensate-film (Eqs. 35 and 37). In our model, the simultaneous influence of the local speed and heat transfer coefficient is considered for solving heat and mass transfer within the air flow (Eqs.25 and 30). Moreover, equation (30) uses in its expression the mass flow of moist air ($\rho_a u_i$), while in Eq. (25), the dry air mass flow is used. This allows the consideration of the effect of condensation on heat and mass transfer only once.

2.4.1 Solving continuity and momentum equations

The problem described by Eqs (15) to (17) is a classical fluid flow problem, as the flow around a cylinder. However, in our case, the fluid flows inside a rectangular channel. In order to analyze the heat and mass transfer fin performance, it is necessary to know the airflow pattern, particularly the distribution of the airflow velocities. The investigation of air velocity field has been carried out either by using the analytical approaches given by Johnson (1998) or by a numerical analysis using the finite-volume method. In the completion of this work, as the Reynolds number based on fin length is less than 2000 (laminar case) and as the air thermo-physical properties are weakly temperature dependent, except the kinetic viscosity, the following expressions of the dimensionless velocities found by Johnson (1998) are approved:

$$u_x^*=1-\frac{1}{x^{*2}+y^{*2}}+\frac{2y^{*2}}{\left(x^{*2}+y^{*2}\right)^2} \tag{45}$$

$$u_y^*=-\frac{2x^*y^*}{\left(x^{*2}+y^{*2}\right)^2} \tag{46}$$

The distributions of these velocities over the physical domain, where the half fin length and high are settled to 2.5, are shown in Fig. 6a and 6b.

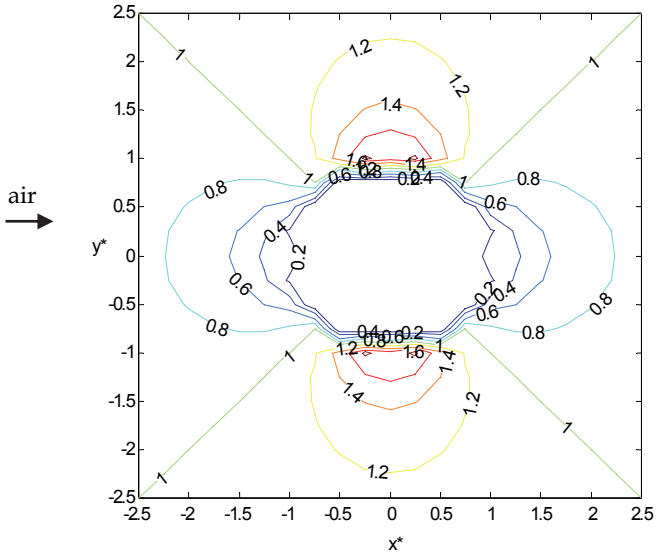

Fig. 6a. Horizontal velocity distribution

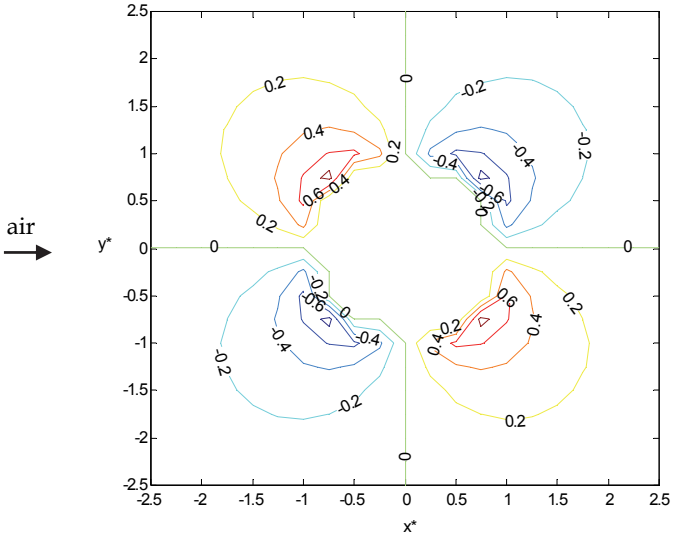

Fig. 6b. Vertical velocity distribution

As shown in Fig. 6a and 6b, the horizontal and vertical velocities fields present an apparent symmetry regarding x and y axes. The horizontal dimensionless velocity at the inlet and outlet tends towards unity, is maximal at the upper and lower fin edges and is minimal close to the tube wall as a result of the channel reduction. Likewise, the vertical dimensionless velocity is close to zero when going up the inlet and outlet or the upper and lower fin edges, and is also minimal near the tube surface.

2.4.2 Solving heat and mass transfer equations

The heat and mass transfer problem has been solved using an appropriate meshing of the calculation domain and a finite-volume discretization method. Fig. 7 illustrates the fin meshing configuration used.

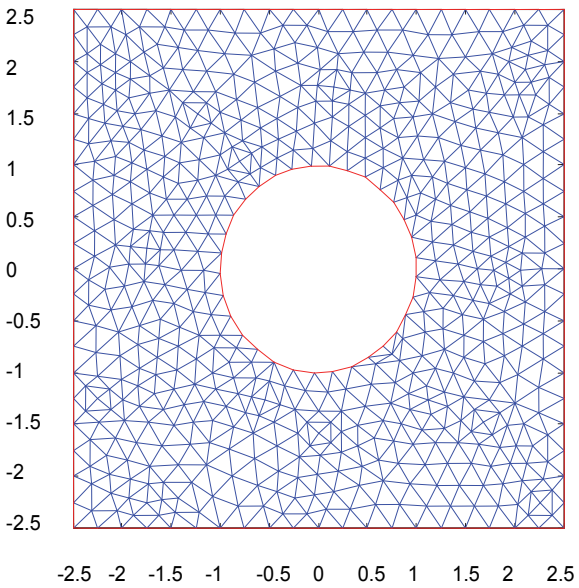

Fig. 7. Fin meshing with 627 nodes. *(h^*=2.5, l^*=2.5)*

In this work, up to 11785 nodes are used in order to take into account the effect of the mesh finesse on the process convergence and results reliability. The deviations on the calculation results of the fin efficiency with the different meshing prove to be less than 0.3 %. The numerical simulation is achieved using MATLAB simulation software. A global calculation algorithm for heat and mass transfer models is developed and presented in Fig. 8.

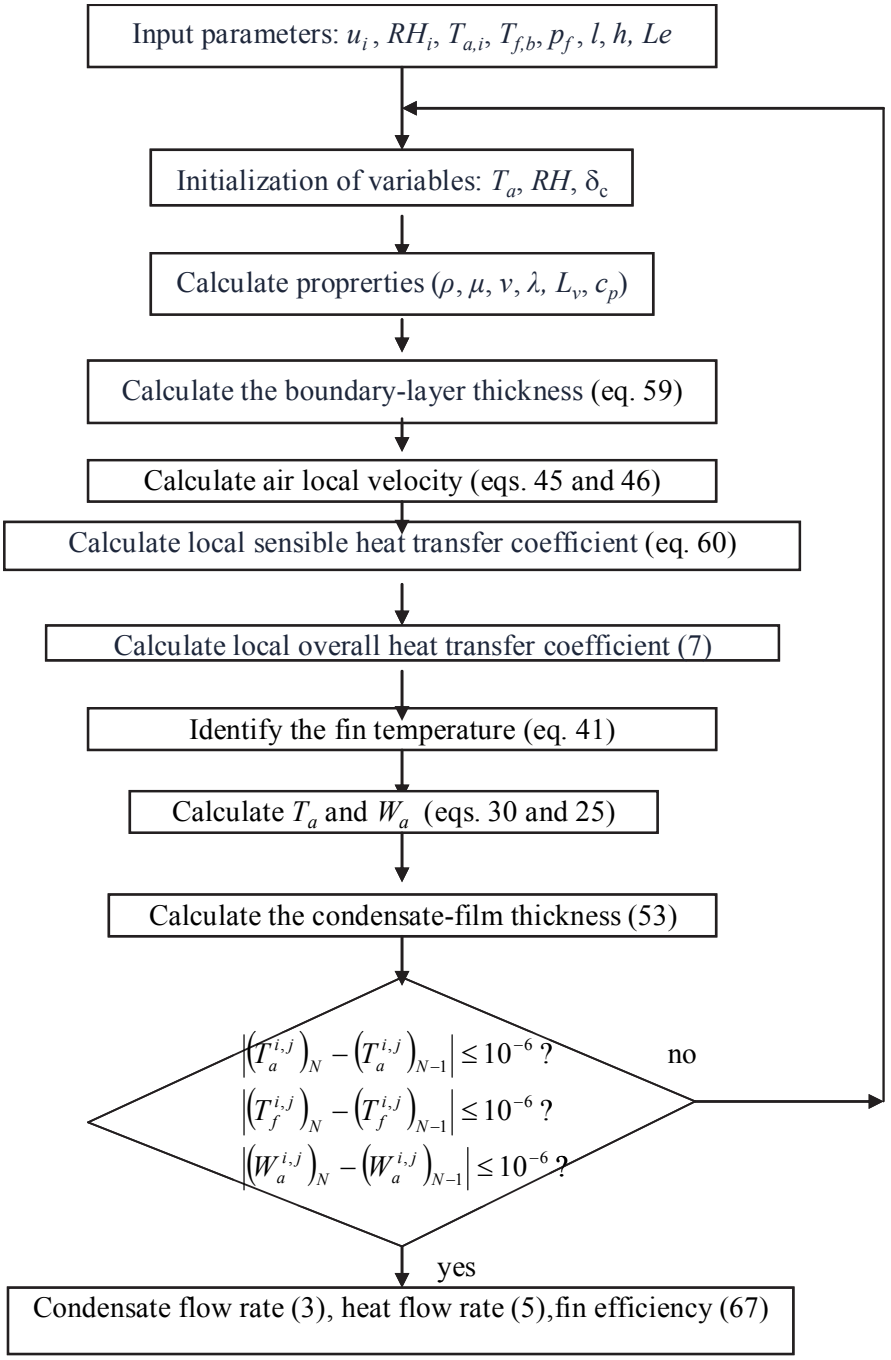

Fig. 8. The global calculation algorithm for heat and mass transfer models

2.5 Heat performance characterization

In order to evaluate the fin thermal characteristics, we need to define the heat transfer coefficients, the Colburn factor j, and the fin efficiency η_f.

2.5.1 Colburn factor

The sensible Colburn factor is expressed as:

$$j_{sen} = \frac{Nu_{sen}}{\mathrm{Re}_{Dh}.\mathrm{Pr}^{1/3}} \tag{47}$$

The Reynolds number based on the hydraulic diameter is defined as follows:

$$\mathrm{Re}_{Dh} = \frac{\rho_a u_{\max,a} D_h}{\mu_a} \tag{48}$$

where the maximal moist air velocity $u_{\max,a}$ is obtained at the contraction section of the flow :

$$u_{\max,a} = \frac{2h^*}{2h^* - 2} u_i \tag{49}$$

By definition, the hydraulic diameter is expressed as:

$$D_h = \frac{8h^* l^* p^* - 2\pi p^*}{4h^* l^* - \pi + \pi p^*} \tag{50}$$

The Nusselt and Prandtl numbers are given by:

$$Nu_{sen} = \frac{\alpha_{sen,hum}.D_h}{\lambda_a} \tag{51}$$

$$\mathrm{Pr} = \frac{\mu_a.c_{p,a}}{\lambda_a} \tag{52}$$

The Colburn factor takes into account the effect of the air speed and the fin geometry in the heat exchanger. Knowing the heat transfer coefficient, the determination of Colburn factor becomes usual.

2.5.2 Heat transfer coefficients

Regarding the physical configuration of the fin-and-tube heat exchanger, the condensate distribution over the fin-and-tube is complex. In this work, the condensate film is assumed uniformly distributed over the fin surface and the effect of the presence of the tube on the film distribution is neglected. The average condensate-film thickness is calculated as follow:

$$\overline{\delta}_c = \frac{\int_{A_t}^{A_f + A_t} \delta_c ds}{A_f} \tag{53}$$

where A_f denotes the net fin area:

$$A_f = 4lh - \pi r^2 \tag{54}$$

And A_t represents the total tube cross section:

$$A_t = \pi r^2 \tag{55}$$

The condensate-thickness δ_c is calculated using equation (37) and can be estimated iteratively. Assuming the temperature profile of the condensate-film to be linear, the heat transfer coefficient of condensation is obtained as follow:

$$\alpha_c = \frac{\lambda_c}{\delta_c} \tag{56}$$

The theory of hydrodynamic flow over a rectangular plate associated with heat and mass transfer allows us to evaluate the sensible heat transfer coefficient. In this case, a hydro-thermal boundary-layer is formed and results from a non-uniform distribution of temperatures, air velocity and water concentrations across the boundary layer (Fig.9).

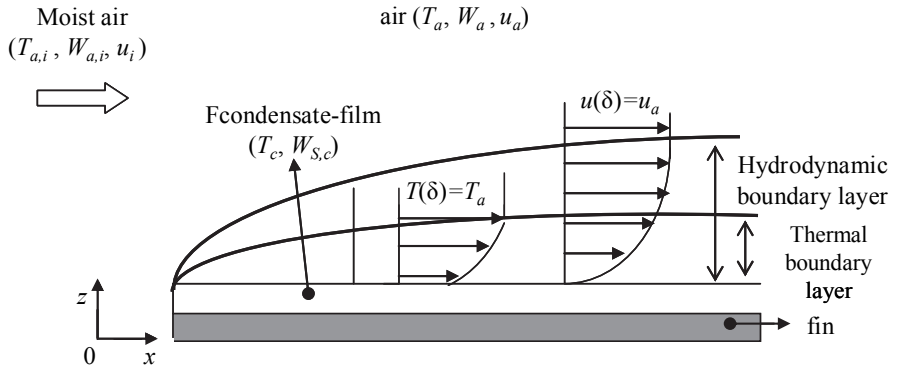

Fig. 9. Thermal and hydrodynamic boundary layer on a plate fin

According to Blasius theory, the hydraulic boundary layer thickness can be defined as follow:

$$\delta_H = \frac{5.x}{\mathrm{Re}_L^{1/2}} \quad \text{with} \quad \mathrm{Re}_L = \frac{u_a.x}{\nu_a} \tag{57}$$

where Re_L is the Reynolds number based on the longitudinal distance x.
By analogy, the thermal boundary layer thickness is associated to the hydraulic boundary layer thickness through the Prandtl number (Hsu, 1963):

$$\frac{\delta_T}{\delta_H} = \mathrm{Pr}^{-1/3} \tag{58}$$

The expression of δ_t takes the following form:

$$\delta_T = \frac{5.x}{\mathrm{Re}_L^{1/2}.\mathrm{Pr}^{1/3}} \tag{59}$$

Assuming a linear profile of temperature along within the boundary layer, the sensible heat transfer coefficient is related to the thermal boundary layer thickness by the following relation:

$$\alpha_{sen,hum} = \frac{\lambda_a}{\overline{\delta}_T} \tag{60}$$

Where, δ_t is the average thickness of the thermal boundary layer.
The overall heat transfer coefficient, estimated from equation (7), involves the sensible heat-transfer coefficient and the part due to mass transfer. The exact values of the average sensible and overall heat-transfer coefficients can be obtained by:

$$\overline{\alpha}_{sen,hum} = \frac{\int_{A_t}^{A_f+A_t} \alpha_{sen,hum} ds}{A_f} \quad \overline{\alpha}_{O,hum} = \frac{\int_{A_t}^{A_f+A_t} \alpha_{O,hum} ds}{A_f} \tag{61}$$

2.5.3 Fin efficiency

In this work, the local fin efficiency in both dry and wet conditions is estimated by the following relations:

$$\eta_{f,dry} = \frac{\alpha_{sen,dry}\left(T_a - T_f\right)}{\alpha_{sen,dry}\left(T_{a,i} - T_{f,b}\right)} = T_a^* - T_f^* \tag{62}$$

$$\eta_{f,hum} = \frac{\alpha_{sen,hum}\left(T_a - T_f\right)\left(1 + \frac{Lv}{Le^{2/3}c_{p,a}}.\frac{W_a - W_{S,f}}{T_a - T_f}\right)}{\alpha_{sen,hum}\left(T_{a,i} - T_{f,b}\right)\left(1 + \frac{Lv}{Le^{2/3}c_{p,a}}.\frac{W_{a,i} - W_{S,f,b}}{T_{a,i} - T_{f,b}}\right)} = \left(T_a^* - T_f^*\right)\frac{\left(1 + \frac{Lv}{Le^{2/3}c_{p,a}}.C\right)}{\left(1 + \frac{Lv}{Le^{2/3}c_{p,a}}.C_i\right)} \tag{63}$$

Where the condensation factors are given by:

$$C = \frac{W_a - W_{S,f}}{T_a - T_f} \tag{64}$$

$$C_i = \frac{W_{a,i} - W_{S,f,b}}{T_{a,i} - T_{f,b}} \tag{65}$$

The averages values of the fin efficiencies over the whole fin are estimated as follow:

$$\overline{\eta}_{f,dry} = \frac{\int_{A_t}^{A_f+A_t} \alpha_{sen,dry}\left(T_a^* - T_f^*\right) ds}{\int_{A_t}^{A_f+A_t} \alpha_{sen,dry} ds} \tag{66}$$

$$\bar{\eta}_{f,hum} = \frac{\int_{A_t}^{A_f+A_t} \alpha_{sen,dry}\left(T_a^* - T_f^*\right)\left(1+\frac{Lv}{Le^{2/3}c_{p,a}}.C\right)ds}{\left(1+\frac{Lv}{Le^{2/3}c_{p,a}}.C_i\right)\int_{A_t}^{A_f+A_t} \alpha_{sen,dry}ds} \tag{67}$$

3. Results and discussion

In This section, the simulation results of the heat and mass transfer characteristics during a streamline moist air through a rectangular fin-and-tube will be shown. The effect of the hydro-thermal parameters such us air dry temperature, fin base temperature, humidity, and air velocity will be analyzed. The key-parameters values for this work are selected and reported in the table 1. A central point is uncovered for the main results representations. This point corresponds to a fully wet condition problem.

Parameter	Central point values	range
Fin high, h^*	2.5	-
Fin length, l^*	2.5	-
Fin spacing, p^*	0.16	-
Inlet air speed, u_i	3 m/s	1-5 m/s
Fin base temperature, $T_{f,b}$	9 °C	1-9 °C
Inlet air dry temperature, $T_{a,i}$	27 °C	24-37 °C
Inlet air relative humidity, RH_i	50 %	20-100 %
Lewis number, Le	1	-

Table 1. Values of the parameters used in this work

3.1 The fully wet condition

Figures 10a and 10b show, respectively, the distribution of the curve-fitted air temperature inside the airflow region and that of the fin temperature for the values of the parameters indicated by the central point.

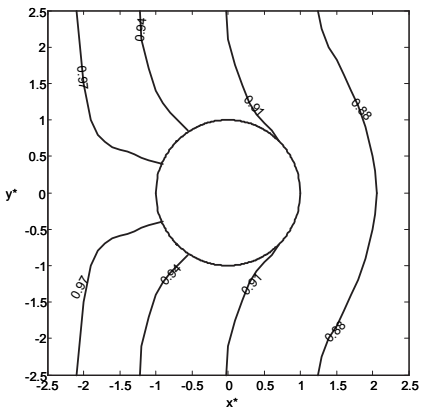

Fig. 10a. Air temperature distribution

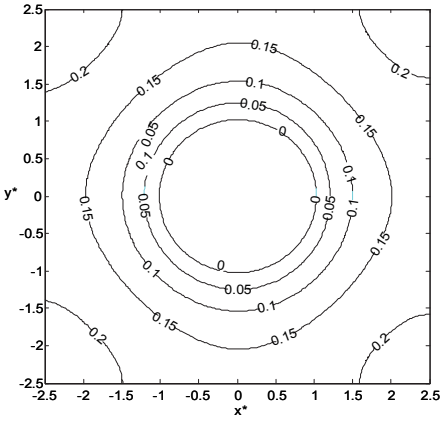

Fig. 10b. Fin temperature distribution

Initially, the air temperature is uniform (T^*_a=1) then decreases along the fin. As the fin temperature is minimal at the vicinity of the tube, air temperature gradient is more important near the tube than by the fin borders. However, at the outlet of the flow, the temperature gradient of air is weaker than at the inlet due to the reduction of the sensible heat transfer upstream the fin. The increasing of the boundary layer thickness along the fin causes a drop of the heat transfer coefficient. It is worth noting that the isothermal temperature curves are normal to the fin borders because of the symmetric boundary condition. Concerning the fin temperature T^*_f, it decreases from the inlet to attain a minimum nearby the fin base surface and then increases again when going away the tube. For this case of calculation, the dew point temperature of air, corresponding to HR_i=50 % and $T_{a,i}$=27 °C, is equal to 16.1 °C, that is greater than the maximal temperature of the fin (13.4 °C) and the fin will be completely wet. The condensation factor C, defined by equation (64), allows us to verify this fact. Fig. 11 illustrates its distribution over the fin region.

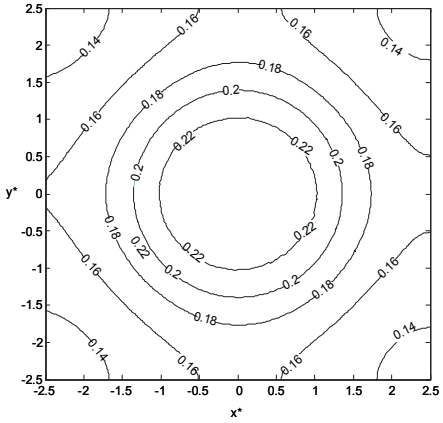

Fig. 11. Condensation factor distribution

As can be observed from Fig. 11, the condensation factor takes the largest values in the vicinity of the tube wall. The difference between the maximal and minimal values is about 30 %. The variation of C against the fin base temperature T_f and relative humidity HR can be demonstrated by the subsequent reasoning. The saturation humidity ratio of air may be approximated by a second order polynomial with respect to the temperature (Coney *et al.*, 1989, Chen, 1991):

$$W_S = a + bT + cT^2 \tag{68}$$

Where a,b and c are positives constants
The relative humidity has the following expression:

$$RH = \frac{P_v}{P_a - P_v} = \frac{W_a}{W_{S,a}} \times \frac{P_a - P_v}{P_a - P_{S,v}} \tag{69}$$

Where P_a, P_v and $P_{s,v}$ respectively represent, air total pressure, water vapor partial pressure and water vapor saturation pressure. If we neglect the water vapor partial and saturation pressures regarding the total pressure, then the following expressions of the absolute humidity arise:

$$W_a \approx RH \times W_{S,a} \tag{70}$$

$$W_{a,i} \approx RH \times W_{S,a,i} \tag{71}$$

Substituting equations (68) to (71) into the relation defining C (Eq. 64) yields:

$$C \approx RH \times \left[b + c\left(T_a + T_f\right) \right] - \left(1 - RH\right) \frac{a + bT_f + cT_f^2}{T_a - T_f} \tag{72}$$

The first and second order derivatives of the condensation factor with respect to the fin temperature can then be obtained readily from the previous equation:

$$\left.\frac{\partial C}{\partial T_f}\right|_{RH} = RH \times c - \left(1 - RH\right) \left[\frac{W_{S,a}}{\left(T_a - T_f\right)^2} - c \right] \tag{73}$$

$$\left.\frac{\partial^2 C}{\partial T_f^2}\right|_{RH} = -\left(1 - RH\right) \left[\frac{2W_{S,a}}{\left(T_a - T_f\right)^3} \right] \tag{74}$$

Obviously, for saturated air stream (RH=1), the first derivative of C takes the value of the constant c and is consequently positive. That demonstrates the increase of the condensation factor C with the fin temperature T_f. Conversely, for a sub-saturated air (RH<1), the second order derivative is always negative, that implies a permanent decrease of the condensation factor gradient with temperature. In this case, the critical point (maximum) for the function C(Tf) can be evaluated when $\left.\frac{\partial C}{\partial T_f}\right|_{RH} = 0$, thus, we obtain:

$$T_{f,cr} = T_a - \sqrt{(1-RH).W_{S,a} / c} \tag{75}$$

or

$$RH_{cr} = 1 - \frac{c\left(T_a - T_f\right)^2}{W_{S,a}} \tag{76}$$

Therefore the following statement is deduced:

- When $T_f > T_{f,cr}$ or RH < RH_{cr}, then $(\delta C/\delta T_f)_{RH} < 0$ and C decreases with T_f.
- When $T_f < T_{f,cr}$ or RH > RH_{cr}, then $(\delta C/\delta T_f)_{RH} > 0$ and C increases with T_f.

Fig. 11 is consistent with the above statement. Indeed, we can observe from Fig.10b and Fig.11 that the local condensation factor decreases with the fin temperature. Also, for the conditions in which the calculation related to Fig.10b and Fig.1 was performed, we get c=9.3458x10-6 and $W_{S,a}$=0.0202, hence, from Eqs. (75) and (76), $T_{f,cr}$=-6°C and RH_{cr}=90 %. Since Fig. 12 shows that $T_f > T_{f,b} > T_{f,cr}$, this observation validates our statement. However, it is also worth noting that the relative humidity of the moist air varies with the fin temperature and as a matter of fact, RH should be temperature dependent and the above statements hold along a constant relative humidity curve. Fig. 12 represents the distribution of air relative humidity in the fin region.

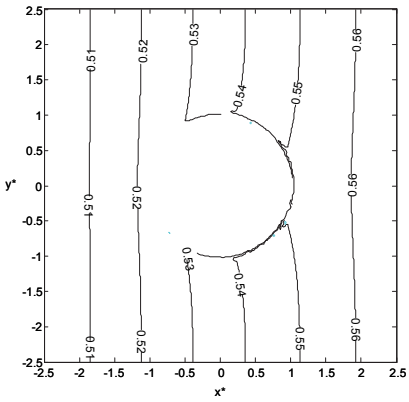

Fig. 12. Relative humidity distribution

As can be observed in Fig. 12, the relative humidity evolves almost linearly along the fin length. There is about 13 % difference between the inlet and outlet airflow. Correspondingly, the distribution of the condensate mass flux and the total heat flux density are carried out and illustrated in Fig. 13 and 14.

As the condensation factor takes place at the surrounding of the tube where the maximum gradient of humidity occurs, the condensate mass flux m''_c gets its maximal value at the fin base. Similarly, the maximal temperature gradient (T_a-T_f) arises at the fin base. That enhances the heat flow rate and a maximal value of q''_t is reached. However, these quantities decrease more and more along the dehumidification process due to the humidity and temperature gradients drop. Further results are shown in Fig.15, where the fin efficiency

curves are plotted. As the condensation factor C and the difference (T_a* - T_f*) grow around the tube, the fin efficiency will be maximal at the centre. As well, the quantities C and (T_a* - T_f*) are weaker at the upper and lower fin borders, that leads to the local reduction of the fin efficiency.

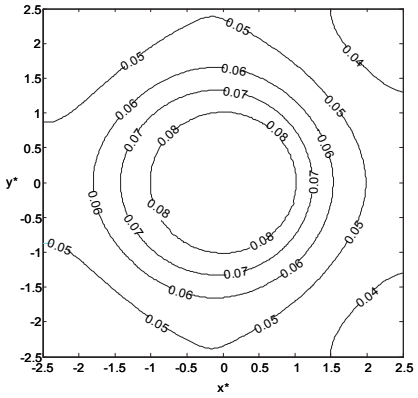

Fig. 13. Condensate mass flux distribution

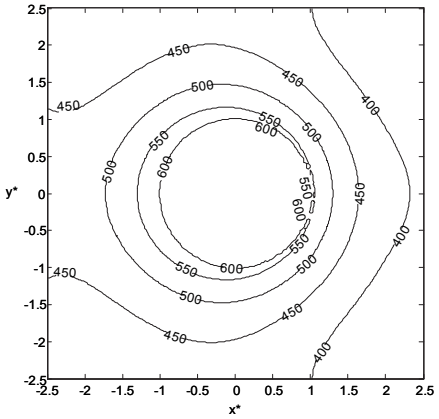

Fig. 14. Heat flux density distribution

3.2 The partially wet condition

The partially wet fin is obtained when the initial conditions are fixed to those of the central point (Table 1) except the inlet relative humidity which is settled to RH = 36 %, since $T_{f,b}$<$T_{dew,a}$< $T_{f,max}$. Condensation factor, relative humidity, total heat flux, and fin efficiency are estimated. The same general observations as those of the fully wet fin can be withdrawn. Condensation factor, total heat flux density and fin efficiency are maximal at the fin tube. However, the condensate droplets come to the end (C=0) from certain distance of the tube. At this point, the effect of some parameters, like inlet temperature, on the heat and mass transfer characteristics will be presented and discussed.

3.3 Effect of the inlet relative humidity

Both ideal and real fins are considered, and it is observed that δ_c starts to increase rapidly at about RH_i=40 %. For this case, the dry fin limit is estimated at RH_i=32 % and the fully wet condition beginning is estimated at RH_i=42 %. The order of magnitude of δ_c is about 0.1 mm, this value is comparable to that of Myers (1967) (0.127 mm) for, approximately, the same conditions. As δ_c increase with RH_i, the thermal resistance of the condensate increases and the heat transfer coefficient of the condensate α_c decreases (Eq.56). This agrees with the result of Coney et al. [10]. It was found also that the sensible heat transfer coefficient $\alpha_{sen,hum}$ is insensitive to RH_i (Fig. 21). Due to the smallness of the condensate film thickness, its thermal resistance ($1/\alpha_c$) is in the order of 0 to 5 % regarding the thermal resistance of the surrounding air. It is usually neglected. Conversely, the average overall heat transfer coefficient increases rapidly as the relative humidity increases. For a dry fin (RH_i<32 %), the total heat amount of both ideal and real fins is constant and consequently the fin efficiency remains constant in this range. The condensation appears from RHi=32 % for an ideal fin and from RH_i=36 % for a real fin. At this range (32%<RH_i<36%), the relative difference between ideal and real heats $\{(Q_{t,id}-Q_{t,r})/Q_{i,id}\}$ is important, thus an abrupt decrease in fin efficiency is noticed. For RH_i=36 %, the condensation begins on the real fin and the total heat exchange rate $Q_{t,r}$ increases, thus the relative difference between ideal and real heats exchanges rates become less important and narrows more and more, therefore, the decrease in fin efficiency is gradual with a slop around 8 %. At RH_i=42 %, a complete wet condition is achieved for the real fin, the relative difference between $Q_{t,r}$ and $Q_{t,id}$ is almost constant. As well, the fin efficiency reduces slightly with a slop less than 4 %. Hence, the condensation, enhanced by increasing the relative humidity, can affect the efficiency and reduces it by 12 %. The fin efficiency gradient regarding relative humidity RH_i in the partial wet condition is more important than in the fully wet condition. The efficiency decreases more quickly in the partial wet condition. This result is similar of those of Rosario & Rahman (1999), Wu & Bong (1999), Liang *et al.* (2000), and Threlkeld (1970). However, Hong & Webb (1996), Elmahdy & Biggs (1983), and Mc Quiston (1975) have observed a more important decrease of the fin efficiency in the complete humidified phase (until 35 %). But, their models assume a constant temperature and relative humidity of the surrounding air. Kandlikar (1990) has re-examined the mathematical model of Elmahdy & Biggs (1983) and demonstrates that the fin efficiency in the fully wet condition should be insensitive to the relative humidity. It can be demonstrated that the results found by Hong & Webb (1996), and Mc Quiston (1975) are the consequence of the assumptions undertaken in their models. Indeed, if we consider again the expression of the fin efficiency in humid conditions (Eq. 67):

$$\eta_{f,hum} = \left(T_a^* - T_f^*\right)\frac{\left(1+\beta.C\right)}{\left(1+\beta.C_i\right)} \tag{77}$$

where;

$$\beta = \frac{Lv}{Le^{2/3}c_{p,a}} \quad \text{and} \quad C_i = \frac{W_{a,i} - W_{S,f,b}}{T_{a,i} - T_{f,b}}$$

Assuming Ta and C to be constant, as in the models of Hong & Webb (1996) and Mc Quiston (1975), the derivation of equation (77) with respect to RH_i yields:

$$\frac{\partial \eta_{f,hum}}{\partial RH_i} = -\frac{\partial T_f^*}{\partial RH_i} - \frac{\eta_{f,hum}.W_{S,a,i}.\beta}{\left(T_{a,i} - T_{f,b}\right)\left(1+\beta.C_i\right)} \tag{78}$$

Performing calculations of the fin efficiency derivative at $\eta_{f,hum}$=0.7 and using the parameters mentioned in figure 25, $T_{a,i}$=27 °C, $T_{f,b}$=9 °C, the following results yields:

$$-\frac{\partial T_f^*}{\partial RH_i} \approx 0.3 \; ; \; \frac{\partial \eta_{f,hum}}{\partial RH_i} \approx -1.1 \text{ for } RH_i=50\ \%$$

$$\text{and} \quad \frac{\partial \eta_{f,hum}}{\partial RH_i} \approx -0.42 \text{ for } RH_i=100\ \%$$

The decrease of the fin efficiency gradient between RH_i=50 % and RH_i=100 % is about 21 %. Therefore, the discordance founded between the different authors about the effect of the relative humidity on the fin efficiency may be the result of the models simplifications adopted.

3.4 Effect of the inlet air temperature

For a fixed RH_i, the increase of the inlet air temperature $T_{a,I}$ leads to increasing both fin and airflow temperatures (T_f and T_a). Thus, it has been noticed that the variations of the dimensionless fin and air temperatures are insignificant. However, the absolute moist air humidity raises and generates a more important humidity gradient between the fin wall and the surrounding air, and hence contributes to increase the condensation factor. Indeed, the derivation of C (Eq. 64) with respect to air temperature yields a positive derivative:

$$\left.\frac{\partial C}{\partial T_a}\right|_{RH} = c.RH + (1-RH).\frac{W_{S,f}}{T_a - T_f} > 0 \tag{79}$$

As the absolute humidity increase with $T_{a,I}$, the mass transfer is enhanced and the condensate-film thickness also increases. On the other hand, the increase of $W_{a,i}$ and W_a results in raising the condensation factor C and the latent heat rate, and that makes the overall heat transfer coefficient more important for a greater temperatures. Nonetheless, in the absence of condensation (RH_i from 0 to about 32 %), the overall and sensible heat transfer coefficients are equivalent and independent of the air temperature. With increasing air temperature, the total heat rate increases and the condensation starts for lower values of RH_i. The vapor condensation appearance is distinguished from RH_i=26 % (ideal fin) or RH_i=32 % (real fin) for $T_{a,i}$=30 °C and from RH_i=38 % (ideal fin) or RH_i=44 % (real fin) for $T_{a,i}$=24 °C. In the dry phase, the heat rate remains constant which implies a constancy of fin efficiency. At this stage, the fin efficiency decreases slightly with the increasing of air temperature. When condensation begins, the total heat rate increases with RHi and an abrupt decrease of fin efficiency is observed. This drop in the fin efficiency is slightly weak for greater air temperatures. In the fully wet condition and for higher relative humidity values, the fin efficiency decreases distinctly when Ta,I increase. These observations match with those reported by Kazeminejad (1995) and Rosario & Rahman (1999).

3.5 Effect of the fin base temperature

As stated above (Eq. 64), the dependence of C on the fin temperature T_f is marked with the existence of a critical value of RH_i where the trend progression is inverted. That is clearly

observed in Fig.30. For $RH_i<RH_{cr}$, the condensation factor decreases with the fin base temperature, whereas, for $RH_i>RH_{cr}$, C increases with $T_{f,b}$. Correspondingly, the trend of C is also inverted depending on whether the fin is real or ideal. Indeed, the ideal C factor is higher than the real C for $RH_i< RH_{cr}$, while it is lower for $RH_i> RH_{cr}$. As the absolute humidity near the fin wall $W_{S,f,b}$ increases with $T_{f,b}$, the amount of condensable vapor decreases, which in turn causes the reduction of the average condensate-film thickness as illustrated in Fig.31. However, the overall heat transfer coefficient follows the same trend as the condensation factor. For the dry condition, the sensible heat transfer is independent on $T_{f,b}$. Conversely, for the humid condition, $\alpha_{t,hum}$ decreases with $T_{f,b}$ when $RH_i< RH_{cr}$ and increases with Tf,b when $RH_i> RH_{cr}$. It is worth noting that since $\alpha_{t,hum}$ is influenced by the boundary layer thickness, the critical relative humidity RH_{cr} for which the trend of $\alpha_{t,hum}$ changes is to some extent different from the critical value obtained with C. In our case, $\alpha_{t,hum}$ begins to increase with $T_{f,b}$ from RH_i=85 % instead of RH_i=78 % as regards to C. The increase of $T_{f,b}$ leads an increase of $W_{S,f,b}$ and thus reduces both the total heat rate and the fin efficiency. In the partially humid condition case, a rapid drop of η_f is confirmed (about 10 %). This drop proves to be smaller for the fully wet condition (about 2%). Nevertheless, the variation of $T_{f,b}$ has no significant effect on the fin efficiency for the dry condition. Our results concerning the fin efficiency behavior with regard to the fin temperature agree with those of Rosario & Rahman (1999) but prove to be dissimilar from those established by Kazeminejad (1995). This is probably due to the fact that Rosario & Rahman consider the condensation factor to be variable while Kazeminejad assumes it as constant.

3.6 Effect of the inlet air speed

Increasing u_i reduces the hydro-thermal boundary layer thickness and increases the heat transfer coefficient. The temperature of air in the flow core also increases since the flow mass increases more rapidly than the heat flow rate, thus the fin temperature will be more important. Furthermore, as the air mass flow rate increases more rapidly than the condensate mass flow rate, the difference between airflow humidity and the saturated air humidity at the fin neighborhood (W_a – $W_{S,f}$) increases. That means an increase in the condensation factor as well as in the condensate thickness. In the same way, as the hydro-thermal boundary layer becomes finer for higher flow regime, the sensible heat transfer is favored. Thus, the sensible and overall heat transfer coefficients increase with u_i. However, this increase narrows down for highest air speed. On the other hand, the influence of u_i on the heat transfer is such as the total heat rate increase with increasing the flow regime. In the case of an ideal fin, the heat transfer increasing is quicker than for a real fin. This result has also been demonstrated numerically by Coney *et al.* (1989). Accounting for that effect, the fin efficiency should decrease with u_i, as mentioned in Fig. 36. Indeed, for lower velocities ui, the residence time of air is more important and the heat and mass transfer is more complete. This result is in adequacy with those of Liang *et al.* (2000) and Coney *et al.* (1989). Moreover, it is found that the difference between dry and humid fin efficiencies ($\eta_{f,dry}$ - $\eta_{f,hum}$) increases with u_i.

4. Conclusions

The present work proposes a two-dimensional model simulating the heat and mass transfer in a plate fin-and-tube heat exchanger. Ones the airflow profile was determined, the water vapor, air stream and fin heat and mass balance equations were solved simultaneously. It

was found that the overall heat transfer coefficient as well as the condensation factor increase with the inlet air temperature, the inlet relative humidity as well as the inlet velocity. Regarding the variations of $\alpha_{t,hum}$ and C with the fin base temperature, a critical value of relative humidity (RH_{cr}), corresponding to a minimum in $\alpha_{t,hum}$ and C was identified. This result still constitutes a point of discordance between many authors. The performed calculations of the wet-fin efficiency have demonstrated the decrease of $\eta_{f,hum}$ with increasing any of the parameters. However, a more important drop of $\eta_{f,hum}$ have been noticed for the partially wet condition. Moreover, the decrease of the fin efficiency with respect to the relative humidity and the fin base temperature, in the fully wet condition, is very weak especially for higher values of RH_i or $T_{f,b}$. The slope is quantified around 2 %.

5. References

Benelmir, R.; Mokraoui, S.; Souayed, A. (2009). Numerical analysis of filmwise condensation in a plate fin-and-tube heat exchanger in presence of non condensable gas, Heat and Mass Transfer Journal, 45, 1561–1573.

Chen, L.T. (1991). Two-dimensional fin efficiency with combined heat and mass transfer between water-wetted fin surface and moving moist airstreams, Int. J. Heat Fluid Flow, 12, 71-76.

Chen, H.T.; Song, J.P.; Wang, Y.T. (2005). Prediction of heat transfer coefficient on the fin inside one-tube plate finned-tube heat exchangers, Int. J. Heat Mass Transfer, 48, 2697-2707.

Chen, H.T. ; Wang, Y.T. (2008). Estimation of heat-transfer characteristics on a fin under wet conditions, Int. J. Heat Mass Transfer, 51, 2123-2138.

Chen, H.T.; Hsu, W.L. (2007). Estimation of heat transfer coefficient on the fin of annular-finned tube heat exchangers in natural convection for various fin spacings, Int. J. Heat Mass Transfer, 50, 1750-1761.

Chen, H.T.; Chou, J.C. (2007). Estimation of heat transfer coefficient on the vertical plate fin of finned-tube heat exchangers for various air speeds and fin spacings, Int. J. Heat Mass Transfer, 50, 47-57.

Choukairy, Kh. ; Bennacer, R. ; El Ganaoui, M. (2006). Transient behaviours inside a vertical cylindrical enclosure heated from the sidewalls, *Num. Heat Transfer (NHT*), 50-8, 773 – 785.

Coney, J.E.R. ; Sheppard, C.G.W. ; El-Shafei, E.A.M. (1989). Fin performance with condensation from humid air, Int. J. Heat Fluid Flow, 10, 224-231.

Elmahdy, A.H. ; Biggs, R.C. (1983). Efficiency of extended surfaces with simultaneous heat transfer and mass transfer, ASHRAE Journal, 89-1A, 135-143.

Hong, T.K. ; Webb, R.L. (1996). Calculation of fin efficiency for wet and dry fins, HVAC & Research, 2-1, 27-41.

Hsu, S.T. (1963). Enginnering heat transfer, D. VanNostrand Company, 240-252.

Johnson, R.W. (1998). The Handbook of Fluid Dynamics, Springer, USA.

Kandlikar, S.G. (1990). Thermal design theory for compact evaporators, Hemisphere Publishing, NY, pp. 245-286.

Kazeminejad, H. (1995). Analysis of one-dimensional fin assembly heat transfer with dehumidification, Int. J. of Heat mass transfer, 38-3, 455-462.

Khalfi, M.S. ; Benelmir, R. (2001). Experimental study of a cooling coil with wet surface conditions, Int. Journal of Thermal Sciences, 40, 42-51.

Lin, C.N.; Jang, J.Y. (2002). A two-dimensional fin efficiency analysis of combined heat and mass transfer in elliptic fins, Int. J. Heat Mass Transfer, 45, 3839-3847.

Lin, Y.T. ; Hsu, K.C. ; Chang, Y.J. ; Wang, C.C. (2001). Performance of rectangular fin in wet conditions: visualization and wet fin efficiency, ASME J. Heat Transfer, 123, 827-836.

Liang, S.Y.; Wong, T.N.; Nathan, G.K. (2000). Comparison of one-dimensional and two-dimensional models for wet-surface fin efficiency of a plate-fin-tube heat exchanger, Appl. Thermal Eng, 20, 941-962.

McQuiston, F.C. (1975). Fin efficiency with combined heat and mass transfer, ASHRAE Journal, 81, 350-355.

Myers, R.J. (1967). The effect of dehumidification on the air-side heat transfer coefficient for a finned-tube coil, Master Sc. Thesis, University of Minnesota.

Nusselt, W. (1916). Die Oberflachenkondensation des Wasserdampfes, Z. Ver. Dt. Ing, . 60, 541-575.

Rosario, L. ; Rahman, M.M. (1999). Analysis of heat transfer in a partially wet radial fin assembly during dehumidification, Int. J. Heat Fluid Flow, 20, 642-648.

Saboya, F.E.M. ; Sparrow, E.M. (1974). Local and average heat transfer coefficients for one-row plate fin and tube heat exchanger configurations, ASME J. Heat Transfer, 96, 265-272.

Threlkeld, J.L. (1970). Thermal Environmental Engineering, Prentice-Hall, New Jersey.

Wu, G. ; Bong, T.Y. (1994). Overall efficiency of a straight fin with combined heat and mass transfer, ASHRAE transactions, Part 1, 100, 367-374.

4

Process Intensification of Steam Reforming for Hydrogen Production

Feng Wang[1], Guoqiang Wang[2] and Jing Zhou[2]
[1]*Key Laboratory of Low-grade Energy Utilization Technologies and Systems (Chongqing University), Ministry of Education, Chongqing,*
[2]*College of Power Engineering, Chongqing University, Chongqing, PR China*

1. Introduction

Hydrogen is considered to be an efficient, clean and environmental, viable energy carrier in the 21st century [1]. Generally, there are many ways to produce hydrogen from both fossil fuels and renewable energy such as solar, wind, geothermal energy and so on [2,3]. Yet it is a realistic and practicable method for hydrogen production through hydrocarbon fuel reforming in the near future [7]. In the three types of fuel reforming technologies, namely steam, partial oxidation, auto-thermal reforming, steam reforming has the advantages of low reaction temperature, low CO content and high H_2 content in the products and that is very favorable for mobile applications such as Proton Exchange Membrane Fuel Cell (PEMFC) [4,5].

However, steam reforming (SR) of hydrocarbon fuels is usually strongly endothermic reaction, the process of SR is often limited by heat and mass transfer in the reactors, so it presents a slow reaction kinetics which is characterized by low dynamic response and cold spot in the reactor catalyst bed [6]. Therefore, study of process intensification and optimization of SR for hydrogen production becomes important for the improvement of the reactor performance by enhancing heat and mass transfer and this can be divided to three classes. One way is to adopt new catalyst materials and additives such as coating catalyst, nanometer particle catalyst and so on to enhance the catalytic reforming reaction process [7]; another way is to reduce size scale of reaction channels in steam reforming reactors, for example, using micro-reactors instead of conventional reactors, which can reduce the heat and mass transport resistance by decreasing the transport distance [8]; in addition, microwave direct heating and membrane separation technology are also used to intensify the strongly endothermic SR process [9].

In this chapter, it is studied and stated that methanol and methane are taken as model hydrocarbon fuels for hydrogen production by steam reforming technology and effective process intensification methods of micro-reactor and coating catalyst. The innovative stainless steel micro-reactors which can be used to adopt both kernel catalyst and coating catalyst was designed and fabricated. A novel catalytic coating fabrication method of cold spray technology was also proposed. Experiments and simulation studies were carried out on methanol steam reforming (MSR) and steam methane reforming (SRM) in the micro-reactor on kernel and coating catalyst respectively.

2. Process intensification of methanol steam reforming by micro-reactor

2.1 Experimental

In order to intensify the transport process of methanol steam reforming for hydrogen production, a stainless steel micro-reactor which performs the functions of preheating, evaporation, superheating and reaction was designed and fabricated as shown in Fig.1. Dimension of the reaction section is 60mm×50mm×3.5mm and the height of it can be regulated according to type of catalyst.

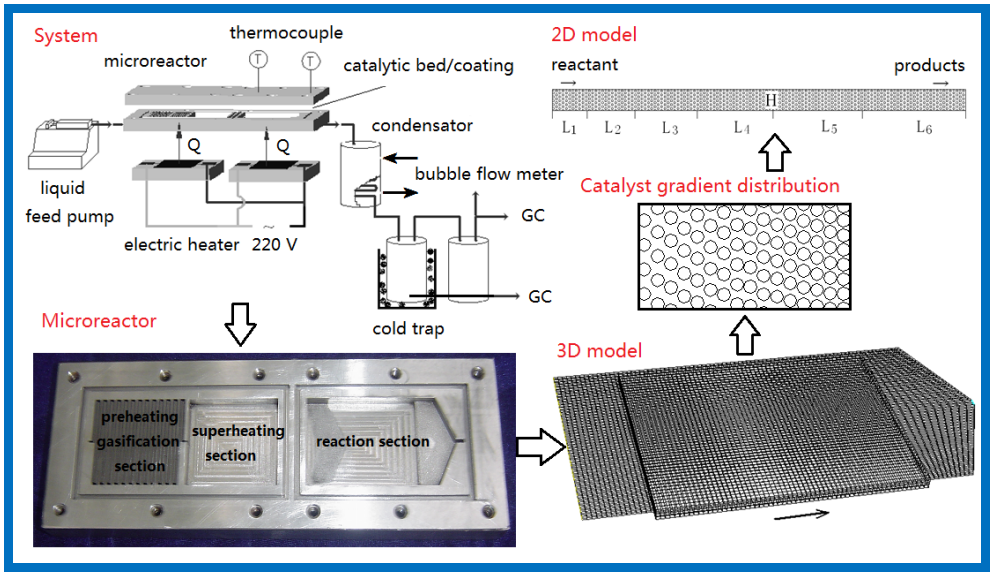

Fig. 1. Methanol steam reforming system, microreactor and the models.

Catalyst used is commercial CB-7 steam reforming catalyst produced by Sichuan Chemical Co. LTD., with the composition of CuO, ZnO, Al_2O_3 and other additives account for 65%, 8%, 8% and 2% respectively. The catalyst was grinded into particles with diameters less than 3 mm and then packed in the reaction section for reactor performance study. As for the catalyst uniform and gradient distribution comparison test, catalyst was grinded to the size of about 1mm.

Inlet de-ionized water and methanol flow rate was controlled by a syringe pump. The micro-reactor was heated by two electric heaters. Product stream was separated using a cold trap maintained at 0℃. The flow rate of dry reformed gas was measured by a soap-bubble meter. Composition of gas and un-reacted liquid products was analyzed by a gas chromatograph (GC2000) equipped with a thermal conductivity detector and two packed columns (Poropak-Q for the separation of un-reacted water and methanol, and TDX-01 for the separation of H_2, CO_2 and CO). Blank run conducted on the empty micro-reactor did not show any detectable methanol conversion. Before the experiment, N_2 gas was filled into the system at a flow rate of 30 ml/min to discharge the air in it and then switched to H_2-N_2 (H_2 3 Vol. %) at a flow rate of 40 ml/min in order to carry out catalyst temperature programmed reduction for 13 hours.

Effects of reaction temperature, water and methanol molar ratio, liquid space velocity on the reactor outlet parameters such as conversion, selectivity and hydrogen concentration were studied through experiments.

2.2 Numerical simulation

A three dimensional physical model of the reaction section was established for simulating reactor performance as shown in Fig.1. Temperature distribution along the flow direction was studied and the MSR kinetic model was obtained by data fitting. In order to study effects of gradient distributed catalyst activity on the transport process in MSR for hydrogen production, a two dimensional physical model of the reaction section was also established. Along the flow direction, reaction section was divided into six segments of different length according to catalyst activity. Catalyst activity was represented by exponential factor k_0 in kinetic equation. In contrast, uniformly distributed catalyst model was also studied with its k_0 equaled to the middle activity of the catalyst.

Methanol steam reforming kinetics which includes steam reforming of methanol (SR) and decomposed of methanol (DE) reactions was obtained by data fitting according to the experiment results, and was coupled to the general finite reaction rate model in CFD software of FLUENT3.2.

$$r_{SR} = 4971000T^{3.0257}\exp(-\frac{99.937}{RT})C_1^{1.6261}C_2^{1.3396}(1-\frac{C_5C_3^3}{K_{SR,C}C_1C_2}) \tag{1}$$

$$r_{DE} = 207600T^{1.1274}\exp(-\frac{121.571}{RT})C_1^{1.1274}(1-\frac{C_4C_3^2}{K_{DE,C}C_1}) \tag{2}$$

In this study, MSR was treated as homogeneous reaction and the heat and mass differences between the catalyst and the reactants were neglected. Gas mixture was regarded as incompressible ideal gases. Flow in the reaction section was assumed laminar and steady flow. Gravity of the gas and the radiation heat transfer were also neglected. Based on the above assumptions, partial differential governing equations for incompressible flow of ideal gas, heat and mass transfer inside reaction region in the Cartesian coordinate system were written as follows.

Mass:

$$\frac{\partial(\rho V_j)}{\partial x_j} = 0 \tag{3}$$

Component:

$$\rho V_j \frac{\partial Y_S}{\partial x_j} = \frac{\partial}{\partial x_j}(\rho D\frac{\partial Y_S}{\partial x_j}) + R_S \tag{4}$$

Momentum:

$$\frac{\partial(\rho V_j V_i)}{\partial x_j} = -\frac{\partial p}{\partial x_i} + \frac{\partial}{\partial x_j}[\mu(\frac{\partial V_i}{\partial x_j} + \frac{\partial V_j}{\partial x_i})] \tag{5}$$

Energy:

$$-\frac{\partial}{\partial x_j}(\lambda\frac{\partial T}{\partial x_j})=\frac{\partial}{x_j}(\sum\rho D\frac{\partial Y_S}{\partial x_j}h_S)+q \tag{6}$$

Ideal gas equation:

$$p=\rho RT\sum\frac{Y_S}{M_S} \tag{7}$$

Where the letters of ρ, V, p and T are the density, velocity, pressure and temperature of the gas mixture respectively. Y_s is mass fraction of gaseous component s; Subscript s represents 1 to 5 for the gaseous component of CH_3OH, H_2O, H_2, CO_2 and CO respectively. The coefficients of D, μ and λ are gas mixture's diffusion coefficient, viscosity coefficient and thermal conductivity respectively. They were computed by using the mixing rule of ideal gas. M_s is the molar mass of gaseous component s. Letters of h_s and q are specific enthalpy of gaseous component s and reaction heat respectively.

$$h_S=h_{0S}+\int C_{PS}dT \tag{8}$$

Where C_{ps} is specific heat at constant pressure of gaseous components.

$$q=\sum H_S^0R_SM_S \tag{9}$$

Where H_S^0 and R_s are standard enthalpy of formation and consumption rate of gaseous component s at reaction region. On micro-reactor inside surface R_s is 0; while in the reaction section, R_s of the component s is given as the following.

$$R_1=-(r_{SR}+r_{DE})M_1,\ R_2=-r_{SR}M_2,\ R_3=(3r_{SR}+2r_{DE})M_3,\ R_4=r_{SR}M_4,\ R_5=r_{DE}M_4$$

Where, R=8.314 J·mol^{-1}·K^{-1} is the universal gas constant.

2.3 Results and discussion

The effects of inlet parameters such as water to methanol mole ratio *W/M*, reaction temperature T_r, liquid space velocity *WHSV* on the reactor performance were investigated.

Methanol conversion ($X(CH_3OH)$) increased from 76.5% to 91.2% when *W/M* increased from 1.0 to 1.5, but the rate of increase was significant at lower *W/M* then small at higher *W/*M. Variation of hydrogen yield and mole content of H_2 ($Y(H_2)$) in the gas products were similar to that of methanol conversion as shown in Fig.2. However, CO mole content decreased with the increasing of *W/M*, presenting an inverse variation trend comparing with $X(CH_3OH)$. The reason was that increase of *W/M* enhanced the positive reaction of SR, which resulted in the increase of methanol conversion, hydrogen yield, molar content of H_2 and the reduction of CO. In addition, increase of *W/M* also promoted the reverse of water gas shift (RWGS) reaction that might exist in the reactor, which led to the increase of H_2 and reducing of CO. Since CO is a poison for PEMFC, it should be reduced to the minimum at outlet of micro-reactor as possible. However, latent heat of water is considerable. In MSR reaction, increase of *W/M* implies increasing of the heat needed for

preheating, evaporation and superheating of water, and this also affects the reaction temperature. So *W/M* should not be too high. In this study, *W/M* of 1.3 is optimal at which the mole content of CO is only 0.4%.

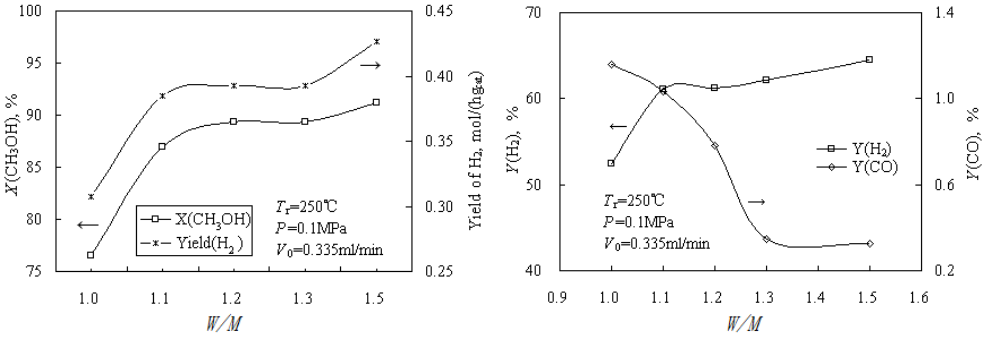

Fig. 2. Effects of *W/M* on methanol conversion, hydrogen yield, H_2 and CO in the products.

Methanol conversion increased with the rise of reaction temperature and it approached to almost 100% at T_r=250 ℃ and *WHSV* = 0.2 h^{-1} as can be seen in Fig.3. Hydrogen yield, mole contents of H_2 and CO also increased with increasing of temperature. Hydrogen yield reached 0.2 mol/(h·g_{cat}) under condition of T_r=260 ℃, *W/M*=1.3 and *WGHV*=0.2 h^{-1}, which can provide hydrogen for 10.2W PEMFC with a hydrogen utilization of 80% and an fuel cell efficiency of 60%. Owing to the strongly endothermic nature of MSR reaction, increasing of reaction temperature can promote SR reaction and then raise methanol conversion and mole content of H_2. However, DE was also a strongly endothermic reaction, so temperature increase can also promote this reaction leading to increase of CO content although it was less than 1% in this study. In practical application, the reaction temperature of MSR for hydrogen production has an optimal value, which depends on *WHSV* and is about 250℃ in this experiment.

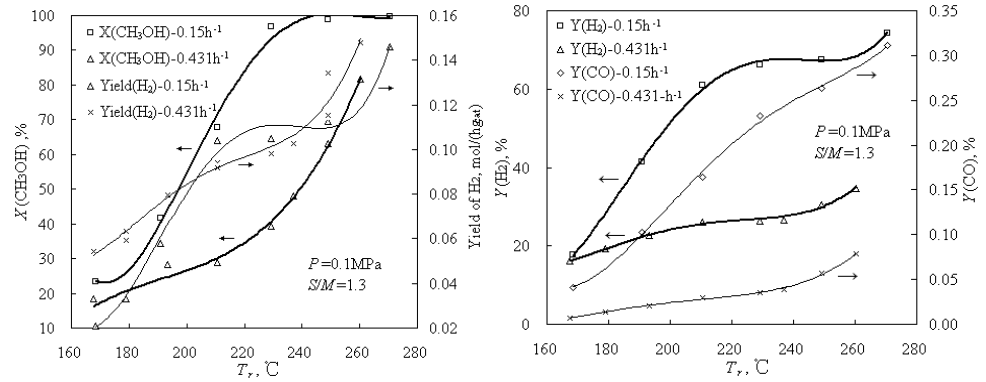

Fig. 3. Effects of temperature on methanol conversion, hydrogen yield, H_2 and CO in the products.

It can be seen in Fig.4 that, with the increasing of *WHSV*, methanol conversion reduced from 95.7% to 49.1%; mole content of H_2 was also decreased from 70.3% to 38.3%, whereas CO rose firstly and then decreased. Hydrogen yield mounted from 0.2mol/(h·g_{cat}.) to about 0.5 mol/(h·g_{cat}), then dropped quickly. With the increase of *WHSV*, residence time of the reactants in the reactor was reduced which resulted in reducing of methanol conversion and H_2 mole content. Consequently, in order to increase methanol conversion at higher *WHSV*, reaction temperature should be increased. However, when *WHSV* was smaller, T_r was the main factor influencing hydrogen production, which promoted positive reaction of DE, and resulted in a gradual increase of CO. When *WHSV* became larger, it became main factor which influenced the composition of products. And this may promote positive reaction of RWGS and further decreasing CO content. On the other hand, although raise of *WHSV* caused a reduction of methanol conversion, the methanol flow rate increased which added to hydrogen yield at certain range of *WHSV*. So hydrogen yield rose firstly and decreased afterwards along with increase of *WHSV*.

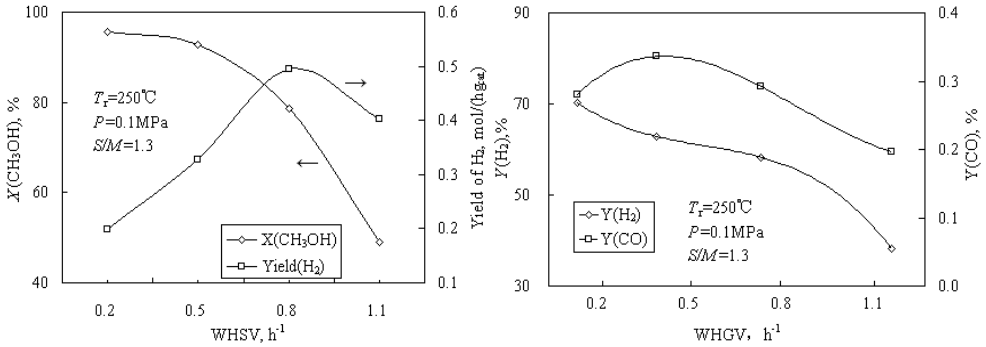

Fig. 4. Effects of liquid space velocity on methanol conversion, hydrogen yield, H_2 and CO content.

Methanol conversion was compared between experiment with 3D simulation as shown in Fig.5. It inferred that numerical model agreed well with experimental results at lower T_r but smaller at higher T_r. This may due to the heating model adopted in simulation as bottom of the reaction area was heated. Whereas in experiment, whole stainless steel micro-reactor including its cover board became a heat source for MSR reaction which led to the increase of methanol conversion. So it was reasonable to use this model to predict the performance of the micro-reactor. In this study, inner surface temperature of the reactor cover was got and compared with simulation as well as reference results. It revealed that a cold spot at the inlet of the reactor of 8.5℃ and 10℃ existed from experiment and simulation results. Comparing with reference, it was much smaller due to reduction of reactor size from convention to micro-scale although reaction temperature was higher [10]. In the experiment of methanol steam reforming, catalyst particles were moving from forepart to the back of the reactor due to washing of catalyst bed by reactants, and this resulted in the distribution of catalyst of sparse to dense along the reactor. The cold spot temperature difference may also become smaller than that in the simulation.

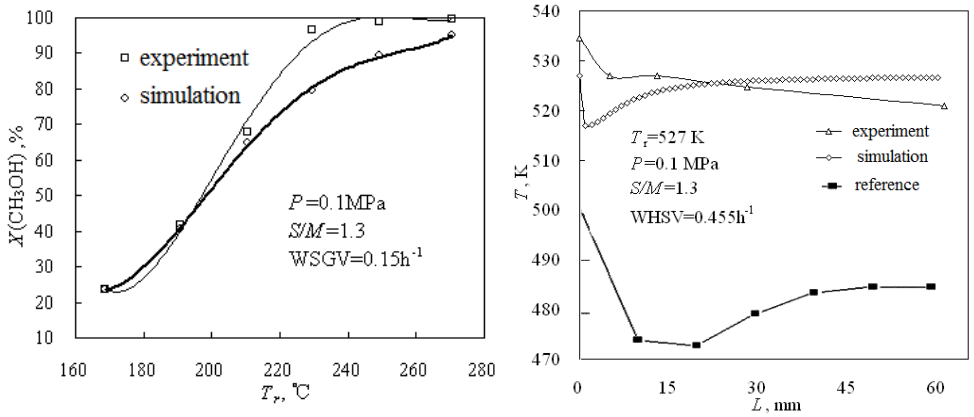

Fig. 5. Experiment, numerical and literature comparisons of methanol conversion and temperature distribution in the reactor.

From the above comparison results of experiment and simulation, it indicated that through controlling of catalytic activity in the reactor, the temperature distribution can be optimized and the cold spot effect can be minimized. So in this section gradient distributed catalyst bed was designed and simulated in 2D model. As can be seen in Fig.6, although the number of cold spot increased under gradient distributed catalyst bed compared with the uniform distributed situation, the maximum cold spot temperature difference decreased about 10K. Furthermore, as heat and mass transport resistances between the catalyst material and the reactants were neglected in 2D and 3D simulation, it can be inferred that this gradient distribution of catalyst will be more beneficial under transport limitation conditions.

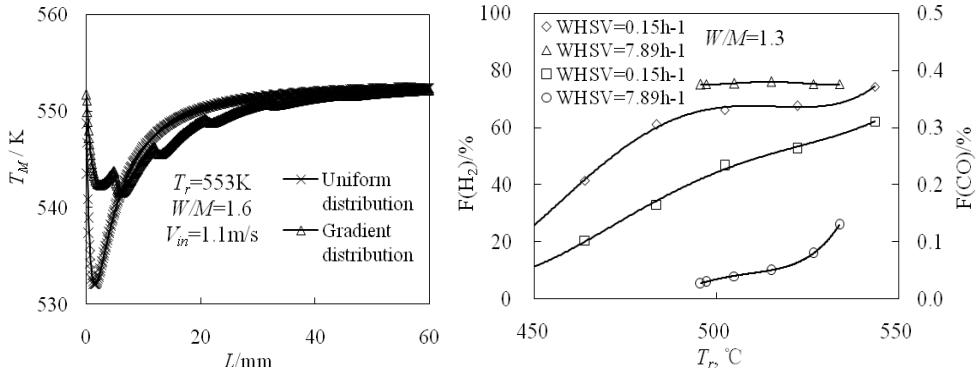

Fig. 6. Comparison of temperature along the centerline of reaction section, outlet H_2 and CO contents under uniform and gradient catalyst distribution conditions.

Although *W/M* of 7.89 h^{-1} at catalyst gradient distribution is far greater than 0.15 h^{-1} at uniform distribution, outlet hydrogen content nearly approached theoretical hydrogen content of 75%, which increased by about 8.5% compared with catalyst uniform distribution condition; while outlet CO content reduced to less than 0.13%. As MSR reaction is a strongly

endothermic process, it can be inferred that gradient catalytic activity distribution is able to reduce the cold spot effect significantly and this effect can be applied to any catalytic reaction with strong heat effect. And it will be more useful in large scale catalyst reactors due to the increasing heat and mass resistance in the catalytic bed.

3. Process intensification of steam reforming by cold sprayed catalytic coating

3.1 Experimental

Except micro-scale reactor adoption, coating catalyst can also be used to reduce heat and mass transfer resistance from the catalyst surface to the main stream. In this section, several kinds of coatings were deposited using the cold spray system developed by Chongqing University for methanol and methane steam reforming. The system includes gas pressure regulators, gas pre-heater, gas flow meters and spraying gun as shown in Fig.7. The gun consists of a gas

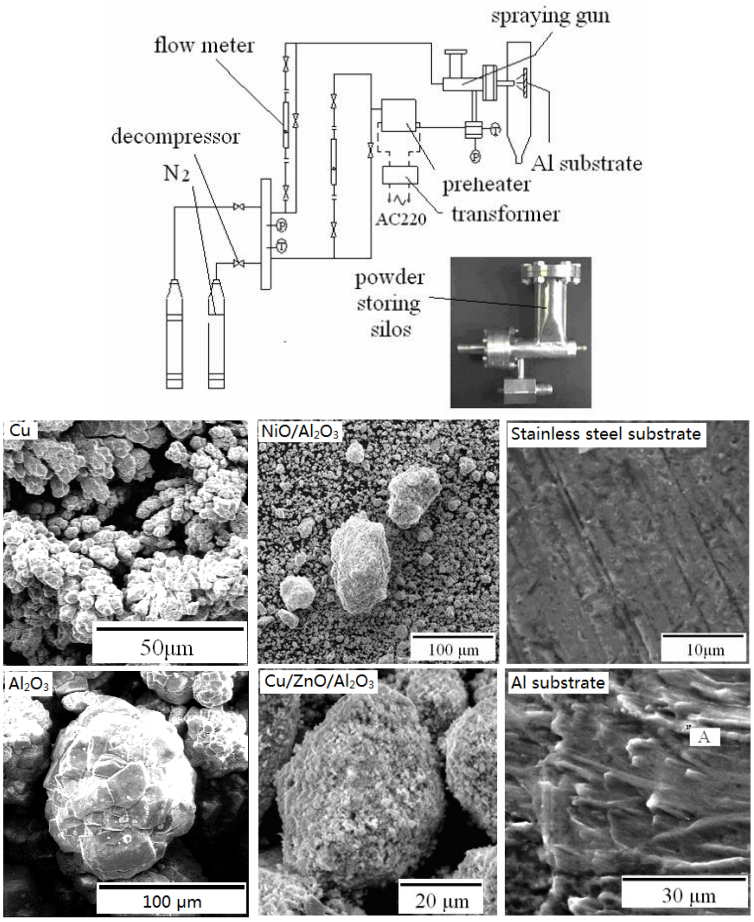

Fig. 7. Schematic of cold spray system, the gun and morphology of different feedstock.

chamber, a powder storage chamber and a convergent-divergent accelerating nozzle. And nozzle throat diameter is 1.5 mm with an exit diameter of 2.6 mm. Length from the throat to the exit is 62.6 mm, among which the expansion section is 12.6mm, the other is straight tube. In this study, nitrogen was used as a driving gas and carrying gas with an inlet pressure of 1.4 and 1.6 MPa for the heating gas and powder carrying gas separately. Heating gas temperature range is 573 K to 773 K. Stand-off distance of the substrate from nozzle exit is 20 mm. During spraying, the substrate was manipulated by a running gear and traversed at a relative speed of 5 mm/s over the substrate.

Four kinds of powders of Cu, Cu-Al_2O_3 composite, milled commercial Cu/ZnO/Al_2O_3 for MSR and primary NiO/Al_2O_3 catalyst for SRM with diameters less than 75μm were used as feedstock. Morphology of the powders and substrate of Al and stainless steel after surface treatment were shown in Fig.7. It can be seen that all the powders are of irregular shape and with different size scale except that of Al_2O_3 with spherical morphology. Cu powder is of arborization morphology, while NiO/Al_2O_3 and CuO/ZnO/Al_2O_3 catalytic powders are irregular kernel morphology. Before spraying, the substrate was polished by sand paper in order to wipe off the oxide film, and then cleaned by ethanol and deionized water.

The morphology of the feed stock and coating before and after methanol and methane steam reforming was observed using scanning electron microscopy (SEM) (TESCAN VEGAII LMU). And the micro-region element composition was examined by EDX. Phase structure was characterized using X-ray diffraction (XRD) system (D/MAX-3C) with Co Kα1 radiation at 35 kV and 30 mA. Scan speed for 2θ was 2.5 °/min during test.

Experiments of methanol and methane steam reforming for hydrogen production were carried out to examine the cold sprayed Cu-based and Ni-based coating performance at atmosphere pressure.

3.2 Results and discussion

Morphology of the cold sprayed coatings before and after steam reforming reaction were shown in Fig.8. Cu-based catalytic coatings were used in methanol steam reforming, whereas Ni-based catalytic coatings were used in methane steam reforming.

It can be seen that the particles are severely deformed in Cu coating, the arborization morphology of the Cu powder is disappeared. After MSR reaction, morphology of the coating changes from piled sheets structure to micro-ramify structure, its porosity obviously increases, but carbon deposition is serious. This structure can be caused by repeatedly oxidization and reduction in MSR because when MSR experiment system shuts down, oxygen in the air may be in touch with the coating, and hydrogen in the reformed gas is able to play a reduction effect. It was also found that copper coating can recover its activity by contacting with oxygen, so the loss of catalytic activity was due to the gradual exhaustion of the surface oxygen on the copper surface. So it was concluded that the active site of Cu-based catalyst for MSR may be copper oxide species, either Cu^+ or Cu^{2+}.

While in the Cu-Al_2O_3 coating, copper powders are not severely deformed. The main reason is that the properties of Cu and Al_2O_3 powders are so different. This results in the different flying speed of the particles which leads to the deposition efficiency and micro-region component in the coating to be ill-proportioned. Another reason is that single Al_2O_3 powder is aggregation of smaller kernels, in collision with the Al substrate, Al_2O_3 powders are shattered to smaller pieces and this cracking makes the situation even worse. This effect is more obvious in the coating after MSR for small pieces of Al_2O_3 with white present region. MSR on the Cu-Al_2O_3 coating shows that it is more stable than the copper coating. Probable

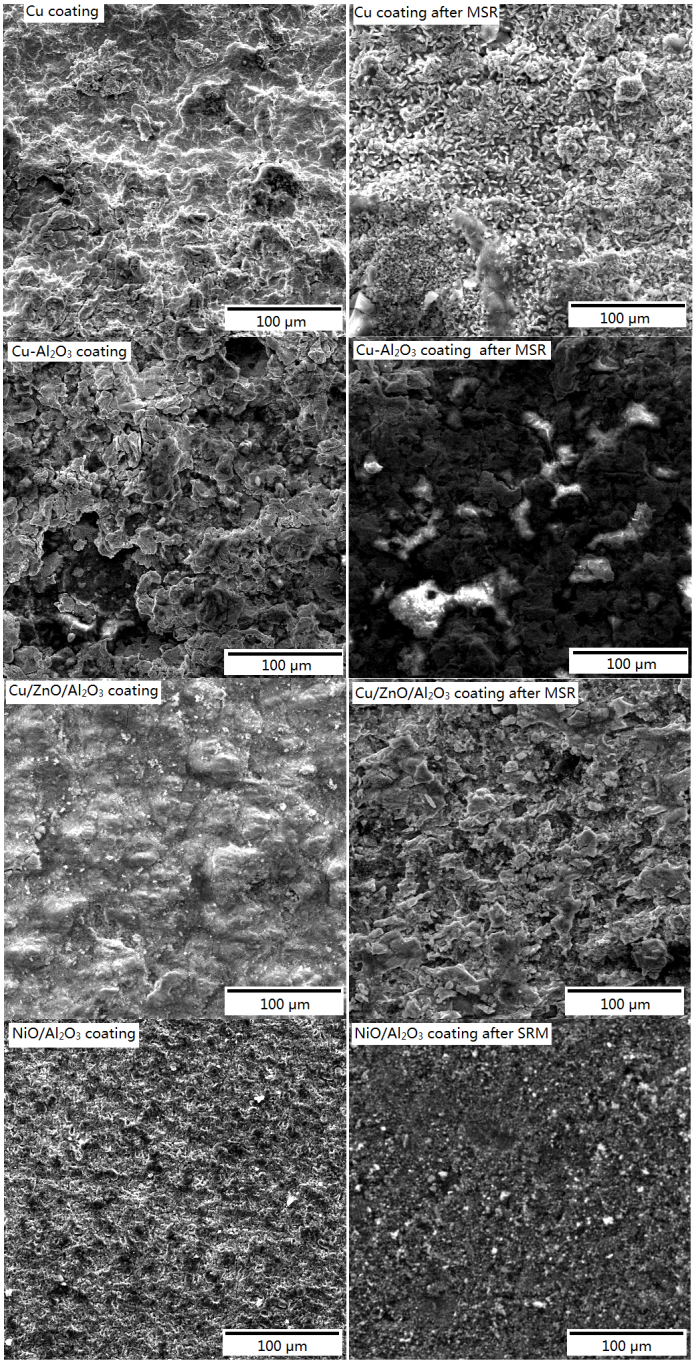

Fig. 8. Morphology of the cold sprayed coatings before and after steam reforming.

reason is that the smashed Al_2O_3 pieces prevent the active Cu in the coating from sintering. What's more, Al_2O_3 component provides and stabilizes the surface oxygen in the Cu-Al_2O_3 coating. In this study it appears that the predominant mechanism for bonding was mechanical interlocking, especially for the Cu-Al_2O_3 composite and CuO/ZnO/Al_2O_3 catalytic coating.

Cold sprayed CuO/ZnO/Al_2O_3 catalytic coating appears to not as porous as the powder in the feedstock. This is due to that binder in the catalyst goes soft in the spraying and colliding process and re-solidifies gradually. After methanol steam reforming, it presents a loosen structure morphology and this is formed by the deposited powder's washing away by the reacting fluid. From the above analysis it can be included that the deposition characteristic of the oxide aggregation feedstock is noticeably different from that of the pure metal powder. The bonding mainly belongs to mechanical bite and physical bonding.

Composition analysis showed that after surface treatment Al substrate contains mainly Al element, and O element in the surface is less than 5.82%. As for the Cu-Al_2O_3 composite coating, O and Al elements increase in the coating after reaction, correspondingly Cu element decreases. In the original feedstock of the composite coating, Cu/Al ratio (wt. %) is about 6.48, whereas in the deposit, Cu/Al ratio decreases dramatically. Before reaction this ratio is 3, after reaction, it decreases to 1.5, it seems that Cu powders are "missing" in the cold spray process. This may be strange because it is known that Cu powder is much more prone to deform than Al_2O_3 powder. The probable reason may lies in the morphology of the powders, although the Cu powder with irregular morphology presents a higher in-flight particle velocity than Al_2O_3 with spherical morphology with same size, the deposition efficiency of Cu is lower than Al_2O_3 powder. Content of component in the coating and feedstock of the CuO/ZnO/Al_2O_3 is approximately the same except that O content in the coating after reaction decreases, while Al increases. Possible reason is that when the small pieces in the coating are not strongly integrated into the substrate and washed off by reacting fluid, the Al phase in the substrate goes into the EDX analysis. And this is just the proof that CuO/ZnO/Al_2O_3 coating fabricated by cold spray is very thin, may be monolayer or at most 2 to 3 layers. Therefore, thickness of the coating is determined by the dimension of feed powders and this provides a kind of nanometer catalytic coating fabrication method. The reason that thickness of CuO/ZnO/Al_2O_3 coating cannot be further increased is that when a first monolayer is formed on the substrate, CuO/ZnO/Al_2O_3 powders arrive at the monolayer surface soon after has to collide with non-deformable CuO/ZnO/Al_2O_3 coating. Here the main process is powder's subsequent tamping effect and this effect results in the smashing of the catalytic powder. Deposition efficiency decreases greatly.

MSR was carried out on the three types of Cu-based coating. Results show that, at the reaction temperature of 190℃ to 200℃, H_2 concentration increases from 28.6% to 42.6%, and reaches 57.4% on Cu-Al_2O_3 coating. H_2 content in the reformed products reaches 74.9% at 250℃ on the Cu coating, but the activity loses very quickly. While at the condition of inlet temperature 265℃, water and methanol molar ratio 1.3, fluid flow rate 0.54ml/min, H_2 content in the products for CuO/ZnO/Al_2O_3 catalytic coating reaches 52.31%, whereas CO content is only 0.60%. Through the weighing of the catalytic plate before and after cold spray process, we get the weight of the catalytic coating of merely 100 mg, and thus the liquid space velocity is equal to 5.10 mol/(g·h) (or 162h^{-1}). Compared to the fixed bed kernels in the reaction section of the reactor, the activity of the cold sprayed CuO/ZnO/Al_2O_3 catalytic coating is much higher [11]. One possible reason may be that heat and mass transfer is fast on the CuO/ZnO/Al_2O_3 catalytic coating than the conventional fixed bed catalyst, especially in micro-reactors.

Morphology of the cold sprayed NiO/Al_2O_3 coating before and after SRM is also shown in Fig.8. It presented a rough surface morphology. Granule appearance of staring NiO/Al_2O_3 powders disappeared in the coating, so it could be inferred that the particles were severely deformed by high speed impact with the stainless steel substrate. Detailed examination of the surface morphology clearly showed that surface structure of the cold sprayed deposit was somewhat different to the powder. Its porosity seemed higher than the feedstock, and this is favorable for catalytic surface reactions because area of the coating surface increased at same volume catalyst. Since NiO/Al_2O_3 powder was aggregation of smaller kernels with different size scale, and it is not easy to deform when colliding with substrate, NiO/Al_2O_3 powders were shattered to smaller pieces due to the high shear rate that occurred when a high velocity particle was arrested by collision with the substrate surface and/or deposited coating surface. Therefore, it could be concluded that the process of oxide aggregated catalytic coating fabrication by cold spray is not like the metal coating fabrication, smashing of the striking powder takes a main role in the coating formation. In this study it appeared that the predominant mechanism for bonding was mechanical interlocking. Although different size scale powders were used as feedstock, the cold sprayed coatings seemed to have a homogeneous distribution of the powders and consisted of several layers. The reason was that when the brittle NiO/Al_2O_3 powders collided with the substrate and/or the coating previously formed, they smashed into small particles, only the particles in suitable size range reached and kept its velocity above the critical velocity and attained valid deposition. The larger one smashed further and the smaller one was washed away by the high speed gas flow. And this is one of the reasons that the coating could not build up further no matter how many passes the deposition was repeated for. Since the deposition efficiency would be dramatically decreased.

After 100h SRM reaction on stream, SEM images showed the formation process of filamentous carbon on the catalytic coatings, and this is one of the reasons that led to the drop of catalyst coating activity since a portion of the active coating surface was covered by deposited carbon. However, activity of catalyst coating remained stable for a relatively long period of 100h in the SRM experiment. In addition, highly dispersed small nickel particles on the cold sprayed catalyst coating were responsible for strong resistance toward carbon deposition in the steam reforming of methane. After 100h SRM reaction, there was no obvious peeling off of the coating, indicating a good bonding between the coating and substrate.

The EDX analysis results showed that Ni content in the cold sprayed coating was higher than the initial catalyst powder, and this could be due to the characteristic of cold spraying process. Since the impact velocity is affected by the spraying material, it will be easier for the powder with higher density to deposit in this situation, so the particles with higher Ni content had more chance to successfully deposit. After SRM reaction, some of the coating surface was covered by carbon, so Ni content decreased.

Primary steam reforming of methane for hydrogen production was carried out in the temperature range of 845K to 995K, and steam to carbon ratio (*S/C*) changed from 2.5 to 10.0, the space velocity ranged from 9.9×10^4/h to 3.0×10^5/h. The results are shown in Fig.9. It can be seen from the data that methane conversion increased with the reaction temperature and decreased with methane space velocity. There was report of 37.4% conversion of methane at the reaction temperature of 973K, reactor pressure of 3.0MPa, steam to carbon ratio (*S/C*) of 2.7 and inlet gas hourly space velocity (*GHSV*) of 0.2×10^5 h^{-1}[7]. At relatively lower *S/C* of 2, much higher *GHSV* of 1.8×10^5 h^{-1} and reaction temperature of 976K, methane conversion in our study was 8.1%. Although this value was lower than the reference above, but

considering the nine times higher *GHSV*, it could be concluded that cold sprayed NiO/Al_2O_3 coating is superior to kernel catalyst in packed bed reactor as its high output. Cold sprayed catalytic coating is excelled catalyst prepared by conventional methods, the fundamental reason lies in the superior bonding of coating with substrate, reduced heat and mass transfer limitation in the reaction.

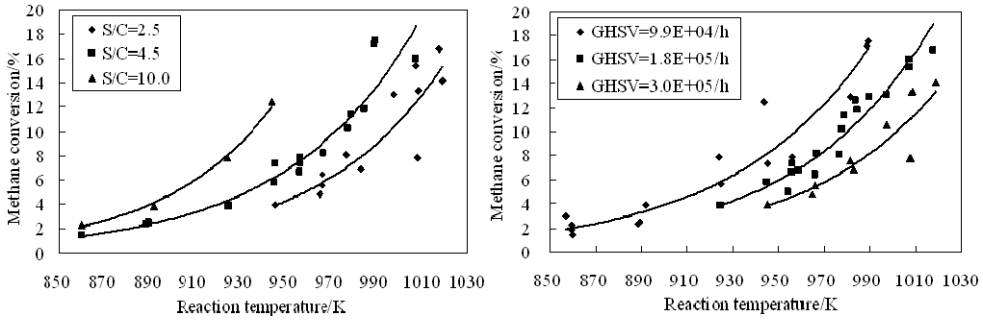

Fig. 9. SRM performance of the cold sprayed coating.

4. Process intensification by catalytic surface and activity distribution

4.1 Simulation method description

For the further optimization of the transport characters of MSR in the micro-reactor with coating catalyst, effects of catalytic surface distribution, catalytic activity distribution on the micro-reactor performance were investigated by numerical simulation. With the application of general finite reaction rate model in CFD software of FLUENT, 2D simulation of this process was carried out.

Along the flow direction, the inner up and down surface of the micro-channel was divided to 12 equal sections as shown in Fig.10. Every section was named by up_i or $down_i$, i=1, 2, 3…12; so the total 24 sections can be selectively combined according to catalytic surface and activity design.

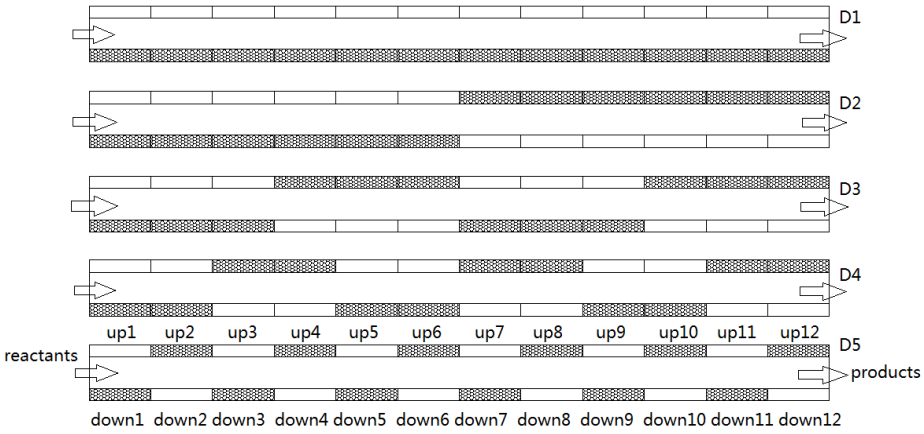

Fig. 10. Design of catalytic surface distribution.

As for the study of catalytic surface distribution effects on the MSR reactor performance, five surface distributions were defined as shown in Table 1. Where, number of interruption represents the number of discontinuous of catalytic surface with non catalytic surface; take D2 distribution for example, there exists an interruption at $down_6$ and up_7 each, so the interruption number is 2.

Types of distribution	Catalytic active surface contained	Number of interruption
D1	$down_1$~$down_{12}$	0
D2	$down_1$~$down_6$, up_7~up_{12}	2
D3	$down_1$~$down_3$, up_4~up_6, $down_7$~$down_9$, up_{10}~up_{12}	6
D4	$down_1$~$down_2$, up_3~up_4, $down_5$~$down_6$, up_7~up_8, $down_9$~$down_{10}$, up_{11}~up_{12}	10
D5	$down_1$, up_2, $down_3$, up_4, $down_5$, up_6, $down_7$, up_8, $down_9$, up_{10}, $down_{11}$, up_{12}	22

Table 1. Types of catalytic surface distribution with same catalytic activity.

As for the catalytic activity distribution study, three types of distributions were defined as shown in Table2. The total length of the reaction channel L is 12 mm, and height of it is 0.5 mm. In order to achieve the above catalytic surface and activity design, cold spray method for catalytic coating fabrication can be used as was studied in section 3 and an example of interrupted Cu coating was prepared by this technology. The activity and surface distribution can be modified by altering the spraying parameters such as material of feedstock, temperature and pressure etc.

The assumption of this simulation study is the same as stated in section 2, However, the kinetic model used was simplified to single rate model because the main purpose of this study is to discuss the effect of surface and activity distribution on the reactor performance. So the MSR power function type kinetic model suitable for $Cu/ZnO/Al_2O_3$ catalyst was adopted.

$$r = k_0 e^{-Ea/(RT)} C_1^{0.60} C_2^{0.45} \tag{10}$$

Where, k_0 is the exponential factor, which represents activity of the catalytic surface. As for the catalytic surface distribution study, it equal to 1.2×10^7 mol/(m²·s); as for the catalytic activity distribution study, k_0 equals to $1.2\times10^7\times2^n$ mol·m^{-2}·s^{-1} (n=0, 1, 2…12). Subscription of 1,2 represents CH_3OH, H_2O respectively. The activation energy Ea is 96.24 kJ·mol^{-1}. Water and methanol molar ratio was set to 1 in all situations.

4.2 Results and discussion

4.2.1 Effect of catalytic surface distribution

With increase of temperature, methanol conversion increased at all types of catalytic surface distributions, and this is coincided with experiment results. In order to obtain inlet temperature T_{in} and velocity V_{in}, catalytic surface distribution effects on methanol conversion, increment of methanol conversion ΔX was defined based on D1 distribution conversion at same conditions.

$$\triangle X = X(Di) - X(D1),\ (i=2, 3, 4, 5) \tag{11}$$

Results showed that ΔX increased with increasing of T_{in}, and at same temperature conditions, ΔX also increased with V_{in}; from D2 to D5 distribution, ΔX increased with respect to D1. This indicated that catalytic surface distribution contribution on methanol conversion increased with temperature, velocity and interruption of catalytic surfaces as shown in Fig.11.

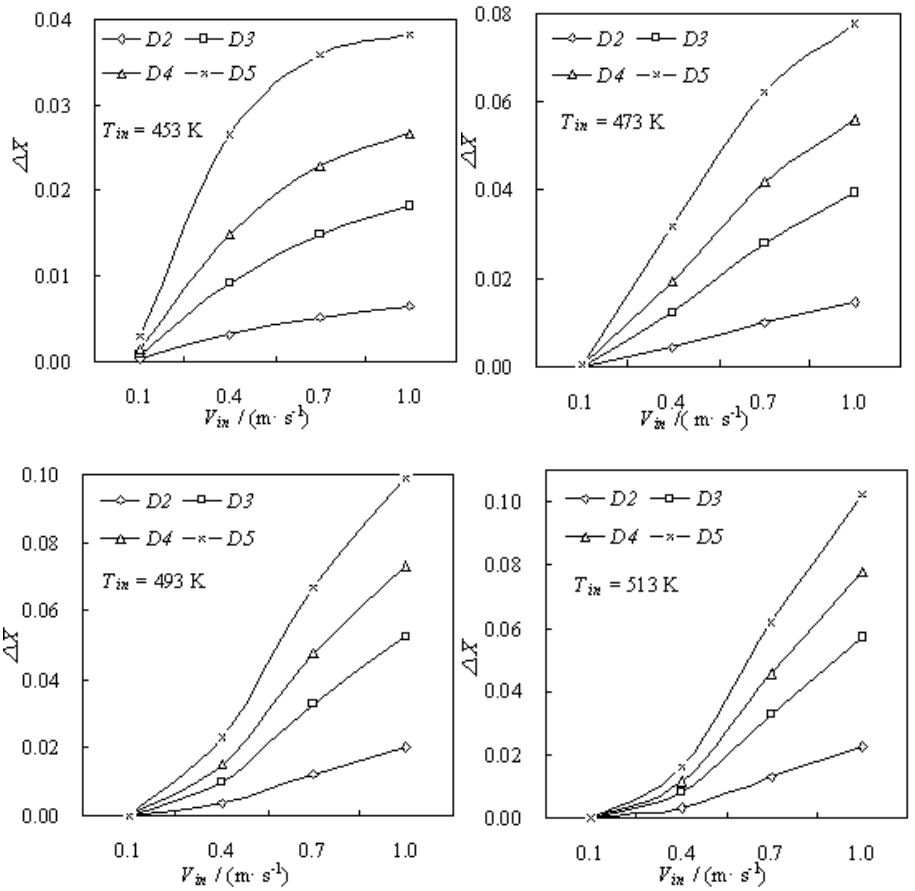

Fig. 11. The effects of V_{in} and Di on $\triangle X$ at different temperatures.

At conditions of T_{in}=513 K, V_{in}=1.0 m/s, compared D5 with D1, methanol conversion increased by 10.2%, so in methanol steam reforming system at the same conversion request, this interrupted distribution of catalytic surface can greatly reduce the load of catalyst especially when the noble metal catalyst was adopted. Furthermore, although methanol conversion increased with inlet T_{in}, V_{in}, the rate of increment was different as can be seen from Fig.11. At inlet temperature of 453 K, rate of $\triangle X$ changed from fast to slow with inlet velocity; at 453 K, rate of $\triangle X$ represented a linearly variation; however, at

inlet temperature of 493 K, 513 K, rate of $\triangle X$ appeared a reverse variation compared to the condition of 453 K. So variation of $\triangle X$ rate existed a turning point with inlet T_{in} and V_{in} and this phenomenon should be considered in design of catalytic surface distribution.

From the above analysis it can be seen that through reasonable catalytic surface distribution, methanol conversion can be increased. The reason is that in reaction channel there existed the diffusion limitation of reactants from main stream to catalytic surface; reasonable catalytic surface distribution can increase the local concentration of the reactants at the interruptions. At condition of 513 K, 1.0 m/s, methanol mass fraction of Y_1 was shown in Fig.12 from D1 to D5 distributions.

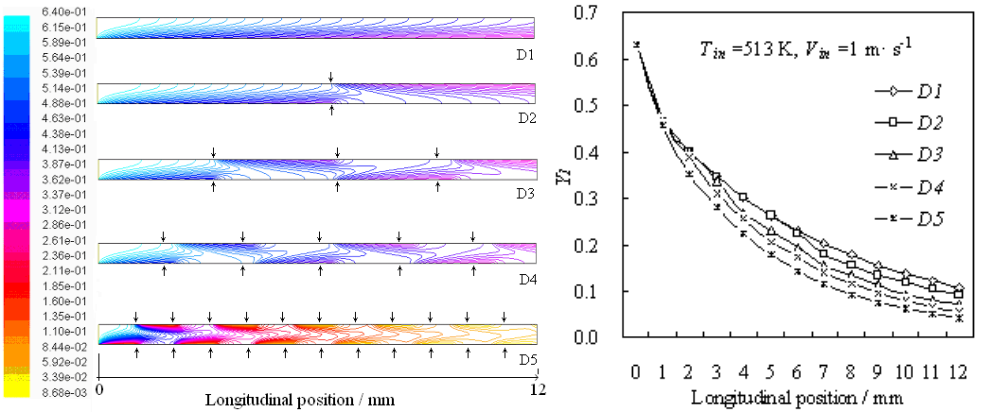

Fig. 12. The change of Y_1 and average Y_1 along the reaction channel.

In conventional reaction channel, concentration distribution of reactants was similar to that of D1 situation, however, from D2 to D5 distribution, catalytic surface interruptions broke the continuous concentration distribution, and this resulted in the concentration was higher at local interruptions so on the next catalytic surface after the interruption, concentration of the reactants increased which enhanced the utilization of the catalytic surface.

It is clear that methanol conversion increased from D1 to D5 distribution; actually from D1 to D5 distribution, the number of surface interruption (n) increased, from 0, 2, 6, 10 to 22 respectively. At condition of T_{in}=513 K, V_{in}=1.0 m/s, methanol conversion increment ΔX was plotting with the surface interruption n as shown in Fig.13. It can be seen that although ΔX increased with n, its rate of increase slowed down, and finally turned into zero. Therefore, it is not that number of surface interruption (n) the bigger the better. In this study surface interruption number n of D5 is enough.

In conclusion, through catalytic surface interrupted distribution methanol conversion increased at the same catalyst loading. So, at the same methanol conversion request, catalyst loading can be reduced. This is not only effective to MSR, but also useful to all the heterogeneous catalysis process on coating catalyst especially for reaction with strong heat effect.

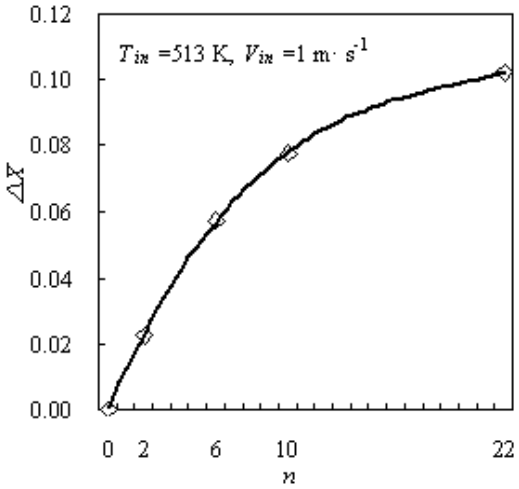

Fig. 13. The change of $\triangle X$ with n.

4.2.2 Effect of catalytic activity distribution

In this section for catalytic activity distribution study, three types of distributions were defined as shown in Table 2. Effects of catalytic activity on methanol conversion X showed that, at the continuous catalytic surface distribution of *D1*, methanol conversion increased with catalytic activity (expressed by activity exponential doubling number n) as shown in Fig.14.

Types of distribution	Exponential factor k_0 (mol·m^{-2}·s^{-1})	Activity exponential doubling number
D1	Activity of down1~down12 surfaces is 1.2×10^7, 2.4×10^7, 4.8×10^7… respectively; Catalytic surface is consecutive, Catalytic activity is identical; So there are 12 groups altogether.	0, 1, 2…11
D2	Activity of down1 is 1.2×10^7, and down2 is 2.4×10^7, and down3 is 4.8×10^7…, Catalytic surface is consecutive, Catalytic activity is multiplying; So there is one group only.	0, 1, 2…11
D3	Activity of down1 is 1.2×10^7, and up2 is 2.4×10^7, and down3 is 4.8×10^7…, Catalytic surface is interrupted, Catalytic activity is multiplying; So there is one group only.	0, 1, 2…11

Table 2. Types of catalytic activity distribution with different catalytic activity.

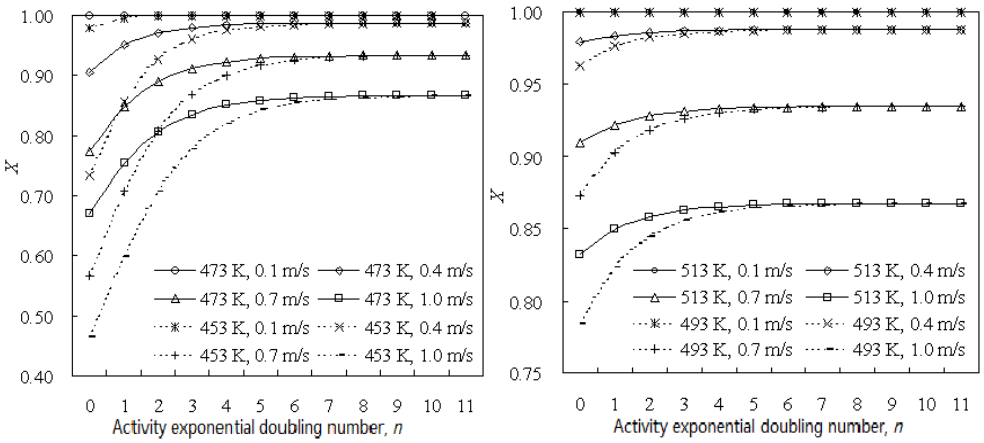

Fig. 14. Effects of V_{in}, n on X at different T_{in}.

At lower inlet velocity such as V_{in}=0.1m·s^{-1}, increment of methanol conversion X with n was small, and nearly approached 100% at all temperatures excepted condition of T_{in}=453K and n=0. This indicated that at lower inlet velocity, MSR was suffered from diffusion limitation, so increasing of catalytic surface activity was non-effective to increment of methanol conversion. However, with the increasing of V_{in}, effect of catalytic surface activity on methanol conversion augmented, indicating a kinetics control effect on methanol conversion. At condition of T_{in}=453 K, V_{in}=1.0 m·s^{-1}, increment of methanol conversion reached 40% with n. On the other hand, with the increase of inlet temperature, effects of catalytic surface activity increment became unconspicuous; at condition of T_{in}=513 K, V_{in}=1.0 m·s^{-1}, methanol conversion increased only 3.5% for n=11 compared with n=0. Therefore, with the inlet temperature became higher and inlet velocity became slower, effect of activity increment on methanol conversion became smaller. For example, at condition of T_{in}=513 K, V_{in}=1.0 m·s^{-1}, methanol conversion became stable when n reached 6; but at condition of T_{in}=453 K, V_{in}=1.0 m·s^{-1}, methanol conversion became stable when n reached 9. This indicated that with the increment of temperature, process of MSR changed from kinetics control to diffusion limitation, and this should be considered when preparing the catalytic coating.

For other types of catalytic activity distribution on discontinuous surfaces with different activity (*D2, D3*), results of comparing with *D1* (n=0 and n=11 were selected) were shown in Fig.15. It can be seen that at all conditions, sequence of methanol conversion is *D3*>(*D1*, n=11)>*D2*>(*D1*, n=0). When considering the catalytic surface activity cost of (*D1*, n=0)<*D2*=*D3*<(*D1*, n=11), it was clear that, methanol conversion of the highest cost of activity was not the biggest. At condition of *D3* distribution, its methanol conversion was much greater than the others even if at high inlet velocities. And that activity cost of *D2* was much lower than *D1*, n=11 situation, but its methanol conversion was closed. Therefore, through reasonable catalytic activity distribution, methanol conversion can be improved or at the same conversion request, catalyst activity cost can be reduced. In this study, the distribution of *D3* is the best, then comes *D2*.

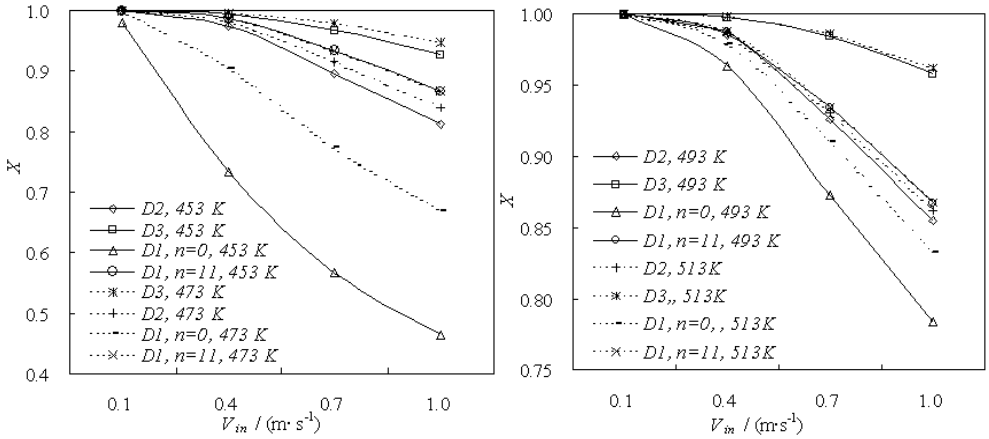

Fig. 15. The effect of V_{in}, D on X at different T_{in}.

It can also be seen from Fig. 15 that, with the increase of V_{in}, X decreased, however, the trends were different. For the distribution of *D1*, n=0, the rate of decrement of X with increase of V_{in} was changing from big to small for 453 K; and almost linear for 473 K, then small to big for 493 K and 513 K. However, for the other distribution as shown in Fig.15, trend of methanol conversion decrement with increase of V_{in} was similar, it was changing from small to big. This indicated that in the kinetics control, diffusion and heat transfer limitation mechanisms of MSR process, it included at least two. At condition of T_{in}=453 K, V_{in}=1.0 m·s^{-1}, methanol conversion for distribution of *D3* is greater than *D1*, n=0 for about 46% 。

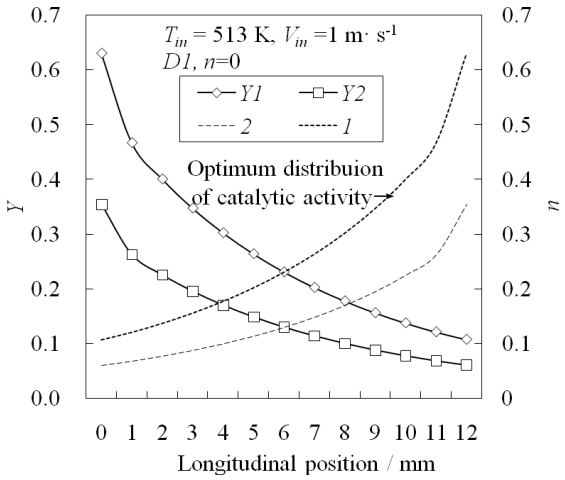

Fig. 16. Mass fraction of methanol (Y_1) and water (Y_2) and optimal catalytic activity distribution T_{in}=513 K, V_{in}=1.0 m· s^{-1} along the reaction channel.

From the analysis above we can draw a conclusion that, although methanol conversion can be increased by increasing of catalyst activity, but cost of catalyst will be also increase. What

is more, as MSR process is a strongly endothermic reaction, if high active catalyst is adopted, there will form a cold spot at inlet of the reactor. And this is obvious at condition of reactor with bigger diameter and worse heat transfer, which finally will be harmful to the catalyst and reactor. Therefore, by reasonable catalyst surface and activity distribution, not only methanol conversion can be increased, but difference of cold spot temperature can also be reduced. Consequently, the optimum catalyst activity distribution should be small at reactor inlet, and gradually increase along the reactor, this is especially important for the heterogeneous catalytic reaction with strong heat effect. For instance, at condition of T_{in}=513 K, V_{in}=1.0 m·s^{-1}, as for the continuous catalyst surface distribution of $D1$, n=0, mass fraction of methanol (Y_1) and water (Y_2) were gradually decreased along the reaction channel, so the optimum distribution of catalytic activity should be inverse with methanol (Y_1) and water (Y_2) as shown in Fig.16.

5. Process intensification by reaction and system integration

5.1 Simulation method description

In this section, process of intensification of methanol steam reforming for hydrogen production by system and reaction integration was designed and analyzed.

As for the system integration analysis, a sub-unit in the designed system as shown in Fig.17 was taken out for simulation. The reactor model included one reaction channel, one intermediate platen to separate heating and reaction channel, one heating channel which adopted hot air to simulate the heat from catalytic combustion; height of both channels is 0.5 mm, catalytic area is 72 mm×42 mm, inlet and outlet diameters of the reactants and products are 10 mm. Steady-state of the model was considered; heating medium of hot air and the reactants were counter flow for heat exchange; outside surface of the unit is adiabatic; gravity of the gases and the radiation heat transfer was also neglected. Kinetic model adopted was the DE and SR parallel mechanism as used in section 2.2.

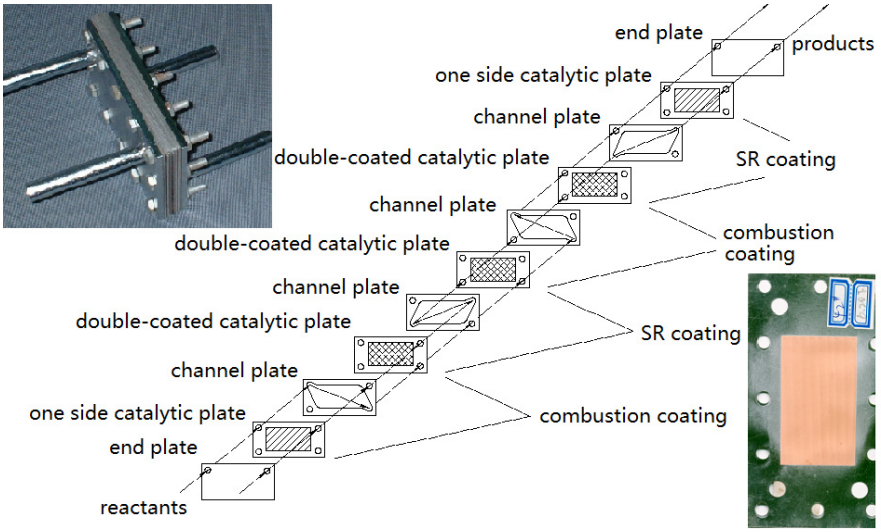

Fig. 17. Methanol steam reformer integration design and the catalytic layer plate.

As for the reaction analysis integration in methanol steam reforming system, methanol steam reforming (MSR) process, water gas shift (WGS) process and CO selective oxidation (PrOX) process were integrated in one reaction channel with respective catalyst coating as shown in Fig.18. The reactants of methanol, water and oxygen can be supplied together from the reactor inlet as was adopted in this study; or water and oxygen can be separately supplied to WGS and PrOX section in the reactor. The postulated condition was the same as the above reactor integration model; length of the total micro-channel is 12 mm and height is 0.5 mm; length of the three sections of the reactions was 4 mm respectively; both up and down of the inner surface in the channel were coated with corresponding catalyst, and the assumption of catalyst coating active to its own reaction only was made.

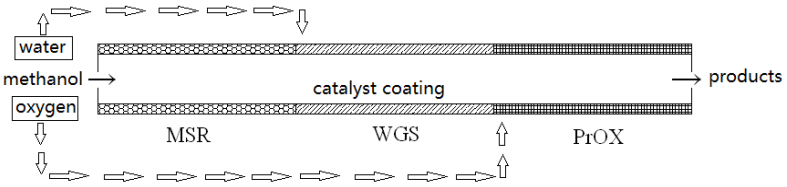

Fig. 18. Reaction integration model in one channel for MSR.

Kinetics of MSR reaction was parallel double rate mechanism model which includs steam reforming (SR) and reverse water gas shift (RWGS) [12]; at the water gas shift section, single rate model of water gas shift reaction was adopted with considering of its reverse reaction [13]; as for the CO selective oxidation model, the single rate model was also used [14]. The reaction equation and its kinetics were listed below.
For the MSR reaction section:

$$CH_3OH+H_2O=CO_2+3H_2 \tag{12}$$

$$CO_2+H_2=CO+H_2O \tag{13}$$

$$r_{SR}=k_{SR}\exp(-\frac{Ea_{SR}}{RT})TC_{CH_3OH}^{0.60}C_{H_2O}^{0.4} \tag{14}$$

$$r_{RWGS}=k_{RWGS}\exp(-\frac{Ea_{RWGS}}{RT})T^2C_{CO_2}C_{H_2} \tag{15}$$

For the WGS reaction section:

$$CO+H_2O \Leftrightarrow CO_2+H_2 \tag{16}$$

$$r_{WGS}=k_{WGS}\exp(-\frac{Ea_{WGS}}{RT})T^2C_{CO}C_{H_2O}(1-\beta) \tag{17}$$

$$\text{其中，}\ \beta=\frac{P_{CO_2}P_{H_2}}{K_{eq}P_{CO}P_{H_2O}},\ K_{eq}=\exp(\frac{4577.8}{T}-4.33)$$

For the PrOX reaction section:

$$CO+0.5O_2=CO_2 \tag{18}$$

$$r_{PrOX} = k_{PrOX} \exp(-\frac{Ea_{PrOX}}{RT})T^{1.02}C_{CO}^{0.68}C_{O_2}^{0.34} \tag{19}$$

All the parameters of the kinetics including the exponential factor k and activation energy E_a of each reaction were shown in Table3. The outer surface temperature was set to the reaction temperature for each reaction section; but this simplification will be difficult in actual process. The inlet temperature T_{in} was set to the temperature of MSR reaction. Four groups of temperatures were calculated, namely MSR-WGS-PrOX of 453K-393K-333K, 473K-413K-353K, 493K-433K-373K, 513K-453K-393; also four groups of reactants inlet ratios m_{H2O}:m_{CH3OH}:m_{O2} were considered as the following: 0.399:0.6:0.0001, 0.449:0.55:0.001, 0.49:0.5:0.01 and 0.5:0.45:0.05; as for the inlet velocity V_{in} effects study, 0.4 m·s^{-1}, 0.7 m·s^{-1}, 1.0 m·s^{-1}, 1.3m·s^{-1} were considered.

section	reaction	k/ mol·m^{-2}·s^{-1}	*Ea* / J·kmol^{-1}
MSR	SR	2.46×10^6	7.6×10^7
	RWGS	2.52×10^5（453K）	1.08×10^8
	RWGS	3.86×10^5（473K）	1.08×10^8
	RWGS	5.72×10^5（493K）	1.08×10^8
	RWGS	8.21×10^5（513K）	1.08×10^8
WGS	WGS	8.12×10^7	4.74×10^7
	RWGS	5.39×10^4（333K）	4.74×10^7
	RWGS	9.19×10^4（353K）	4.74×10^7
	RWGS	1.58×10^5（373K）	4.74×10^7
	RWGS	2.52×10^5（393K）	4.74×10^7
PrOX	PrOX	4.89×10^3	2.7×10^7

Table 3. Parameters of kinetic models.

5.2 Results and discussion

5.2.1 Microreactor integration simulation results

In calculation, inlet hot air temperature is 750 K and inlet velocity is 3 m/s. Effect of different inlet parameters on outlet product molar fraction F_m, methanol conversion *X(MeOH)* and outlet temperature T_{out} was considered. The range of temperature T_{in} of reactants was 493K to 613 K; range of inlet velocity V_{in} was 0.144 m/s to 2.88 m/s; inlet water methanol molar ratio was 1 to 1.6. The similar variation trend of increasing of methanol conversion and hydrogen yield with inlet temperature was got because MSR process is a strongly endothermic reaction; with the increase of inlet velocity, the contact time of reactants with catalyst reduced, part of the reactants flowed out the reactor without reaction which resulted in the lower conversion of methanol and respectively higher content of methanol and water; similarly, with the increase of water and methanol molar ratio, methanol conversion increased, however, hydrogen content in the products decreased as shown in Fig.19 with constant inlet velocity of 2.88 m/s.

Analysis of outlet temperature showed that, it rarely changed with inlet temperature, indicating that with the rise of inlet temperature, the absorption of heat by the reaction also increased. With the increase of inlet velocity, although methanol conversion decreased, the total mass of reactant reacted increased, therefore, at same heating condition, there formed a temperature decrease of 4 K. When water and methanol molar ratio increased, there was a fluctuation of the outlet temperature, this stated that water in the MSR system exist an optimum value for the heat balance, it was about 1.3. To sum up, fluctuation of outlet temperature with inlet parameter of reactants was small, so it was enough for the heat needed supplied by hot air.

At condition of V_{in}=2.88 m/s, T_{in}=493K, S/M=1.3, temperature distribution in the channel was studied and a temperature drop was found at inlet of both hot air channel and reactant reaction channel. This is consistent with the above study in section 1 for cold spot discussion.

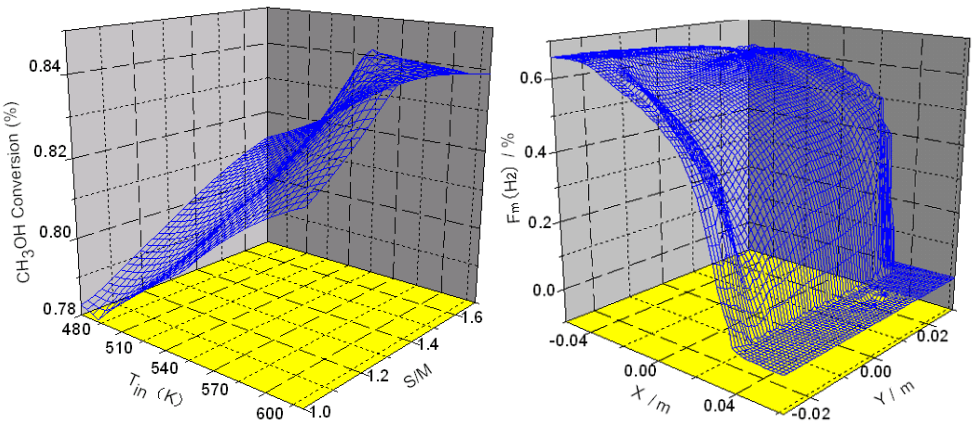

Fig. 19. Methanol conversion with S/M, T_{in} (V_{in}=2.88 m/s) and $F_m(H_2)$ distribution in reaction channel (V_{in}=2.88 m/s, T_{in}= 493 K, S/M =1.3).

Based on the previous accounts, temperature in the reaction channel can be optimized by properly coupling of inlet hot air temperature and reactant inlet temperature. Another way to improve reactor performance is the altering of reactor sizes and catalytic surface and activity distribution. At condition of V_{in}=2.88 m/s, T_{in}= 493 K, S/M=1.3, methanol conversion in the reactor was shown in Fig.19. The reactor outlet methanol conversion reached 79.8%, so it can be seen that microreactor can maintain higher hydrogen molar fraction and methanol conversion at high reactant flow rate.

5.2.2 Reaction integration simulation results

In this section, effects of inlet parameters such as inlet temperature T_{in}, inlet velocity V_{in} and inlet water, methanol, oxygen mass fraction ratio m_{H2O}:m_{CH3OH}:m_{O2} on methanol conversion X_{CH3OH}, oxygen conversion X_{O2}, outlet hydrogen and CO molar fraction F_{H2} and F_{CO} were investigated. Results showed that, X_{CH3OH} decreased with inlet velocity, and increased with methanol, oxygen mass fraction ratio; at condition of T_{in}=493 K, V_{in}=0.4 m·s^{-1}, it reached its maximum value of 0.995; however, increasing of oxygen inlet mass fraction was disadvantageous to outlet hydrogen content; at condition of T_{in}=453 K, V_{in}=0.4 m·s^{-1} and m_{H2O}:m_{CH3OH}:m_{O2}=0.3999:0.60:0.0001, F_{H2} reached its maximum value.

The conversion of oxygen X_{O2} was not the same with methanol; at water, methanol, oxygen molar ratio of 0.3999:0.60:0.0001 and inlet temperature of 453 K, X_{O2} changed from increase to decrease with inlet velocity and reached it maximum of 0.977 at V_{in}=0.4 m·s^{-1}; however, at inlet temperature of 493 K and 513K, X_{O2} decreased with inlet velocity; when oxygen increased in the reactant to m_{H2O}:m_{CH3OH}:m_{O2} of 0.449:0.55:0.001, at inlet temperature of 453 K and 473 K, X_{O2} increased with inlet velocity; but, at temperature of 493 K and 513 K, it increased firstly and then decreased with V_{in}. At the other m_{H2O}:m_{CH3OH}:m_{O2} condition of 0.49:0.50:0.01 and 0.50:0.45:0.05, X_{O2} increased with inlet velocity; therefore inlet oxygen content in this reaction model is very sensitive and should be carefully adjusted.

As for the CO outlet molar fraction F_{CO}, it increased with inlet velocity at same temperature and inlet component and this is not the same compared with MSR process. At condition of T_{in}=453 K, V_{in}=0.4 m·s^{-1} and m_{H2O}:m_{CH3OH}:m_{O2}=0.50:0.45:0.05, minimum CO molar fraction of 4.03×10^{-9} was got. Because CO concentration limitation for PEMFC is below 50 ppm, outlet of hydrogen molar fraction for the reformer should be increased to its greatest extent in this CO requirement. In this study, the optimum condition was that T_{in}=453 K, V_{in}=0.4 m·s^{-1} and m_{H2O}:m_{CH3OH}:m_{O2}=0.3699: 0.63:0.0001, at which methanol conversion reached 98.8%, oxygen conversion reached 15.2%, and outlet hydrogen molar fraction and CO molar fraction were 74% and 3.43×10^{-8} respectively.

At optimum condition of T_{in}, V_{in}, and m_{H2O}:m_{CH3OH}:m_{O2}, the component mass fraction along the flow direction in the reactor channel was studied as shown in Fig.20.

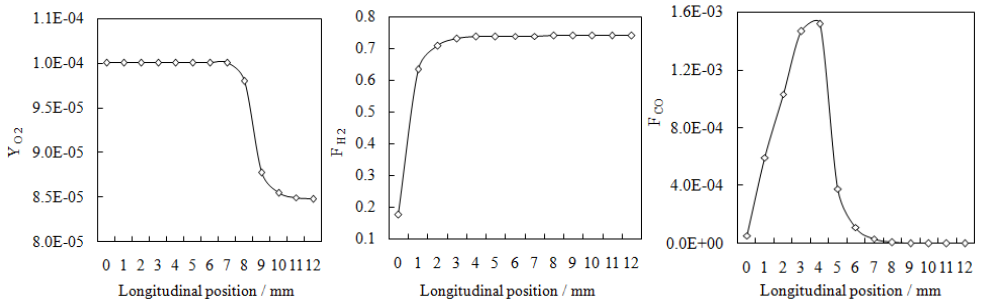

Fig. 20. Mass fraction distribution along the reaction channel.

As can be seen from Fig.20, marginala oxygen from inlet of the reactor was mainly consumed at the PrOX section, which received a conversion of only 15.2%; however, it was just due to the marginala oxygen that CO reduced to 3.43×10^{-8} from the MSR section outlet of 0.152%. Through the WGS reaction section, CO reduced to 1.0×10^{-5}, which was still greater than the requirement of PEMFC. But the hydrogen content in the reactor after MSR reaction section did not increased notably; After WGS reaction section, it only increased by 0.314% and even slightly reduced after the PrOX section.

6. Conclusions and challenges

1. Through the adoption of micro-reactors, cold spot effect of methanol steam reforming for hydrogen production can be decreased compared with conventional reactors.

Optimum conditions of the reactor were obtained. Hydrogen yield reached 0.2 mol/(h·g_{cat}) under condition of T_r=260 ℃, W/M=1.3 and $WGHV$=0.2 h^{-1}, which can provide hydrogen for 10.2W PEMFC with a hydrogen utilization of 80% and an fuel cell efficiency of 60%. A 3-D model coupling with parallel reaction kinetics was obtained by data fitting to describe its performance. Furthermore, gradually increased catalyst activity in the reaction channel can be used to further reduce the cold spot effect; Hydrogen content at reactor outlet increased by about 8.5% compared with catalyst uniform distribution condition; while outlet CO content reduced to less than 0.13%.

2. Cold spray technology was successfully used to catalytic coatings fabrication for fuel reforming reaction and all the powers were effectively deposited onto the substrates. Components of the coatings were approximately identical to the initial powders. Performance of the coating was influenced by impact velocity and broken character of the particles especially for the NiO/Al_2O_3 and $CuO/ZnO/Al_2O_3$ catalytic coatings. For the Cu coating, carbon deposition is serious which resulted in nonstable activity in methanol steam reforming compared with $Cu\text{-}Al_2O_3$ coating. At condition of inlet temperature 265℃, W/M of 1.3, space velocity of 162h^{-1}, H_2 content in the products for $CuO/ZnO/Al_2O_3$ catalytic coating reaches 52.3%, whereas CO content is only 0.60%. Methane primary steam reforming on cold sprayed NiO/Al_2O_3 coating also indicated a superior character to kernel catalyst in packed bed reactor as its high output.
3. Through interrupted distribution of catalytic surface, at same conditions methanol conversion could be improved although the temperature in reaction channel became uneven. So in micro-reactors which utilize coating catalyst, this interrupted distribution of surface can improve the efficiency of catalyst and thus reduce loading and cost of reforming catalyst. The optimal activity distribution was that the activity should be low at inlet, along with the reactor channel, the activity gradually increased. This kind of activity distribution can also be used to decrease the cold spot temperature difference in the reactor. The 3-D simulation results of MSR for hydrogen production in self-designed plate micro reactor showed that micro-reactors can maintain a high hydrogen molar fraction and methanol conversion at high reactant flow rate. It is also reasonable to integrate all reaction units in fuel reforming system in one channel to mach up PEMFC for CO requirement.

Therefore, through the adoption of both micro-scale reactors and coating catalyst, heat and mass transfer in the reaction channel for hydrogen production by fuel reforming can be enhanced resulting in the improvement of reactor performance. Nowadays, research of process intensification by the above methods becomes more and more, and it is beneficial for the development of hydrogen production through hydrocarbon fuel reforming technology. All the endeavors will promote the application of hydrogen energy. We look forward to the day of hydrogen economy coming soon.

7. Acknowledgements

The authors acknowledge the support of National Natural Science Foundation of China (50906104) and project No.CDJZR10140010 supported by Fundamental Research Funds for the Central Universities.

8. Nomenclature

C	molar concentration, kmol/m^3	P	mixed gas pressure, Pa
C_p	Isobaric specific heat capacity, J/(mol·K)	μ	mixed gas viscosity coefficient, kg/(m·s)
D	effective diffusion coefficient, m^2/s or thickness, mm; or catalyst and catalytic coating distribution types	T , T_r	mixed gas temperature and reaction temperature, K or ℃
ρ	mixed gas density, kg/m^3	L	Channel length or channel subsection length, mm
V , v	mixed gas velocity, m/s	M	molar mass, kg/mol
Y , F	component molar fraction, %	m	mass fraction, %
V	mixed gas velocity, m/s or rate of inlet liquid flow, ml/min	S	selectivity, %
q , q	heat of reaction, W/m^2	S/M, W/M	water methanol ratio
R , r , a	reaction rate, mol/(g_{cat}h)	E_a	activation energy, kJ/mol
r'	reaction rate, kmol/(m^{2}s)	h	height of channel, mm or specific enthalphy, J/kg
R	universal gas constant, kJ/(molK)	H	height of channel, mm
H^0	standard enthalpy of formation, J/kg	X	conversion, %
k	reaction rate constant, mol/(kg_{cat}s)	WHSV	liquid space velocity, h^{-1}
K	reaction equilibrium constant	k_0 , k_0'	frequency factor, mol/(kg_{cat}s)
a, b	thickness, mm	up, down	mark of up and down channel
n	number of interruption or activity exponential doubling number	W/F	ratio of mole flow rate and catalyst weight, g·h/mol
Subscript:			
0, in	inlet parameters	out	outlet parameters
1, 2	mark of channel or catalyst coating subsection	s=1~5	reactants and products of CH_3OH, H_2O, H_2, CO, CO_2
i	mark of channel or catalyst coating subsection	(CH_3OH)	represent of methanol parameter
w	reaction channel wall	(CO_2)	represent of CO_2 parameter
cat.	represent of catalyst parameter	(H_2)	represent of H_2 parameter
(F)	molar fraction	(H_2O)	represent of H_2O parameter
WGS	water gas shift reaction	(CO)	represent of CO parameter
SR	steam reforming reaction	O_2	represent of O_2 parameter
DE	methanol decomposition	△	variable difference
RWGS	reverse water gas shift reaction	(X)	represent of conversion

9. References

[1] Carl-Jochen Winter. (2009). Hydrogen energy — Abundant, efficient, clean: A debate over the energy-system-of-change. *International Journal of Hydrogen Energy*, Vol. 34, No. 14, Supplement 1, (July 2009), pp. (S1-S52), 0360-3199

[2] Anand S. Joshi, Ibrahim Dincer, Bale V. Reddy. (2010). Exergetic assessment of solar hydrogen production methods. *International Journal of Hydrogen Energy*, Vol. 35, No. 10, (May 2010), pp. (4901-4908), 0360-3199

[3] Jianlong Wang, Wei Wan. (2009). Experimental design methods for fermentative hydrogen production: A review. *International Journal of Hydrogen Energy*, Vol. 34, No. 1, (January 2009), pp. (235-244), 0360-3199

[4] Michael G. Beaver, Hugo S. Caram, Shivaji Sircar. (2010). Sorption enhanced reaction process for direct production of fuel-cell grade hydrogen by low temperature catalytic steam–methane reforming. *Journal of Power Sources*, Vol. 195, No. 7, 2, (April 2010), pp. (1998-2002), 0378-7753

[5] Guangming Zeng, Ye Tian, Yongdan Li. (2010). Thermodynamic analysis of hydrogen production for fuel cell via oxidative steam reforming of propane. *International Journal of Hydrogen Energy*, Vol. 35, No. 13, (July 2010), pp. (6726-6737), 0360-3199

[6] Stefan Martin, Antje Wörner. (2011). On-board reforming of biodiesel and bioethanol for high temperature PEM fuel cells: Comparison of autothermal reforming and steam reforming. *Journal of Power Sources*, Vol. 196, No. 6, 15, (March 2011), pp. (3163-3171), 0378-7753

[7] Feng Wang, Dingwen Zhang, Shiwei Zheng, Bo Qi. (2010). Characteristic of cold sprayed catalytic coating for hydrogen production through fuel reforming. *International Journal of Hydrogen Energy*, Vol. 35, No. 15, (August 2010), pp. (8206-8215), 0360-3199

[8] M. H. Akbari, A. H. Sharafian Ardakani, M. Andisheh Tadbir. (2011). A microreactor modeling, analysis and optimization for methane autothermal reforming in fuel cell applications. *Chemical Engineering Journal*, Vol. 166, No. 3, 1 (February 2011), pp. (1116-1125), 1385-8947

[9] Akira Nishimura, Nobuyuki Komatsu, Go Mitsui, Masafumi Hirota, Eric Hu. (2009). CO_2 reforming into fuel using TiO_2 photocatalyst and gas separation membrane. *Catalysis Today*, Vol. 148, No. 3-4, 30 (November 2009), pp. (341-349), 0920-5861

[10] Feng Wang, Longjian Li, Bo Qi, Wenzhi Cui, Mingdao Xin, Qinghua Chen, Lianfeng Deng. (2008). Methanol steam reforming for hydrogen production in a minireactor. *Journal of Xi 'An J iao Tong University*, Vol. 42, No. 4, (April 2008), pp. (341-349), 509-514, 0253-987X

[11] Feng Wang, Jing Zhou, Zilong An, Xinjing Zhou. (2011). Characteristic of Cu-based catalytic coating for methanol steam reforming prepared by cold spray. *Advanced Materials Research*, Vol. 156-157, (2011), pp. (68-73), 1022-6680

[12] H. Purnama, T. Ressler, R. E. Jentoft, H. Soerijanto, R. Schlögl, R. Schomäcker. (2004). CO Formation / Selectivity for Steam Reforming of Methanol with a Commercial $CuO/ZnO/Al_2O_3$ Catalyst. *Applied Catalysis A: General*, Vol. 259, No.1, 8, (March 2004), pp. (83-94), 0926-860X

[13] Yongtaek Choi, Harvey G Stenger. (2003). Water Gas Shift Reaction Kinetics and Reactor Modeling for Fuel Cell Grade Hydrogen. *Journal of Power Sources*, Vol. 124, No. 2, (November 2003), pp. (432-439), 0378-7753

[14] Y. H. Wang, J. L. Zhu, J. C. Zhang, L.F. Song, J. Y. Hu, S. L. Ong, W. J. Ng. (2006). Selective Oxidation of CO in Hydrogen-rich Mixtures and Kinetics Investigation on Platinum-gold Supported on Zinc Oxide Catalyst. *Journal of Power Sources*, Vol. 155, No. 2, (April 2006), pp. (440-446), 0378-7753

5

Heat and Mass Transfer in External Boundary Layer Flows Using Nanofluids

Catalin Popa, Guillaume Polidori, Ahlem Arfaoui and Stéphane Fohanno
Université de Reims Champagne-Ardenne, GRESPI/Thermomécanique (EA4301)
Moulin de la Housse, BP1039, 51687 Reims cedex 2,
France

1. Introduction

The application of additives to base liquids in the sole aim to increase the heat transfer coefficient is considered as an interesting mean for thermal systems. Nanofluids, prepared by dispersing nanometer-sized solid particles in a base-fluid (liquid), have been extensively studied for more than a decade due to the observation of an interesting increase in thermal conductivity compared to that of the base-fluid (Xuan & Roetzel, 2000; Xuan & Li, 2000). Initially, research works devoted to nanofluids were mainly focussed on the way to increase the thermal conductivity by modifying the particle volume fraction, the particle size/shape or the base-fluid (Murshed et al., 2005; Wang & Mujumdar, 2007). Using nanofluids strongly influences the boundary layer thickness by modifying the viscosity of the resulting mixture leading to variations in the mass transfer in the vicinity of walls in external boundary-layer flows. Then, research works on convective heat transfer, with nanofluids as working fluids, have been carried out in order to test their potential for applications related to industrial heat exchangers. It is now well known that in forced convection (Maïga et al. 2005) as well as in mixed convection, using nanofluids can produce a considerable enhancement of the heat transfer coefficient that increases with the increasing nanoparticle volume fraction. As concerns natural convection, the fewer results published in the literature (Khanafer et al. 2003; Polidori et al., 2007; Popa et al., 2010; Putra et al. 2003) lead to more mixed conclusions. For example, recent works by Polidori et al. (2007) and Popa et al. (2010) have led to numerical results showing that the use of Newtonian nanofluids for the purpose of heat transfer enhancement in natural convection was not obvious, as such enhancement is dependent not only on nanofluids effective thermal conductivities but on their viscosities as well. This means that an exact determination of the heat transfer parameters is not warranted as long as the question of the choice of an adequate and realistic effective viscosity model is not resolved (Polidori et al. 2007, Keblinski et al. 2008). It is worth mentioning that this viewpoint is also confirmed in a recent work (Ben Mansour et al., 2007) for forced convection, in which the authors indicated that the assessment of the heat transfer enhancement potential of a nanofluid is difficult and closely dependent on the way the nanofluid properties are modelled. Therefore, the aim of this paper is to present theoretical models fully describing the natural and forced convective heat and mass transfer regimes for nanofluids flowing in semi-infinite geometries, i.e. external boundary layer flows along

flat plates. In order to reach this goal, the integral formalism is extended to nanofluids. This work is the continuation of previous studies carried out to develop free and forced convection theories of external boundary layer flows by using the integral formalism (Polidori et al., 1999; Polidori et al., 2000; Polidori & Padet, 2002; Polidori et al., 2003; Varga et al., 2004) as well as to investigate convective heat and mass transfer properties of nanofluids (Fohanno et al., 2010; Nguyen et al., 2009; Polidori et al., 2007; Popa et al., 2010) where both viscosity and conductivity analytical models have been used and compared with experimental data. The Brownian motion has also been taken into account. Nevertheless these studies focused mainly heat transfer. Free and forced convection theories have been developed both in the laminar and turbulent regimes and applied to conventional fluids such as water and air. Application of the integral formalism to nanofluids has been recently proposed in the case of laminar free convection (Polidori et al., 2007; Popa et al. 2010).

In order to develop these models, nanofluids will be considered flowing in the laminar regime over a semi-infinite flat plate suddenly heated with arbitrary heat flux densities. The laminar flow regime in forced and natural convection is investigated for Prandtl numbers representative of nanofluids. The nanofluids considered for this study, at ambient temperature, are water-alumina and water-CuO suspensions composed of solid alumina nanoparticles with diameter of 47 nm (ρ_p=3880 kg/m^3) and solid copper oxide nanoparticles with diameter of 29 nm (ρ_p = 6500 kg/m^3) with water as base-fluid. The thermophysical properties of the nanofluids are obtained by using empirical models based on experimental data for computing viscosity and thermal conductivity of water-alumina and water-CuO suspensions, and based on a macroscopic modelling for the other properties. The influence of the particle volume fraction is investigated in the range $0\% \leq \phi \leq 5\%$.

The chapter is organized as follows. First, the development of the integral formalism (Karman Pohlhausen approach) for both types of convection (free and forced) in the laminar regime is provided in Section 2. Then, Section 3 details a presentation of nanofluids. A particular attention is paid on the modelling of nanofluid thermophysical properties and their limitations. Section 4 is devoted to the application of the theoretical models to the study of external boundary-layer natural and forced convection flows for the two types of nanofluids. Results are presented for particle volume fractions up to 5%. Results on the flow dynamics are first provided in terms of velocity profiles, streamlines and boundary layer thickness. Heat transfer characteristics are then presented by means of wall temperature distribution and convective heat transfer coefficients.

2. Mathematical formulation

2.1 Natural convection

Consider laminar free convection along a vertical plate initially located in a quiescent fluid under a uniform heat flux density thermal condition. Denote U and V respectively the velocity components in the streamwise x and crosswise y directions. Assuming constant fluid properties and negligible viscous dissipation (Boussinesq's approximations) the continuity, boundary-layer momentum and energy equations are:

Continuity equation:

$$\frac{\partial U}{\partial x} + \frac{\partial V}{\partial y} = 0 \tag{1}$$

Momentum equation:

$$U\frac{\partial U}{\partial x}+V\frac{\partial U}{\partial y}=g\beta(T_w-T_\infty)+\vartheta\frac{\partial^2 U}{\partial y^2} \tag{2}$$

Energy equation:

$$U\frac{\partial T}{\partial x}+V\frac{\partial T}{\partial y}=\frac{\vartheta}{Pr}\frac{\partial^2 T}{\partial y^2} \tag{3}$$

Using the Karman-Pohlhausen integral method (Kakaç and Yener, 1995 ; Padet, 1997), physically polynomial profiles of fourth order are assumed for flow velocity and temperature across the corresponding hydrodynamic and thermal boundary layers (see Figure 1). The major advantage in using such a method is that the resulting equations are solved anatically.

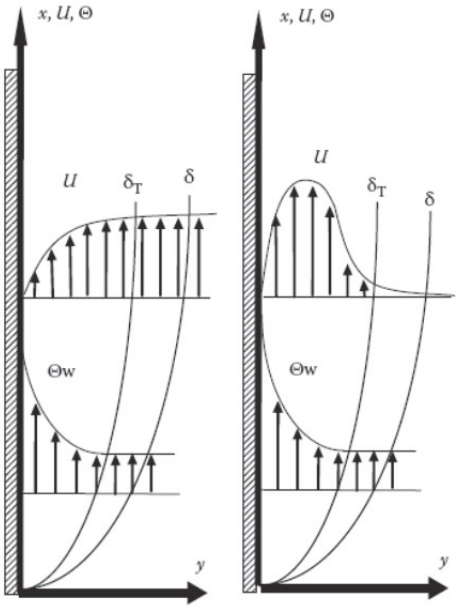

Fig. 1. Schematization of external boundary layer flows in forced convection (left) and free convection (right)

The method of analysis assumes that the velocity and temperature distributions have temporal similarity (Polidori et al., 2000) meaning that the ratio Δ between the temperature δ_T and the velocity δ layers depends only upon the Prandtl number.

$$\Delta=\frac{\delta_T}{\delta} \tag{4}$$

Thus, combining relation (4), the Fourier's law and adequate boundary conditions leads to the following U-velocity and Θ temperature polynomial distributions depending mainly upon the δ dynamical parameter:

$$U = \frac{g\beta\varphi_w\Delta\delta^3}{12k\vartheta}(-\eta^4 + 3\eta^3 - 3\eta^2 + \eta) \tag{5}$$

$$\Theta = T - T_\infty = \frac{\varphi_w\Delta\delta}{2k}\left(-\eta_T^4 + 2\eta_T^3 - 2\eta_T + 1\right) \tag{6}$$

Where $\eta = \frac{y}{\delta} \leq 1$, $\eta_T = \frac{y}{\delta_T} \leq 1$, β is the volumetric coefficient of thermal expansion, k is the thermal conductivity of the fluid, ϑ is the fluid kinematic viscosity, and φ_w is the heat flux density.

With the correlation (4), the integral forms of the boundary-layer momentum and energy conservation equations become :

$$\frac{\partial}{\partial x}\int_0^\delta U^2 dy = g\beta\frac{\partial}{\partial x}\int_0^{\delta_T}\Theta dy - \vartheta\left(\frac{\partial U}{\partial y}\right)_{y=0} \tag{7}$$

$$\frac{\partial}{\partial x}\int_0^{\delta_T}\Theta U dy = -\frac{\vartheta}{Pr}\left(\frac{\partial\Theta}{\partial y}\right)_{y=0} \tag{8}$$

The analytical resolution of the system (Eq. 7 and Eq. 8) leads to the knowledge of the boundary layer ratio Δ (Polidori et al., 2000) and on the other hand gives the steady evolution of the asymptotical δ solution.

Thus, introducing the parameter $K = \ln(Pr)$, the evolution of the ratio $\Delta(Pr)$ is found to be suitable whatever Pr > 0.6 and satisfactorily approached with the following relation :

$$\Delta = 1.576 \times 10^{-4}K^4 - 4.227 \times 10^{-3}K^3 + 4.282 \times 10^{-2}K^2 - 0.1961K + 0.901 \tag{9}$$

The asymptotical limit of the dynamical boundary layer thickness is analytically expressed as :

$$\delta(x) = \Omega x^{\frac{1}{5}} \tag{10}$$

where

$$\Omega = \left[\frac{432k\vartheta^2}{g\beta\varphi_w\Delta}(9\Delta - 5)\right]^{\frac{1}{5}} \tag{11}$$

The best way to understand how the mass transfer occurs and how the boundary layer is feeded with fluid is to access the paths following by the fluid from the streamline patterns. For this purpose, let introduce a stream function Ψ(x,y) such that $\frac{\partial\Psi}{\partial y} = U$ and $\frac{\partial\Psi}{\partial x} = \int_0^y \frac{\partial U}{\partial x}dy$ with the condition Ψ(x,0) = 0 so that the continuity equation (1) is identically satisfied. The analytical resolution leads to the following steady state solution :

$$\Psi(x, y, t \to \infty) = \frac{g\beta\varphi_w\Delta}{12k\vartheta}\left(-\frac{1}{5\Omega}y^5x^{-\frac{1}{5}} + \frac{3}{4}y^4 - \Omega y^3x^{\frac{1}{5}} + \frac{\Omega^2}{2}y^2x^{\frac{2}{5}}\right) \tag{12}$$

$$\Theta_w = T_w - T_\infty = \left[\frac{27\varphi_w^4\vartheta^2\Delta^4}{2g\beta k^4}(9\Delta - 5)x\right]^{\frac{1}{5}} \tag{13}$$

Newton's law:

$$h = \frac{\varphi_w}{\Theta_w} \tag{14}$$

2.2 Forced convection

The schematization of the forced convection physical problem is seen in Figure 1. The mathematical approach is based on the energy semi-integral equation resolution within the thermal boundary layer, by using the Karman-Pohlhausen method applied to both velocity and temperature flow fields.

$$\frac{\partial}{\partial x}\int_0^{\delta_T}\Theta U dy = -\frac{\nu}{Pr}\left(\frac{\partial\Theta}{\partial y}\right)_{y=0} \tag{15}$$

The determination of the Δ ratio (steady relative thickness of both thermal and dynamical boundary layers) is made from the resolution of the steady form of the energy equation (Padet, 1997) from which it is shown that this parameter appears to be only fluid Prandtl number dependent. The resulting equation in the Prandtl number range covering the main usual fluids, namely Pr > 0.6, is written as :

$$\frac{\Delta^6}{180} - \frac{3\Delta^5}{140} + \frac{2\Delta^3}{15} - \frac{37}{630Pr} = 0 \tag{16}$$

Using the 4th order Pohlhausen method with convenient velocity and thermal boundary conditions leads to the following velocity and temperature profiles :

$$U = U_\infty(\eta^4 - 2\eta^3 + 2\eta) \tag{17}$$

$$\Theta = \Theta_w(-\eta_T^4 + 2\eta_T^3 - 2\eta_T + 1) \tag{18}$$

These profiles are directly used to define dynamical parameters qualifying both heat and mass transfer, such as the dynamical boundary layer thickness $(\delta(x))$ and the thermal flow rate (Q_{th}) defined as follows :

$$\delta(x) = \sqrt{\frac{1260}{37}}\frac{x}{\sqrt{Re_x}} \tag{19}$$

$$Q_{th} = \rho C_p \int_0^{\eta_T}\Theta U dy \tag{20}$$

In such a case, the convective heat transfer coefficient is expressed as :

$$h(x) = \frac{2}{\Delta\delta(x)} = \sqrt{\frac{37}{315\Delta^2}}\frac{\sqrt{Re_x}}{x} \tag{21}$$

3. Thermophysical properties of nanofluids

The thermophysical properties of the nanofluids, namely the density, volume expansion coefficient and heat capacity have been computed using classical relations developed for a two-phase mixture (Pak and Cho, 1998 ; Xuan and Roetzel, 2000 ; Zhou and Ni, 2008):

$$\rho_{nf} = (1-\phi)\rho_{bf} + \phi\rho_p \tag{22}$$

$$\beta_{nf} = (1-\phi)\beta_{bf} + \phi\beta_p \tag{23}$$

$$\left(\rho C_p\right)_{nf} = (1-\phi)\left(\rho C_p\right)_{bf} + \phi\left(\rho C_p\right)_p \tag{24}$$

It is worth noting that for a given nanofluid, simultaneous measurements of conductivity and viscosity are missing. In the present study, on the basis of statistical nanomechanics, the dynamic viscosity is obtained from the relationship proposed by Maïga et al. 2005, 2006 for water-γAl_2O_3 nanofluid (Eq. 25):

$$\mu_{nf} = \mu_{bf}(123\phi^2 + 7.3\phi + 1) \tag{25}$$

and Nguyen et al., 2007 for water-CuO nanofluid (Eq. 26), and derived from experimental data:

$$\mu_{nf} = \mu_{bf}(0.009\phi^3 + 0.051\phi^2 - 0.319\phi + 1.475) \tag{26}$$

Most recently, Mintsa et al. 2009 proposed the following correlation based on experimental data for the water-γAl_2O_3 nanofluid (Eq. 27)

$$k_{nf} = k_{bf}(1.72\phi + 1.0) \tag{27}$$

and for the water-CuO nanofluid (Eq. 28):

$$k_{nf} = k_{bf}(1.74\phi + 0.99) \tag{28}$$

Volume fraction	ρ	c_p	μ	β	k
%	$\frac{kg}{m^3}$	$\frac{J}{kg.K}$	$\frac{kg}{m.s}$	$\frac{1}{K}$	$\frac{W}{m.K}$
0	998.2	4182	1.002E-03	2.060E-04	0.600
1	1053.22	3971.61	1.218E-03	2.040E-04	0.604
2	1108.24	3782.11	1.115E-03	2.020E-04	0.615
3	1163.25	3610.54	1.222E-03	2.000E-04	0.625
4	1218.27	3454.46	1.594E-03	1.980E-04	0.636
5	1273.29	3311.87	2.285E-03	1.960E-04	0.646

Table 1. Thermophysical properties of CuO / water nanofluid

Volume fraction	ρ	c_p	μ	β	k
%	$\frac{kg}{m^3}$	$\frac{J}{Kg.K}$	$\frac{kg}{m.s}$	$\frac{1}{K}$	$\frac{W}{m.K}$
0	998.2	4182	1.002E-03	2.060E-04	0.600
1	1027.02	4053.21	1.087E-03	2.042E-04	0.610
2	1055.84	3931.45	1.198E-03	2.024E-04	0.621
3	1084.65	3816.16	1.332E-03	2.005E-04	0.631
4	1113.47	3706.84	1.492E-03	1.987E-04	0.641
5	1142.29	3603.03	1.676E-03	1.969E-04	0.652

Table 2. Thermophysical properties of Alumina / water nanofluid

4. Results

To ensure laminar conditions for both the forced convection and the free convection problems, the imposed initial conditions have been respectively $\varphi_w = 100\ W/m^2$ for the heat flux density in free convection and $\varphi_w = 1000\ W/m^2;\ U = 1\,m/s$ for the heat flux density and external flow in forced convection.

4.1 Natural convection velocity

First, to analyse how the mass transfer occurs using nanofluids in thermal convection regimes, we have focused the following parameters:

- Velocity boundary layer thickness,
- Velocity profiles within the boundary layer,
- Streamline patterns,

Because nanofluids are mainly used in hydrodynamics to enhance the heat transfer and because in free convection the thermal and dynamical problems and conditions are coupled together, we have also focused :

- Temperature profiles in the thermal boundary layer,
- Heat transfer coefficient at wall,
- Thermal flow rate.

In figures 2 and 3 are presented the steady velocity boundary layer thickness along the wall, for the two tested nanofluids (Alumina/water and CuO/Water), in the range of Newtonian behaviour nanofluid (Fohano et al., 2010), namely for small values of particle volume fraction $\phi < 5\%$.

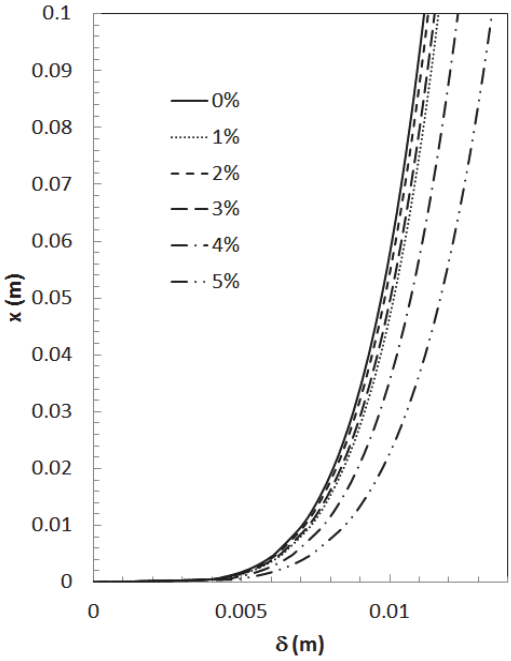

Fig. 2. Velocity boundary layer for CuO / water nanofluid

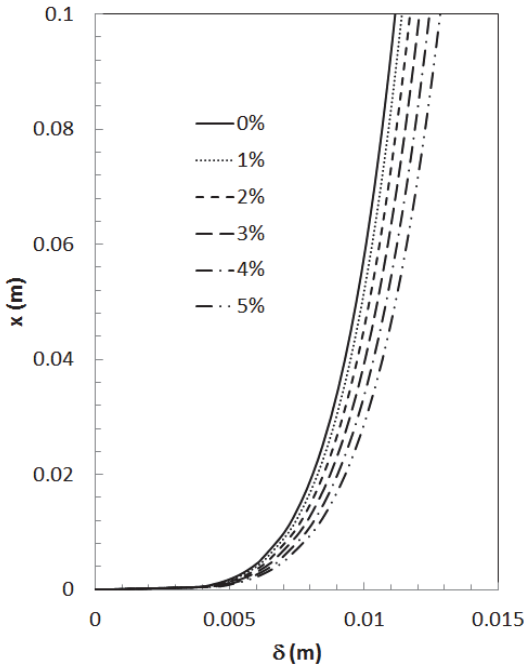

Fig. 3. Velocity boundary layer for Alumina / water nanofluid

Because varying the particle volume fraction highly influences the viscosity of the mixture, one can clearly see the resulting variation in thickness of the viscous boundary layer. Whatever the nanofluid is, an augmentation of the particle volume fraction value induces a higher thickness of the velocity boundary layer. Nevertheless, this phenomenon is more pronounced for the CuO/water nanofluid than for the alumina/water mixture, because the variation reaches respectively 22% and 16% at ϕ = 5% in comparison with the reference case (base fluid only).

The velocity profiles within the velocity boundary layer are drawn in Figures 4 and 5 at a given x=0.1m abscissa, in the same range of particle volume fraction less than 5%.

One observes similar trends whatever the nanofluid is :

- Flattening of the velocity profiles with the increase of the particle volume fraction,
- Modification in space of the location of the maximum velocity, following the evolution of the boundary layer thickness,
- Presence of a singular point, at the intersection of the profiles.

Focusing the volumetric flow rate leads to introduce a new parameter, called ε defined as follows:

$$\varepsilon = \left(\frac{Q_{v_{nf}}}{Q_{v_{bf}}} - 1\right) * 100 \tag{29}$$

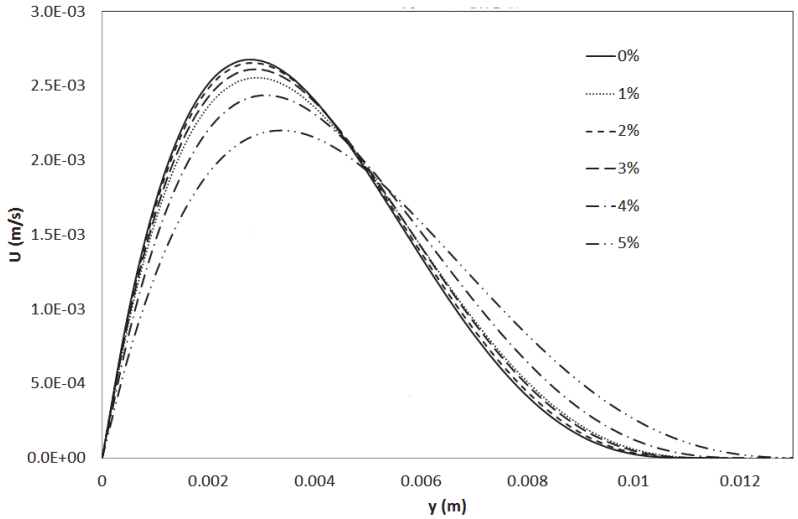

Fig. 4. Velocity profiles at x = 0.1 m abscissa for CuO / water nanofluid

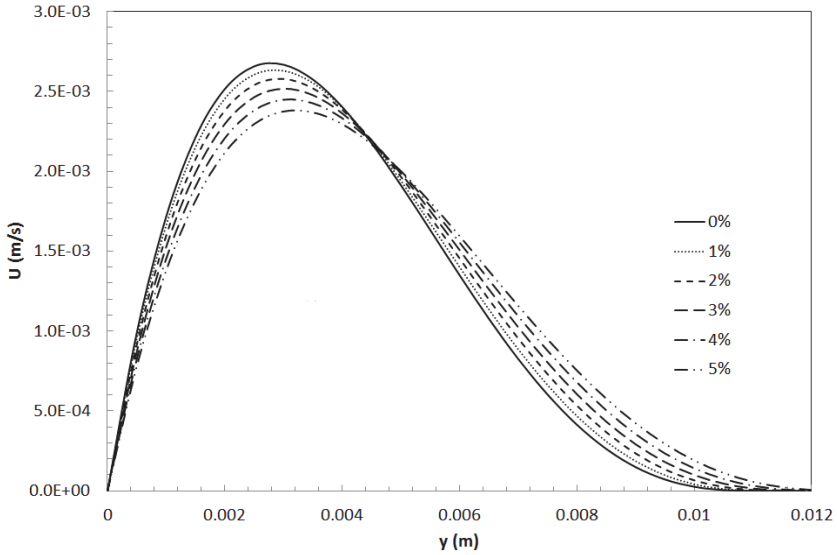

Fig. 5. Velocity profiles at x = 0.1 m abscissa for Alumina / water nanofluid

Table 3 summarizes the evolution of this parameter with the particle volume fraction, for both nanofluids. It clearly appears that the volumetric flow rate is no ϕ dependent, traducing conservation trend for the flow rate. Indeed, the volumetric flow rate for the mixture is close to that of the base fluid, not exceeding a 1% value. The boundary layer ratio Δ is also mentioned in Table 3.

	CuO/ water nanofluid			Alumina / water nanofluid		
Volume fraction (%)	Pr	Δ	ε	Pr	Δ	ε
0	6.984	0.653	0.00%	6.984	0.653	0.00%
1	8.006	0.643	-0.11%	7.222	0.650	0.00%
2	6.860	0.654	0.34%	7.586	0.647	0.44%
3	7.058	0.652	0.70%	8.058	0.643	0.51%
4	8.662	0.638	0.83%	8.623	0.638	0.55%
5	11.709	0.621	0.10%	9.267	0.634	0.59%

Table 3. Nanofluids properties in natural convection

To complete this dynamical analysis, the streamline patterns are plotted in Figures 6 and 7 versus the y-direction. These streamline patterns are plotted for two particle volume fractions (2% and 5 %) and are compared to a base fluid (0%). The observed phenomena are similar for both nanofluids (CuO/water and Alumina/water).
The conclusion extracted from Figures 6 and 7 are that the mass flow has an intense upward motion close to the wall (y=0) while the viscous layer is mainly fed with fluid coming from the crosswise direction from the wall.

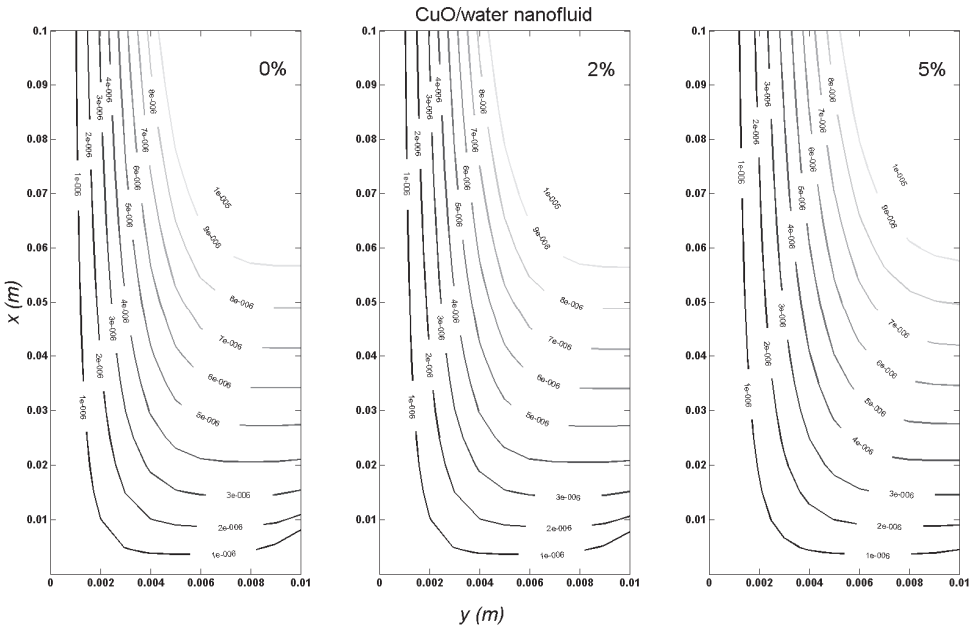

Fig. 6. Streamline patterns within the dynamic boundary layer for CuO / water nanofluid

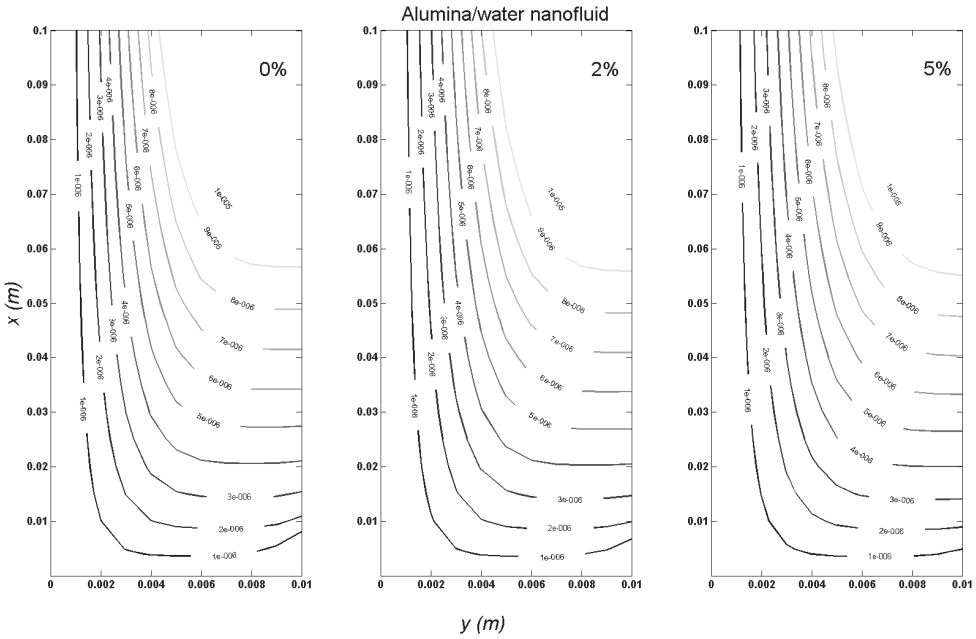

Fig. 7. Streamline patterns within the dynamic boundary layer for Alumina / water nanofluid

To make the analysis of such convection problems more complete, and because free convection induces the coupling of thermal and dynamical features of the flow, we present in Figures 8 and 9, the temperature profiles within the thermal boundary layers at a given abscissa (x = 0.1m).

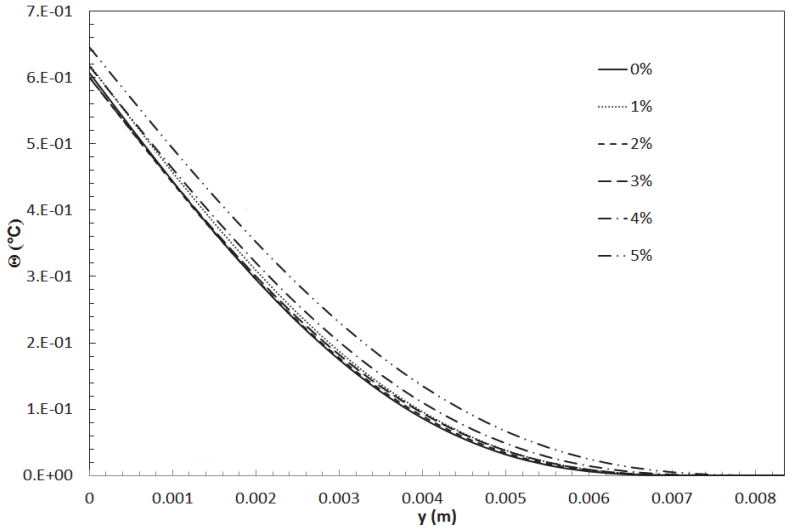

Fig. 8. Temperature profiles at x = 0.1 m abscissa for CuO / water nanofluid

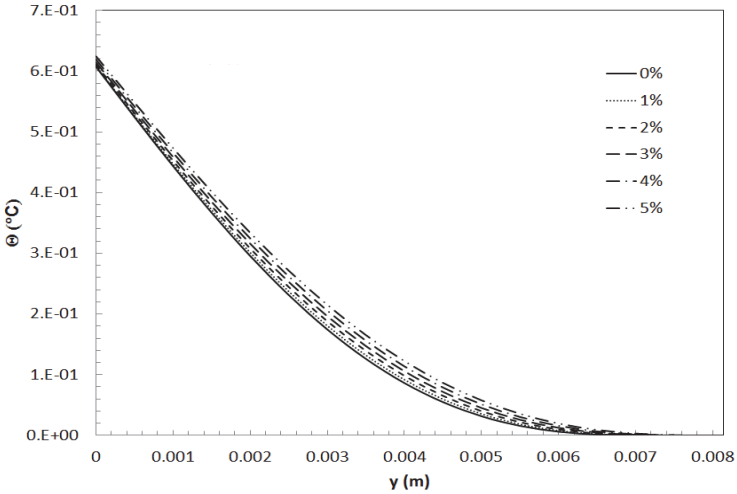

Fig. 9. Temperature profiles at x = 0.1 m abscissa for Alumina / water nanofluid

There are no major differences between the temperature profiles for the two nanofluids. The common trend is that the increase of the particle volume fraction leads to increase the temperature at wall and within the thermal boundary layer whose thickness also increases compared to that of the base fluid.

The resolution of a heat transfer problem between a fluid and a wall often requires the knowledge of the heat transfer coefficient, called "h", which depends as the flow dynamic features as on the thermal properties of both fluid and wall. Due to Newton's law, "h" is seen to evolve as $1/\Theta_w$.

Figures 10 and 11 highlight the evolution of the convective exchange coefficient "h". It is clearly seen that increasing the particle volume fraction leads to a degradation in the heat

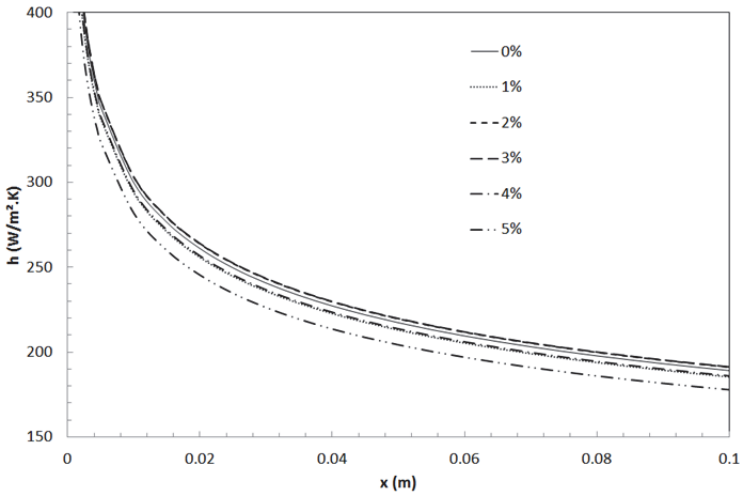

Fig. 10. Heat transfer coefficient at wall for CuO / water nanofluid

transfer enhancement. This result appears to be consistent with that from a previous published work (Putra et al., 2003) in which the authors mentioned that, unlike conduction or forced convection, a systematic and definite deterioration in free convective heat transfer has been found while using nanofluids. This apparent paradoxical behaviour when increasing the particle volume fraction can be explained as follows. Adding solid nanoparticles is expected to increase the thermal conductivity, thus resulting in higher heat transfer.

However, an augmentation of the particle volume fraction also increases the mixture viscosity. For the natural convection flow of this study, it appears that the effect of increased viscosity is dominant over the increase of thermal conductivity.

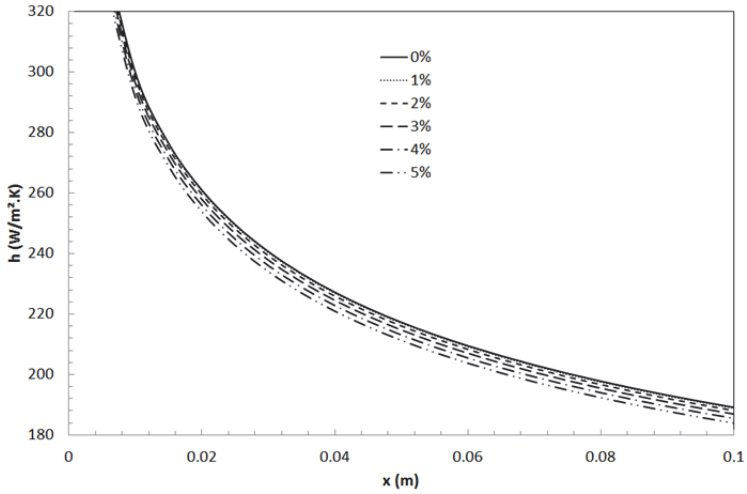

Fig. 11. Heat transfer coefficient at the wall for Alumina / water nanofluid

4.2 Forced convection

We consider now the external boundary layer flow past a semi-infinite flat plate in a thermal equilibrium state, as defined in Figure 1. The flow is laminar and assumed to be incompressible. Its thermal properties are considered as constant. A uniform heat flux density whose value is 1000 W/m² is applied at the upper surface of the plate. The velocity of the free external stream is 1 m/s.

Like the natural convection problem, we first focuse the dynamical features of the two nanofluid flows and finally consider the heat transfer characteristics, varying the particle volume fraction.

In figures 12 and 13 are presented the steady velocity boundary layer thickness along the wall, for the two tested nanofluids (CuO/Water andAlumina/water), in the range of Newtonian behaviour, namely for small values of particle volume fraction $\phi < 5\%$.

Because the viscosity of the mixture increases with the particle volume fraction, it is seen that the thickness of the boundary layer increases. This phenomenon is similar to that observed with the free convection case. Moreover, this increase in thickness is also found to be more important with the CuO/water nanofluid.

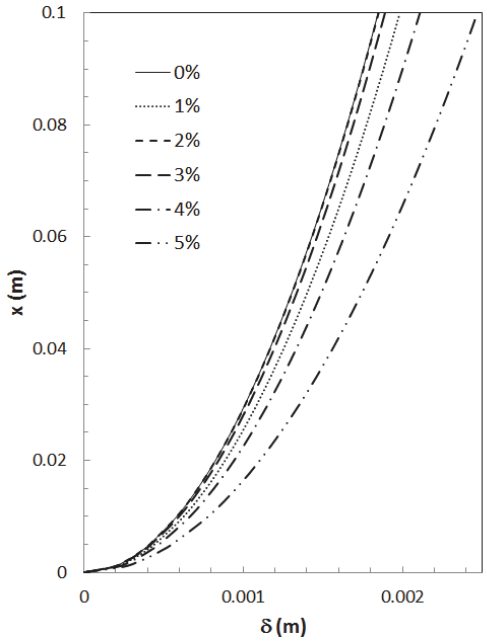

Fig. 12. Velocity boundary layer for CuO / water nanofluid

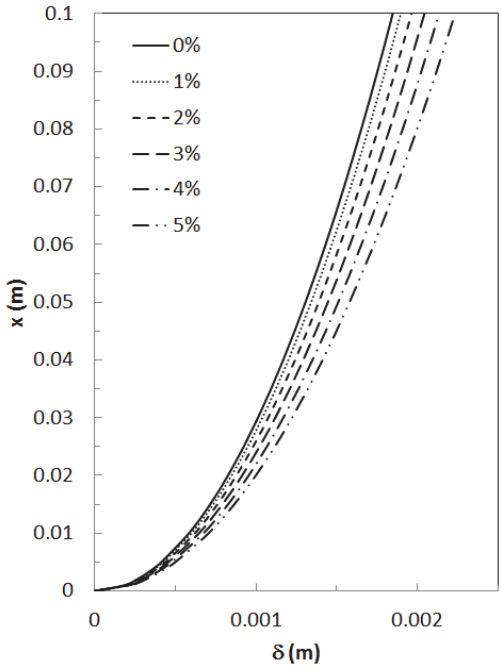

Fig. 13. Velocity boundary layer for Alumina / water nanofluid

Consequently, the velocity profiles drawn in Figures 14 and 15 seem to follow this trend with respect to the volumetric flow rate conservation law. It is the reason why in the neighborhood of the wall, the velocity decreases with the particle volume fraction. This diminution is also more pronounced for the CuO/water nanofluid.

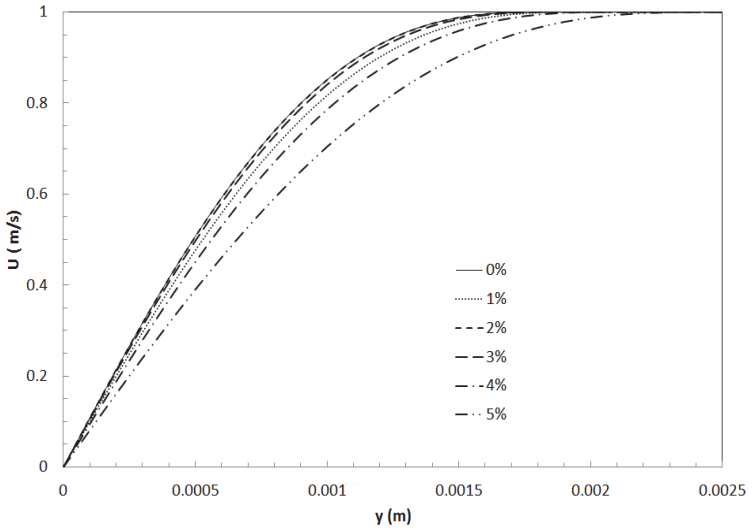

Fig. 14. Velocity profiles at x = 0.1 m abscissa for CuO / water nanofluid

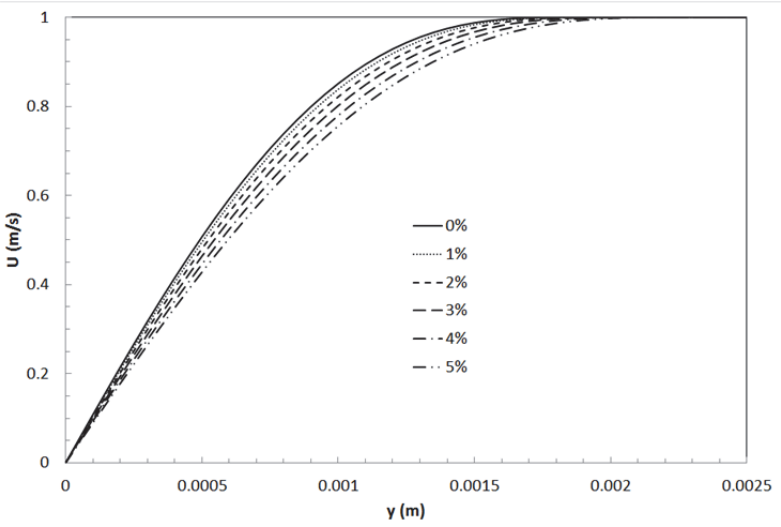

Fig. 15. Velocity profiles at x = 0.1 m abscissa for Alumina / water nanofluid

The temperature profiles have been drawn for the two nanofluids at a given abscissa within the thermal boundary layer thickness. Globally, the temperature is seen to increase in the boundary layer when the particle volume fraction increases as shown in Figures 16 and 17.

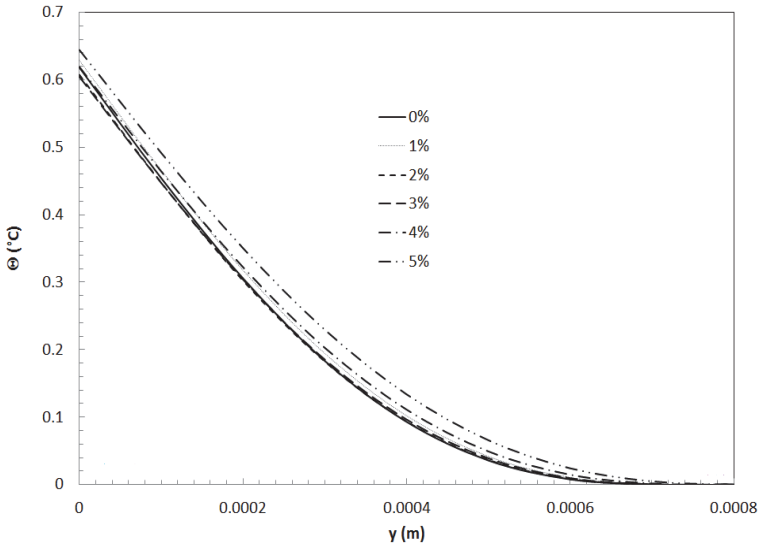

Fig. 16. Temperature profiles at x = 0.1 m abscissa for CuO / water nanofluid

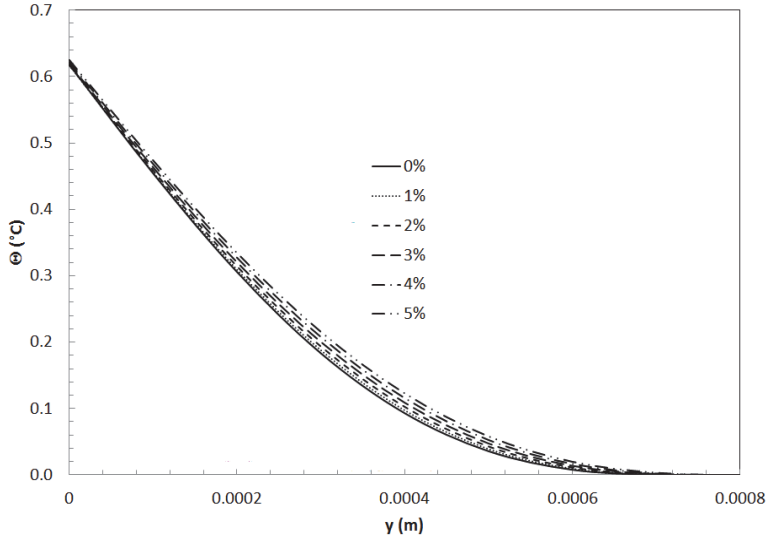

Fig. 17. Temperature profiles at x = 0.1 m abscissa for Alumina / water nanofluid

From both velocity and thermal parameters, we have chosen to access the thermal flow rate defined in Eq. 20.

This parameter, drawn in Figures 18 and 19, which is calculated within the thermal boundary layer, evolves linearly along the wall. Strong differences are observed with the variation of the particle volume fraction.

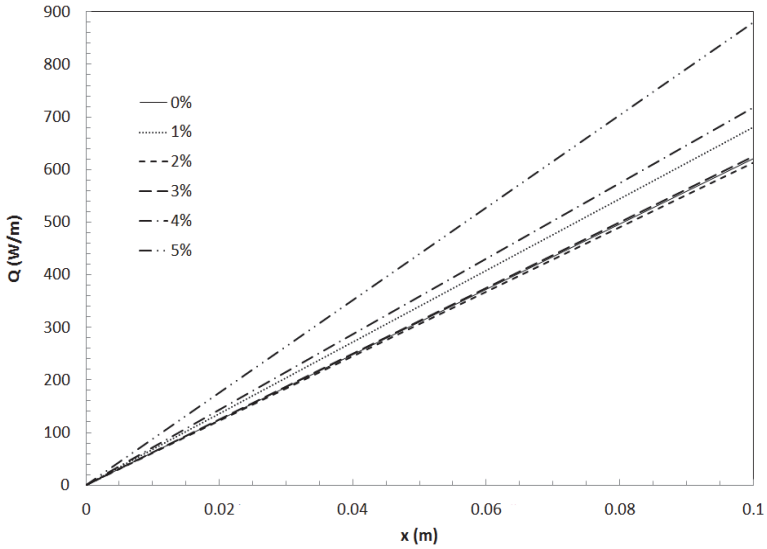

Fig. 18. Thermal flow rate for CuO / water nanofluid

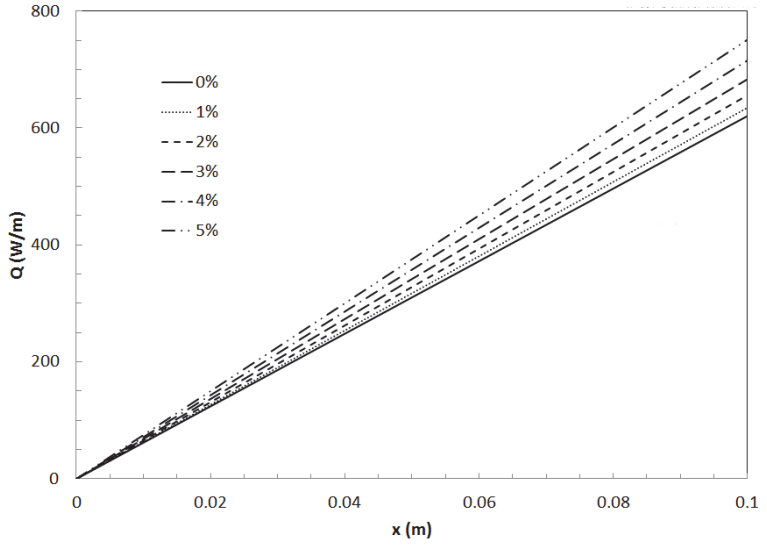

Fig. 19. Thermal flow rate for Alumina / water nanofluid

To have a quantitative idea on how the thermal flow rate evolves with the particle volume fraction, the parameter ε_{st} is introduced :

$$\varepsilon_{th} = \left(\frac{Q_{th_{nf}}}{Q_{th_{bf}}} - 1\right) * 100 \tag{30}$$

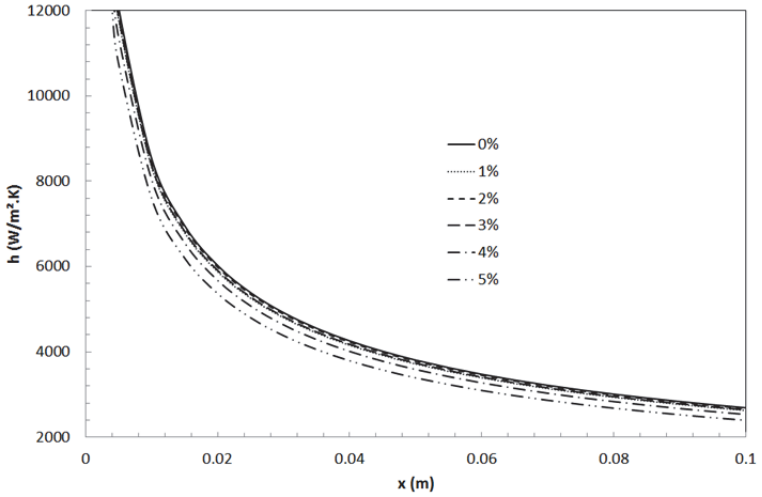

Fig. 20. Heat transfer coefficient at wall for CuO / water nanofluid

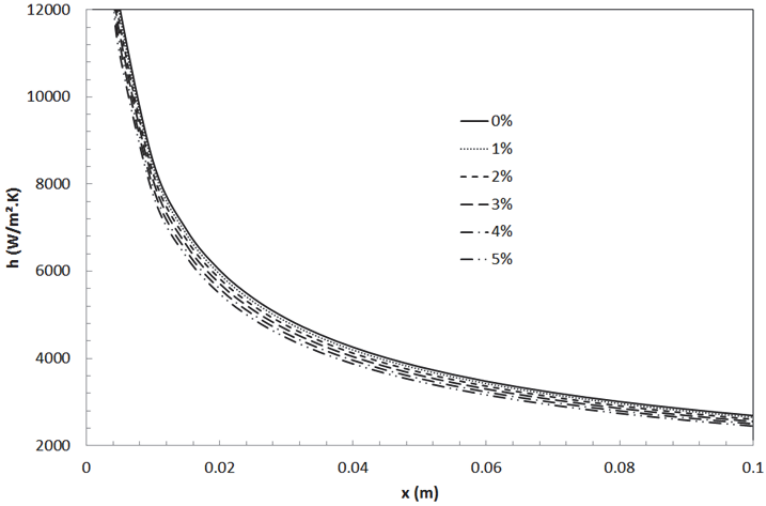

Fig. 21. Heat transfer coefficient at wall for Alumina / water nanofluid

Table 4 summarizes the evolution of this parameter with the particle volume fraction, for both nanofluids, traducing both heat and mass transfer in forced convection. It clearly appears that the thermal flow rate is strongly ϕ dependent.

In comparison with the reference base fluid case, an enhancement in the thermal flow rate is observed, up to 42% for the CuO/water nanofluid and 21% for the Alumina/water nanofluid.

	CuO/ water nanofluid			Alumina / water nanofluid		
Volume fraction (%)	Pr	Δ	ε_{th}	Pr	Δ	ε_{th}
0	6.984	0.402	0.00%	6.984	0.402	0.00%
1	8.006	0.383	9.64%	7.222	0.397	2.28%
2	6.860	0.404	-1.23%	7.586	0.390	5.72%
3	7.058	0.400	0.69%	8.058	0.382	10.13%
4	8.662	0.373	15.66%	8.623	0.374	15.31%
5	11.709	0.337	41.72%	9.267	0.365	21.03%

Table 4. Nanofluids properties in forced convection

5. Conclusion

In the present study, both free convection and forced convection problems of Newtonian CuO/water and alumina/water nanofluids over semi-infinite plates have been investigated from a theoretical viewpoint, for a range of nanoparticle volume fraction up to 5%. The analysis is based on a macroscopic modelling and under assumption of constant thermophysical nanofluid properties.

Whatever the thermal convective regime is, namely free convection or forced convection, it seems that the viscosity, whose evolution is entirely due to the particle volume fraction value, plays a key role in the mass transfer. It is shown that using nanofluids strongly influences the boundary layer thickness by modifying the viscosity of the resulting mixture leading to variations in the mass transfer in the vicinity of walls in external boundary-layer flows. It has been shown that both viscous boundary layer and velocity profiles deduced from the Karman-Pohlhausen analysys, are highly viscosity dependent.

Concerning the heat transfer, results are more contrasted. Whatever the nanofluid, increasing the nanoparticle volume fraction leads to a degradation in the external free convection heat transfer, compared to the base-fluid reference. This confirms previous conclusions about similar analyses and tends to prove that the use of nanofluids remains illusory in external free convection.

A contrario, the external forced convection analyses shows that the use of nanofluids is a powerful mean to modify and enhance the heat transfer, and the thermal flow rate which are strongly dependent of the nanoparticle volume fraction.

6. Nomenclature

Cp specific heat capacity $J.kg^{-1}.K^{-1}$
g acceleration of the gravity $m.s^{-2}$
h heat transfer coefficient $W.m^{-2}.K^{-1}$

k thermal conductivity $W.m^{-1}.K^{-1}$
K parameter
Pr Prandtl number $\left(=\frac{\mu C_p}{k}\right)$
Re Reynolds number
T temperature K
U x velocity $m.s^{-1}$
V y velocity $m.s^{-1}$
x, y parallel and normal to the vertical plane m

6.1 Greek symbols

β coefficient of thermal expansion K^{-1}
δ dynamical boundary layer thickness m
δ_T thermal boundary layer thickness m
Δ thermal to velocity layer thickness ratio
ε, Ω parameters
ϕ particle volume fraction %
φ heat flux density $W.m^{-2}$
ν kinematic viscosity $m^2.s^{-1}$
ρ density $kg.m^{-3}$
Ψ streamline function s^{-1}
Θ temperature °C

6.2 Subscripts

bf base-fluid
nf nanofluid
p nanoparticle
th thermal
w wall

7. References

Ben Mansour, R., Galanis, N. & Nguyen, C.T., (2007). Effect of uncertainties in physical properties on forced convection heat transfer with nanofluids. *Appl. Therm. Eng.* Vol. 27 (2007) pp.240-249.

Brinkman, H.C. (1952). The viscosity of concentrated suspensions and solutions. *J. Chem. Phys.* Vol. 20 (1952) pp. 571-581.

Fohanno, S., Nguyen, C.T. & Polidori, G. (2010). Newtonian nanofluids in convection, In: *Handbook of Nanophysics (Chapter 30),* K. Sattler (Ed.), CRC Press, ISBN 978-142-0075-44-1, New-York, USA

Kakaç, S. & Yener, Y., Convective heat transfer, Second Ed., CRC Press, Boca Raton, 1995.

Keblinski, P., Prasher, R. & Eapen, J. (2008). Thermal conductance of nanofluids: is the controversy over*? J. Nanopart. Res.* Vol.10. pp.1089-1097.

Khanafer, K., Vafai, K., Lightstone, M., (2003). Buoyancy-driven heat transfer enhancement in a two-dimensional enclosure using nanofluids. *Int. J. Heat Mass Transf.* Vol. 46 pp.3639-3653.

Maïga, S.E.B. Palm, S.J., Nguyen, C.T., Roy, G. & Galanis, N. (2005). Heat transfer enhancement by using nanofluids in forced convection flows. *Int. J. Heat Fluid Flow* Vol. 26 (2005) pp.530-546.

Maïga S.E.B., Nguyen C.T., Galanis N., Roy G., Maré T., Coqueux M., Heat transfer enhancement in turbulent tube flow using Al2O3 nanoparticle suspension, Int. J. Num. Meth. Heat Fluid Flow, 16- 3 (2006) 275-292.

Mintsa H.A., Roy G., Nguyen C.T., Doucet D., New temperature dependent thermal conductivity data for water-based nanofluids, Int. J. of Thermal Sciences, 48 (2009) 363-371.

Murshed, S.M.S., Leong, K.C., Yang, C. (2005). Enhanced thermal conductivity ofTiO2ewater based nanofluids. *Int. J. Therm. Sci.* Vol.44 pp.367-373.

Nguyen C.T., Desgranges F., Roy G., Galanis N., Maré T., Boucher S., Mintsa H. Angue, Temperature and particle-size dependent viscosity data for water-based nanofluids – Hysteresis phenomenon, International Journal of Heat and Fluid Flow, 28 (2007) 1492–1506.

Nguyen, C.T., Galanis, N., Polidori, G., Fohanno, S., Popa, C.V. & Le Bechec A. (2009). An experimental study of a confined and submerged impinging jet heat transfer using Al2O3-water nanofluid, *International Journal of Thermal Sciences*, Vol. 48, pp.401-411

Pak B. C., Cho Y. I., Hydrodynamic and heat transfer study of dispersed fluids with submicron metallic oxide particles, Exp. Heat Transfer, 11- 2 (1998) 151-170.

Padet, J. Principe des transferts convectifs, Ed. polytechnica, Paris, 1997.

Polidori, G., Rebay, M. & Padet J. (1999). Retour sur les résultats de la théorie de la convection forcée laminaire établie en écoulement de couche limite 2D. *Int. J. Therm. Sci.*, Vol. 38 pp.398-409.

Polidori, G., Mladin, E.-C. & de Lorenzo, T. (2000). Extension de la méthode de Kármán–Pohlhausen aux régimes transitoires de convection libre, pour Pr > 0,6. *Comptes-Rendus de l'Académie des Sciences,* Vol.328, Série IIb, pp. 763-766

Polidori, G. & Padet, J. (2002). Transient laminar forced convection with arbitrary variation in the wall heat flux. *Heat and Mass Transfer,* Vol.38, pp. 301-307

Polidori, G., Popa, C. & Mai, T.H. (2003). Transient flow rate behaviour in an external natural convection boundary layer. *Mechanics Research Communications,* Vol.30, pp. 615-621.

Polidori, G., Fohanno, S. & Nguyen, C.T. (2007). A note on heat transfer modelling of Newtonian nanofluids in laminar free convection. *Int. J. Therm. Sci.* Vol.46 (2007) pp. 739-744.

Popa, C.V., Fohanno, S., Nguyen, C.T. & Polidori G. (2010). On heat transfer in external natural convection flows using two nanofluids, *International Journal of Thermal Sciences*, Vol. 49, pp. 901-908

Putra, N., Roetzel, W. & Das S.K. (2003). Natural convection of nanofluids. *Heat Mass Transfer,* Vol.39 pp. 775-784.

Varga, C., Fohanno, S. & Polidori G. (2004). Turbulent boundary-layer buoyant flow modeling over a wide Prandtl number range. *Acta Mechanica* Vol.172. pp.65-73.

Xuan, Y. & Li, Q. (2000). Heat transfer enhancement of nanofluids. *Int. J. Heat Fluid Flow,* Vol.21 (2000) pp.58-64.

Xuan, Y. & Roetzel, W. 2000. Conceptions for heat transfer correlation of nanofluids. *Int. J. Heat Mass Transfer*, Vol.43 pp.3701-3707.

Wang, X.-Q. &, Mujumdar, A.S. (2007). Heat transfer characteristics of nanofluids : a review. *Int. J. Thermal Sciences* vol.46 pp.1-19.

Zhou S.-Q., Ni R., Measurement of specific heat capacity of water-based Al2O3 nanofluid, Applied Physics Letters, 92 (2008) 093123.

6

Optimal Design of Cooling Towers

Eusiel Rubio-Castro[1], Medardo Serna-González[1],
José M. Ponce-Ortega[1] and Arturo Jiménez-Gutiérrez[2]
[1]*Universidad Michoacana de San Nicolás de Hidalgo, Morelia, Michoacán,*
[2]*Instituto Tecnológico de Celaya, Celaya, Guanajuato,*
México

1. Introduction

Process engineers have always looked for strategies and methodologies to minimize process costs and to increase profits. As part of these efforts, mass (Rubio-Castro et al., 2010) and thermal water integration (Ponce-Ortega et al. 2010) strategies have recently been considered with special emphasis. Mass water integration has been used for the minimization of freshwater, wastewater, and treatment and pipeline costs using either single-plant or inter-plant integration, with graphical, algebraic and mathematical programming methodologies; most of the reported works have considered process and environmental constraints on concentration or properties of pollutants. Regarding thermal water integration, several strategies have been reported around the closed-cycle cooling water systems, because they are widely used to dissipate the low-grade heat of chemical and petrochemical process industries, electric-power generating stations, and refrigeration and air conditioning plants. In these systems, water is used to cool down the hot process streams, and then the water is cooled by evaporation and direct contact with air in a wet-cooling tower and recycled to the cooling network. Therefore, cooling towers are very important industrial components and there are many references that present the fundamentals to understand these units (Foust et al., 1979; Singham, 1983; Mills, 1999; Kloppers & Kröger, 2005a).

The heat and mass transfer phenomena in the packing region of a counter flow cooling tower are commonly analyzed using the Merkel (Merkel, 1926), Poppe (Pope & Rögener, 1991) and effectiveness-NTU (Jaber & Webb, 1989) methods. The Merkel's method (Merkel, 1926) consists of an energy balance, and it describes simultaneously the mass and heat transfer processes coupled through the Lewis relationship; however, these relationships oversimplify the process because they do not account for the water lost by evaporation and the humidity of the air that exits the cooling tower. The NTU method models the relationships between mass and heat transfer coefficients and the tower volume. The Poppe's method (Pope & Rögener, 1991) avoids the simplifying assumptions made by Merkel, and consists of differential equations that evaluate the air outlet conditions in terms of enthalpy and humidity, taking into account the water lost by evaporation and the NTU. Jaber and Webb (Jaber & Webb, 1989) developed an effectiveness-NTU method directly applied to counterflow or crossflow cooling towers,

basing the method on the same simplifying assumptions as the Merkel's method. Osterle (Osterle, 1991) proposed a set of differential equations to improve the Merkel equations so that the mass of water lost by evaporation could be properly accounted for; the enthalpy and humidity of the air exiting the tower are also determined, as well as corrected values for NTU. It was shown that the Merkel equations significantly underestimate the required NTU. A detailed derivation of the heat and mass transfer equations of evaporative cooling in wet-cooling towers was proposed by Kloppers & Kröger (2005b), in which the Poppe's method was extended to give a more detailed representation of the Merkel number. Cheng-Qin (2008) reformulated the simple effectiveness-NTU model to take into consideration the effect of nonlinearities of humidity ratio, the enthalpy of air in equilibrium and the water losses by evaporation.

Some works have evaluated and/or compared the above methods for specific problems (Chengqin, 2006; Nahavandi et al., 1975); these contributions have concluded that the Poppe´s method is especially suited for the analysis of hybrid cooling towers because outlet air conditions are accurately determined (Kloppers & Kröger, 2005b). The techniques employed for design applications must consider evaporation losses (Nahavandi et al., 1975). If only the water outlet temperature is of importance, then the simple Merkel model or effectiveness-NTU approach can be used, and it is recommended to determine the fill performance characteristics close to the tower operational conditions (Kloppers & Kröger, 2005a). Quick and accurate analysis of tower performance, exit conditions of moist air as well as profiles of temperatures and moisture content along the tower height are very important for rating and design calculations (Chengqin, 2006). The Poppe´s method is the preferred method for designing hybrid cooling towers because it takes into account the water content of outlet air (Roth, 2001).

With respect to the cooling towers design, computer-aided methods can be very helpful to obtain optimal designs (Oluwasola, 1987). Olander (1961) reported design procedures, along with a list of unnecessary simplifying assumptions, and suggested a method for estimating the relevant heat and mass transfer coefficients in direct-contact cooler-condensers. Kintner-Meyer and Emery (1995) analyzed the selection of cooling tower range and approach, and presented guidelines for sizing cooling towers as part of a cooling system. Using the one-dimensional effectiveness-NTU method, Söylemez (2001, 2004) presented thermo-economic and thermo-hydraulic optimization models to provide the optimum heat and mass transfer area as well as the optimum performance point for forced draft counter flow cooling towers. Recently, Serna-González et al. (2010) presented a mixed integer nonlinear programming model for the optimal design of counter-flow cooling towers that considers operational restrictions, the packing geometry, and the selection of type packing; the performance of towers was made through the Merkel method (Merkel, 1926), and the objective function consisted of minimizing the total annual cost. The method by Serna-González et al. (2010) yields good designs because it considers the operational constraints and the interrelation between the major variables; however, the transport phenomena are oversimplified, the evaporation rate is neglected, the heat resistance and mass resistance in the interface air-water and the outlet air conditions are assumed to be constant, resulting in an underestimation of the NTU.

This chapter presents a method for the detailed geometric design of counterflow cooling towers. The approach is based on the Poppe's method (Pope & Rögener, 1991), which

rigorously addresses the transport phenomena in the tower packing because the evaporation rate is evaluated, the heat and mass transfer resistances are taken into account through the estimation of the Lewis factor, the outlet air conditions are calculated, and the NTU is obtained through the numerical solution of a differential equation set as opposed to a numerical integration of a single differential equation, thus providing better designs than the Merkel´s method (Merkel, 1926). The proposed models are formulated as MINLP problems and they consider the selection of the type of packing, which is limited to film, splash, and tickle types of fills. The major optimization variables are: water to air mass ratio, water mass flow rate, water inlet and outlet temperatures, operational temperature approach, type of packing, height and area of the tower packing, total pressure drop of air flow, fan power consumption, water consumption, outlet air conditions, and NTU.

2. Problem statement

Given are the heat load to be removed in the cooling tower, the inlet air conditions such as dry and wet bulb temperature (to calculate the inlet air humidity and enthalpy), lower and upper limits for outlet and inlet water temperature, respectively, the minimum approach, the minimum allowable temperature difference, the minimal difference between the dry and wet bulb temperature at each integration interval, and the fan efficiency. Also given is the economic scenario that includes unit cost of electricity, unit cost of fresh water, fixed cooling tower cost, and incremental cooling tower cost based on air mass flow rate and yearly operating time. The problem then consists of determining the geometric and operational design parameters (fill type, height and area fill, total pressure drop in the fill, outlet air conditions, range and approach, electricity consumption, water and air mass flowrate, and number of transfer units) of the counterflow cooling tower that satisfy the cooling requirements with a minimum total annual cost.

3. Model formulation

The major equations for the heat and mass transfer in the fill section and the design equations for the cooling tower are described in this section. The indexes used in the model formulation are defined first: *in* (inlet), *out* (outlet), *j* (constants to calculate the transfer coefficient), *k* (constants to calculate the loss coefficient), *r* (makeup), *ev* (evaporated water), *d* (drift), *b* (blowdown), *m* (average), *w* (water), *a* (dry air), *wb* (wet-bulb), *n* (integration interval), *fi* (fill), *fr* (cross-sectional), *misc* (miscellaneous), *t* (total), *vp* (velocity pressure), *f* (fan), *ma* (air-vapor mixture), *e* (electricity), *s* (saturated) and *v* (water vapor). In addition, the superscript *i* is used to denote the type of fill and the scalar *NTI* is the last interval integration. The nomenclature section presents the definition of the variables used in the model. The model formulation is described as follows.

3.1 Heat and mass transfer in the fill section for unsaturated air

The equations for the evaporative cooling process of the Poppe´s method are adapted from Poppe & Rögener (1991) and Kröger (2004), and they are derived from the mass balance for the control volume shown in Figures 1 and 2. Figure 1 shows a control volume in the fill of a counter flow wet-cooling tower, and Figure 2 shows an air-side control volume of the fill illustrated in Figure 1.

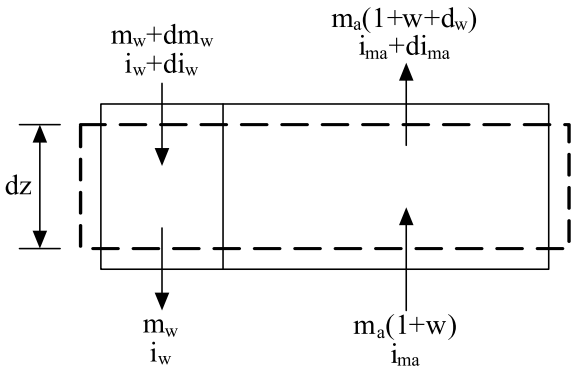

Fig. 1. Control volume of the counter flow fill

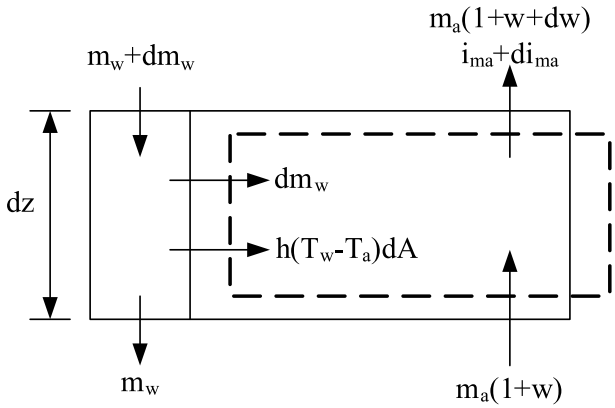

Fig. 2. Air-side control volume of the fill

$$\frac{dw}{dT_w} = \frac{cp_w \frac{m_w}{m_a}\left(w_{s,w} - w\right)}{i_{ma,s,w} - i_{ma} + \left(Lef - 1\right)\left[i_{ma,s,w} - i_{ma} - \left(w_{s,w} - w\right)i_v\right] - \left(w_{s,w} - w\right)cp_w T_w} \tag{1}$$

$$\frac{di_{ma}}{dT_w} = \frac{m_w cp_w}{m_a}\left(1 + \frac{cp_w T_w\left(w_{s,w} - w\right)}{i_{ma,s,w} - i_{ma} + \left(Lef - 1\right)\left[i_{ma,s,w} - i_{ma} - \left(w_{s,w} - w\right)i_v\right] - \left(w_{s,w} - w\right)cp_w T_w}\right) \tag{2}$$

$$\frac{dNTU}{dT_w} = \frac{cp_w}{i_{ma,s,w} - i_{ma} + \left(Lef - 1\right)\left[i_{ma,s,w} - i_{ma} - \left(w_{s,w} - w\right)i_v\right] - \left(w_{s,w} - w\right)cp_w T_w} \tag{3}$$

where w is the humidity ratio through the cooling tower, T_w is the water temperature, cp_w is the specific heat at constant pressure at water temperature, m_w is the water flow rate through the cooling tower, m_a is the air flow rate, $i_{ma,s,w}$ is the enthalpy of saturated air evaluated at water temperature, i_{ma} is the enthalpy of the air-water vapor mixture per mass

of dry-air, i_v is the enthalpy of the water vapor, $w_{s,w}$ is the humidity saturated ratio evaluated at the water temperature, *NTU* is the number of transfer units, and *Lef* is the Lewis factor. This relationship is an indication of the relative rates of heat and mass transfer in an evaporative process, which for unsaturated air can be determined by (taken from Kloppers & Kröger, 2005b):

$$Lef = 0.865^{-0.665}\left(\frac{w_{s,w}+0.622}{w+0.622}-1\right)\Bigg/\left[\ln\left(\frac{w_{s,w}+0.622}{w+0.622}\right)\right] \tag{4}$$

The ratio of the mass flow rates changes as the air moves towards the top of the fill, and it is calculated by considering the control volume of a portion of the fill illustrated in Figure 3.

$$\frac{m_w}{m_a}=\frac{m_{w,in}}{m_a}\left(1-\frac{m_a}{m_{w,in}}\left(w_{out}-w\right)\right) \tag{5}$$

where $m_{w,in}$ is the water flow rate inlet to the cooling tower and w_{out} is the outlet humidity ratio from the cooling tower.

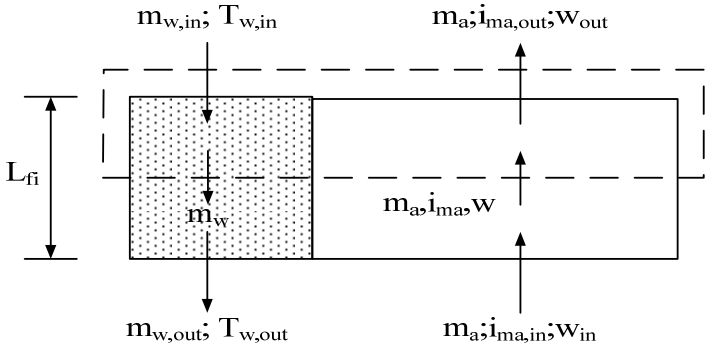

Fig. 3. Control volume of the fill

The Poppe model consists of the above set of coupled ordinary differential and algebraic equations, which can be solved simultaneously to provide the air humidity, the air enthalpy, the water temperature, the water mass flow rate and the NTU profiles in the cooling tower. Also, the state of the outlet air from the cooling tower can be fully determined with this model. The Merkel model can be derived from the Poppe model by assuming a Lewis factor equal to one (*Lef* = 1) and negligible water evaporation (i.e., $dm_w = 0$).

A model with ordinary differential equations and algebraic equations is quite complex for MINLP optimization purposes. Therefore, the set of ordinary differential equations comprising the Poppe model is converted into a set of nonlinear algebraic equations using a fourth-order Runge-Kutta algorithm (Burden & Faires, 1997; Kloppers & Kröger, 2005b), and the physical properties are calculated with the equations shown in Appendix A. Note that the differential equations (1-3) depend of the water temperature, the mass fraction humidity and the air enthalpy, which can be represented as follow,

$$\frac{dw}{dT_w} = f\left(i_{ma}, w, T_w\right) \tag{1'}$$

$$\frac{di_{ma}}{dT_w} = f\left(i_{ma}, w, T_w\right) \tag{2'}$$

$$\frac{dNTU}{dT_w} = f\left(i_{ma}, w, T_w\right) \tag{3'}$$

To convert these differential equations into algebraic equations using the Runge-Kutta algorithm, the first step is to divide the range of water temperature in the fill into a number of intervals,

$$\Delta T_w = \frac{T_{w,in} - T_{w,out}}{N} \tag{6}$$

Here, ΔT_w is the increase of the water temperature in the integration intervals, $T_{w,in}$ is the water inlet temperature on the cooling tower, $T_{w,out}$ is the water outlet temperature on the cooling tower and N is the number of intervals considered for the discretization of the differential equations. **Figure 4** shows a graphical representation of the Runge-Kutta algorithm using five intervals; once the conditions at level 0 that corresponds to the bottom of the cooling tower are known, the conditions at level N+1 can be calculated successively to reach the last level corresponding the top of the tower with the following set of algebraic equations,

$$w_{n+1} = w_n + \left(J_{(n+1,1)} + 2J_{(n+1,2)} + 2J_{(n+1,3)} + J_{(n+1,4)}\right)\Big/6 \tag{7}$$

$$i_{ma,n+1} = i_{ma,n} + \left(K_{(n+1,1)} + 2K_{(n+1,2)} + 2K_{(n+1,3)} + K_{(n+1,4)}\right)\Big/6 \tag{8}$$

$$NTU_{n+1} = NTU_n + \left(L_{(n+1,1)} + 2L_{(n+1,2)} + 2L_{(n+1,3)} + L_{(n+1,4)}\right)\Big/6 \tag{9}$$

where

$$J_{(n+1,1)} = \Delta T_w \cdot f\left(T_{w,n}, i_{ma,n}, w_n\right) \tag{10}$$

$$K_{(n+1,1)} = \Delta T_w \cdot g\left(T_{w,n}, i_{ma,n}, w_n\right) \tag{11}$$

$$L_{(n+1,1)} = \Delta T_w \cdot h\left(T_{w,n}, i_{ma,n}, w_n\right) \tag{12}$$

$$J_{(n+1,2)} = \Delta T_w \cdot f\left(T_{w,n} + \frac{\Delta T_w}{2}, i_{ma,n} + \frac{K_{(n+1,1)}}{2}, w_n + \frac{J_{(n+1,1)}}{2}\right) \tag{13}$$

$$K_{(n+1,2)} = \Delta T_w \cdot g\left(T_{w,n} + \frac{\Delta T_w}{2}, i_{ma,n} + \frac{K_{(n+1,1)}}{2}, w_n + \frac{J_{(n+1,1)}}{2}\right) \tag{14}$$

$$L_{(n+1,2)} = \Delta T_w \cdot h\left(T_{w,n} + \frac{\Delta T_w}{2}, i_{ma,n} + \frac{K_{(n+1,1)}}{2}, w_n + \frac{J_{(n+1,1)}}{2} \right) \tag{15}$$

$$J_{(n+1,3)} = \Delta T_w \cdot f\left(T_{w,n} + \frac{\Delta T_w}{2}, i_{ma,n} + \frac{K_{(n+1,2)}}{2}, w_n + \frac{J_{(n+1,2)}}{2} \right) \tag{16}$$

$$K_{(n+1,3)} = \Delta T_w \cdot g\left(T_{w,n} + \frac{\Delta T_w}{2}, i_{ma,n} + \frac{K_{(n+1,2)}}{2}, w_n + \frac{J_{(n+1,2)}}{2} \right) \tag{17}$$

$$L_{(n+1,3)} = \Delta T_w \cdot h\left(T_{w,n} + \frac{\Delta T_w}{2}, i_{ma,n} + \frac{K_{(n+1,2)}}{2}, w_n + \frac{J_{(n+1,2)}}{2} \right) \tag{18}$$

$$J_{(n+1,4)} = \Delta T_w \cdot f\left(T_{w,n} + \Delta T_w, i_{ma,n} + K_{(n+1,3)}, w_n + J_{(n+1,3)} \right) \tag{19}$$

$$K_{(n+1,4)} = \Delta T_w \cdot g\left(T_{w,n} + \Delta T_w, i_{ma,n} + K_{(n+1,3)}, w_n + J_{(n+1,3)} \right) \tag{20}$$

$$L_{(n+1,4)} = \Delta T_w \cdot h\left(T_{w,n} + \Delta T_w, i_{ma,n} + K_{(n+1,3)}, w_n + J_{(n+1,3)} \right) \tag{21}$$

Here *J*, *K* and *L* are the recursive relations to determine the increase of the air ratio humidity, air enthalpy and number of transfer units, respectively. Notice that the differential equations are now represented by a set of algebraic equations, whose solution gives the profiles of the air humidity ratio, air enthalpy and number of transfer units through the fill. In addition, the number of algebraic equations and variables depends of the number of intervals and sub-intervals considered to get the above profiles, and the start point for their solution. **Figure 5** represents one interval of **Figure 4** divided into subintervals; the conditions at the bottom of the fill provide the starting N point for the calculations of the conditions in the next level N+1. In addition, the specifications of the conditions at the bottom and the top of the cooling tower should be included for estimating the design variables, which include the water inlet temperature, water outlet temperature, water inlet mass flow rate, inlet mass-fraction humidity of air stream, outlet mass-fraction humidity of air stream, inlet dry bulb temperature of air stream, outlet dry bulb temperature of air stream, inlet wet bulb temperature of air stream, outlet wet bulb temperature of air stream and the inlet and outlet enthalpy of air stream,

$$T_{w,in} = T_{w,n=NTI} \tag{22}$$

$$T_{w,out} = T_{w,n=0} \tag{23}$$

$$m_{w,in} = m_{w,n=NTI} \tag{24}$$

$$m_{w,out} = m_{w,n=0} \tag{25}$$

$$w_{in} = w_{n=0} \tag{26}$$

$$w_{out} = w_{n=NTI} \tag{27}$$

$$T_{a,in} = T_{a,n=0} \tag{28}$$

$$T_{a,out} = T_{a,n=NTI} \tag{29}$$

$$T_{wb,in} = T_{wb,n=0} \tag{30}$$

$$T_{wb,out} = T_{wb,n=NTI} \tag{31}$$

$$i_{ma,in} = i_{ma,n=0} \tag{32}$$

$$i_{ma,out} = i_{ma,n=NTI} \tag{33}$$

The system of equations above described is only valid for unsaturated air; one should keep in mind that only this region is considered in the design of wet-cooling towers because the air exiting from the tower cannot be saturated before leaving the packing section.

3.2 Design equations

The relationships to obtain the geometric design of the cooling tower are presented in this section; they are used in conjunction with a numerical technique for the solution of the Poppe's equations.

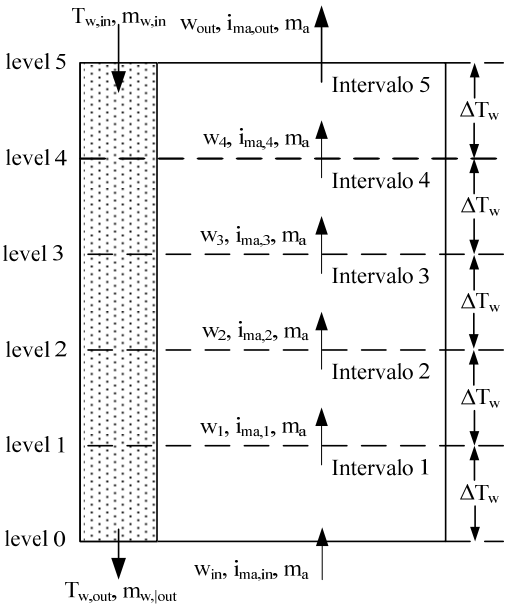

Fig. 4. Graphical representation of the Runge-Kutta method

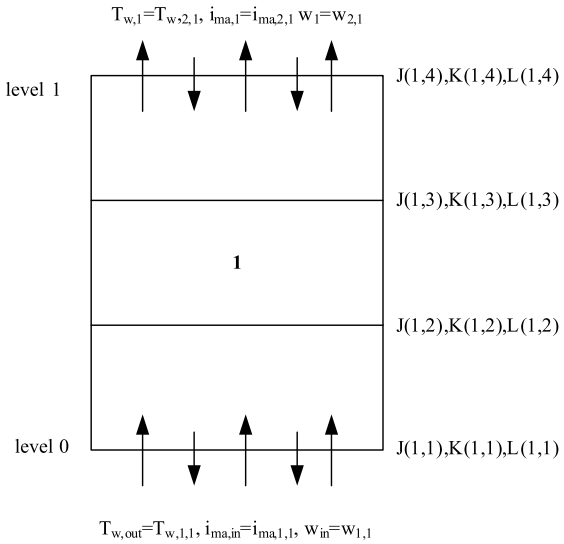

Fig. 5. Representation of one integration interval of the fill

3.2.1 Heat load

The heat of the water stream removed in the cooling tower (Q) is calculated as follows:

$$Q = cp_{w,in} m_{w,in} T_{w,in} - cp_{w,out} m_{w,out} T_{w,out} \tag{34}$$

where $cp_{w,in}$ is the specific heat at constant pressure at inlet water temperature, $cp_{w,out}$ is the specific heat at constant pressure at outlet water temperature, $T_{w,in}$ is the inlet water temperature to the cooling tower, $T_{w,out}$ is the outlet water temperature from the cooling tower, and $m_{w,out}$ is the outlet water flow rate, which is obtained from the following relationship:

$$m_{w,out} = m_{w,in} - m_a \left(w_{out} - w_{in} \right) - m_{w,d} \tag{35}$$

where $m_{w,d}$ is the drift water for air flow rate. Notice that equation (34) is an improved equation for the heat rejection rate, according to the Merkel or effectiveness-NTU methods; it is used when there are water losses by evaporation and it is included in the energy balance (Kloppers & Kröger, 2005a), situation modeled in Poppe's method.

3.2.2 Transfer and loss coefficients

The transfer coefficients are related to the NTU and they depend on the fill type (Kloppers & Kröger, 2005c). The value of Merkel's number at the last level (*NTI*) is given by:

$$NTU_{n=NTI} = c_1 \left(\frac{m_{w,m}}{A_{fr}} \right)^{c2} \left(\frac{m_a}{A_{fr}} \right)^{c3} \left(L_{fi} \right)^{1+c4} \left(T_{w,in} \right)^{c5} \tag{36}$$

where A_{fr} is the packing area, L_{fi} is the height of packing, c_1 and c_5 are constants that depend on the type of fill, and $m_{w,m}$ is the average water flow rate, calculated as follows:

$$m_{w,m} = \frac{m_{w,in} + m_{w,out}}{2} \tag{37}$$

Table 1 shows the values for the a_j^i constants (Kloppers & Kröger, 2005c) for different types of fills.

j	a_j^i		
	i=1 (splash fill)	i=2 (trickle fill)	i=3 (film fill)
	0.249013	1.930306	1.019766
2	-0.464089	-0.568230	-0.432896
3	0.653578	0.641400	0.782744
4	0	-0.352377	-0.292870
5	0	-0.178670	0

Table 1. Constants for transfer coefficients

The following disjunction and its reformulation through the convex hull technique (Vicchietti, et al., 2003) is used for the optimal selection of fill type:

$$\begin{bmatrix} Y^1 \\ (splash\ fill) \\ c_j = c_j^1, \quad j = 1,...,5 \end{bmatrix} \vee \begin{bmatrix} Y^2 \\ (trickle\ fill) \\ c_j = c_j^2, \quad j = 1,...,5 \end{bmatrix} \vee \begin{bmatrix} Y^3 \\ (film\ fill) \\ c_j = c_j^3, \quad j = 1,...,5 \end{bmatrix}$$

$$y^1 + y^2 + y^3 = 1 \tag{38}$$

$$c_j = c_j^1 + c_j^2 + c_j^3, \quad j = 1,...,5 \tag{39}$$

$$c_j^i = a_j^i y^i, \quad i = 1,...,3. \quad j = 1,...,5 \tag{40}$$

The loss coefficients (K_{fi}) in cooling towers are analogous to the friction factors in heat exchangers; they are used to estimate the pressure drop through the fill using the following correlation for different types of fills (Kloppers & Kröger, 2003):

$$K_{fi} = \left[d_1 \left(\frac{m_{w,m}}{A_{fr}} \right)^{d2} \left(\frac{m_a}{A_{fr}} \right)^{d3} + d_4 \left(\frac{m_{w,m}}{A_{fr}} \right)^{d5} \left(\frac{m_a}{A_{fr}} \right)^{d6} \right] L_{fi} \tag{41}$$

The following disjunction is used to select the fill type:

$$\begin{bmatrix} Y^1 \\ (splash\ fill) \\ d_k = d_k^1, \quad k = 1,...,6 \end{bmatrix} \vee \begin{bmatrix} Y^2 \\ (trickle\ fill) \\ d_k = d_k^2, \quad k = 1,...,6 \end{bmatrix} \vee \begin{bmatrix} Y^3 \\ (film\ fill) \\ d_k = d_k^3, \quad k = 1,...,6 \end{bmatrix}$$

The disjunction is reformulated as follows:

$$d_k = d_k^1 + d_k^2 + d_k^3, \quad k = 1,\ldots,6 \tag{42}$$

$$d_k^i = b_k^i \, y^i, \quad i = 1,\ldots,3. \quad k = 1,\ldots,6 \tag{43}$$

Values for b_k^i coefficients for different fill types are shown in Table 2 (Kloppers & Kröger, 2003).

3.2.3 Pressure drop in the cooling tower

According to Li & Priddy (1985), the total pressure drop (ΔP_t) in mechanical draft cooling towers is the sum of the static and dynamic pressure drops (ΔP_{vp}). The first type includes the pressure drop through the fill (ΔP_{fi}) and the miscellaneous pressure drop (ΔP_{misc}). The pressure drop through the fill is calculated from (Kloppers & Kröger, 2003):

k	b_k^i		
	i=1 (splash fill)	i=2 (trickle fill)	i=3 (film fill)
1	3.179688	7.047319	3.897830
2	1.083916	0.812454	0.777271
3	-1.965418	-1.143846	-2.114727
4	0.639088	2.677231	15.327472
5	0.684936	0.294827	0.215975
6	0.642767	1.018498	0.079696

Table 2. Constants for loss coefficients

$$\Delta P_{fi} = K_{fi} L_{fi} \frac{mav_m^2}{2\rho_m A_{fr}^2} \tag{44}$$

Here ρ_m is the harmonic mean air vapor flow rate through the fill, mav_m is an average air-vapor flow rate, calculated from:

$$mav_m = \frac{mav_{in} + mav_{out}}{2} \tag{45}$$

$$\rho_m = 1/\left(1/\rho_{in} + 1/\rho_{out}\right) \tag{46}$$

$$mav_{in} = m_a + w_{in} m_a \tag{47}$$

$$mav_{out} = m_a + w_{out} m_a \tag{48}$$

where ρ_{in} and ρ_{out} are the inlet and outlet air density, respectively. The miscellaneous pressure drop is calculated as follows:

$$\Delta P_{misc} = 6.5 \frac{mav_m^2}{2\rho_m A_{fr}^2} \tag{49}$$

The other part is the dynamic pressure drop. According to Li & Priddy (1985), it is equal to 2/3 of the static pressure drop,

$$\Delta P_{vp} = (2/3)\left(\Delta P_{fi} + \Delta P_{misc}\right) \tag{50}$$

Combining equations (44), (49) and (50), the total pressure drop is,

$$\Delta P_t = 1.667\left(\Delta P_{fi} + \Delta P_{misc}\right) \tag{51}$$

3.2.4 Power demand

The power requirements for the fan (*HP*) can be calculated by multiplying the total pressure drop times the volumetric flow rate, which depends on the localization of the fan. For mechanical draft cooling towers we have (Serna-González et al., 2010):

$$HP = \frac{mav_{in}\Delta P_t}{\rho_{in}\eta_f} \tag{52}$$

where η_f is the fan efficiency.

3.2.5 Water consumption

In cooling towers, water losses are due to the water evaporated ($m_{w,ev}$), the drift water for air flow rate ($m_{w,d}$), and the blowdown ($m_{w,b}$) to avoid salts deposition,

$$m_{w,ev} = m_a\left(w_{out} - w_{in}\right) \tag{53}$$

$$m_{w,b} = \frac{m_{w,r}}{n_{cycle}} - m_{w,d} \tag{54}$$

where n_{cycle} is the number of concentration cycles that are required. Usually n_{cycle} has a value between 2 and 4 (Li & Priddy, 1985). For an efficient design, the loss for drift should not be higher than 0.2% of the total water flow rate (Kemmer, 1988),

$$m_{w,d} = 0.002 m_{wi,n} \tag{55}$$

Combining Equations (53), (54) and (55), we can calculate the water consumption ($m_{w,r}$) as,

$$m_{w,r} = \frac{n_{cycle} m_{w,ev}}{n_{cycle} - 1} \tag{56}$$

3.2.6 Feasibility constraints

The temperature difference between the water at the outlet and the wet-bulb temperature of the air entering the tower is called the tower approach. In practice, the water outlet temperature should be at least 2.8°C above the wet-bulb temperature (Li & Priddy, 1985),

$$T_{w,out} - T_{wb,in} \geq 2.8 \tag{57}$$

The dry bulb air temperature should be higher than the wet bulb air temperature through the packing at least in the last integration interval (NTI),

$$T_{a,n} \geq T_{wb,n} + \Delta T_{n \neq NTI} \tag{58}$$

From thermodynamic principles, the outlet water temperature from the cooling tower should be lower than the lowest outlet process stream of the cooling network, and the inlet water temperature to the cooling tower cannot be higher than the hottest inlet process stream in the cooling network. Additionally, to avoid pipe fouling, a maximum temperature of 50°C is usually specified for the water entering the cooling tower (Douglas, 1988),

$$T_{w,in} \leq TMPI - DTMIN \tag{59}$$

$$T_{w,out} \leq TMPO - DTMIN \tag{60}$$

$$T_{w,in} \leq 50^{\circ} C \tag{61}$$

Here $TMPO$ is the outlet temperature of the coldest hot process streams in the cooling network, $TMPI$ is the inlet temperature of the hottest hot process stream in the cooling network, and $DTMIN$ is the minimum allowable temperature difference. Although cooling towers can be designed for any ratio of the mass flow rate, designers suggest the following limits (Singham, 1983):

$$0.5 \leq \frac{m_{w,m}}{m_a} \leq 2.5 \tag{62}$$

The correlations for the transfer and loss coefficients are limited to (Kloppers & Kröger, 2003, 2005c),

$$2.90 \leq \frac{m_{w,m}}{A_{fr}} \leq 5.96 \tag{63}$$

$$1.20 \leq \frac{m_a}{A_{fr}} \leq 4.25 \tag{64}$$

3.2.7 Objective function

The objective function is the minimization of the total annual cost (TAC), which consists of the capital annualized cost (CAP) and operational costs (COP),

$$TAC = K_F CAP + COP \tag{65}$$

where K_F is an annualization factor. Water consumption and power requirements determine the operational costs, and they are calculated using the following relationship,

$$COP = H_Y cu_w m_{w,r} + H_Y cu_e HP \tag{66}$$

where H_Y is the annual operating time, cu_w is the unit cost of fresh water, and cu_e is the unit cost of electricity. The capital cost for the cooling tower depends on the fixed cooling tower cost (C_{CTF}), packing volume and air flow rate (Kintner-Meyer & Emery, 1995),

$$CAP = C_{CTF} + C_{CTV} A_{fr} L_{fi} + C_{CTMA} m_a \tag{67}$$

C_{CTV} depends on the type of packing; therefore, the following disjunction, along with a convex hull reformulation (Vicchietti et al., 2003), is used:

$$\begin{bmatrix} Y^1 \\ (splash\ fill) \\ C_{CTV} = C^1_{CTV} \end{bmatrix} \vee \begin{bmatrix} Y^2 \\ (trickle\ fill) \\ C_{CTV} = C^2_{CTV} \end{bmatrix} \vee \begin{bmatrix} Y^3 \\ (film\ fill) \\ C_{CTV} = C^3_{CTV} \end{bmatrix}$$

$$C_{CTV} = C^1_{CTV} + C^2_{CTV} + C^3_{CTV} \tag{68}$$

$$C^i_{CTV} = e^i\, y^i, \quad i = 1,...,3 \tag{69}$$

Common values for unit costs e^i are reported in Table 3.

	i=1	i=2	i=3
e^i	(splash fill)	(trickle fill)	(film fill)
	2,006.6	1812.25	1,606.15

Table 3. Cost coefficients C^k_{CTV} for each type of fill

The proposed model consists of equations (4) to (69), plus the discretization of the governing equations and the relationships to estimate of physical properties presented in Appendix A. The model was implemented in the software GAMS (Brooke et al., 2006) and it was solved using the DICOPT solver.

4. Results and discussion

To demonstrate the application of the proposed model, six case studies taken from Serna-González et al. (2010) were considered. The values for the parameters H_Y, K_F, n_{cycles}, cu_w, cu_e, C_{CTF}, C_{CTMA}, η_f and P_t, are 8150 hr/year, 0.2983 year^{-1}, 4, 5.283 x 10^{-04} US$/kg-water, 0.085 US$/kWh, 31185 US$, 1097.5 US$s/kg-dry-air, 0.75 and 101325 Pa, respectively. In addition, 25 intervals to discretize the differential equations were used. The results obtained are compared with the ones reported by Serna-González et al. (2010), where the Merkel method was used to represent the behavior of the cooling tower. Tables 4 and 5 show the results obtained using the Merkel (Merkel, 1926) and Poppe models (Pope & Rögener, 1991). For examples 1, 3, 4 and 6, the designs obtained using the Poppe's method are cheaper because of low operating costs, which depend on the makeup water cost and power cost. The effect of the air flowrate and ranges over evaporated water rate is shown in Figures 6a and 6b; it can be observed how the relation between air flowrate and the range generates the optimum evaporative rate. Figure 7 presents a sensibility analysis on the evaporative rate with respect to the air flowrate and range; notice the higher impact of the range factor.

The prediction of power fan cost using the Poppe's method is higher than with the Merkel´s method because more air is estimated for the same range; this means that the cooling capacity of the inlet air in the Merkel´s method is overestimated and the outlet air is oversaturated. This is proved by the solution of Equations (1)-(3) using the results obtained ($T_{w,in}$, $T_{w,out}$, $m_{w,in}$ and m_a) from the Merkel´s method, and plotting the dry and wet bulb air temperatures for the solution intervals. Notice in Figure 6 that the air saturation ($T_{wb} \geq T_a$) is obtained before of the outlet point of the packing section.

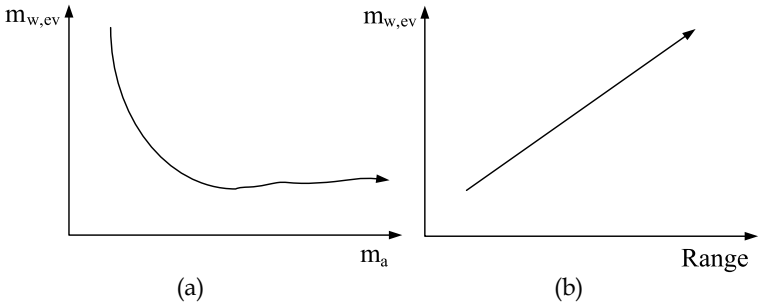

Fig. 6. Evaporate profile respect to air flow rate and range

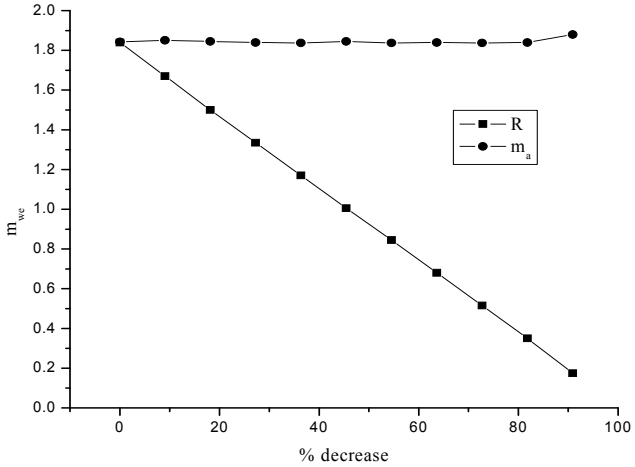

Fig. 7. Sensitivity analysis of the evaporate rate with respect to air flowrate and range

With respect to the capital cost for cases 1 and 6, the estimations obtained using the Poppe's method are more expensive because of the higher air flowrate, area and height packing. However, for examples 3 and 4 both capital and operating costs are predicted at lower levels with the Poppe's method; the capital cost is lower because the inlet air is relatively dry and therefore it can process higher ranges with low air flowrates, which requires a lower packing volume. This can be explained because of the effect that the range and air flow rate have in the packing volume, and the effect that the range has in the capital cost of the towers

(see Figure 8a, 8b and 8c). Notice in Figure 9 that there exists an optimum value for the range to determine the minimum capital cost.

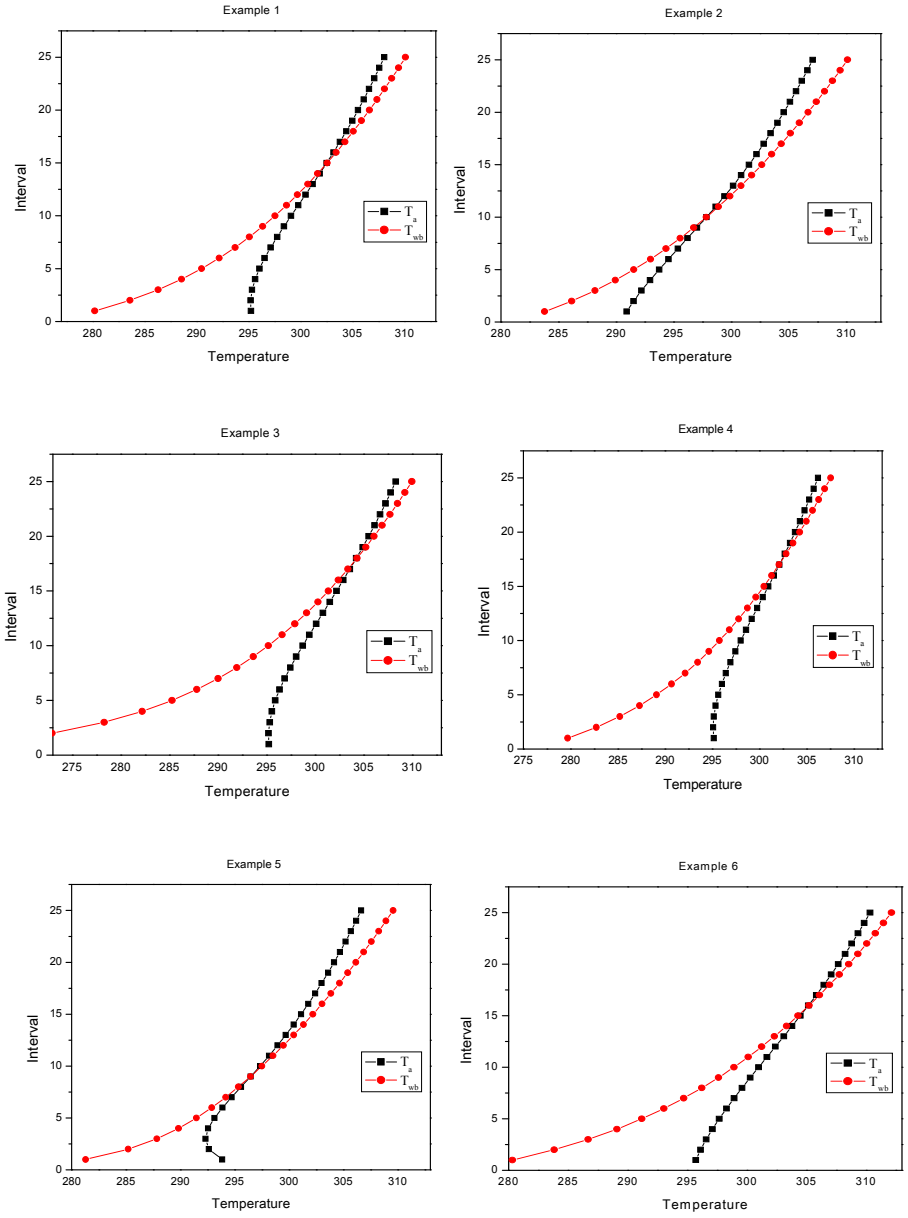

Fig. 8. Air temperature profile in the packing section

		Examples					
		1		2		3	
		Merkel	Poppe	Merkel	Poppe	Merkel	Poppe
DATA	Q (kW)	3400	3400	3400	3400	3400	3400
	$T_{a,in}$ (°C)	22	22	17	17	22	22
	$T_{wb,in}$ (°C)	12	12	12	12	7	7
	TMPI (°C)	65	65	65	65	65	65
	TMPO (°C)	30	30	30	30	30	30
	DTMIN (°C)	10	10	10	10	10	10
	w_{in} (kg water/kg dry air)	0.0047	0.0047	0.0067	0.0067	0.0002	0.0002
RESULTS	$T_{w,in}$ (°C)	50	38.8866	50	29.5566	50	45.4517
	$T_{w,out}$ (°C)	20	20	20	20	20	20
	$m_{w,in}$ (kg/s)	25.720	29.9843	25.794	60.0479	25.700	22.1726
	m_a (kg/s)	31.014	43.2373	31.443	71.2273	28.199	31.4714
	$m_{w,m}/m_a$ (kg/s)	0.829	0.6824	0.820	0.8358	0.911	0.6897
	$m_{w,r}$ (kg/s)	1.541	1.1234	1.456	1.0492	1.564	1.1268
	$m_{w,e}$ (kg/s)	1.156	0.8425	1.092	0.7869	1.173	0.8451
	$T_{a,out}$ (kg/s)	37.077	28.3876	36.871	23.3112	36.998	30.2830
	Range (°C)	30.00	18.8866	30.00	9.5566	30.00	25.4517
	Approach (°C)	8	8	8	8	13	13
	A_{fr} (m^2)	8.869	10.1735	8.894	20.5291	8.862	7.4847
	L_{fi} (m)	2.294	1.2730	2.239	0.9893	1.858	1.0631
	P (hP)	24.637	29.7339	24.474	25.6701	15.205	18.2297
	Fill type	Film	Film	Film	Film	Film	Film
	NTU	3.083	2.3677	3.055	1.6901	2.466	2.0671
	Makeup water cost (US$/year)	23885.1	17412.4	22566.4	16262.7	24239.8	17465.3
	Power fan cost (US$/year)	12737.6	32785.4	12653.7	13271.9	7861.0	9425.1
	Operation cost (US$/year)	36622.7	32785.4	35220.0	29534.7	32100.8	26890.4
	Capital cost (US$/year)	29442.4	29866.7	29384.6	42637.0	26616.0	23558.2
	Total annual cost (US$/year)	**66065.1**	**62652.1**	**64604.6**	**72171.7**	**58716.8**	**50448.6**

Table 4. Results for Examples 1, 2 and 3

		Examples					
		4		5		6	
		Merkel	Poppe	Merkel	Poppe	Merkel	Poppe
DATA	Q (kW)	3400	3400	3400	3400	3400	3400
	$T_{a,in}$ (°C)	22	22	22	22	22	22
	$T_{wb,in}$ (°C)	12	12	12	12	12	12
	TMPI (°C)	55	55	65	65	65	65
	TMPO (°C)	30	30	25	25	30	30
	DTMIN (°C)	10	10	10	10	10	10
	w_{in} (kg water/kg dry air)	0.0047	0.0047	0.0047	0.0047	0.0047	0.0047
RESULTS	$T_{w,in}$ (°C)	45	38.8866	50	24.1476	50	42.9877
	$T_{w,out}$ (°C)	20	20	15	15	25	25
	$m_{w,in}$ (kg/s)	30.973	29.9843	22.127	59.2602	30.749	31.0874
	m_a (kg/s)	36.950	43.2373	32.428	85.9841	27.205	35.8909
	$m_{w,m}/m_a$ (kg/s)	0.838	0.6824	0.682	0.6824	1.130	0.8530
	$m_{w,r}$ (kg/s)	1.547	1.1234	1.542	1.2539	1.540	1.0960
	$m_{w,e}$ (kg/s)	1.160	0.8425	1.157	0.9404	1.155	0.8220
	$T_{a,out}$ (kg/s)	34.511	28.3876	36.411	21.2441	39.083	30.6240
	Range (°C)	25.00	18.8866	35.00	9.1476	25.00	17.9877
	Approach (°C)	8	8	3	3	13	13
	A_{fr} (m^2)	10.680	10.1735	7.630	20.2316	9.296	10.5566
	L_{fi} (m)	2.154	1.2730	6.299	3.0518	1.480	0.7831
	P (hP)	26.852	29.7339	97.077	123.3676	10.754	10.9003
	Fill type	Film	Film	Film	Film	Film	Film
	NTU	2.293	2.3677	7.335	4.3938	1.858	1.4101
	Makeup water cost (US$/year)	23983.4	17412.4	23901.7	19435.6	23865.9	16988.0
	Power fan cost (US$/year)	13882.8	32785.4	50190.5	63783.4	5559.9	5635.7
	Operation cost (US$/year)	37866.2	32785.4	74092.2	83218.9	29425.8	22623.7
	Capital cost (US$/year)	32667.7	29866.7	43186.5	67320.6	25030.3	25202.8
	Total annual cost (US$/year)	**70533.9**	**62652.1**	**117278.7**	**150539.6**	**54456.0**	**47826.5**

Table 5. Results for Examples 4, 5 and 6

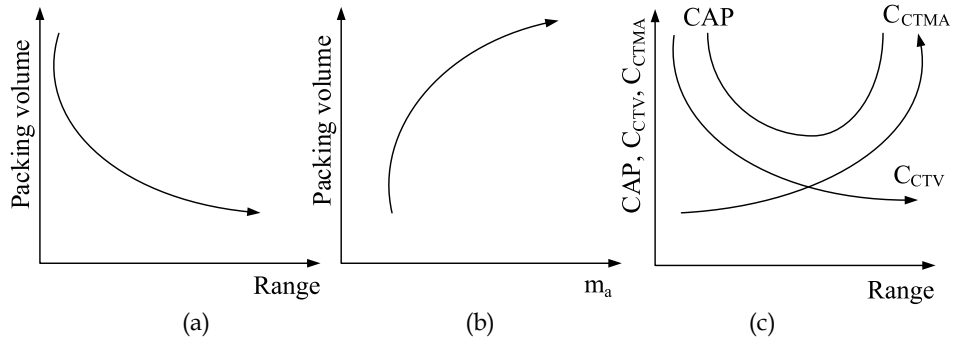

Fig. 9. Effect of range and air flow rate over packing volume and capital cost

For Examples 2 and 5, the designs obtained using the Merkel´s method are cheaper than the ones obtained using the Poppe´s model; this is because the lower capital cost estimation. In Example 2 there is a high inlet wet air temperature and therefore air with poor cooling capacity, whereas in Example 5 there is a low outlet water temperature with respect to the wet bulb air temperature, which reduces the heat transfer efficiency (see Figure 10).

To demostrate that the Merkel´s method is less acurate, one can see cases 1 and 4, in which the inlet air conditions are the sames but the maximum allowable temperatures are 50°C and 45°C. For the Merkel´s method the designs show the maximum possible range for each case; however, the design obtained from the Poppe's method are the same because the inlet air conditions determine the cooling capacity.

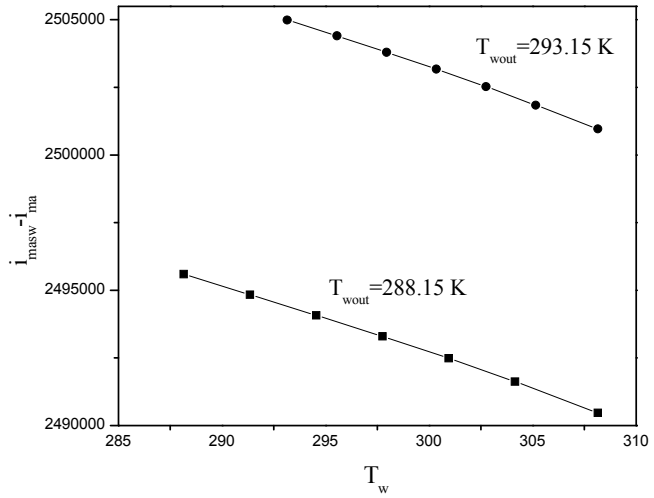

Fig. 10. Effect of the outlet water temperature over driving force

5. Conclusions

A mixer integer nonlinear programming model for the optimal detailed design of counter-flow cooling towers has been presented. The physical properties and the transport phenomena paramenters are rigorously modeled for a proper prediction. The objective function consists of the minimization of the total annual cost, which considers operating and capital costs. Results show that low wet temperatures for the air inlet and high ranges favor optimal designs. The operating costs are proportional to the range, and the capital costs require an optimal relation between a high range and a low air flow rate; therefore, the strongest impact of the physical representation of the transport phenomenal is over the capital cost. For all cases analyzed here the minimum possible area was obtained, which means that the packing area is a major variable affecting the total annual cost. The cooling capacity of the inlet air determines the optimum relation between range and air flowrate. Since the model here presented is a non-convex problem, the results obtained can only guaranty local optimal solutions. Global optimization techniques must be used if a global optimal solution is of primary importance.

6. Appendix A

The relationships for physical properties were taken from Kröger [25]. All temperatures are expressed in degrees Kelvin. The enthalpy of the air-water vapor mixture per unit mass of dry-air is:

$$i_{ma} = cp_a\left(T_a - 273.15\right) + w\left[i_{fgwo} + cp_v\left(T_a - 273.15\right)\right] \tag{A.1}$$

The enthalpy for the water vapor is estimated from:

$$i_v = i_{fgwo} + cp_{v,w}\left(T_w - 273.15\right) \tag{A.2}$$

The enthalpy of saturated air evaluated at water temperature is:

$$i_{ma,s,w} = cp_{a,w}\left(T_w - 273.15\right) + w_{s,w}\left[i_{fgwo} + cp_{v,w}\left(T_w - 273.15\right)\right] \tag{A.3}$$

The specific heat at constant pressure is determined by:

$$cp_a = 1.045356x10^3 - 3.161783x10^{-1}T + 7.083814x10^{-4}T^2 - 2.705209x10^{-7}T^3 \tag{A.4}$$

Specific heat of saturated water vapor is determined by:

$$cp_v = 1.3605x10^3 + 2.31334T - 2.46784x10^{-10}T^5 + 5.91332x10^{-13}T^6 \tag{A.5}$$

The latent heat for water is obtained from:

$$i_{fgwo} = 3.4831814x10^6 - 5.8627703x10^3T + 12.139568T^2 - 1.40290431x10^{-2}T^3 \tag{A.6}$$

The specific heat of water is:

$$cp_w = 8.15599x10^3 - 2.80627x10T + 5.11283x10^{-2}T^2 - 2.17582x10^{-13}T^6 \tag{A.7}$$

The humidity ratio is calculated from:

$$w = \left(\frac{2501.6 - 2.3263\left(T_{wb} - 273.15\right)}{2501.6 + 1.8577\left(T - 273.15\right) - 4.184\left(T_{wb} - 273.15\right)} \right) \left(\frac{0.62509 P_{v,wb}}{P_t - 1.005 P_{v,wb}} \right) - \left(\frac{1.00416\left(T - T_{wb}\right)}{2501.6 + 1.8577\left(T - 273.15\right) - 4.184\left(T_{wb} - 273.15\right)} \right) \tag{A.8}$$

The vapor pressure is:

$$P_v = 10^z \tag{A.9}$$

$$z = 10.79586\left(1 - \frac{273.16}{T}\right) + 5.02808 \log_{10}\left(\frac{273.16}{T}\right) + 1.50474 x 10^{-4}\left[1 - 10^{-8.29692\left[\left(\frac{T}{273.16} - 1\right)\right]}\right] + 4.2873 x 10^{-4}\left[10^{4.7695\left(1 - \frac{273.16}{T}\right)} - 1\right] + 2.786118312 \tag{A.10}$$

7. Nomenclature

a_j^i	disaggregated coefficients for the estimation of NTU
A_{fr}	cross-sectional packing area, m²
b_k^i	disaggregated coefficients for the estimation of loss coefficient
c_1-c_5	correlation coefficients for the estimation of NTU
CAP	capital cost, US$/year
C_{CTF}	fixed cooling tower cost, US$
C_{CTMA}	incremental cooling tower cost based on air mass flow rate, US$ s/kg
C_{CTV}	incremental cooling tower cost based on tower fill volume, US$/m³
C_{CTV}^i	disaggregated variables for the capital cost coefficients of cooling towers
COP	annual operating cost, US$/year
c_j	variables for NTU calculation
c_j^i	disaggregated variables for NTU calculation
cp_a	specific heat at constant pressure, J/kg-K
cp_v	specific heat of saturated water vapor, J/kg-K
cp_w	specific heat of water, J/kg-K
$cp_{w,in}$	specific heat of water in the inlet of cooling tower, J/kg-K
$cp_{w,out}$	specific heat of water in the outlet of cooling tower, J/kg-K
cu_e	unitary cost of electricity, US$/kW-h
cu_w	unitary cost of fresh water, US$/kg
d_1-d_6	correlation coefficients for the estimation of loss coefficient, dimensionless
d_k	variables used in the calculation of the loss coefficient

d_k^i	disaggregated variables for the calculation of the loss coefficient
$DTMIN$	minimum allowable temperature difference, ^oC or K
e^i	coefficient cost for different fill type
H_Y	yearly operating time, hr/year
HP	power fan, HP
i_{fgwo}	heat latent of water, J/kg
i_{ma}	enthalpy of the air-water vapor mixture per mass of dry-air, J/kg dry-air
$i_{ma,s,w}$	enthalpy of saturated air evaluated at water temperature, J/kg dry-air
i_v	enthalpy of the water vapor, J/kg dry-air
J	recursive relation for air ratio humidity
K	recursive relation for air enthalpy
K_{fi}	loss coefficient in the fill, m^{-1}
K_F	annualization factor, $year^{-1}$
K_{misc}	component loss coefficient, dimensionless
L	recursive relation for number of transfer units
L_{fi}	fill height, m
Lef	Lewis factor, dimensionless
m_a	air mass flow rate, kg/s
mav_{in}	inlet air-vapor flow rate, kg/s
mav_m	mean air-vapor flow rate, kg/s
mav_{out}	outlet air-vapor flow rate, kg/s
m_w	water mass flow rate, kg/s
$m_{w,b}$	blowdown water mass flow rate, kg/s
$m_{w,d}$	drift water mass flow rate, kg/s
$m_{w,ev}$	mass flow rate for the evaporated water, kg/s
$m_{w,in}$	inlet water mass flow rate in the cooling tower, kg/s
$m_{w,m}$	average water mass flow rate in the cooling tower, kg/s
$m_{w,out}$	outlet water mass flow rate from the cooling tower, kg/s
$m_{w,r}$	makeup water mass flow rate, kg/s
NTU	number of transfer units, dimensionless
n_{cycle}	number of cycles of concentration, dimensionless
P	vapor pressure, Pa
P_t	total vapor pressure, Pa
$P_{v,wb}$	saturated vapor pressure, Pa
Q	heat load, W or kW
T_a	dry-bulb air temperature, ^oC or K
TAC	total annual cost, US$/year
$T_{a,n}$	dry-bulb air temperature in the integration intervals, ^oC or K
$TMPI$	inlet of the hottest hot process stream, ^oC or K
$TMPO$	inlet temperature of the coldest hot process streams, ^oC or K
T_w	water temperature, ^oC or K
T_{wb}	wet-bulb air temperature, ^oC or K

$T_{wb,in}$	inlet wet-bulb air temperature in the cooling tower, °C or K
$T_{wb,n}$	wet-bulb air temperature in the integration intervals, °C or K
$T_{w,in}$	inlet water temperature in the cooling tower, °C or K
$T_{w,out}$	outlet water temperature in the cooling tower, °C or K
w	mass-fraction humidity of moist air, kg of water/kg of dry-air
w_{in}	inlet humidity ratio in the cooling tower, kg of water/kg of dry-air
w_{out}	outlet humidity ratio in the cooling tower, kg of water/kg of dry-air
$w_{s,w}$	humidity saturated ratio, kg of water/kg of dry-air

7.1 Binary variables

y^k	used to select the type of fill

7.2 Greek symbols

ΔP_t	total pressure drop, Pa
ΔP_{vp}	dynamic pressure drop, Pa
ΔP_{fi}	fill pressure drop, Pa
ΔP_{misc}	miscellaneous pressure drop, Pa
η_f	fan efficiency, dimensionless
ρ_{in}	inlet air density, kg/m^3
ρ_m	harmonic mean density of air-water vapor mixtures, kg/m^3
ρ_{out}	outlet air density, kg/m^3

7.3 Subscripts

a	dry air
b	blowdown water
d	drift water
e	electricity
ev	evaporated water
f	fan
fi	packing or fill
fr	cross-sectional
in	inlet
j	constants to calculate the transfer coefficient depending of the fill type
k	constants to calculate the loss coefficient depending of the fill type
m	average
ma	air-vapor mixture
$misc$	miscellaneous
n	integration interval
out	outlet
r	makeup

s	saturated
t	total
v	water vapor
vp	velocity pressure
w	water
wb	wet-bulb temperature

7.4 Superscripts

i	fill type, *i*=1, 2, 3

8. References

Brooke, A., Kendrick, D., Meeraus, A. & Raman, R. (2006). *GAMS User's Guide* (edition), The Scientific Press, USA.

Burden, R.L. & Faires, J.D. (2005). *Numerycal Analysis* (8th edition), Brooks/Cole Publishing Company, ISBN 9780534392000, California, USA.

Chengqin, R. (2006). An analytical approach to the heat and mass transfer processes in counterflow cooling towers. *Journal of Heat Transfer*, Vol. 128, No. 11, (November 2006), pp. 1142-1148, ISSN 0022-1481.

Cheng-Qin, R. (2008). Corrections to the simple effectiveness-NTU method for counterflow cooling towers and packed bed liquid desiccant-air contact systems. *International Journal of Heat and Mass Transfer*, Vol. 51, No. 1-2, (January 2008), pp. 237-245, ISSN 0017-9310.

Douglas, J.M. (1988). Conceptual Design of Chemical Processes, McGraw-Hill, ISBN 0070177627, New, York, USA.

Foust A.S.; Wenzel, L.A.; Clump, C.W.; Maus, L. & Anderson, L.B. (1979). *Principles of Unit Operations* (2nd edition), John Wiley & Sons, ISBN 0471268976, New, York, USA.

Jaber, H. & Webb, R.L. (1989). Design of cooling towers by the effectiveness-NTU Method. *Journal of Heat Transfer*, Vol. 111, No. 4, (November 1989), pp. 837-843, ISSN 0022-1481.

Kemmer, F.N. (1988). *The NALCO water handbook* (second edition). McGraw-Hill, ISBN 1591244781, New, York, USA.

Kintner-Meyer, M. & Emery, A.F. (1995). Cost-optimal design for cooling towers. *ASHRAE Journal*, Vol. 37, No. 4, (April 1995), pp. 46-55. ISSN 0001-2491.

Kloppers, J.C. & Kröger, D.G. (2003). Loss coefficient correlation for wet-cooling tower fills. *Applied Thermal Engineering*. Vol. 23, No. 17, (December 2003), pp. 2201-2211. ISSN 1359-4311.

Kloppers, J.C. & Kröger, D.G. (2005a). Cooling tower performance evaluation: Merkel, Poppe, and e-NTU methods analysis. *Journal of Engineering for Gas Turbines and Power*, Vol. 127, No. 1, (January 2005), pp. 1-7, ISSN 0742-4795.

Kloppers, J.C. & Kröger, D.G. (2005b). A critical investigation into the heat and mass transfer analysis of counterflow wet-cooling towers. *International Journal of Heat and Mass Transfer*, Vol. 48, No. 3-4, (January 2005), pp. 765-777, ISSN 0017-9310.

Kloppers, J.C. & Kröger, D.G. (2005c). Refinement of the transfer characteristic correlation of wet-cooling tower fills. *Heat Transfer Engineering*, Vol. 26, No. 4, (May 2005). pp. 35-41, ISSN 0145-7632.

Kröger, D.G. (2004). *Air-Cooled Heat Exchangers and Cooling Towers*. PennWell Corp., ISBN 978-0-87814-896-7, Tulsa, Oklahoma, USA.

Li, K.W. & Priddy, A.P. (1985). *Power Plant System Design* (first edition), John Wiley & Sons, ISBN 978-0-471-88847-5, New, York, USA.

Merkel, F. (1926). Verdunstungskühlung. *VDI Zeitchrift Deustscher Ingenieure*, Vol. 70, pp. 123-128.

Mills, A. E. (1999). *Basic Heat and Mass Transfer* (2nd edition), Prentice Hall, ISBN 0130962473, N.J., USA.

Nahavandi, A.N.; Rashid, M.K. & Benjamin, J.S. (1975). The effect of evaporation losses in the analysis of counterflow cooling towers. *Nuclear Engineering and Design*, Vol. 32, No. 1, (April 1975), pp. 29-36, ISSN 0029-5493.

Olander, D.R. (1961). Design of direct cooler-condensers. *Industrial and Engineering Chemistry*, Vol. 53, No. 2, (February 1961), pp. 121-126, ISSN 0019-7866.

Oluwasola, O. (1987). A procedure for computer-aided design of water-cooling towers, *The Chemical Engineering Journal*, Vol. 35, No. 1, (May 1987), pp. 43-50, ISSN 1385-8947.

Osterle, F. (1991). On the analysis of counter-flow cooling towers. *International Journal of Heat and Mass Transfer*, Vol. 34, No. 4-5, (April-May 1991), pp. 1313-1316, ISSN 0017-9310.

Ponce-Ortega, J.M.; Serna-González, M. & Jiménez-Gutiérrez, A. (2010). Optimization model for re-circulating cooling water systems. *Computers and Chemical Engineering*, Vol. 34, No. 2, (February 2010), pp. 177-195, ISSN 0098-1354.

Poppe, M. & Rögener, H. (1991). Berechnung von Rückkühlwerken. *VDI-Wärmeatlas*, pp. Mi 1-Mi 15.

Roth, M. (2001). Fundamentals of heat and mass transfer in wet cooling towers. All well known or are further development necessary. *Proceedings of 12th IAHR Cooling Tower and Heat Exchangers*, pp. 100-107, UTS, Sydney, Australia, November 11-14, 2001.

Rubio-Castro, E.; Ponce-Ortega, J.M.; Nápoles-Rivera, F.; El-Halwagi, M.M.; Serna-González, M. & Jiménez-Gutiérrez, A. (2010). Water integration of eco-industrial parks using a global optimization approach. *Industrial and Engineering Chemistry Research*, Vol. 49, No. 20, (September 2010), pp. 9945-9960, ISSN 0888-5885.

Serna-González, M.; Ponce-Ortega, J.M. & Jiménez-Gutiérrez, A. (2010). MINLP optimization of mechanical draft counter flow wet-cooling towers. *Chemical Engineering and Design*, Vol. 88, No. 5-6, (May-June 2010), pp. 614-625, ISSN 0263-8762.

Singham, J.R. (1983). *Heat Exchanger Design Handbook*, Hemisphere Publishing Corporation, USA.

Söylemez, M.S. (2001). On the optimum sizing of cooling towers. *Energy Conversion and Management*, Vol. 42, No. 7, (May 2001), pp. 783-789, ISSN 0196-8904.

Söylemez, M.S. (2004). On the optimum performance of forced draft counter flow cooling towers. *Energy Conversion and Management*, Vol. 45, No. 15-16, (September 2004), pp. 2335-2341, ISSN 0196-8904.

Vicchietti, A.; Lee, S. & Grossmann, I.E. (2003). Modeling of discrete/continuous optimization problems characterization and formulation of disjunctions and their relaxations. *Computers and Chemical Engineering*, Vol. 27, No. 3, (March 2003), pp. 433-448, ISSN 0098-1354.

7

Some Problems Related to Mathematical Modelling of Mass Transfer Exemplified of Convection Drying of Biological Materials

Krzysztof Górnicki and Agnieszka Kaleta
Warsaw University of Life Sciences, Faculty of Production Engineering
Poland

1. Introduction

Drying is a widely used industrial process, consuming 7-15% of total industrial energy production in the industrialized world (Dincer & Dost, 1996). Drying is one of the most common and the oldest ways of biological materials preservation such as vegetables and fruits. The main objective in drying biological materials is the removal of water in the solids up to a certain level, at which microbial spoilage and deterioration chemical reactions are greatly minimalized.

The most important aspect of drying technology is the mathematical modelling of the drying processes and the equipment. Its purpose is to allow design engineers to choose the most suitable operating conditions and then size the drying equipment and drying chamber accordingly to meet desired operating conditions. Full-scale experimentation for different products and systems configurations is sometimes costly or even not possible (Sacilik et al., 2006).

Convection drying of biological products is a complex process that involves heat and mass transfer phenomena between the airflow and the product. Mathematical modelling of the drying process of vegetables, fruits and grass is especially difficult because of high initial moisture content (80-95% w.b.) and occurrence of shrinkage during drying.

The course and time of drying process depend on drying conditions, on temperature and moisture profiles developed during the drying process, and above all, on moisture movement in the material. Moisture movement is governed by the properties, form and size of the product and the type of moisture bond in the material (Sander et al., 2003). The major factors affecting the moisture transport during solids drying can be classified as:

i. external factors: these are the factors related to the properties of the surrounding air such as temperature, pressure, humidity, velocity and area of the exposed surface,
ii. internal factors: these are the parameters related to the properties of the material such as moisture diffusivity, moisture transfer coefficient, water activity, structure and composition, etc. (Dincer & Hussain, 2004).

The development of mathematical models to describe the drying process has been the topic of many research studies for several decades (Sander et al., 2003). Presently, more and more sophisticated drying models are becoming available, but a major question that still remains is the accuracy of predictions of drying processes using mathematical models. It is highly

dependent on the completeness of the mathematical model and the relationships used to describe heat and mass transfer phenomena of dried products. However, professional literature provides insufficient information on the mathematical modelling of mass transfer during drying of biological materials with a high initial moisture content. Therefore, the aim of the present chapter was to discuss in detail the main problems related to description of the drying process of such materials using differential transport equations.

2. Differential transport equations for drying

According to the theory of convection drying of bodies with sufficiently high initial moisture content, the process of convection drying should proceed in the first period of drying until the critical moisture content is reached. The factors that influence the drying process in the first period of drying are the conditions of external heat and mass exchange in the system: drying product and surrounding air movement. For the case when moisture content of the body is less than its critical moisture content, the second period of drying begins. The process is decided by internal conditions of mass exchange and inner diffusion of water because the internal resistance to water transfer in the body is greater than the external resistance to water transfer from the body (Pabis, 1999; Pabis & Jaros, 2002).

2.1 The first drying period

The course of the drying process at the first drying period is decided by external conditions of mass transfer. In this period the rate of drying is determined by the following equation (Pabis, 1999):

$$\frac{dM}{dt} = -\frac{hA_0}{W_s L}\left(T_a - T_A\right) = -k = \text{const} \tag{1}$$

Eq. (1) resulted from the assumption that all heat delivered to the solid being dried at the first drying period is used for vaporizing water. The solution of Eq. (1) with the assumption valid for the first period of drying

$$T_A = T_{wb} \tag{2}$$

with initial condition $M(t=0)=M_0$ and with assumption that all parameters on the right side of Eq. (1) are constant is the linear model

$$M(t) = -kt + M_0 \tag{3}$$

The linear model means the acceptance of the assumption that the shrinkage can be neglected. Biological materials with a high initial moisture content undergo, however, shrinkage and deformation during hot-air drying. When water is removed from such a material, a pressure unbalance is produced between the inner of the material and the external pressure, generating contracting stresses that lead to material shrinkage or collapse, changes in shape and occasionally cracking of the product. Mayor and Sereno (2004) gave a detailed physical description of the shrinkage mechanism and presented a classification of the different models proposed to describe this behaviour in materials with high initial moisture content undergoing drying. The models were classified in two main groups: empirical and fundamental models. Empirical models are convenient and easy to use and

therefore they are mainly applied to drying models. Acceptance of the assumption that the surface of dried body changes because of the shrinkage means that A_0 in Eq. (1) should be replaced by A. The solution of such changed Eq. (1) with assumption (2), initial condition $M(t=0)=M_0$, equation

$$\frac{A}{A_0}=\left(\frac{V}{V_0}\right)^{2/3} \tag{4}$$

and with the use of shrinkage model (Pabis, 1999)

$$\frac{V}{V_0}=(1-b)\frac{M}{M_0}+b \tag{5}$$

is the model of the first drying period which takes into account drying shrinkage

$$M(t)=M_0\left[\frac{1}{1-b}\left(1-\frac{1-b}{3M_0}kt\right)^3-\frac{b}{1-b}\right] \tag{6}$$

$$b=\frac{0.85}{1+M_0} \tag{7}$$

Replacing shrinkage model described with Eq. (5) by model proposed by Karathanos (1993)

$$\frac{V}{V_0}=\left(\frac{M}{M_0}\right)^n \tag{8}$$

gives the following model of the first drying period

$$M(t)=\left[\frac{(2n-3)kt+3M_0}{3M_0^{2n/3}}\right]^{3/(3-2n)} \tag{9}$$

Eq. (4) means that the constancy of the body shape during drying is taken into consideration. However, such a situation not always occur in the case of the drying of biological materials with a high initial moisture content and thus the dependence Eq. (4) should also, for this reason, be regarded as approximate. In this connection, the accuracy of calculation of A can be improved by introducing into Eq. (4) an empirical coefficient $n_1 \geq 1$, which changes Eq. (4) to (Pabis, 1999)

$$\frac{A}{A_0}=\left(\frac{V}{V_0}\right)^{2/3n_1} \tag{10}$$

and Eq. (6) (after substitution of $3n_1/(3n_1-2)=N$) to

$$M(t)=M_0\left[\frac{1}{1-b}\left(1-\frac{1-b}{NM_0}kt\right)^N-\frac{b}{1-b}\right] \tag{11}$$

The parameter k, which occurs in the models of the first drying period, determines the initial drying rate.

2.2 The second period of drying

It can be accepted that the water movement inside the dried solid is only a diffusion movement in the convection drying process of biological materials with a high initial moisture content. Therefore the equation applied to the description of the second drying period of biological materials takes the following form (Luikov, 1970):

$$\frac{\partial M}{\partial t} = D\nabla^2 M \tag{12}$$

Certain simplifications were made in this equation. It was assumed that shape and volume of dried particle do not change, and that water diffusion coefficient is constant. (The discussion how to take into account shrinkage and changeability of the water diffusion coefficient will be conducted in Section 2.3).

The following initial and boundary conditions can be adopted:

i. the initial condition: the same moisture content at any point of dried material at the beginning of the second drying period (material before drying is cut into small pieces and therefore this assumption can be accepted)

$$M\big|_{t=0} = M_c \tag{13}$$

ii. one of the three boundary conditions can be taken:
   - the boundary condition of the first kind means that the external resistance to mass transfer is negligible (i.e., the surface of the solid is at equilibrium with the surrounding air for the time considered) and therefore the moisture content on the solid surface is equal to the equilibrium moisture content

$$M\big|_A = M_e \tag{14}$$

   - the boundary condition of the second kind means that the mass (water) flux from the surface of the solid is known for the time considered

$$\dot{W}\big|_A = f_A(t) \tag{15}$$

   - the boundary condition of the third kind means that the mass (water) flux from the surface of the solid is expressed in terms of moisture content difference between the surface and the equilibrium moisture content

$$-D\frac{\partial M}{\partial n}\bigg|_A = h_m\left(M\big|_A - M_e\right) \tag{16}$$

For the mass transfer at the surface of the biological materials with a high initial moisture content being dried the first kind and the third kind boundary conditions are mostly used in mathematical models of the drying process (Markowski, 1997).

Biological materials before drying are cut into small pieces, mostly slices or cubes. Therefore Eq. (12) applied to the description of the second drying period of biological materials takes the following form (Luikov, 1970):

for an infinite plane (slices):

$$\frac{\partial M}{\partial t} = D\frac{\partial^2 M}{\partial x^2} \qquad \left(t > 0; -R_c < x < +R_c\right) \tag{17}$$

for a finite cylinder (slices):

$$\frac{\partial M}{\partial t} = D\left(\frac{\partial^2 M}{\partial r^2} + \frac{1}{r}\frac{\partial M}{\partial r} + \frac{\partial^2 M}{\partial z^2}\right) \qquad \left(t > 0; 0 < r < R_c; -h < z < +h\right) \tag{18}$$

for cubes:

$$\frac{\partial M}{\partial t} = D\left(\frac{\partial^2 M}{\partial x^2} + \frac{\partial^2 M}{\partial y^2} + \frac{\partial^2 M}{\partial z^2}\right) \qquad \left(t > 0; -R_1 < x < +R_1; -R_2 < y < +R_2; -R_3 < z < +R_3\right) \tag{19}$$

The initial conditions (Eq. (13)) are following:
for an infinite plane

$$M(x,0) = M_c = \text{const.} \tag{20}$$

for a finite cylinder

$$M(r,z,0) = M_c = \text{const.} \tag{21}$$

for cubes

$$M(x,y,z,0) = M_c = \text{const.} \tag{22}$$

The boundary conditions of the third kind (Eq. (16)) take following form:
for an infinite plane

$$\pm D\frac{\partial M(\pm R_c, t)}{\partial x} = h_m\left[M(\pm R_c, t) - M_e\right] \tag{23}$$

for a finite cylinder

$$-D\frac{\partial M(R_c, z, t)}{\partial r} = h_m\left[M(R_c, z, t) - M_e\right] \tag{24}$$

$$\frac{\partial M(0, z, t)}{\partial r} = 0, M(0, z, t) \neq \infty \tag{25}$$

$$-D\frac{\partial M(r, h, t)}{\partial z} = h_m\left[M(r, h, t) - M_e\right] \tag{26}$$

$$\frac{\partial M(r,0,t)}{\partial z}=0 \tag{27}$$

for cubes

$$\pm D\frac{\partial M(\pm R_1,y,z,t)}{\partial x}=h_m\left[M(\pm R_1,y,z,t)-M_e\right] \tag{28}$$

$$\pm D\frac{\partial M(x,\pm R_2,z,t)}{\partial y}=h_m\left[M(x,\pm R_2,z,t)-M_e\right] \tag{29}$$

$$\pm D\frac{\partial M(x,y,\pm R_3,t)}{\partial z}=h_m\left[M(x,y,\pm R_3,t)-M_e\right] \tag{30}$$

An analytical solution of: (i) Eq. (17) at the initial and boundary conditions given by Eqs. (20) and (23), (ii) Eq. (18) at the initial and boundary conditions given by Eqs. (21) and (24)-(27), and (iii) Eq. (19) at the initial and boundary conditions given by Eqs. (22) and (28)-(30) with respect to mean moisture content as a function of time, take the following form (Luikov, 1970):
for an infinite plane

$$\frac{M(t)-M_e}{M_c-M_e}=\sum_{i=1}^{\infty}B_i\exp\left(-\mu_i^2\frac{D}{R_c^2}t\right) \tag{31}$$

where

$$B_i=\frac{2Bi^2}{\mu_i^2\left(Bi^2+Bi+\mu_i^2\right)};\ \operatorname{ctg}\mu_i=\frac{1}{Bi}\mu_i$$

for a finite cylinder

$$\frac{M(t)-M_e}{M_c-M_e}=\sum_{i=1}^{\infty}\sum_{j=1}^{\infty}B_{i,1}B_{j,2}\exp\left[-\left(\frac{\mu_{i,1}^2}{R_c^2}+\frac{\mu_{j,2}^2}{h^2}\right)Dt\right] \tag{32}$$

where

$$B_{i,1}=\frac{2Bi^2}{\mu_{i,1}^2\left(Bi^2+Bi+\mu_{i,1}^2\right)}\qquad B_{j,2}=\frac{2Bi^2}{\mu_{j,2}^2\left(Bi^2+Bi+\mu_{j,2}^2\right)}$$

$$\operatorname{ctg}\mu_{i,1}=\frac{1}{Bi}\mu_{i,1};\ \operatorname{ctg}\mu_{j,2}=\frac{1}{Bi}\mu_{j,2}$$

for cubes

$$\frac{M(t)-M_e}{M_c-M_e}=\sum_{n=1}^{\infty}\sum_{m=1}^{\infty}\sum_{k=1}^{\infty}B_{n,1}B_{m,2}B_{k,3}\times \\ \times\exp\left[-\left(\frac{\mu_{n,1}^2}{R_1^2}+\frac{\mu_{m,2}^2}{R_2^2}+\frac{\mu_{k,3}^2}{R_3^2}\right)Dt\right] \tag{33}$$

where

$$B_{n,1} = \frac{2Bi^2}{\mu_{n,1}^2\left(Bi^2 + Bi + \mu_{n,1}^2\right)} \quad B_{m,2} = \frac{2Bi^2}{\mu_{m,2}^2\left(Bi^2 + Bi + \mu_{m,2}^2\right)}$$

$$B_{k,3} = \frac{2Bi^2}{\mu_{k,3}^2\left(Bi^2 + Bi + \mu_{k,3}^2\right)}$$

$$\text{ctg}\,\mu_{n,1} = \frac{1}{Bi}\mu_{n,1};\ \text{ctg}\,\mu_{m,2} = \frac{1}{Bi}\mu_{m,2};\ \text{ctg}\,\mu_{k,3} = \frac{1}{Bi}\mu_{k,3}$$

and for a cubic geometry $R_1=R_2=R_3$.

In the literature on drying boundary conditions of the first kind are almost always taken into account (it is easier to obtain the solution using such boundary conditions) and like for boundary conditions of the third kind the infinite series constitute appropriate solutions. Several researches showed that for large drying times an analytical solution of Eq. (12) for sphere at the appropriate initial condition and boundary condition of the first kind with respect to mean moisture content, can be reduced to the first term of infinite series (Jayas et al., 1991). Pabis et al. (1998) found the relationship between the optimum number of terms in infinite series and Fourier number for sphere and stated that the optimum number of terms increases with the decreasing value of Fo. González-Fésler et al., (2008) demonstrated that for values of Fourier number Fo ($Fo=Dt/R_c^2$)≥0.1 the mathematical solution for the finite cylinder drying including only the first term of each infinite series represents 95% of the complete solution, so that terms with n>1 could be neglected. The number of terms in analytical solution of Eq. (12) for an infinite plane (at the appropriate initial condition and boundary condition of the first kind with respect to mean moisture content) necessary for calculating the moisture ratio MR with accuracy δ=4% is i=5 for the initial phase of drying (Fo=0), whereas i=20 and i=193 are needed to achieve an accuracy of 1% and 0.1% respectively. The accuracy was defined as $100(M_\infty-M_i)/M_\infty$, where M_∞ and M_i are the exact and truncated solutions, respectively (Efremov et al., 2008).

2.3 Determination of the parameters necessary for using the models of the second drying period

Knowledge of the value of the critical moisture content, equilibrium moisture content, water (moisture) diffusion coefficient, mass transfer coefficient and Biot number is necessary for using model of the second drying period.

The critical moisture content M_c could be determined assuming the continuity of the drying process. The continuity of the process required that when M is equal to M_c, the drying rate in the first and second period be equal, that is when $(dM/dt)_I=(dM/dt)_{II}$ (Jaros & Pabis, 2006). Górnicki & Kaleta (2007a) used the drying rate and the temperature of the dried particle as a criterion of division into the first and the second drying period. The modelling of the second drying period following the first drying period requires introducing into Eqs. (31), (32), and (33) structure of corrected drying time t minus t_c, where t_c is the drying time to the critical moisture content.

Equilibrium moisture content represents the moisture content that the material will attain if dried for an infinite time at a particular relative air humidity and temperature. The relation

between the material moisture content and the relative humidity in equilibrium with the product at the same temperature used to reach the equilibrium is termed the sorption isotherm (the equilibrium moisture content – equilibrium relative humidity relationship). The sorption isotherms of biological and food materials are the sigmoid shape, under the Brunauer classification (Brunauer, 1943) of type II. The existing isotherm equations can be divided into two separate groups: (i) empirical or partly empirical equations using exponential, power or logarithmic functions and (ii) equations with some theoretical basis and/or their combinations (Blahovec, 2004). It turned out that at least seventy seven isotherm equations are available in the literature (van den Berg & Bruin, 1981). The commonly used equations for biological materials are: the Langmuir, Brunauer-Emmett-Teller (BET), Iglesias-Chirife, the modified Henderson, Chen, Chung-Pfost, Halsey, Oswin, and Guggenheim-Anderson-de Boer (GAB) (Rizvi, 1995). The problems related to fitting abilities of the existing isotherm equations for biological materials and selecting the best equations are still under discussion (Castillo et al., 2003; Furmaniak et al., 2007; Kaleta & Górnicki, 2007; Timmermann et al., 2001).

The value of the equilibrium moisture content is relatively small (especially for low air relative humidity) compared to M(t) or M_0 and therefore the dimensionless moisture content (moisture ratio) $MR=[M(t)-M_e]/(M_0-M_e)$ for the whole process of drying could be simplified to $M(t)/M_0$ (Doymaz & Pala, 2002; Zielinska & Markowski, 2007).

In biological materials with a high initial moisture content water can be transported by water diffusion, vapour diffusion, Knudsen diffusion, internal evaporation and condensation effects, capillary flow, and hydrodynamic flow. Often there is a mixture of various transport mechanisms, and the contributions of the different mechanisms to the total transport varies from place to place and changes as drying progresses (Bruin & Luyben, 1980). Therefore the water diffusion coefficient in the model of the second drying period describes the total transport of moisture and is called the effective diffusivity. The values of moisture diffusion coefficient for biological materials reported in the literature lie within the range of 10^{-12} – 10^{-8} m^2s^{-1} (mostly about 10^{-10} m^2s^{-1}) (Doulia et al., 2000; Maroulis et al., 2001). It is known that moisture diffusion coefficient depends strongly on temperature (e.g. Cuningham et al., 2007; Garcia-Pascual et al., 2006; Kaymak-Ertekin, 2002) and often very strongly indeed on the moisture content (e.g. Maroulis et al., 2001; Waananen & Okos, 1996) and on material structure (e.g. Ruiz-Cabrera et al., 1997). Nevertheless, there is no diffusion theory that is sufficiently well formulated and verified. Therefore the most commonly used method for determining the moisture diffusion coefficient in biological materials is by fitting the diffusion-based drying equations to the experimental data in the second drying period. It should be emphasized, however, that moisture diffusion coefficient determined with this method is limited in application to the diffusion-based drying equation from which it was calculated and to the moisture range in which experiments were conducted (Pabis et al., 1998). In the case of shrinkage and changeability of the water diffusion coefficient the coefficient is determined from the diffusion-based drying equation applying the method of inverse problem (Jaros et al., 1992; Górnicki & Kaleta, 2004).

In the literature concerning mathematical modelling of convection drying of biological materials the value of the water diffusion coefficient is mostly considered as a constant. An Arrhenius – type equation is sometimes used to describe the relationship between the diffusion coefficient and temperature of dried material:

$$D = D_0 \exp\left[-E_a R^{-1} \left(T + 273.15 \right)^{-1} \right] \tag{34}$$

Mulet et al. (1989a,b) expressed the water diffusion coefficient by the following empirical formula:

$$D = a \cdot \exp\left[b \left(T + 273.15 \right)^{-1} \right] \tag{35}$$

The water diffusion coefficient as a function of moisture content and dried material temperature was described by Mulet et al. (1989a,b):

$$D = \exp\left[a + b \left(T + 273.15 \right)^{-1} + cM \right] \tag{36}$$

and Parti & Dugmanics (1990):

$$\frac{D}{R^2} = a \cdot \exp\left(\frac{-b}{T + 273.15} + cM \right) \tag{37}$$

Dincer and Dost (1996) developed and verified analytical techniques to characterise the mass transfer during the drying of geometrically (infinite slab, infinite cylinder, sphere) and irregularly (by use of a shape factor) shaped objects. Drying process parameters, namely drying coefficient S and lag factor G:

$$\frac{M(t) - M_e}{M_c - M_e} = G \exp(-St) \tag{38}$$

were introduced based on an analogy between cooling and drying profiles, both of which exhibit an exponential form with time. The moisture diffusivity D was computed using:

$$D = \frac{SR^2}{\mu_1^2} \tag{39}$$

The coefficient μ_1 was determined by evaluating the root of the corresponding characteristic equation (Dincer et al., 2000):
for slab shapes:

$$\mu_1 = -419.24G^4 + 2013G^3 - 3615.8G^2 + 2880.3G - 858.94 \tag{40}$$

for cylindrical shapes:

$$\mu_1 = -3.4775G^4 + 25.285G^3 - 68.43G^2 + 82.468G - 35.638 \tag{41}$$

for spherical shapes:

$$\mu_1 = -8.3256G^4 + 54.842G^3 - 134.01G^2 + 145.83G - 58.124 \tag{42}$$

Babalis & Belessiotis (2004) used the following method of calculation of effective moisture diffusivity. If following assumptions are accepted in Eq. (31):

i. the external mass transfer resistance is negligible, but the internal mass transfer resistance is large (Bi→∞),
ii. the first term of infinite series is taken into account, successive terms are small enough to be neglected,

its simplified form can be expressed as follows:

$$\frac{M(t)-M_e}{M_c-M_e}=\frac{6}{\pi^2}\exp\left(-\pi^2\frac{Dt}{R^2}\right) \tag{43}$$

Logarithmic simplification of Eq. (43) leads to a linear form:

$$\ln\left[\frac{M(t)-M_e}{M_c-M_e}\right]=\ln\left(\frac{6}{\pi^2}\right)-\left(\pi^2\frac{Dt}{R^2}\right) \tag{44}$$

By plotting the measured data plotted in a logarithmic scale, the effective moisture diffusivity was calculated from the slope of the line k_1 as presented:

$$k_1=\frac{\pi^2 D}{R^2} \tag{45}$$

Local mass (water) flux on the external surface A of the dried solid biological material, can be described with the equation (right side of Eq. (16)):

$$\dot{W}=h_m\left(M|_A-M_e\right) \tag{46}$$

The mass transfer coefficient can be determined by the following equations (Markowski, 1997; Simal et al., 2001; Magge et al., 1983):

$$h_m=-\frac{V}{A_w}\frac{\partial\bar{M}/dt}{M|_A-M_e} \tag{47}$$

$$h_m=\frac{4}{2\pi R}D_{wa} \tag{48}$$

$$h_m=aC^bT^c \tag{49}$$

The mass transfer coefficient can be also calculated from the dimensionless Sherwood number Sh. The Sherwood number can be expressed:

i. for forced convection as a function of the Reynolds number Re and the Schmidt number Sc (Beg, 1975)

$$Sh=a\,Re^b\,Sc^c \tag{50}$$

$$Sh=a+b\,Re^c\,Sc^d \tag{51}$$

$$Sh=Sh_0+a\,Re^b\,Sc^c \tag{52}$$

ii. for natural convection as a function of the Grashof number (mass) Gr_m and the Schmidt number Sc (Sedahmed, 1986; Schultz, 1963):

$$Sh = aGr_m^b Sc^c \tag{53}$$

$$Sh = 2 + aGr_m^b Sc^c \tag{54}$$

iii. for vacuum-microwave drying as a function of the Archimedes number Ar and the Schmidt number Sc (Łapczyńska-Kordon, 2007)

$$Sh = a\left(Ar \cdot Sc\right)^b \tag{55}$$

The dimensionless moisture distributions for three shapes of products are given in a simplified form as Eq. (38) and for:
slab shapes:

$$G = \exp\left(\frac{0.2533Bi}{1.3 + Bi}\right) \tag{56}$$

cylindrical shapes:

$$G = \exp\left(\frac{0.5066Bi}{1.7 + Bi}\right) \tag{57}$$

and spherical shapes:

$$G = \exp\left(\frac{0.7599Bi}{2.1 + Bi}\right) \tag{58}$$

Using the experimental drying data taken from literature sources for different geometrical shaped products (e.g. slab, cylinder, sphere, cube, etc.), Dincer & Hussain (2004) obtained the Biot number–lag factor correlation for several kinds of food products subjected to drying as (R^2= 0.9181):

$$Bi = 0.0576G^{26.7} \tag{59}$$

The dimensionless Biot number Bi for moisture transfer can be calculated using its definition as:

$$Bi = \frac{h_m R}{D} \tag{60}$$

2.4 Equation of heat balance of dried biological material heating

Heat supplied to the particles of dried biological material is used to increase the particle temperature and to vaporize water. Material before drying is cut into small pieces (slices, cubes). It turned out from the experiments that the average value of the dried particle temperature did not differ in essential manner from the temperature value of the solid surface at any instant during process (Górnicki & Kaleta, 2002; Pabis et al., 1998). Therefore equation of heat balance of the dried solid heating obtains the following form (Górnicki & Kaleta, 2007b):

$$c\left(M + 1\right)\frac{dT}{dt} = -\frac{hA}{\rho_s V_s}\left(T - T_a\right) + L\frac{dM}{dt} \tag{61}$$

The specific heat of biological materials with a high initial moisture content depends on composition of the material, moisture content and temperature. Typically the specific heat increases with increasing moisture content and temperature and linear correlation between specific heat and moisture content in biological materials is observed mostly. Most of the specific heat models for discussed materials are empirical rather than theoretical. The present state of the empirical data is not precise enough to support more theoretically based models which in some cases are very complicated. Kaleta (1999) presented a classification of the different specific heat models of biological materials with a high initial moisture content.
Shrinkage model (e.g. Eq. (5) or Eq. (8)) and expression (4) or (10) can be used for determination of the surface area of dried solid presented in Eq. (61).
The heat transfer coefficient can be calculated from the dimensionless Nusselt number Nu. The Nusselt number can be expressed:

i. for forced convection as a function of the Reynolds number Re and the Prandtl number Pr

$$\mathrm{Nu} = a\,\mathrm{Re}^{b}\,\mathrm{Pr}^{c} \tag{62}$$

ii. for natural convection as a function of the Grashof number Gr and the Prandtl number Pr

$$\mathrm{Nu} = a\left(\mathrm{Gr}\cdot\mathrm{Pr}\right)^{b} \tag{63}$$

The constants a, b, and c can be found in Holman (1990).
For materials of moisture content above approximately 0.14 d.b. it can be assumed that to overcome the attractive forces between the adsorbed water molecules and the internal surfaces of material the same energy is needed as heat required to change the free water from liquid to vapour (Pabis et al., 1998).
Eq. (61) can be used for temperature modelling of biological materials during the second drying period.
According to the theory of drying the initial temperature of dried material reaches the psychrometric wet-bulb temperature T_{wb} (Eq. (2)) and remains at this level during the first period of drying. Beginning with the second period of drying, the temperature of material continuosly increases (Eq. (61)) and if the drying lasts long enough, the temperature reaches the temperature of the drying air.

3. Discussion of some results of modelling convection drying of parsley root slices

The authors' own results of research are presented in this chapter.
Cleaned parsley roots were used in research. Samples were cut into 3 mm slices and dried under natural convection conditions. The temperature of the drying air was 50°C. The following measurements were replicated four times under laboratory conditions: (i) moisture content changes of the examined samples during drying, (ii) temperature changes of the examined samples during drying, (iii) volume changes of the examined samples during drying. Measurements of the moisture content changes were carried out in a laboratory dryer KCW-100 (PREMED, Marki, Poland). The samples of 100 g mass were dried. Such a mass ensured final maximum relative error of evaluation of sample moisture content not exceeding 1 %. The mass of samples during drying and dry matter of samples

were weighed with the electronic scales WPE-300 (RADWAG, Radom, Poland). The changes of temperature of samples undergoing drying were measured by thermocouples TP3-K-1500 (NiCr-NiAl of 0.2 mm diameter, CZAKI THERMO-PRODUCT, Raszyn, Poland). Absolute error of temperature measurement was 0.1°C and maximum relative error was 0.7 %. Measurements of moisture content changes and the temperature changes were done at the same time. The volume changes of parsley root slices during drying were measured by buoyancy method using petroleum benzine. Maximum relative error was 5 %.
Figure 1 shows drying curve and changes of the temperature during drying of parsley root slices. The drying curve represents empirical formula approximating results of the four measurement repetitions of the moisture content changes in time.
Figure 2 presents the changes of the temperature during drying of parsley root slices and the results of the temperature modelling using Eq. (61).

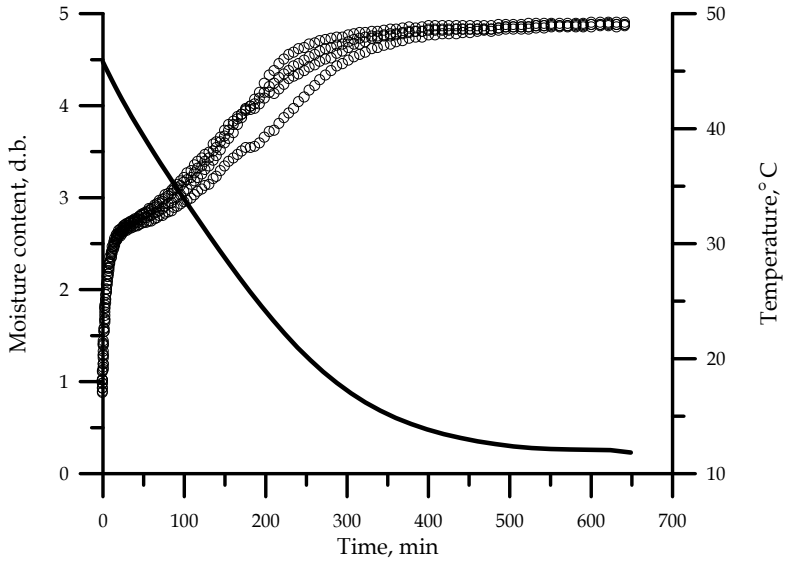

Fig. 1. Moisture content vs. time and temperature vs. time for drying of 3 mm thick parsley root slices at 50°C under natural convection condition: (—) – empirical formula approximating moisture content changes in time, (○) – temperature

At the beginning of the drying, temperature of slices increases rapidly because of heating of the materials. Then, for some time temperature is almost constant and afterwards slices temperature rises quite rapidly, attaining finally temperature of the drying air. The occurrence of period of almost constant temperature suggests that during drying of parsley root slices there is a period of time during which the conditions of external mass transfer determine course of the process. It can be seen from Fig. 2 that Eq. (61) predicts the temperature of parsley root slices during second period of drying quite well.
The course of drying curve of parsley root slices at the first drying period was described with Eqs. (3), (9), and (11), respectively. Following statistical test methods were used to evaluate statistically the performance of the drying models:
the determination coefficient R^2

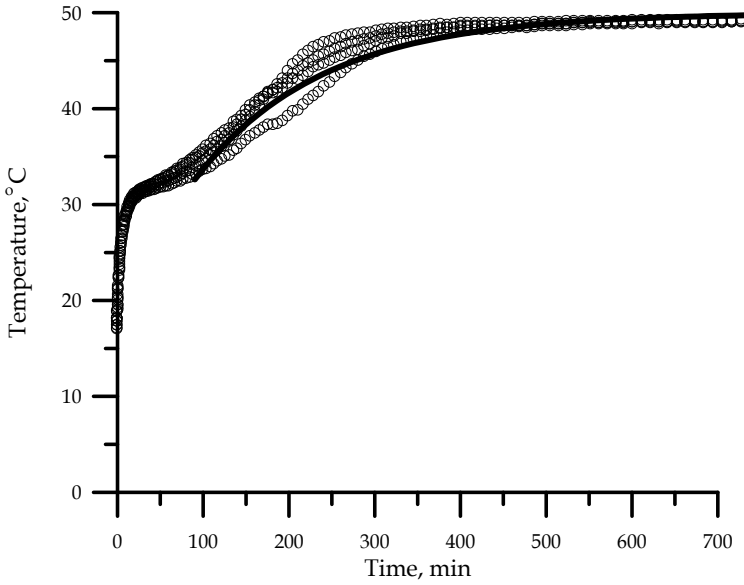

Fig. 2. Changes of the temperature during drying of 3 mm thick parsley root slices at 50°C under natural convection condition: (○) – experimental data, (—) – Eq. (61)

$$R^2 = \frac{\sum_{i=1}^{N}\left(MR_i - MR_{pre,i}\right)\cdot\sum_{i=1}^{N}\left(MR_i - MR_{exp,i}\right)}{\sqrt{\left[\sum_{i=1}^{N}\left(MR_i - MR_{pre,i}\right)^2\right]\cdot\left[\sum_{i=1}^{N}\left(MR_i - MR_{exp,i}\right)^2\right]}} \tag{64}$$

and the root mean square error RMSE

$$RMSE = \left[\frac{1}{N}\sum_{i=1}^{N}\left(MR_{pre,i} - MR_{exp,i}\right)^2\right]^{1/2} \tag{65}$$

The higher the value of R^2, and lower the value of RMSE, the better the goodness of the fit. Coefficients of the models of the first drying period and the results of the statistical analyses are given in Table 1.

Model of the first drying period	Coefficients	R^2	RMSE
Eq. (3)	k=0.0164	0.998	0.0224
Eq. (9)	k=0.0164; n=0.7829	0.999	0.0097
Eq. (11)	k=0.0164; b=0.15531; N=2.6	0.999	0.0165

Table 1. Coefficients of the models of the first drying period and the results of the statistical analyses

It was assumed that the models describe drying kinetics correctly when values of the relative error of model (3) do not exceed 1 %, and of models (9) and (11) do not exceed 3 %. A decision was taken to increase the value of the relative error to 3 % due to the nature of the course of the relative error for the models with drying shrinkage. At first, the relative error for these models reached negative value, afterwards it increased reaching zero value and then grew rapidly. As can be seen from the statistical analysis results, high coefficient of determination R^2 and low values of RMSE were found for all models. Therefore, it can be stated that all considered models may be assumed to represent the drying behaviour of parsley root slices in the first drying period.

It turned out that models of the first drying period describe the course of drying curve in different ranges of application. The linear model Eq. (3) describes the process for 80 min but the models of the first drying period which take into account drying shrinkage Eqs. (9) and (11) describe the process for 340 min and 305 min, respectively. Comparison with the course of the slices temperature (Fig. 1) points towards the following conclusions: (i) the linear model describes the drying from the beginning of the process till the end of period of constant temperature, (ii) models with shrinkage describe the process till the moment when slices temperature almost approach to drying air temperature. The analysis of the results obtained indicates that the course of the whole drying curve of parsley root slices could be described satisfactorily by using only the models with drying shrinkage. Such a description can be useful from the practical point of view because the solution of the model with drying shrinkage is easy to obtain.

The course of drying curve of parsley root slices at the second drying period was described with Eq. (31). Biot number Bi was calculated from Eqs. (56) and (59). The extreme case, when $Bi \to \infty$ (the boundary condition of the first kind, Eq. (14)) was also considered. Such a case is very often applied in the literature. The moisture diffusion coefficient was calculated from Eq. (39) and by fitting Eq. (31) to the experimental data considering the lowest value of RMSE (Eq. (65)). As it was shown, the models of the first drying period (Eqs. (3), (9), and (11)) describe the course of drying curve for different range of time. Therefore Eq. (31) begins to model the second drying period in different moments and the values of the Biot number depend on the model applied for description of the first drying period. The various number of terms in analytical solution of Eq. (31) were taken into account. Moisture diffusion coefficients and the results of the statistical analyses are given in Table 2.

As can be seen from the statistical analysis results, the following model can be considered as the most appropriate: the model of the first drying period taking into account shrinkage (Eq. (11)) followed by the model of the second drying period for which moisture diffusion coefficient was calculated by fitting Eq. (31) to the experimental data considering the lowest value of RMSE. The mentioned model of the second drying period can be also considered as the most appropriate when the course of the drying curve at the second drying period is only taken under consideration. As the least appropriate for describing the course of the whole drying curve, the linear model of the first drying period followed by the model of the second drying period can be considered. It can be also noticed that the model of the second drying period for which moisture diffusion coefficient was calculated from Eq. (39) gives worse results comparing to model for which coefficient was calculated considering the lowest value of RMSE. Figure 3 presents the result of consistency verification of calculation results with empirical data. Analysis of obtained graph shows that results of calculations obtained from the discussed models are very well correlated with empirical data. The model of the first drying period taking into account shrinkage (Eq. (11)) is better correlated with

empirical data comparing to model of the second drying period. Results of the statistical analyses (Table 1 and 2) confirm this regularity.

Model of the first drying period	Biot number Bi	Method of calculation of Bi	Number of terms in infinite series	Method of calculation of D	Moisture diffusion coefficient D	R^2 (for the second drying period)	RMSE (for the second drying period)	R^2 (for the whole drying process)	RMSE (for the whole drying process)
Eq. (3)	∞	-	10	Min(RMSE)	4.65×10^{-09}	0.986	0.2330	0.986	0.1901
			1		4.70×10^{-09}	0.994	0.2758	0.981	0.2247
	5.4	Eq. (56)	10	Eq. (39)	6.37×10^{-09}	0.991	0.1948	0.994	0.1592
			1			0.993	0.2107	0.992	0.1721
			10	Min(RMSE)	7.36×10^{-09}	0.991	0.1589	0.994	0.1303
			1		7.36×10^{-09}	0.996	0.1783	0.992	0.1460
	2.7	Eq. (59)	10	Eq. (39)	6.37×10^{-09}	0.982	0.3955	0.994	0.3218
			1			0.980	0.3971	0.992	0.3231
			10	Min(RMSE)	1.01×10^{-08}	0.994	0.1338	0.996	0.1101
			1		1.00×10^{-08}	0.996	0.1418	0.995	0.1166
Eq. (9)	∞	-	10	Min(RMSE)	3.01×10^{-11}	0.941	0.0464	0.999	0.0451
			1		3.19×10^{-11}	0.940	0.0479	0.999	0.0440
	0.07	Eq. (56)	10	Eq. (39)	9.51×10^{-10}	0.765	0.1970	0.999	0.0886
			1			0.765	0.1970	0.998	0.1064
			10	Min(RMSE)	8.92×10^{-09}	0.971	0.0332	0.999	0.0338
			1		9.10×10^{-09}	0.973	0.0331	0.999	0.0277
	0.04	Eq. (59)	10	Eq. (39)	9.51×10^{-10}	0.797	0.1624	0.999	0.0886
			1			0.797	0.1624	0.999	0.0886
			10	Min(RMSE)	5.44×10^{-09}	0.975	0.0344	0.999	0.0282
			1		5.48×10^{-09}	0.975	0.0344	0.999	0.0282
Eq. (11)	∞	-	10	Min(RMSE)	3.35×10^{-10}	0.992	0.0262	0.999	0.0207
			1		3.38×10^{-10}	0.973	0.0602	0.999	0.0269
	0.16	Eq. (56)	10	Eq. (39)	1.79×10^{-09}	0.867	0.2005	0.998	0.1149
			1			0.867	0.2005	0.998	0.1149
			10	Min(RMSE)	7.32×10^{-09}	0.992	0.0250	0.999	0.0233
			1		7.07×10^{-09}	0.991	0.0247	0.999	0.0233
	0.12	Eq. (59)	10	Eq. (39)	1.79×10^{-09}	0.848	0.2411	0.997	0.1377
			1			0.847	0.2411	0.997	0.1377
			10	Min(RMSE)	9.27×10^{-09}	0.991	0.0262	0.999	0.0238
			1		9.59×10^{-09}	0.992	0.0258	0.999	0.0238

Table 2. Moisture diffusion coefficients and the results of the statistical analyses

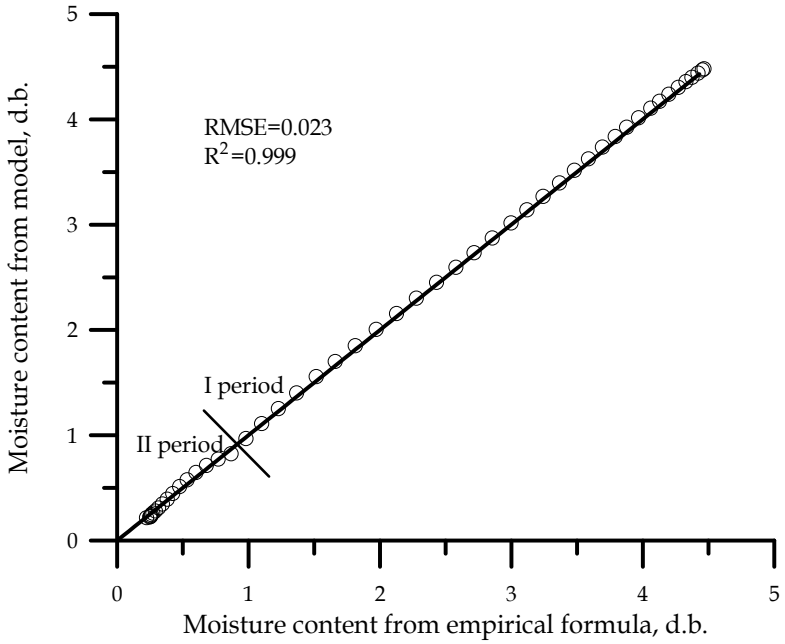

Fig. 3. Moisture content from model vs. experimental moisture content: I – first drying period, Eq. (11), II – second drying period, Bi=0.16, D from min(RMSE), 10 terms in infinite series

The determined moisture diffusion coefficient was found to be between $3.01 \cdot 10^{-11}$ m^2s^{-1} and $1.01 \cdot 10^{-8}$ m^2s^{-1} for the parsley root slices (Table 2). These values are within the general range for biological materials. Figures 4 and 5 show the influence of number of terms in infinite series in Eq. (31) on the value of obtained moisture diffusion coefficient and on the accuracy of verification of models of the second drying period. It can be accepted (Fig. 4) that the number of terms in infinite series do not influence much the value of the moisture diffusion coefficient. Its value was found to be between $3.33 \cdot 10^{-10}$ m^2s^{-1} and $3.41 \cdot 10^{-10}$ m^2s^{-1}. The influence of number of terms on RMSE was greater especially for number between i=1 (RMSE=0.06) and i=4 (RMSE=0.029). For higher number of terms the RMSE diminished very slowly and for i=10 reached the value of 0.026. Figure 5 presents the influence of number of terms in infinite series in Eq. (31) on the root mean square error RMSE and coefficient of determination R^2. The moisture diffusion coefficient determined for the first term in infinite series was then accepted in terms of higher number. It can be seen that the first four terms influence the accuracy of verification of Eq. (31) in higher degree than the next terms. The number of terms in Eq. (31) influences the obtained value of moisture ratio especially for values $0<Fo<0.08$, so in the beginning of the second drying period (Fig. 6). The first four terms influence the calculated moisture ratio in higher degree than the next terms. For values $Fo>0.08$, the solutions for various number of terms in infinite series are lying close together and truncating the series results in negligible errors.

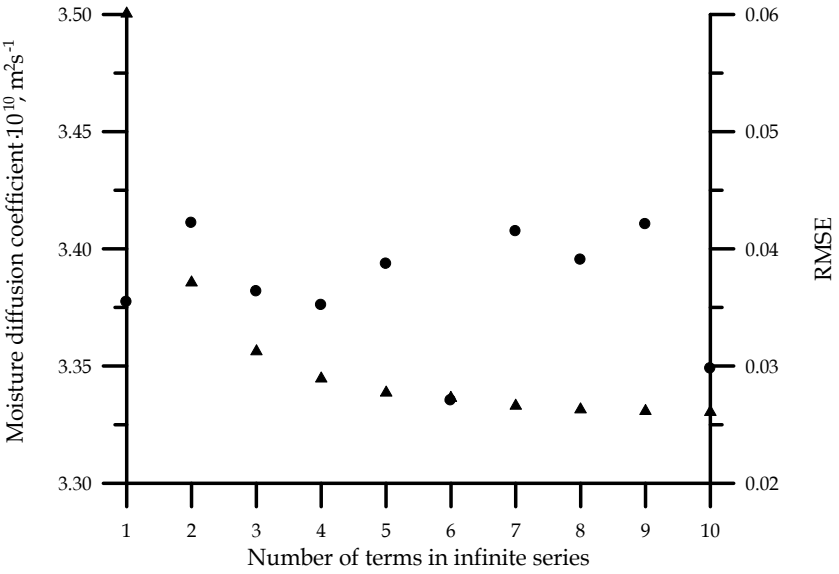

Fig. 4. Moisture diffusion coefficient vs. number of terms in infinite series in Eq. (31) and RMSE vs. number of terms in infinite series in Eq. (31) (first drying period – Eq. (11), Bi→∞): (●) – moisture diffusion coefficient, (▲) – RMSE

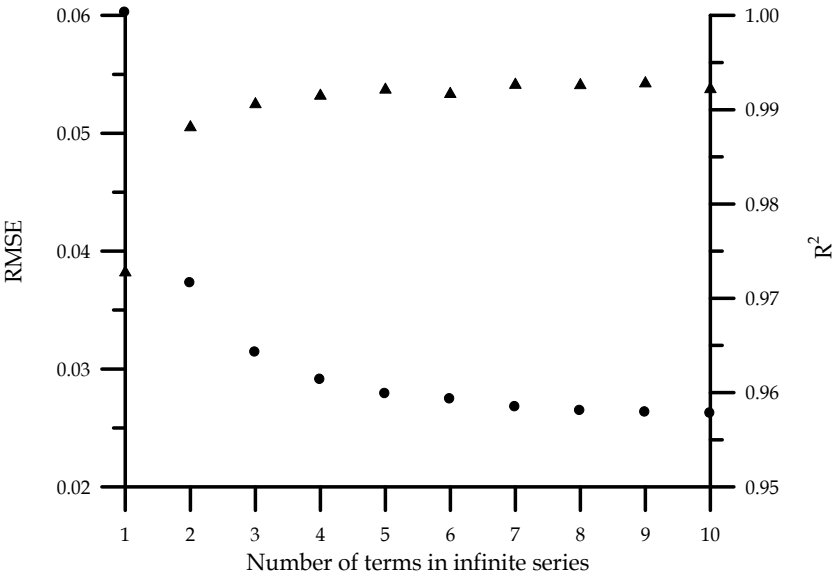

Fig. 5. RMSE vs. number of terms in infinite series in Eq. (31) and R^2 vs. number of terms in infinite series in Eq. (31) (first drying period – Eq. (11), Bi→∞): (●) – RMSE, (▲) – R^2

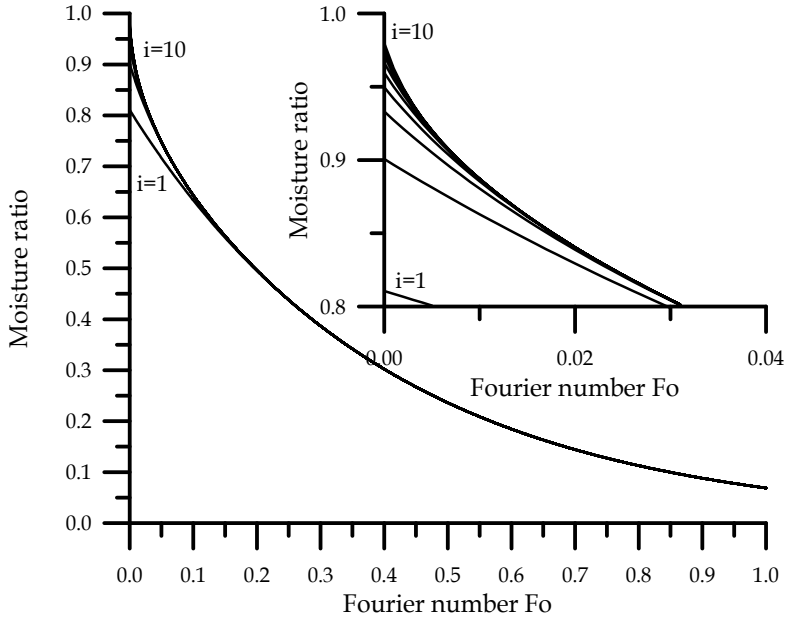

Fig. 6. Moisture ratio vs. Fourier number for various number of terms in infinite series in Eq. (31) (first drying period – Eq. (11), Bi→∞)

4. Conclusions

The results obtained from experiments and from mathematical model suggest that during the convective drying of parsley root slices there is a period of time during which the conditions of external mass transfer determine course of the process. The results of the linear model Eq. (3) verification indicate that during the drying of parsley root slices the period of constant drying rate takes place. Verified models of the first drying period Eqs. (9) and (11) taking into account drying shrinkage confirm that the decrease of the drying rate during the first drying period of parsley root slices can be caused by the shrinkage of drying slices.
Model of infinite plane drying accurately predicts the drying curve in the second drying period for parsley root slices. The determined moisture diffusion coefficient was found to be between $3.01 \cdot 10^{-11}$ m^2s^{-1} and $1.01 \cdot 10^{-8}$ m^2s^{-1}. These values are within the general range for biological materials. The number of terms in model of infinite plane drying influences the obtained solution especially in the beginning of the second drying period.
The course of the whole drying curve for parsley root slices could be described satisfactorily by using only the model with drying shrinkage. This model do not explain, however, the phenomenon of drying in the second period therefore applying such a model to the whole drying curve has only practical meaning.

5. Nomenclature

A surface area of dried solid (m^2)
a,b constants (Eqs. (35), (55), and (63))

a, b, c constants (Eqs. (36), (37), (49), (50), (52), (53), (54), and (62))
a, b, c, d constants (Eq. (51))
A_0 initial surface area of dried solid (m^2)
Ar Archimedes number ($Ar=gR^3\Delta\rho/\nu^2\rho$)
A_w the part of surface A on which mass flux is not equal to zero (m^2)
b dimensionless empirical coefficient of shrinkage model (Eq. (5))
Bi Biot number ($Bi=h_mR/D$)
c specific heat ($J\ kg^{-1}\ K^{-1}$)
D moisture diffusion coefficient (effective diffusivity) ($m^2\ s^{-1}$)
D_0 diffusion coefficient at the reference temperature ($m^2\ s^{-1}$)
D_{wa} diffusion coefficient of water vapour ($m^2\ s^{-1}$)
E_a activation energy ($J\ mol^{-1}$)
Fo Fourier number ($Fo=Dt/R^2$)
g acceleration of gravity ($m\ s^{-2}$)
G lag factor
Gr Grashof number ($Gr=gR^3\beta\Delta T/\nu^2$)
Gr_m Grashof number (mass) ($Gr_m=gR^3\beta'\Delta p/\nu^2$)
h half of cylinder height (m)
h heat transfer coefficient ($Wm^{-2}K^{-1}$)
h_m mass transfer coefficient ($m\ s^{-1}$)
k initial drying rate (s^{-1})
k_{th} thermal conductivity ($Wm^{-1}\ K^{-1}$)
L latent heat of water vaporization ($J\ kg^{-1}$)
M moisture content (dry basis)
M_0 initial moisture content (dry basis)
M_c critical moisture content (dry basis)
M_e equilibrium moisture content (dry basis)
MR dimensionless moisture content, moisture ratio
MR_{exp} experimental moisture ratio
MR_{pre} predicted moisture ratio
N dimensionless empirical coefficient (Eq. (11))
Nu Nusselt number ($Nu=hR/k_{th}$)
n dimensionless empirical coefficient of shrinkage model (Eq. (8))
n orthogonal to surface A
n_1 dimensionless empirical coefficient (Eq. (10))
p pressure (Pa)
Pr Prandtl number ($Pr=\nu/\alpha$)
R universal gas constant ($J\ mol^{-1}\ K^{-1}$)
R characteristic dimension (m)
R_1, R_2, R_3 half of cube thickness (m)
R_c half of plane thickness or cylinder radius (m)
Re Reynolds number ($Re=uR/\nu$)
RMSE root mean square error
R^2 coefficient of determination
r, x, y, z coordinates (m)
S drying coefficient (s^{-1})
Sc Schmidt number ($Sc=\nu/D_{wa}$)

Sh Sherwood number ($Sh=h_mR/D_{wa}$)
T temperature (°C)
T_a temperature of drying air (°C)
T_A temperature of solid surface (°C)
T_{wb} wet-bulb temperature (°C)
t time (s)
t_c time of drying while moisture content $M=M_c$ (s)
u velocity (m s^{-1})
V volume of the dried solid (m^3)
V_0 initial volume of the dried solid (m^3)
V_s volume of the dry matter (m^3)
W_s dry matter of solid (kg)
$\dot{W}$ mass flux (kg $m^{-2}s^{-1}$)
α thermal diffusivity ($m^2\,s^{-1}$)
β volumetric expansion coefficient (K^{-1})
β' coefficient ($m^2\,N^{-1}$)
ν kinematic viscosity ($m^2\,s^{-1}$)
ρ_s density of dry matter (kg m^{-3})
Δ increment

5.1 Subscripts
A outer surface of body

5.2 Superscripts
$\bar{}$ average value in volume V

6. References

Babalis, S.J. & Belessiotis, V.G. (2004). Influence of Drying Conditions on the Drying Constants and Moisture Diffusivity During the Thin-Layer Drying of Figs. *Journal of Food Engineering*, Vol. 65, No. 3, (December 2004) , pp. 449–458, ISSN 0260-8774

Beg, S.A. (1975). Forced Convective Mass Transfer Studies from Spheroids. *Wärme- und Stoffübertragung*, Vol. 8, No. 2, (June 1975), pp. 127-135, ISSN 1432-1181

Blahovec, J. (2004). Sorption Isotherms in Materials of Biological Origin Mathematical and Physical Approach. *Journal of Food Engineering*, Vol. 65, No. 4, (December 2004), pp. 489-495, ISSN 0260-8774

Bruin, S. & Luyben, K.Ch.A.M. (1980). Drying of Food Materials : a Review of Recent Developments, In : *Advances in Drying*, Vol. 1, A.S. Mujumdar, (Ed.), 155-215, Hemisphere Publishing Corp., ISBN 0-8911-6185-6, Washington, DC, USA

Brunauer, S. (1943). *The Adsorption of the Gases and Vapors I. Physical Adsorption*, Princeton University Press, Princeton, USA

Castillo, M.D.; Martínez, E.J.; González, H.H.L.; Pacin, A.M. & Resnik, S.L. (2003). Study of Mathematical Models Applied to Sorption Isotherms of Argentinean Black Bean Varieties. *Journal of Food Engineering*, Vol. 60, No. 4, (December 2003), pp. 343-348, ISSN 0260-8774

Cunningham, S.E.; McMinn, W.A.M.; Magee, T.R.A. & Richardson, P.S. (2007). Modelling Water Absorption of Pasta During Soaking. *Journal of Food Engineering* Vol. 82, No. 4 (October 2007), pp. 600–607, ISSN 0260-8774

Dincer, I. & Dost, S. (1996). A Modelling Study for Moisture Diffusivities and Moisture Transfer Coefficients in Drying of Solid Objects. *International Journal of Energy Research*, Vol. 20, No. 6, (June 1996), pp. 531-539, ISSN 1099-114X

Dincer, I. & Hussain, M.M. (2004). Development of a New Biot number and Lag Factor Correlation for Drying Applications. *International Journal of Heat and Mass Transfer*, Vol. 47, No. 4, (February 2004), pp. 653-658, ISSN 0017-9310

Dincer, I.; Sahin, A.Z.; Yilbas, B.S.; Al-Farayedhi, A.A. & Hussain, M.M. (2000). Exergy and Energy Analysis of Food Drying Systems. Progress Report 2, KFUPM Project # ME/ENERGY/203.

Doulia, D.; Tzia, K. & Gekas, V. (2000). A Knowledge Base for the Apparent Mass Diffusion Coefficient (DEFF) of Foods. *International Journal of Food Properties*, Vol. 3, No.1, (March 2000), pp. 1 – 14, ISSN 1532-2386

Doymaz, I. & Pala, M. (2002). The Effects of Dipping Pretreatments on Air-Drying Rates of the Seedless Grapes. *Journal of Food Engineering*, Vol. 52, No. 4, (May 2002), pp. 413–417, ISSN 0260-8774

Efremov, G.; Markowski, M.; Białobrzewski, I. & Zielinska, M. (2008). Approach to Calculation Time-Dependent Moisture Diffusiviy for Thin Layered Biological Materials. *International Communications in Heat and Mass Transfer,* Vol. 35, No. 9, (November 2008), pp. 1069-1072, ISSN 0735-1933

Furmaniak, S.; Terzyk, A.P. & Gauden, P.A. (2007). The General Mechanism of Water Sorption on Foodstuffs-Importance of the Multitemperature Fitting of Data and the Hierarchy of Models. *Journal of Food Engineering*, Vol. 82, No. 4, (October 2007), pp. 528-535, ISSN 0260-8774

González-Fésler, M.; Salvatori, D.; Gómez, P. & Alzamora, S.M. (2008). Convective Air Drying of Apples as Affected by Blanching and Calcium Impregnation. *Journal of Food Engineering*, Vol. 87, No. 3, (August 2008), pp. 323-332, ISSN 0260-8774

Górnicki, K. & Kaleta, A. (2002). Kinetics of Convectional Drying of Parsley Root Particles. *Polish Journal of Food and Nutrition Sciences*, Vol. 11/52, No. 2, (June 2002), pp. 13-19, ISSN 1230-0322

Górnicki, K. & Kaleta, A. (2004). Course Prediction of Drying Curve of Parsley Root Particles under Conditions of Natural Convection. *Polish Journal of Food and Nutrition Sciences*, Vol. 13/54, No. 1, (January 2004), pp. 11-19, ISSN 1230-0322

Górnicki, K. & Kaleta, A. (2007a). Modelling Convection Drying of Blanched Parsley Root Slices. *Biosystems Engineering*, Vol. 97, No. 1, (May 2007), pp. 51-59, ISSN 1537-5110

Górnicki, K. & Kaleta, A. (2007b). Drying Curve Modelling of Blanched Carrot Cubes under Natural Convection Condition. *Journal of Food Engineering*, Vol. 82, No. 2, (September 2007), pp. 160-170, ISSN 0260-8774

Holman, J.P. (1990). *Heat Transfer*, 7-th ed., Mc Graw-Hill, ISBN 0-079-09388-4, New York, USA

Jaros, M.; Cenkowski, S. ; Jayas, D.S. & Pabis, S. (1992). A Method of Determination of the Diffusion Coefficient Based on Kernel Moisture Content and Its Temperature. *Drying Technology*, Vol. 10, No 1, (January 1992), pp. 213-222, ISSN 0737-3937

Jaros, M. & Pabis, S. (2006). Theoretical Models for Fluid Bed Drying of Cut Vegetables. *Biosystems Engineering*, Vol. 93, No. 1, (January 2006), pp. 45-55, ISSN 1537-5110

Jayas, D.S.; Cenkowski, S.; Pabis, S. & Muir W.E. (1991). Review of Thin-Layer Drying and Wetting Equations. *Drying Technology*, Vol. 9, No. 3, (June 1991), pp. 551-588, ISSN 1532-2300

Kaleta A. & Górnicki, K. (2007). Influence of Equilibrium Moisture Content Data on Results of Vegetable Drying Simulation. *Polish Journal of Food and Nutrition Sciences*, Vol. 57, No. 2(A), (June 2007), pp. 83-87, ISSN 1230-0322

Kaleta, A. (1999). *Thermal Properties of Plant Materials*, Warsaw Agricultural University Press, ISBN 83-7244-039-5, Warsaw, Poland

Karathanos, V. (1993). Collapse of Structure During Drying of Celery. *Drying Technology*, Vol. 11, No. 5, pp. 1005-1023, ISSN 1532-2300

Kaymak-Ertekin, F. (2002). Drying and Rehydrating Green and Red Pappers. *Journal of Food Science,* Vol. 67, No. 1, (January 2002), pp. 168-175, ISSN 1750-3841

Łapczyńska-Kordon, B. (2007). Model Suszenia Mikrofalowo-Podciśnieniowego Owoców i Warzyw (Model of Vacuum-Microwave Drying of Fruits and Vegetables), Inżynieria Rolnicza XI 10(98), Rozprawy habilitacyjne 26, ISSN 1429-7264 (in Polish)

Luikov, A.V. (1970). *Analytical Heat Diffusion Theory*, Academic Press Inc., ISBN 0-124-59756-3, New York, USA

Magee, T.R.A., Hassaballah, A.A. & Murphy, W.R., (1983). Internal Mass Transfer During Osmotic Dehydration of Apple Slices in Sugar Solutions. *Irish Journal of Food Science and Technology*, Vol. 7, No. 2, (June 1983), pp. 147–152, ISSN 0332-0375

Markowski, M. (1997). Air Drying of Vegetables: Evaluation of Mass Transfer Coefficient. *Journal of Food Engineering*, Vol. 34, No. 1, (October 1997), pp. 55-62, ISSN 0260-8774

Maroulis, Z.B.; Saravacos, G.D.; Panagiotou, N.M. & Krokida, M.K. (2001). Moisture Diffusivity Data Compilation for Foodstuffs: Effect of Material Moisture Content and Temperature. *International Journal of Food Properties*, Vol. 4. No 2, (July 2001), pp. 225 – 237, ISSN 1532-2386

Mayor, L. & Sereno, A.M. (2004). Modelling Shrinkage During Convective Drying of Food Materials: a Review. *Journal of Food Engineering*, Vol. 61, No. 3, (February 2004), pp. 373-386, ISSN 0260-8774

Mulet, A.; Berna, A. & Rosselló, C. (1989a). Drying of Carrots: Drying Models. *Drying Technology*, Vol. 7, No. 3, pp. 537-557, ISSN 1532-2300

Mulet, A.; Berna, A.; Rosselló, C. & Pinaga, F. (1989b). Drying of Carrots: II Evaluation of Drying Models. *Drying Technology*, Vol. 7, No. 4, pp. 641-661, ISSN 1532-2300

Pabis, S. (1999). The Initial Phase of Convection Drying of Vegetables and Mushrooms and the Effect of Shrinkage. *Journal of Agricultural Engineering Research*, Vol. 72, No. 2, (February 1999), pp. 187-195, ISSN 0021-8634

Pabis, S. & Jaros, M. (2002). The First Period of Convection Drying of Vegetables and the Effect of Shape-Dependent Shrinkage. *Biosystems Engineering*, Vol. 81, No. 2, (February 2002), pp. 201-211, ISSN 1537-5110

Pabis, S.; Jayas, D.S. & Cenkowski, S. (1998). *Grain Drying. Theory and Practice*, John Wiley & Sons, Inc., ISBN 0-471-57387-6, New York, USA

Parti, M. & Dugmanics, I. (1990). Diffusion Coefficient for Corn Drying. *Transaction of ASAE*, Vol. 33, No. 5, pp. 1652-1656, ISSN 0001-2351

Rizvi, S.S.H. (1995). Thermodynamic Properties of Foods in Dehydration, In: *Engineering Properties of Foods*, M.A. Rao & S.S.H. Rizvi, (Eds.), 133-214, Marcel Dekker, Inc., ISBN 0-824-78943-1, New York, USA

Ruiz-Cabrera, M.A.; Salgano-Cervantes, M.A.; Waliszewski-Kubiak, K.N. & Garcia-Alvaro, M.A. (1997). The Effect of Path Diffusion on the Effective Moisture Diffusivity in Carrot Slabs. *Drying Technology*, Vol. 15, No. 1, (January 1997), pp. 169-181, ISSN 1532-2300

Sacilik, K.; Keskin, R. & Elicin, A.K. (2006). Mathematical Modelling of Solar Tunnel Drying of Thin Layer Organic Tomato. *Journal of Food Engineering*, Vol. 73, No. 3, (April 2006), pp. 231-238, ISSN 0260-8774

Sander, A.; Skansi, D. & Bolf, N. (2003). Heat and Mass Transfer Models in Convection Drying of Clay Slabs. *Ceramics International*, Vol. 29, No. 6, pp. 641-653, ISSN 0272-8842

Schutz, G. (1963). Natural Convection Mass-Transfer Measurements on Spheres and Horizontal Cylinders by an Electrochemical Method. *International Journal of Heat and Mass Transfer*, Vol. 6, No. 10, (October, 1963), pp. 873-879, ISSN 0017-9310

Sedahmed, G.H. (1986). Free Convection Mass Transfer at Horizontal Cylinders. *Chemical Engineering Communications*, Vol. 48, No. 4-6, (November 1986), pp. 207 – 213, ISSN 1563-5201

Simal, S.; Sánchez, E.S.; Bon, J.; Femenia, A. & Rosselló, C. (2001). Water and Salt Diffusion During Cheese Ripening: Effect of the External and Internal Resistances to Mass Transfer. *Journal of Food Engineering*, Vol. 48, No. 3, (May 2001), pp. 269-275, ISSN 0260-8774

Timmermann, E.O.; Chirife, J. & Iglesias, H.A. (2001). Water Sorption Isotherms of Food and Foodstuffs: BET or GAB Parameters?, *Journal of Food Engineering*, Vol. 48, No. 1, (April 2001), pp. 19-31, ISSN 0260-8774

van den Berg, C. & Bruin, S. (1981). Water Activity and Its Estimation in Food Systems: Theoretical Aspects, In: *Water Activity: Influences on Food Quality*, L.B. Rockland & G.F. Stewart, (Eds.), 1-61, Academic Press, ISBN 0-12-591350-8, New York, USA

Waananen, K.M. & Okos, M.R. (1996). Effect of Porosity on Moisture Diffusion Drying of Pasta. *Journal of Food Engineering,* Vol. 28, No. 2, (May 1996), pp. 121-137, ISSN 0260-8774

Zielinska, M. & Markowski, M. (2007). Drying Behavior of Carrot Dried in a Spout-Fluidized Bed Dryer. *Drying Technology*, Vol. 25, No. 1 (January 2007), pp. 261-270, ISSN 0737-3937

8

Modeling and Simulation of Chemical System Vaporization at High Temperature: Application to the Vitrification of Fly Ashes and Radioactive Wastes by Thermal Plasma

Imed Ghiloufi
College of Sciences, Department of Physics,
Al-Imam Muhammad Ibn Saud University, Riyadh,
Kingdom of Saudi Arabia

1. Introduction

The treatment, at high temperatures, of such chemical systems as the fly ashes and radioactive wastes requires the control of its element volatility. Precisely, it requires following the evolution of the system during treatment and determining the composition of the system in all phases.

For a closed chemical system, the calculation of its composition is carried out by the method of free enthalpy minimization developed by Eriksson [1]. However, for open systems, the problem is not definitively solved yet. A computer code simulating the volatility of the elements present in an oxide system was developed by Pichelin [2] and Badie [3]. This computer code was modified by Ghiloufi to control the vaporization of the elements present in a chloride and oxide system during the fly ashes vitrification by plasma and to study the radioelement volatility during the treatment of radioactive wastes by thermal plasma [4-9].

In this chapter we present a method used in our computer code, which is developed to simulate and to modulate a chemical system vaporization at high temperature. This method is based on the calculation of composition by free energy minimization of the system, coupled with the mass transfer equation at the reactional interface. This coupling is ensured by fixing the equivalent partial pressure of oxygen in the mass transfer equation and those characterizing the complex balances.

This chapter contains five parts: In the first part we will present the method used to the calculation of composition by free energy minimization of a closed system, precisely we will develop the equations characterizing the complex balances at the reactional interface. In the second part we will give the mass transfer equation of oxygen. In the third part we will present the method used in our study to determine the diffusion coefficients of gas species essentially for complex molecules like vapor metals. In the fourth part we will apply the computer code to simulate the radioelement volatility during the vitrification of radioactive wastes by thermal plasma. In the last part we will present the results obtained by the computer code during the study of radioaelement volatility.

2. Description of the model

In the model, the species distribution in the liquid and gas phases is obtained iteratively using the calculation of system composition coupled with the mass transfer equation. The quantity of matter formed in the gas phase is distributed into three parts: The first part is in equilibrium with the bath, the second part is diffused in the diffusion layer, and the third part is retained by the bath under the electrolysis effects (Figure 1). The gas composition at the surface is thus modified. It is not the result of a single equilibrium liquid-gas, but instead, it is the outcome of a dynamic balance comprising: a combined action of reactional balances, electrolysis effects, and diffusive transport.

The flux density of a gas species i (J_i^L) lost in each iteration is given by:

$$J_i^L = J_i^D - J_i^R \tag{1}$$

Where J_i^D and J_i^R are, respectively, the diffusion flux density and the flux retained by the bath for the gas species i.

The vaporization model is applicable to several types of complex chemical systems. It is independent of the geometrical configuration of the vaporization system, but it is developed based on the following three hypotheses:

a. The chemical system consists of two phases: a vapor phase, whose species are regarded as perfect gases, and a homogeneous isothermal liquid phase.
b. The model is mono-dimensional: it does not introduce discretization on the variable space, but enables to calculate the composition of the two phases at each time interval.
c. The mass transfer at the interface is controlled by the gas species diffusion in the carrier gas because the reaction kinetics at the liquid/gas interface are very fast.

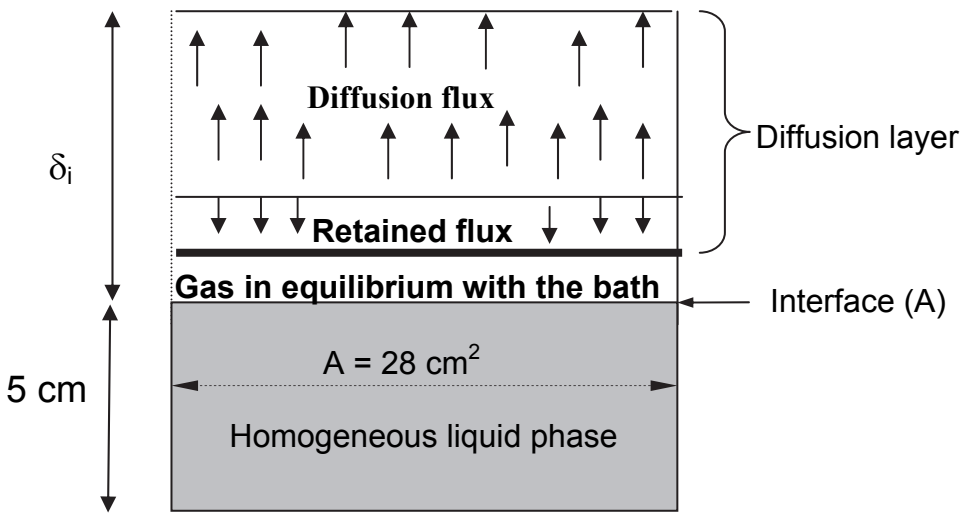

Fig. 1. Simplified diagram used to establish the assumptions of the model

3. Calculation of the gas/ liquid system composition

The free energy of a system made up of two phases; a vapor phase formed by Ml(1) species and a condensed phase consisting of Ml (2) species is as follows:

$$G = \sum_{i=1}^{Ml(1)} n_i \left(g_i^0 + RTLogp_i \right) + \sum_{i=Ml(1)+1}^{Ml(1)+Ml(2)} n_i \left(g_i^0 + RTLogX_i \right) \tag{2}$$

where g_i^0 is the formation free enthalpy of a species under standard conditions, R is the perfect gas constant, T is the temperature, and n_i is the mole number of species *i*. The two terms p_i and X_i are, respectively, the partial pressure of a gas species, assumed a perfect gas, and the molar fraction of species *i* in the liquid phase assumed ideal.
Equation (2) can be written differently as:

$$F = \frac{G}{RT} = \sum_{i=1}^{Ml(1)} n_i \left[\frac{g_i^0}{RT} + LogP + Log \frac{n_i}{\bar{n}_g} \right] + \sum_{i=Ml(1)+1}^{Ml(1)+Ml(2)} n_i \left[\frac{g_i^0}{RT} + Log \frac{n_i}{\bar{n}_l} \right] \tag{3}$$

where P is the total pressure, $\bar{n}_g$ represents the total mole number of the species in the gas phase ($\bar{n}_g = \sum_{i=1}^{Ml(1)} n_i$) and $\bar{n}_l$ represents the total mole number of the species in the condensed phase ($\bar{n}_l = \sum_{i=Ml(1)+1}^{Ml(1)+Ml(2)} n_i$).

Let us assume that the system under study consists of L basic elements. Hence, the conservation of the elements mass results in:

$$\sum_{i=1}^{Ml(1)} a_{ij} n_i + \sum_{i=Ml(1)+1}^{Ml(1)+Ml(2)} a_{ij} n_i = B_j \quad j \in [1, L] \tag{4}$$

where a_{ij} is the atoms grams number of the element *j* in the chemical species *i* and B_j is the total number of atoms grams of the element *j* in the system.
The equivalent partial pressure of oxygen is given by:

$$P_{O2} = \frac{n_{O2}}{\bar{n}_g} P \tag{5}$$

where n_{O2}, representing the equivalent mole number of oxygen, is given by:

$$n_{O2} = \sum_{i=1}^{Ml(1)} a_{iL} n_i \tag{6}$$

where a_{iL} is the atoms grams number of oxygen in the chemical species *i*. Combining (5) and (6) leads to:

$$\bar{n}_g \frac{P_{O2}}{P} = \sum_{i=1}^{Ml(1)} a_{iL} n_i \tag{7}$$

The calculation of the system composition to the balance coupled with the mass transfer equation, at constant temperature T and constant pressure P, consists of minimizing the function F under the constraints of (4) and (7). The Lagrange function becomes:

$$L(n_i) = \xi(n_i) + \sum_{j=1}^{L} \Pi_j \left(- \sum_{i=1}^{Ml(1)+Ml(2)} a_{ij} n_i + B_j \right) + \Pi_{L+1} \left(- \sum_{i=1}^{Ml(1)} a_{iL} n_i + \frac{P_{O2}}{P} \bar{n}_g \right) \tag{8}$$

where Π_j represents the Lagrange multipliers and the function ξ (n_i) is the Taylor series expansion of F (with orders higher than two being neglected).
To minimize F (ni) subject to (4) and (7), it is required to have:

$$\frac{\partial L}{\partial n_i} = 0 \quad i=1,\ldots,Ml(1)+Ml(2) \tag{9}$$

$$\frac{\partial L}{\partial \Pi_j} = 0 \quad j=1,\ldots,L,\ L+1 \tag{10}$$

From (9), the expression of the mole number of a species *i* in the vapor phase or in the liquid phase can be deduced. That is to say:
For gases:

$$n_i = \left(-\frac{g_i^0}{RT} - LogP - Ln\left(\frac{n_i^0}{\bar{n}_g^0}\right) + \frac{\bar{n}_g}{\bar{n}_g^0} + \sum_{j=1}^{L} \Pi_j a_{ij} + \Pi_{L+1}\left(a_{iL} - \frac{P_{O2}}{P}\right)\right) n_i^0 \tag{11}$$

For liquid:

$$n_i = \left(-\frac{g_i^0}{RT} - Ln\left(\frac{n_i^0}{\bar{n}_l^0}\right) + \frac{\bar{n}_l}{\bar{n}_l^0} + \sum_{j=1}^{L} \Pi_j a_{ij}\right) n_i^0 \tag{12}$$

with $\bar{n}_g^0 = \sum_{i=1}^{Ml(1)} n_i^0$ and $\bar{n}_l^0 = \sum_{i=Ml(1)+1}^{Ml(1)+Ml(2)} n_i^0$

Substituting (11) and (12) in (10) results in a system of L+3 equations, whose unknown factors are the Lagrange multipliers ($\Pi_1, \Pi_2, \ldots, \Pi L, \Pi_{L+1}$), u_1, and u_2.

with $u_1 = \frac{\bar{n}_g}{\bar{n}_g^0} - 1$ and $u_2 = \frac{\bar{n}_l}{\bar{n}_l^0} - 1$.

Solving this set of equations then using (11) or (12), as needed, gives the values of n_i. These values n_i represent the improved values over the first iterations $n_i^{(1)}$. A loop of iterations is thus defined by using $n_i^{(k)}$ in the place of the n_i^{k-1} for the k^{th} iteration.

4. Transfer equation

4.1 Determination of the stoichiometric coefficient

To simplify the writing and calculation of the mass transfer equation at the interface, a dimensionless quantity X_j, called stoichiometric coefficient of a metal 'J', has been introduced and corresponding to :

$$X_j = \frac{n_{O-j}}{n_{M_j}} \tag{13}$$

where n_{O-j} is the mole number of oxygen in the liquid phase related to metal 'J', whereas the term n_{M_j} represents the total mole number of metal 'J' in the liquid phase, which contains m species. For example if N is the total mole number of metals in the mixing melted material, for an unspecified metal 'J', the expressions of X_j is as follows :

$$X_j = \frac{\sum_{i=1}^{m} a_{ik} n_i \dfrac{a_{ij}\upsilon_{ij}}{\sum_{j=1}^{N} a_{ij}\upsilon_{ij}}}{\sum_{i=1}^{m} a_{ij} n_i} \tag{14}$$

a_{ij} and a_{ik} are respectively the stoichiometric coefficients of the element 'J', and oxygen in species 'i'. n_i represents the number of moles of species 'i'. υ_{ij} is the valence of metal 'J' in oxide 'i'.

4.2 Example

In an initial mixture of Al-Si-Fe-O-Cl, for example, the species which can exist in the liquid phase at 1700 K are as follows: SiO_2, Fe_2SiO_4, Fe_3O_4, FeO, Al_2O_3, $AlCl_3$, $FeCl_2$. The iron stoichiometric coefficients X_{Fe} in the system is given by the following expression:

$$X_{Fe} = \frac{(4\, n_{Fe_2SiO_4} \times \frac{4}{8}) + 4\, n_{Fe_3O_4} + n_{FeO}}{2\, n_{Fe_2SiO_4} + 3\ n_{Fe_3O_4} + n_{FeO}} \tag{15}$$

4.3 Transfer equation

From equation (13), the oxygen mole number in the liquid phase related to metal 'J', can be deduced, i.e.

$$n_{O-j} = X_j . n_{M_j} \tag{16}$$

If equation (16) is differentiated relatively to time and each term is divided by the surface of the interface value A, it comes :

$$-\frac{1}{A}\frac{dn_{O-j}}{dt} = -\frac{1}{A} X_j \frac{dn_{M_j}}{dt} - \frac{1}{A} n_{M_j} \frac{dX_j}{dt} \tag{17}$$

The interfacial density of molar flux of a species 'i' is:

$$J_i = -\frac{1}{A}\frac{dn_i}{dt} \text{ (mole.s}^{-1}\text{.m}^{-2}\text{)} \tag{18}$$

Introducing equation (18), in equation (17), leads to:

$$(J_O^L)_{M_j} = \mathrm{X}_j.(J_{M_j}^L) - \frac{n_{M_j}}{A}\frac{d\mathrm{X}_j}{dt} \tag{19}$$

$(J_O^L)_{M_j}$ represent the surfacic molar flux densities of oxygen related to metal 'J' from the liquid phase, whereas $(J_{M_j}^L)$ is the equivalent density of molar flux of a metal J from the liquid phase.
The total surfacic densities of molar flux of oxygen from the liquid phase is expressed by:

$$(J_O^L) = \sum_{j=1}^{N}(J_O^L)_{M_j} \tag{20}$$

If in the equation (20) $(J_O^L)_{M_j}$ is replaced by its expression given by the equation (19) it follows:

$$(J_O^L) = \sum_{j=1}^{N}\mathrm{X}_j(J_{M_j}^L) - \frac{1}{A}\sum_{j=1}^{N}n_{M_j}.\frac{d\mathrm{X}_j}{dt} \tag{21}$$

Indicating by Ng, the number of species which can exist in the vapor phase, the expressions of the total densities of molar flux of oxygen and an unspecified metal 'J' in gas phase are:

$$(J_O^G) = \sum_{i=1}^{Ng}a_{ik}J_i^G \tag{22}$$

$$(J_{M_j}^G) = \sum_{i=1}^{Ng}a_{ij}J_i^G \tag{23}$$

where J_i^G is the molar flux density of a gas species 'i'.
The mass balance at the interfacial liquid to gas is expressed by the equality between the equivalent densities of molar flux of an element in the two phases, i.e. :

$$(J_i^L) = (J_i^G) \tag{24}$$

The use of matter conservation equations at the interface, for oxygen and metals, and the combination of equations (16), (17), (18), (19) and (20), lead to the following equation.

$$\sum_{j=1}^{N}X_j(J_{M_j}^G) - \sum_{i=1}^{Ng}a_{ik}J_i^G - \frac{1}{A}\sum_{j=1}^{N}n_{M_j}.\frac{dX_j}{dt} = 0 \tag{25}$$

The equation (25) is the oxygen matter conservation equation or the transfer equation at the interface. Argon is used as a carrier gas. In the plasma conditions, it is supposed that argon is an inert gas, so its molar flux density is zero:

$$J_{Ar}^{G} = 0 \tag{26}$$

The density flux for a gas species 'i' is given by:

$$J_i^G = -\frac{D_i}{RT}\left(\frac{p_i^x - p_i^w}{\delta_i}\right) + J_T.p_i^w \tag{27}$$

where p_i^w and p_i^x represent the interfacial partial pressure and the partial pressure in the carrier gas of species 'i' respectively; J_T is the total mass flux density with $J_T = \sum_{i=1}^{n-1} J_i^G$, $J_{Ar}^G = 0$ *and* $\sum_{i=1}^{n} p_i^w = 1atm$, δ_i is boundary layer thickness, and D_i is diffusion coefficient.

5. Flux retained by the bath

The Faraday's first law of electrolysis states that the mass of a substance produced at an electrode during electrolysis is proportional to the mole number of electrons (the quantity of electricity) transferred at that electrode [10]:

$$m = \frac{Q}{q\upsilon}\frac{M}{N_A} \tag{28}$$

where m is the mass of the substance produced at the electrode (in grams), Q is the total electric charge passing through the plasma (in coulombs), q is the electron charge, v is the valence number of the substance as an ion (electrons per ion), M is the molar mass of the substance (in grams per mole), and N_A is Avogadro's number. If the mole number of a substance i is initially n_i^0, its mole number produced at the electrode is:

$$n_i = \frac{Q}{q\upsilon N_A} n_i^0 \tag{29}$$

The interfacial density of molar flux of a species 'i' is:

$$J_i = \frac{1}{A}\frac{dn_i}{dt} \ (\text{mole.s}^{-1}.\text{m}^{-2}) \tag{30}$$

The density (J_i^R), of molar flux of a species i retained by the bath under the electrolyses effects, can be obtained by substituting (29) in (30) to yield:

$$J_i^R = \frac{1}{A}\frac{dn_i}{dt} = \frac{1}{A}\frac{d\left(\frac{Q}{q\upsilon N_A} n_i^0\right)}{dt} = \frac{n_i^0}{A.qN_A.\upsilon}\frac{dQ}{dt} \tag{31}$$

$\frac{dQ}{dt} = I$ represents the current in the plasma and $F = qN_A = 96485\ C.mol^{-1}$ is Faraday's constant. Equation (31) becomes:

$$J_i^R = \frac{I}{A.F.v} n_i^0 \tag{32}$$

6. Numerical solution

Newton's numerical method solves the mass balance equations (26), (27) and (28) with respect to the interfacial thermodynamic equilibrium, the unknown parameters being the interfacial partial pressure P_i^w, the stoichiometric coefficient X_J and the molar flux densities J_i^G.

The convergence scheme is as follows:

- We calculate the liquid-gas interfacial chemical composition of the closed system by using Ericksson's program. The oxygen partial pressure is then defined by the convergence algorithm.
- The recently known values of p_i^w and X_J are introduced into the mass equilibrium equations which can be solved after a series of iterative operations up to the algorithm convergence.
- At the beginning of the next vaporization stage, the system is restarted with the new data of chemical composition. The time increment is not constant and should be adjusted to the stage in order to prevent convergence instabilities when a sudden local variation of the mass flux density occurs.

7. Estimation of the diffusion coefficients

Up to temperatures of about 1000 K, the binary diffusion coefficients are known for current gases, oxygen, argon, nitrogen…etc. For temperatures higher than 1000 K, the diffusion coefficients of the gas species in the carrier gas are calculated according to level 1 of the CHAPMAN-ENSKOG approximation [11]:

$$D_{ij} = 0.002628 \frac{\sqrt{T^3 (M_i + M_j) / 2M_i M_j}}{P\sigma_{ij}^2 \Omega_{ij}^{(1.1)^*}(T_{ij}^*)} \tag{33}$$

In this equation D_{ij} is the binary diffusion coefficient (in $cm^2.s^{-1}$), M_i and M_j are the molar masses of species 'i' and 'j'. P is the total pressure (in atm), T is the temperature (in K), $T^* = T\frac{k}{\varepsilon_{ij}}$ is the reduced temperature, K is the Boltzmann constant, σ_{ij} is the collision diameter (in Å), ε_{ij} is the binary collision energy and $\Omega_{ij}^{(1.1)^*}(T^*)$ is the reduced collision integral.

For an interaction between two non-polar particles 'i' and 'j':

$$\varepsilon_{ij} = \sqrt{\varepsilon_i \varepsilon_j} \tag{34}$$

$$\sigma_{ij} = \frac{1}{2}\left(\sigma_i + \sigma_j\right) \tag{35}$$

The values relating to current gases needed for our calculations are those of Hirschfelder [11]. For the other gas species, such as the metal vapor, the parameters of the intermolecular potential remain unknown whatever the interaction potential used. This makes impossible the determination of the reduced collision integral. For this reason the particles are regarded as rigid spheres and the collision integrals are assimilated to those obtained with the rigid spheres model [12]. That is equivalent to the assumption:

$$\Omega_{ij}^{(1.1)^*}(T^*) = 1 \tag{36}$$

$$\sigma_{ij} = r_i + r_j \tag{37}$$

The terms r_i and r_j are the radii of the colliding particles. For the monoatomic particles, the atomic radii are already found. For the polyatomic particles, the radii of the complex molecules A_nB_m are unknown. Thus it has been supposed that they had a spherical form and their radii were estimated according to [12]:

$$r_{A_nB_m} = \left| n r_A^3 + m r_B^3 \right|^{1/3} \tag{38}$$

In the above expression, r_A and r_B are either of the ionic radius, or of the covalence radius according to the existing binding types. The radii of all the ions which form metal oxides and chlorides are extracted from the Shannon tables [13].
At high temperature (T > 1000 K), the D_{ij} variation law with the temperature is close to the power 3/2 [14]. For this reason the diffusion coefficients of the gas species are calculated with only one value of temperature (1700 K). For the other temperatures the following equation is applied:

$$D_{ij}(T_2) = D_{ij}(T_1).\left(\frac{T_2}{T_1}\right)^{3/2} \tag{39}$$

8. Application of the model

To simulate the same emission spectroscopy conditions in which the experimental measurement are obtained, the containment matrix used for this study is formed by basalt, and its composition is given in table 1.
At high temperatures (T > 1700K), in the presence of oxygen and argon, the following species are preserved in the model:

- In the vapor phase: O_2, O, Mg, MgO, K, KO, Na, Na_2, NaO, Ca, CaO, Si, SiO, SiO_2, Al, AlO, AlO_2, Fe, FeO, Ti, TiO, TiO_2, and Ar.
- In the condensed phase : $CaSiO_3$,Ca_2SiO_4, $CaMgSi_2O_6$, $K_2Si_2O_5$, SiO_2, Fe_2SiO_4, Fe_3O_4, FeO, $FeNaO_2$, Al_2O_3, CaO, Na_2O, Na_2SiO_3, $Na_2Si_2O_5$, K_2O, K_2SiO_3, MgO, $MgAl_2O_4$, $MgSiO_3$, Mg_2SiO_4, $CaTiSiO_5$, $MgTi_2O_5$, Mg_2TiO_4, $Na_2Ti_2O_5$, $Na_2Ti_3O_7$, TiO, TiO_2, Ti_2O_3, Ti_3O_5, and Ti_4O_7.

Elements	Mg	K	Na	Ca	Si	Al	Fe	Ti
Chemical form	MgO	K_2O	Na_2O	CaO	SiO_2	Al_2O_3	FeO	TiO_2
% in mass	10.2	1.2	3	8.8	50.4	12.2	11.9	2.2
Cation mole number	0.253	0.021	0.154	0.157	0.838	0.239	0.165	0.034

Table 1. Composition of basalt

This study focuses on the three radioelements ^{137}Cs, ^{60}Co, and ^{106}Ru. Ruthenium is a high activity radioelement, and it is an emitter of α, β and γ radiations, with long a radioactive period. However, Cesium and Cobalt are two low activity radioelements and they are emitters of β and γ radiations with short-periods on the average (less than or equal to 30 years) [15]. To simplify the system, the radioelements are introduced separately in the containment matrix, in their most probable chemical form. Table 2 recapitulates the chemical forms and the mass percentages of the radioelements used in the system. The mass percentages chosen in this study are the same as that used in experimental measurements made by [9, 16].

radioelement	^{137}Cs	^{60}Co	^{106}Ru
Most probable chemical form	Cs_2O	CoO	Ru
% in mass	10	10	5

Table 2. Chemical Forms and Mass Percentages of radioelement

The addition of these elements to the containment matrix, in the presence of oxygen, leads to the formation of the following species:

- In the vapor phase: Cs, Cs_2, CsK, CsNa, CsO, Cs_2O, Cs_2O_2, Ru, RuO, RuO_2, RuO_3, RuO_4, Co, Co_2, and CoO.
- In the condensed phase: Cs, Cs_2O, Cs_2O_2, Cs_2SiO_3, $Cs_2Si_2O_5$, $Cs_2Si_4O_9$, Ru, CoAl, CoO, Co_2SiO_4, CoSi, $CoSi_2$, Co_2Si, and Co.

These species are selected with the assistance of the HSC computer code [17]. In the simulation, the selected formation free enthalpies of species are extracted from the tables of [18-20].

9. Simulation results

In this part we will present only the results of radioelement volatility obtained by our computer code during the treatment of radioactive wastes by plasma. However the results of heavy metal volatility during fly ashes treatment by thermal plasma can be find in [4,5].

9.1 Temperature influence

To have the same emission spectroscopy conditions in which the experimental measurement are obtained [9, 16], in this study the partial pressure of oxygen in the carrier gas P_{O_2} is fixed at 0.01 atm, the total pressure P at 1 atm, and the plasma current I at 250 A. Figures 2 and 3 depict respectively, the influence of bath surface temperatures on the Cobalt and Ruthenium volatility. Up to temperatures of about 2000 K, Cobalt is not volatile. Beyond this

value, any increase of temperature causes a considerable increase in both the vaporization speed and the vaporized quantity of ^{60}Co. This behavior was also observed for ^{137}Cs [8]. Contrarily to Cobalt, Ruthenium has a different behavior with temperature. For temperatures less than 1700 K and beyond 2000 K, Ruthenium volatility increases whith temperature increases. Whereas in the temperature interval between 1700 K and 2000 K, any increase of temperature decreases the ^{106}Ru volatility.
To better understand this Ru behavior, it is necessary to know its composition at different temperatures. Table 3 presents the mole numbers of Ru components in the gas phase at different temperatures obtained from the simulation results.

	species	Ru	RuO	RuO_2	RuO_3	RuO_4
Mole numbers	1700K	6.10^{-14}	3.10^{-10}	4.10^{-6}	7.10^{-5}	1.10^{-6}
	2000K	5.10^{-11}	2.10^{-8}	1.10^{-5}	3.10^{-5}	1.10^{-7}
	2500K	1.10^{-7}	2.10^{-6}	8.10^{-5}	1.10^{-5}	2.10^{-8}

Table 3. Mole numbers of Ru components in the gas phase at different temperatures

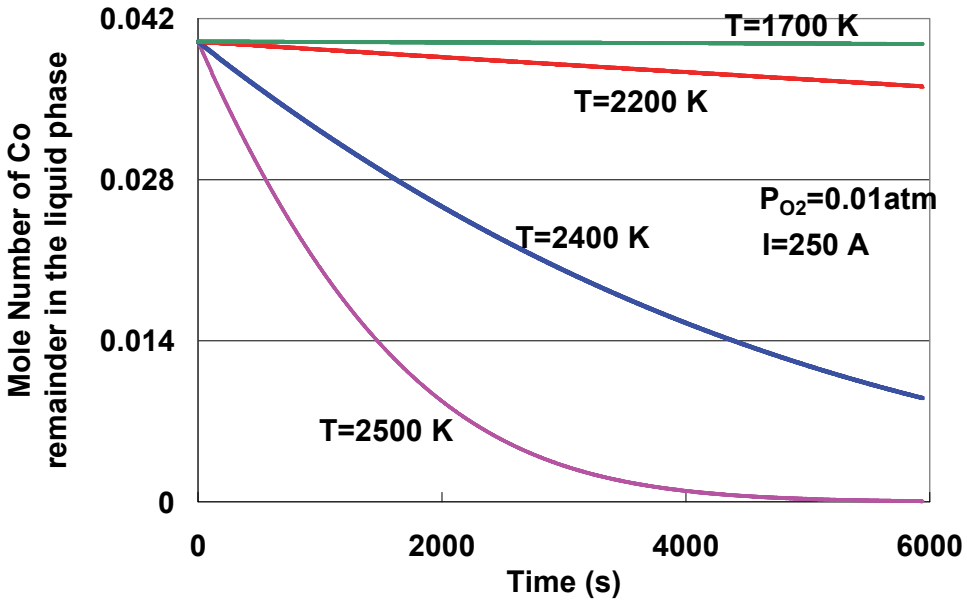

Fig. 2. Influence of temperature on Co volatility

The first observation that can be made is that the mole numbers of Ru, RuO, and RuO_2 increase with temperature, contrary to RuO_3 and RuO_4 whose mole numbers decrease with increasing temperatures. These results are logical because the formation free enthalpies of Ru, RuO, and RuO_2 decrease with temperature. Therefore, these species become more stable when the temperature increases, while is not the case for RuO_3 and RuO_4. A more interesting observation is that at temperatures between 1700 and 2000 K the mole numbers of Ru, RuO, and RuO_2 increase by an amount smaller that the amount of decrease of the

mole numbers of RuO_3 and RuO_4 resulting in an overall reduction of the total mole numbers formed in the gas phase. At temperature between 2000 and 2500 K the opposite phenomenon occurs.

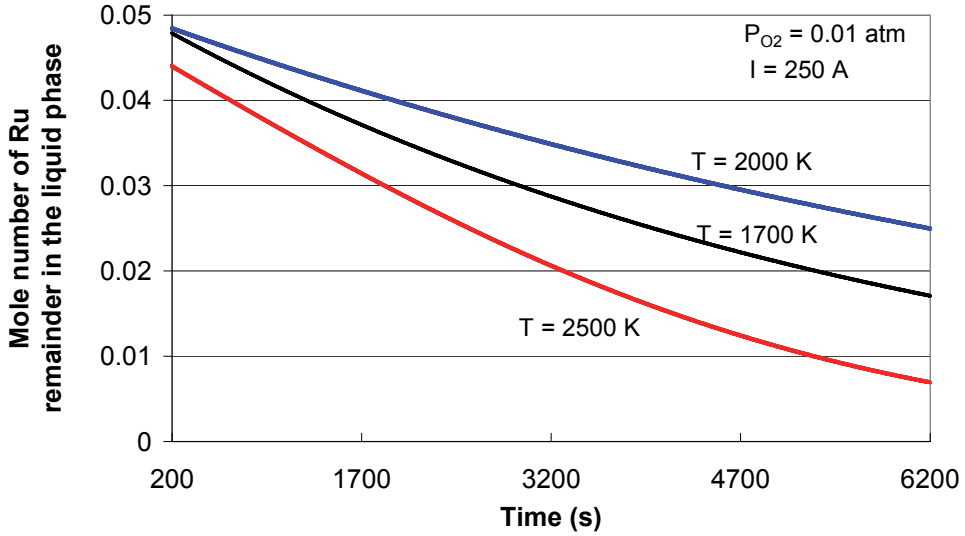

Fig. 3. Influence of temperature on Ru volatility

9.2 Effect of the atmosphere

The furnace atmosphere is supposed to be constantly renewed with a composition similar to that of the carrier gas made up of the mixture argon/oxygen. For this study, the temperature is fixed at 2500 K, the total pressure P at 1 atm and the plasma current I at 250 A. Figures 4 and 5 present the results obtained for ^{60}Co and ^{106}Ru as a function of P_{O_2}.

For ^{60}Co, a decrease in the vaporization speed and in the volatilized quantity can be noticed when the quantity of oxygen increases, i.e., when the atmosphere becomes more oxidizing. The presence of oxygen in the carrier gas supports the incorporation of Cobalt in the containment matrix. The same behavior is observed in the case of ^{137}Cs in accordance with P_{O_2} [8].

When studying the Ruthenium volatility presented in the curves of figure 5 it is found that, contrary to ^{60}Co, this volatility increases with the increase of the oxygen quantity. This difference in the Ruthenium behavior compared to Cobalt can be attributed to the redox character of the majority species in the condensed phase and gas in equilibrium. For ^{60}Co, the oxidation degree of the gas species is smaller than or equal to that of the condensed phase species, hence the presence of oxygen in the carrier gas supports the volatility of ^{60}Co. Whereas ^{106}Ru, in the liquid phase, has only one form (Ru). Hence, the oxidation degree of the gas species is greater than or equal to that of liquid phase species and any addition of oxygen in the gas phase increases its volatility.

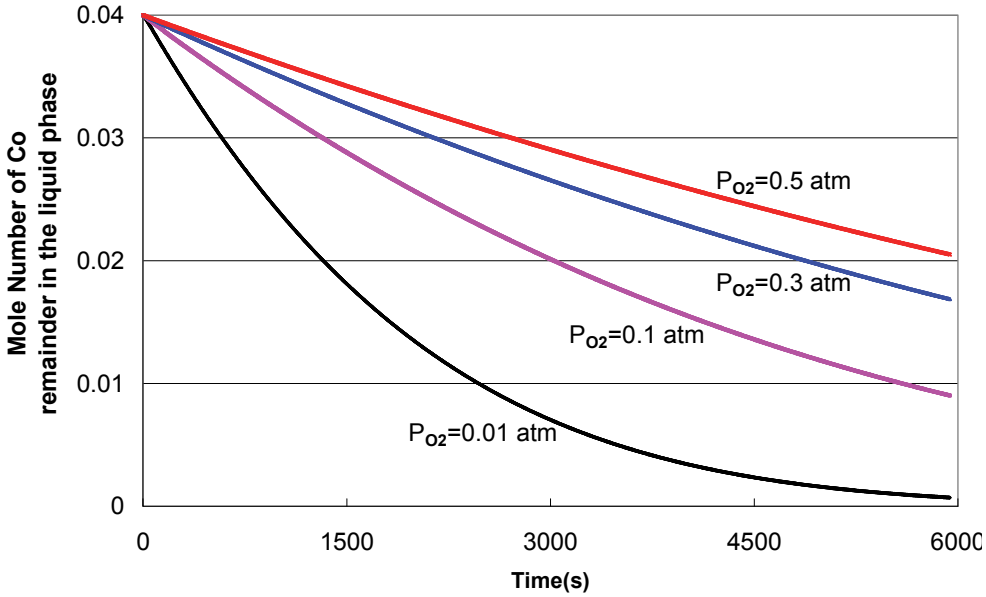

Fig. 4. Influence of the atmosphere nature on the Co volatility

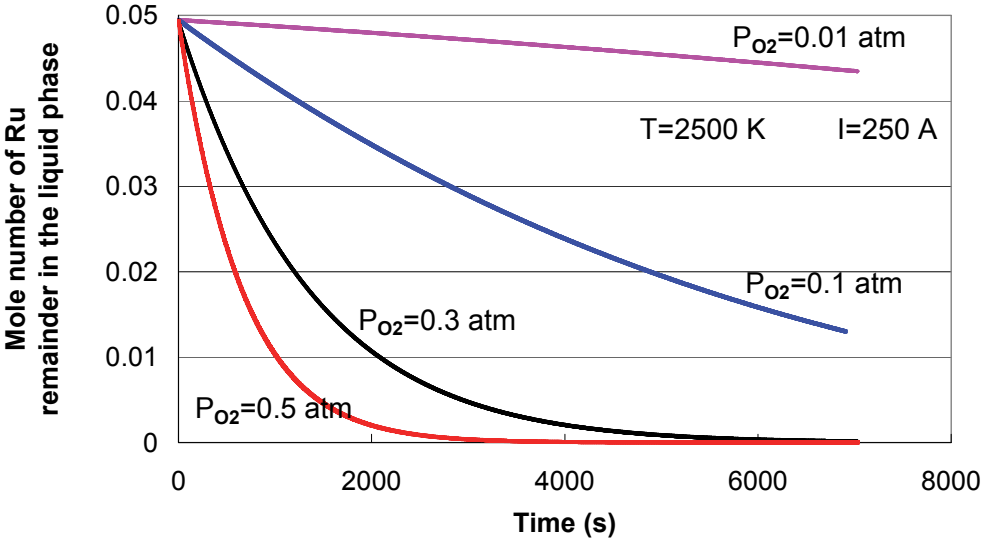

Fig. 5. Influence of the atmosphere nature on the Ru volatility

9.3 Influence of current

To study the influence of the current on the radioelement volatility, the temperature and the partial pressure of oxygen are fixed, respectively, at 2200 K and at 0.2 atm, whereas the plasma current is varied from 0 A to 600 A. Figures 6 and 7 depict the influence of plasma

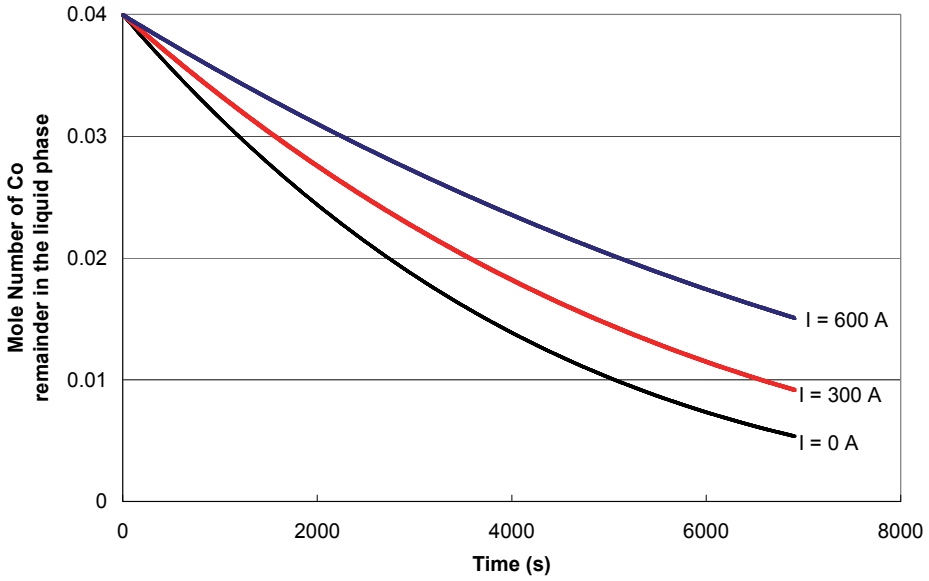

Fig. 6. Influence of plasma current on Co volatility

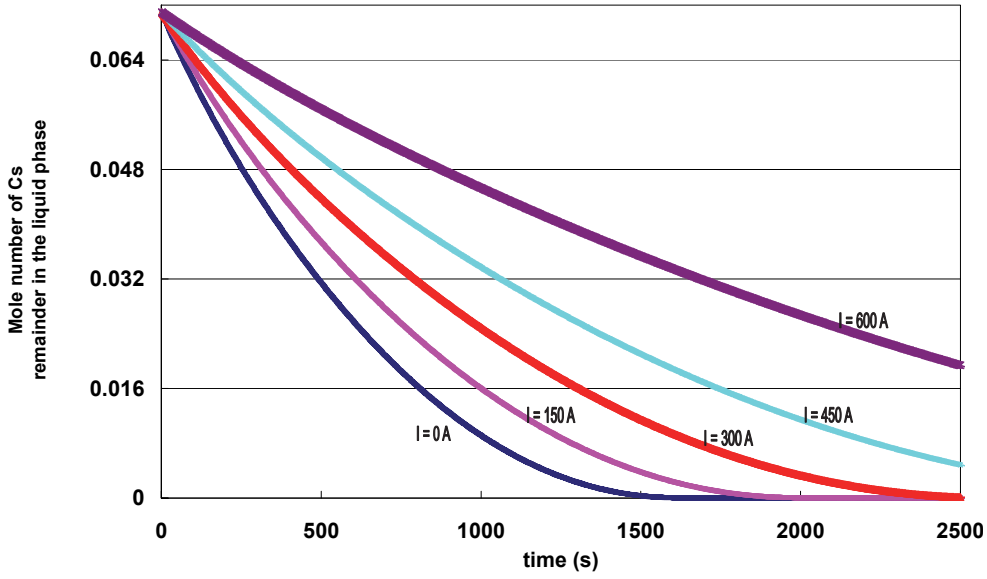

Fig. 7. Influence of current on Cs volatility

current on the Cobalt and Cesium volatility. The curves of these figures indicate that the increase of the plasma current considerably increases both the vaporization speed and the vaporized quantity of ^{60}Co and ^{137}Cs.
In the model, the electrolyses effects are represented by the ions flux retained by the bath, given by equation (32), which depends essentially on the plasma current. As the evaporation kinetics decrease with intensity current, the bath is in cathode polarization which prevents ^{60}Co and ^{137}Cs from leaving the liquid phase. Theses results assert the validity of equation (32) used by this computer code and conforms to the experimental results obtained by spectroscopy emission [9, 16]. The same behavior is observed in the case of ^{106}Ru as a function of plasma current.

9.4 Influence of matrix composition

Three matrices are used in this study and their compositions are given in table 4. Matrix 1 is obtained by the elimination of 29 g of Silicon for each 100 g of basalt, whereas matrix 2 is obtained by the addition of 65 g of Silicon for each 100 g of basalt, and matrix 3 is basalt. Figures 8 and 9 depict the influence of containment matrix composition, respectively, on the Cobalt and Cesium volatility. The increase of silicon percentage in the containment matrix supports the incorporation of ^{60}Co and ^{137}Cs in the matrix.
For ^{137}Cs, the increase of silicon percentage in the containment matrix is accompanied by an increase in mole numbers of $Cs_2Si_2O_5$ and $Cs_2Si_4O_9$ in the condensed phase. The presence of these two species in addition to Cs_2SiO_3 in significant amounts (between 10^{-3} and 10^{-2} mole) prevents Cs from leaving the liquid phase and reduces its volatility. For Cobalt, the increase of silicon percentage in the system supports the confinement of ^{60}Co in the condensed phase in the Co_2SiO_4 form. Ruthenium is not considered in this study because, in the liquid phase, it has only the Ru form and any modification in the containment matrix has no effect on its volatility.

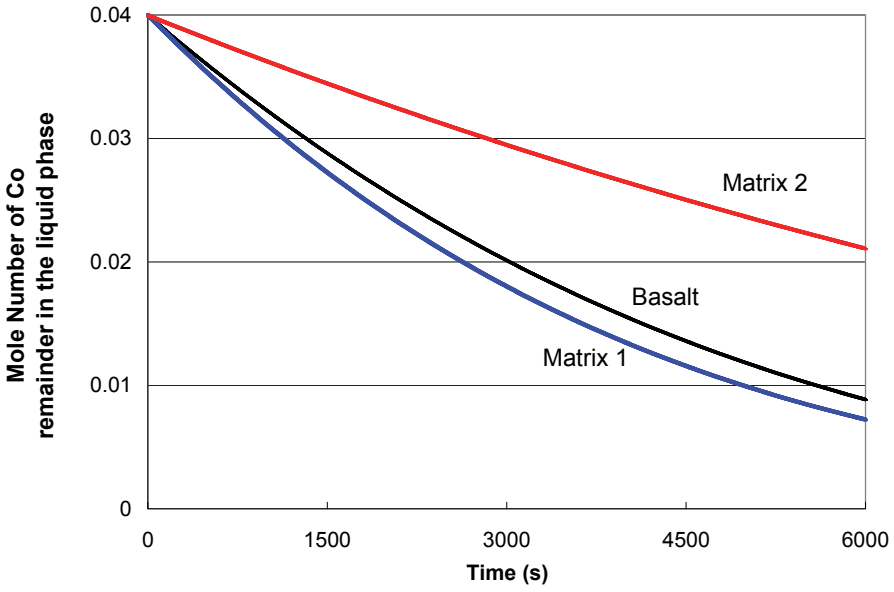

Fig. 8. Influence of matrix composition on Co volatility

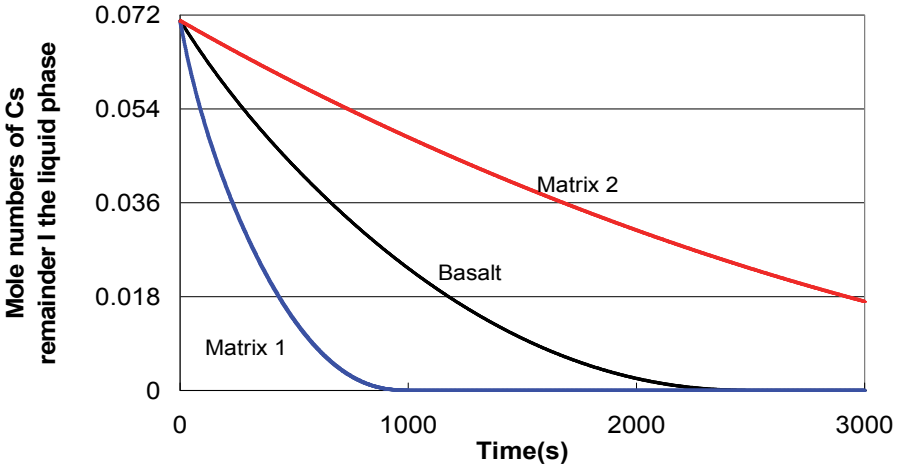

Fig. 9. Influence of matrix composition on Cs volatility

9.5 Distribution of Co and Ru on its elements during the treatment

Figures 10 and 11 depict the distribution of Cobalt components on the liquid and gas phases. In the gas phase, Cobalt exists essentially in the form of Co and, to a smaller degree, in the CoO form. In the liquid phase, Cobalt is found in quasi totality in CoO, Co and Co_2SiO_4 forms. Figure 12 presents the distribution of Ruthenium components on the liquid and gas phases. In the gas phase, Ruthenium exists essentially in the form of RuO_2 and, to a smaller degree, in the form of RuO_3 and RuO, whereas Ru and RuO_4 exist in much smaller quantities compared to the other forms. In the liquid phase, Ruthenium has only the Ru form.

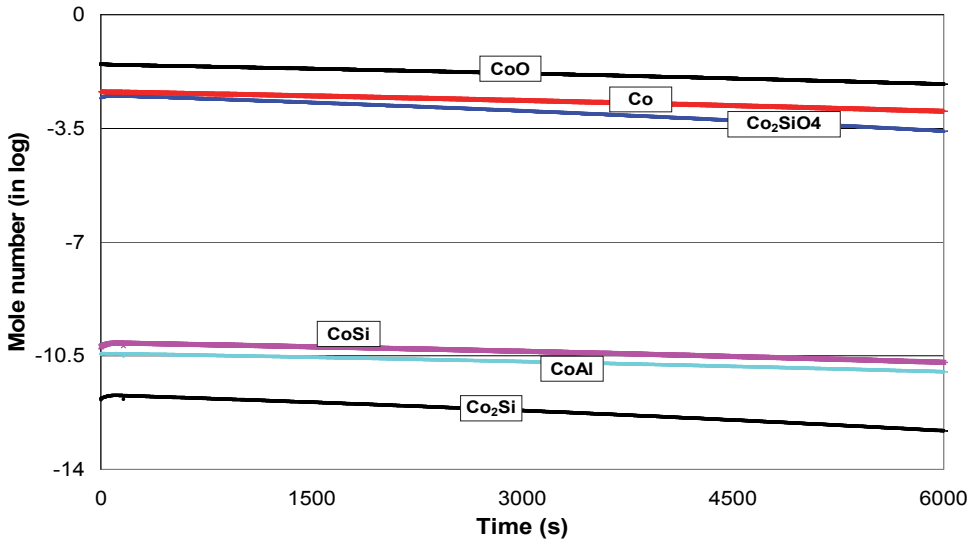

Fig. 10. Variation of the mole numbers of Co composition in the gas phase

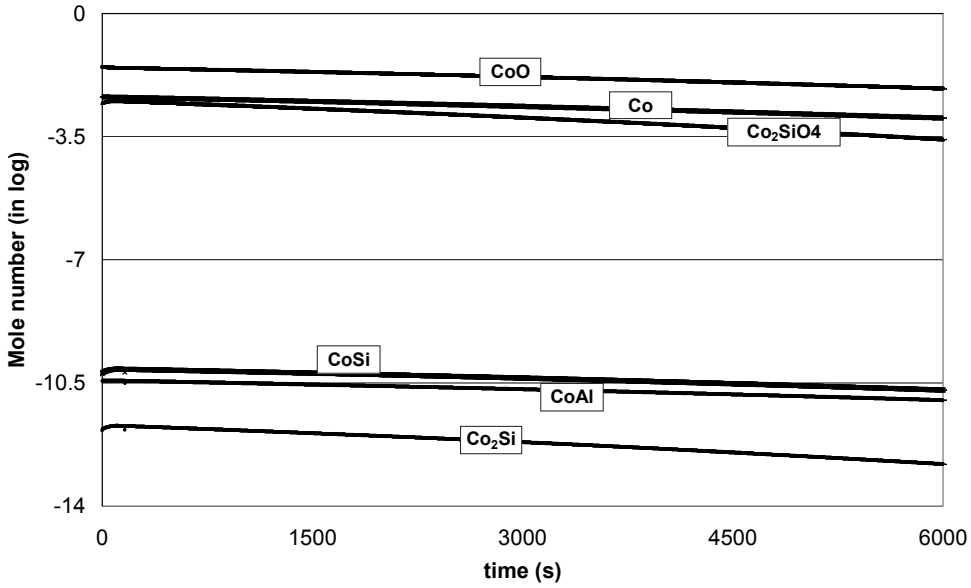

Fig. 11. Variation of the mole numbers of Co composition in the liquid phase

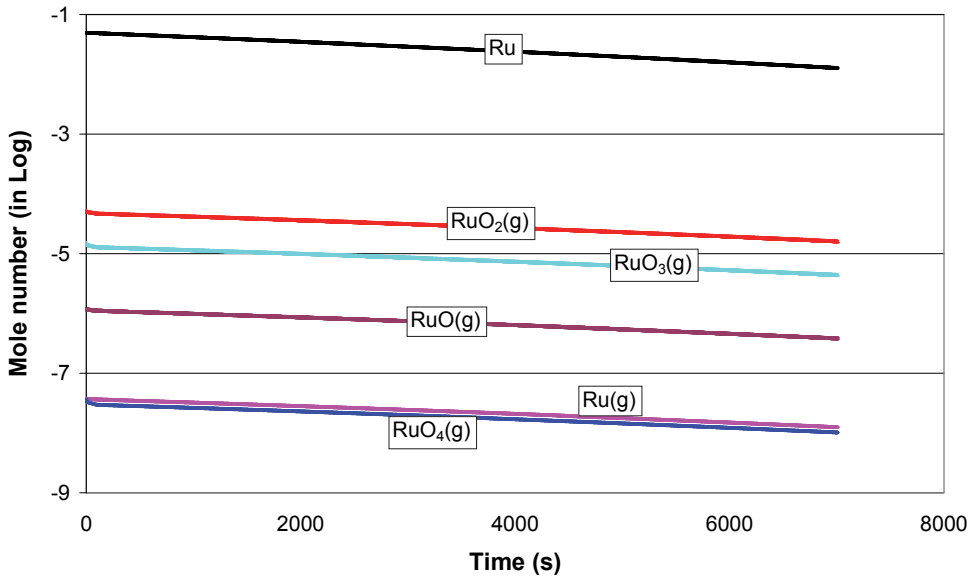

Fig. 12. Variation of the mole numbers of Ru composition in the gas and liquid phases

10. Comparison with the experimental results

The experimental setup is constituted of a cylindrical furnace, which supports a plasma device with twin-torch transferred arc system. The two plasma torches have opposite polarity. The reactor and the torches are cooled with water under pressure by two completely independent circuits. Argon is introduced at the tungsten cathode and the copper anode while oxygen, helium and hydrogen are injected through a water-cooled pipe [21]. To perform spectroscopic diagnostic above the molten surface, a water cooled stainless-steel crucible is placed under the coupling zone of the twin plasma torches. This crucible is filled with basalt and 10 % in oxide mass of Cs. On the cooled walls, the material does not melt and, hence, runs as a self-crucible. The intensities of the Ar line (λ = 667.72 nm) and the Cs line (λ = 672.32 nm) are measured by using an optical emission spectroscopy method (figure 13). The molar ratio Cs/Ar is deduced from the intensity ratio of the two lines [9, 16].

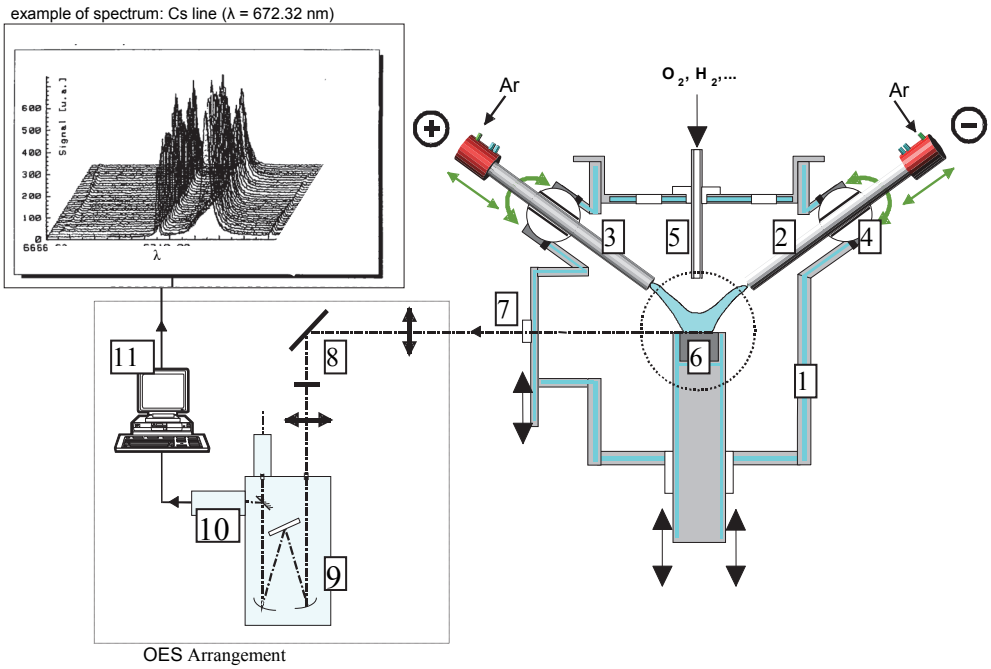

Fig. 13. Schematic of the experimental setup: (1) reactor vessel; (2) cathode torch; (3) anode torch; (4) spherical-bearing arrangement; (5) injection lance; (6) crucible; (7) porthole; (8) optical system; (9) monochromator; (10) OMA detector; (11) computer.

Figure 14 shows the code results in comparison with the experimental measurements. This figure reveals that the experimental and simulation results are relatively close. The

small difference between the simulation results and the experimental measurements can be attributed to the measurements errors. In fact, the estimated error committed on the measurement of the ratio Cs/Ar is around 10% [9, 16]. The model calculations assumed a bath fully melted and homogeneous from the beginning (t = 0s), while in practice the inside of the crucible is not fully melted and there is a progress of fusion front that allows a permanent alimentation of the liquid phase in elements from the solid. These causes explain the perturbation of the experimental measurements and the large gap between these measurements and the results obtained by the model in the first few minutes.

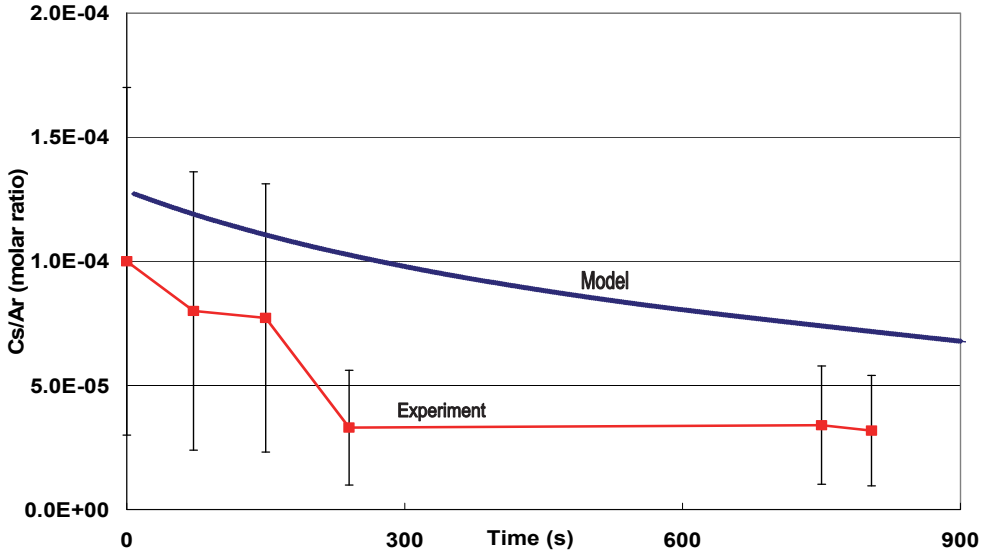

Fig. 14. Comparison between the simulation and experimental results in the case of Cs

11. Conclusion

The objective of this method is to improve the evaporation phenomena related to the radioelement volatility and to examine their behavior when they are subjected to a heat treatment such as vitrification by arc plasma. The main results show that up to temperatures of about 2000 K, Cobalt is not volatile. For temperatures higher than 2000 K, any increase in molten bath temperature causes an increase in the Cobalt volatility. Ruthenium, however, has a different behavior with temperature compared to Cobalt. For temperatures less than 1700 K and beyond 2000 K, Ruthenium volatility increases when temperature increases. Whereas in the temperature interval from 1700 K to 2000 K, any increase of temperature decreases the Ru volatility. Oxygen flux in the carrier gas supports the radioelement incorporations in the containment matrix, except in the case of the Ruthenium which is more volatile under an oxidizing atmosphere. For electrolyses

effects, an increase in the plasma current considerably increases both the vaporization speed and the vaporized quantities of Cs and Co. The increase of silicon percentage in the containment matrix supports the incorporation of Co and Cs in the matrix. The comparison between the simulation results and the experimental measurements reveals the adequacy of the computer code.

12. Acknowledgements

This work was supported by the National Plan, for Sciences, Technology and innovation, at Al Imam Muhammed Ibn Saud University, college of Sciences, Kingdom of Saudi Arabia.

13. Nomenclature

J_i^D :	diffusion flux density for the gas species *i*.
J_i^R :	flux retained by the bath for the gas species *i*.
G:	free energy of a system
g_i^0 :	formation free enthalpy of a species under standard conditions,
R :	perfect gas constant,
T :	temperature,
n_i :	mole number of species *i*.
p_i :	partial pressure of a gas species
X_i :	molar fraction of species *i* in the liquid phase.
P :	total pressure,
$\bar{n}_g$:	total mole number of the species in the gas phase,
$\bar{n}_l$:	total mole number of the species in the condensed phase
a_{ij} :	atoms grams number of the element *j* in the chemical species *i*
B_j :	total number of atoms grams of the element *j* in the system.
n_{O2}:	equivalent mole number of oxygen
L:	Lagrange function
$\prod_j$:	Lagrange multipliers
$\xi(n_i)$:	Taylor series expansion of F (F=G/RT)
$n_{O\text{-}j}$:	mole number of oxygen in the liquid phase related to metal 'J'
n_{M_j} :	total mole number of metal 'J' in the liquid phase
υ_{ij} :	valence of metal 'J' in oxide 'i'
A:	value of interface surface
J_i :	interfacial density of molar flux of a species 'i'
δ_i :	boundary layer thickness
D_i :	diffusion coefficient
m :	mass of the substance produced at the electrode
Q :	total electric charge passing through the plasma
q :	electron charge
v :	valence number of the substance as an ion (electrons per ion)

M : molar mass of the substance
N_A : Avogadro's number
I: current in the plasma
F: Faraday's constant
$T^* = T\frac{k}{\varepsilon_{ij}}$: reduced temperature
K : Boltzmann constant
σ_{ij}: collision diameter
ε_{ij} : binary collision energy
$\Omega_{ij}^{(1.1)^*}(T^*)$: reduced collision integral
r_i : radius of a particle

14. References

[1] Eriksson G., Rosen E., J. Chemica Scripta, 4:193, (1973)
[2] Pichelin G., Rouanet A., *J. Chemical Engineering Science,* 46:1635, (1991)
[3] Badie J. M., Chen X., Flamant G., *J. Chemical Engineering Science,* 52:4381, (1997)
[4] Ghiloufi I., Baronnet J. M., *J. High Temperature Materials Process,* volume 10, Issue 1, p. 117-139, (2006)
[5] Ghiloufi I., *J. High Temperature Materials Process,* volume12, Issue1, p.1-10, (2008)
[6] Ghiloufi, I., *J. Hazard. Mater.* 163, 136-142, (2009)
[7] Ghiloufi, I., *J. Plasma Chemistry and Plasma Processing,* Volume 29, Number 4 321-331, (2009)
[8] Ghiloufi I., Amouroux J., *J. High Temperature Materials Process,* volume 14, Issue 1, p. 71-84, (2010)
[9] Ghiloufi I., Girold C., *J. Plasma Chemistry and Plasma Processing,* 31:109–125, (2011)
[10] Serway, Moses, and Moyer, *Modern Physics*, third edition (2005)
[11] Hirschfelder, J. O., Curtis, C. F., and Bird, R. B., (1954), *Molecular Theory of Gases and Liquids*, John Willey & Sons, New-York.
[12] Razafinimanana, M., (1982), "Etude des coefficients de transport dans les mélanges hexafluorure de soufre azote application à l'arc électrique", Thèse, Université de Toulouse.
[13] Shannon R. D., Prewitt C. T., (1969), "Effective Ionic Radii Oxides and Fluorides", Acta Cryst., Vol. B25, pp. 925-946.
[14] Bird R. B., Stewart W. E., Lightfood E. N., (1960): "Transport phenomena" Ed. Willy.
[15] M. Jorda, E. Revertegat, Les clefs du CEA, n°30, 1995, pp. 48–61.
[16] C. Girold, Incinération/vitrification de déchets radioactifs et combustion de gaz de pyrolyse en plasma d'arc, Ph.D. Thesis, Université de Limoges, France, 1997.
[17] Outokumpu HSC Chemistry, Chemical Reaction and Equilibrium Modules with Extensive Thermochemical Database, Version 6, (2006)
[18] Barin I., Thermochemical Data of Pure Substances, Weinheim; Basel, Switzerland; Cambridge; New York: VCH, (1989)

[19] Chase Malcolm, NIST-JANAF, Thermochemical Tables, Fourth Edition, J. of Phys. and Chem. Ref. Data, Monograph No. 9, (1998)
[20] Landolt-Bornstein, Thermodynamic Properties of Inorganic Material, Scientific Group Thermodata Europe (SGTE), Springer-Verlag, Berlin-Heidelberg, (1999)
[21] S. Megy, S. Bousrih, J.M.,Baronnet, E.A. Ershov-Pavlov, J.K. Williams, D.M. Iddles, J. Plasma Chemistry and Plasma Processing, 15, n° 2, (1995), 309 - 319.

9

Nonequilibrium Fluctuations in Micro-MHD Effects on Electrodeposition

Ryoichi Aogaki[1] and Ryoichi Morimoto[2]
[1]*Polytechnic University, Ryogoku, Sumida-ku, Tokyo,*
[2]*Saitama Prefectural Okubo Water Filtration Plant*
Shuku, Sakura-ku, Saitama-shi, Saitama,
Japan

1. Introduction

In copper electrodeposition under a magnetic field parallel to electrode, it is well known that though the drastic enhancement of deposition rate, a deposit surface receives specific levelling. This is because the Lorentz force generated by the interaction between magnetic field and electrolytic current induces a solution flow called magnetohydrodynamic (MHD) flow with micro-vortex called micro-MHD flow (Figs. 1 and 5a). The former is a laminar main flow, promoting mass transfer process (MHD effect), and the latter emerges inside the boundary layer, which often interacts with nonequilibrium fluctuations controlling electrochemical reactions.

MHD effect is exhibited by the following MHD current equation, where the promotion of mass transfer by the laminar flow is expressed by the increase of the average current density $\langle J_z \rangle$ (Aogaki et al., 1975).

$$\langle J_z \rangle = H^* B_0{}^{1/3} \theta_\infty^{*4/3} \tag{1}$$

where '< >' denotes the average with regard to electrode surface, H^* is a constant, B_0 is the magnetic flux density, and θ_∞^* is the concentration difference between the bulk and surface.

As one of the characteristic results of the electrodeposition in a parallel magnetic field, the interaction of the micro-MHD flow with nonequilibrium fluctuations called symmetrical fluctuations suppresses the three-dimensional (3D) nuclei with the order of 0.1 μm in diameter to yield a flat surface (1st micro-MHD effect) (Aogaki, 2001; Morimoto et al., 2004). However, after long-term deposition in the same magnetic field, instead of leveling, semi-spherical secondary nodules with the order of 100 μm in diameters are self-organized from two-dimensional (2D) nuclei together with the other nonequilibrium fluctuations, i.e., asymmetrical fluctuations (2nd micro-MHD effect) (Aogaki et al., 2008a, 2009a, 2010).

On the other hand, in a magnetic field vertical to electrode surface, minute vortexes vertical to the electrode surface emerge under a macroscopic tornado-like rotation called vertical MHD flow (Fig. 2); the formers come from 2D nucleation, whereas the latter is generated by the distortion of current lines in front of a disk electrode. As a result, a characteristic deposit with regular holes with about 100 μm diameter called micro-mystery circles appears.

Recently, using an electrode fabricated by the electrodeposition in a vertical magnetic field, the appearance of chirality in enantiomorphic electrochemical reactions was found, and it was suggested that the selectivity of the reactions comes from the chirality of the vortexes formed on the electrode (Mogi & Watanabe, 2005; Mogi, 2008).

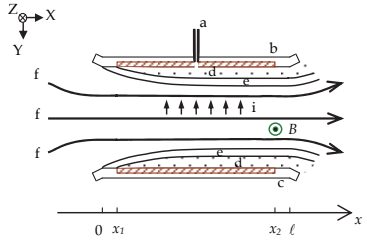

Fig. 1. MHD main flow and boundary layer. a, Luggin capillary; b, working electrode; c, counter electrode; d, diffusion layer; e, hydrodynamic boundary layer; f, streamline (Aogaki et al., 1975).

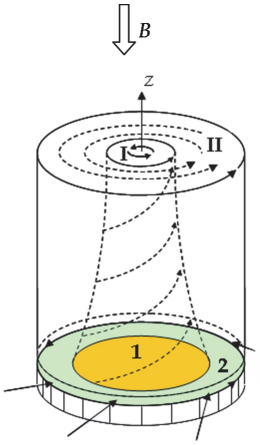

Fig. 2. Vertical MHD flow. 1, electrode; 2, electrode sheath; I, upward spiral flow; II, rotating flow; B, magnetic field (Sugiyama et al., 2004).

All these phenomena are attributed to the evolution or suppression process of nucleus by nonequilibrium fluctuations in a magnetic field. Generally, nucleation is classified into two types; one is 2D nucleation, i.e, expanding lateral growth, and the other is 3D nucleation, i.e., protruding vertical growth. These two types of nucleation result from different nonequilibrium fluctuations. Figure 3 shows two kinds of nonequilibrium fluctuations; one is asymmetrical fluctuation, which arises from electrochemical reactions in an electrical double layer. As shown in this figure, this fluctuation one-sidedly changes from an electrostatic equilibrium state toward cathodic reaction side, controlling 2D nucleation. The other is symmetrical fluctuation changing around an average value of its physical quantity in a diffusion layer. This fluctuation controls 3D nucleation. These concentration fluctuations are defined by

$$c_m(x,y,z,t)^a \equiv C_m(x,y,z,t) - C_m^*(z,t) \tag{2}$$

$$c_m(x,y,z,t)^s \equiv C_m(x,y,z,t) - \langle C(x,y,z,t) \rangle \tag{3}$$

where superscripts 'a' and 's' imply the asymmetrical and symmetrical fluctuations, respectively. $C_m(x,y,z,t)$ and $C_m^*(z,t)$ are the concentration and the concentration in electrostatic equilibrium, respectively. $\langle C(x,y,z,t) \rangle$ is the average concentration over the electrode surface.

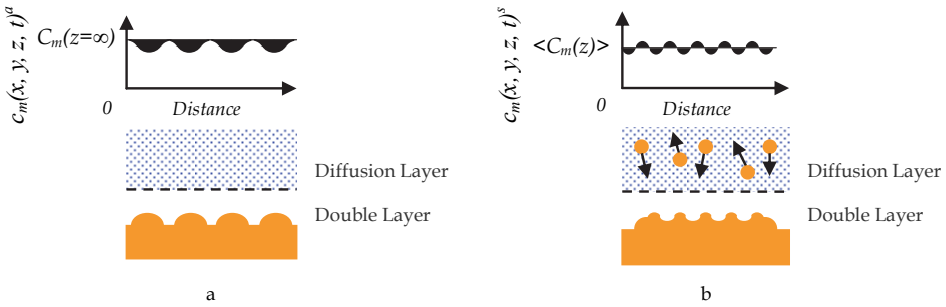

Fig. 3. Nonequilibrium fluctuations in electrodeposition. a, asymmetrical concentration fluctuation, which occurs in the electric double layer, controlling 2D nucleation in the scale of the order of 100 μm. b, symmetrical concentration fluctuation, which occurs in the diffusion layer, controlling 3D nucleation on 2D nuclei in the scale of the order of 0.1 μm. $C_m(z=\infty)$, bulk concentration; $\langle C_m(z) \rangle$, average concentration (Aogaki et al., 2010).

At the early stage of electrodeposition in the absence of magnetic field, there are two different kinds of the unstable processes of fluctuations. The first unstable process takes place in the electric double layer. In the case of electrodeposition without any specific adsorption, the overpotential of the double layer becomes negative with a positive gradient. Supposing that a minute 2D nucleus is accidentally formed in the diffuse layer of the double layer, at the top of the nucleus, due to the positive shifting of the potential, the double-layer overpotential decreases with the nucleation, so that with the unstable growth of the fluctuation, 2D nucleus is self-organized. As the reaction proceeds, outside the double layer, a diffusion layer emerges. In electrodeposition, due to the depletion of metallic ions at the electrode, the concentration gradient is also positive, so that the top of a 3D nucleus contacts with higher concentration than other parts. This means that the concentration overpotential decreases at the top of the nucleus. As a result, mass transfer is enhanced there, then the symmetrical fluctuations turn unstable, and the 3D nucleus is self-organized (Fig. 4a). In the presence of magnetic field, however, except for early stage, depending on the direction of magnetic field, nucleation proceeds in different ways; under a parallel magnetic field, as shown in Fig. 4b, from the interference of the micro-MHD flow to the concentration fluctuation in the diffusion layer, symmetrical fluctuations are always suppressed together with 3D nucleation (1st micro-MHD effect).

In the secondary nodule formation after long-term deposition, it has been newly found that the flow mode of the solution changes from a laminar MHD flow to a convective micro-MHD flow induced by the asymmetrical fluctuations, so that the diffusion layer thickness slowly decreases with time, increasing electrolytic current. The mass transfer to 2D nuclei is thus enhanced, and secondary nodules are self-organized (2nd micro-MHD effect). Figure 5 schematically exhibits the change in the flow mode.

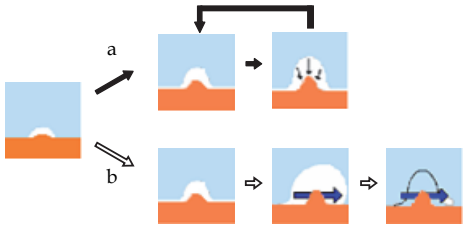

Fig. 4. Disturbance of symmetrical concentration fluctuation around a 3D nucleus by micro-MHD flow. a, without magnetic field, positive feedback process; b, with magnetic field, suppression of fluctuation by micro-MHD flow.

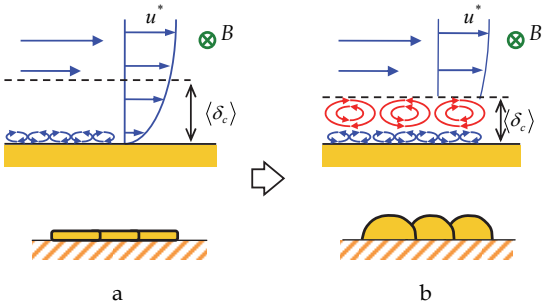

Fig. 5. Change in the flow mode from laminar one (a) to convective one (b). u^*, velocity; B, magnetic flux density; $\langle \delta_c \rangle$, convective-diffusion layer thickness..

In a vertical magnetic field, for the appearance of chirality in vortex motion, ionic vacancy formed with electrodeposition plays an important role; as shown in Fig. 6, ionic vacancy is a vacuum void with a diameter of ca. 1 nm surrounded by ionic cloud (Aogaki, 2008b; Aogaki et al., 2009b), which expands the distance between solution particles, decreasing their interaction as a lubricant. In Fig. 7, it is shown that the vacancy generation during electrodeposition yields two kinds of electrode surfaces; a usual rigid surface with friction under a downward spiral flow of vortex, and a frictionless free surface covered with the vacancies under an upward spiral flow. This is because at the bottom of the downward flow, generated vacancies are swept away from the center, whereas under the upward flow, they are gathered to the center of the bottom. Theoretical examination suggests that the vortex rotation on the free surface is opposite to that on the rigid surface. As shown in Fig. 8, in a system rotating counterclockwise from a bird view, on the rigid surface, due to friction only a downward counterclockwise flow is permitted, while on a free surface, due to slipping of solution, only an upward clockwise flow is permitted.

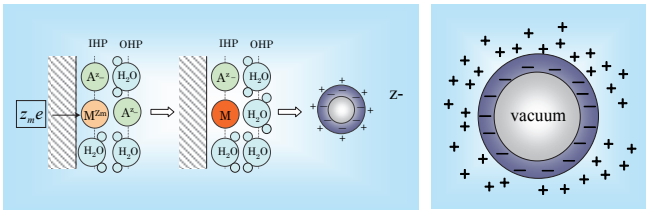

Fig. 6. Ionic vacancy. a, formation process, b, structure (Aogaki, 2008b). IHP, inner Helmholtz plane; OHP, outer Helmholtz plane; M^{zm+}, metallic ion; A^{z-}, counter anion.

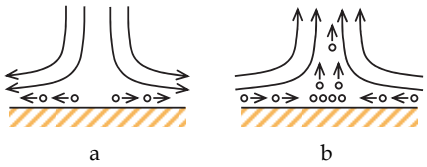

Fig. 7. Formation of free and rigid surfaces by vacancies. ○, Vacancy; a, rigid surface exposed without vacancies; b, free surface covered with vacancies (Aogaki et al., 2009c).

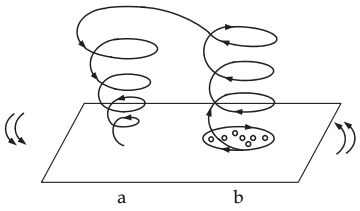

Fig. 8. Two kinds of vortexes on rigid and free surfaces in a counterclockwise rotating system from a bird view. ○, Vacancy; a, rigid surface; b, free surface (Aogaki et al., 2009c).

In such a system, not always magnetic field, but also macroscopic rotation such as vertical MHD flow and system rotation mentioned above are required; the magnetic field generates micro-MHD vortexes, and the macroscopic rotation, as shown in Fig. 9, bestows rotation direction and precession on them, which induces the interference of the vortexes with the concentration fluctuations. On the free surface of 2D nucleus, the metallic ions deposit in keeping the clockwise motion, yielding micro-mystery circles with chiral screw dislocations. This is the process of the formation of micro-mystery circle with chiral structure. On the rigid surface of 2D nucleus, due to friction of the electrode surface, a stationary diffusion layer is formed. Inside the static diffusion layer, in a fractal-like way, 3D nucleation induces smaller micro-MHD vortexes of symmetrical fluctuation, creating concentric deposits called nano-mystery circles. In the following sections, the roles of these nonequilibrium fluctuations will be more precisely elucidated.

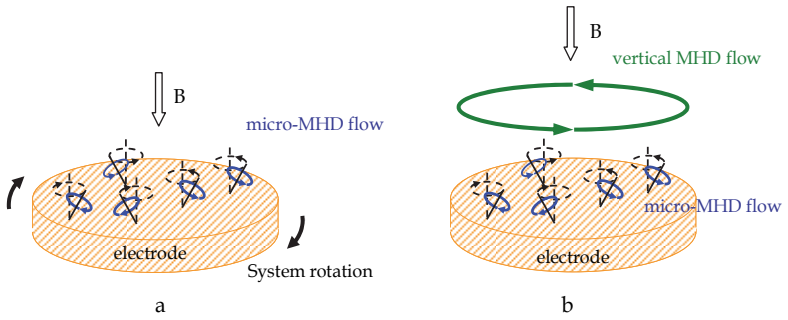

Fig. 9. Precession of micro-MHD flows. a, by system rotation; b, by vertical MHD flow.

2. Instability in electrochemical nucleation

2.1 The first instability occurring in 2D nucleation

Assuming that a minute 2D nucleus is accidentally formed in the diffuse layer belonging to electric double layer, we can deduce the first instability of asymmetrical fluctuations (Aogaki, 1995). The electrochemical potential fluctuation of metallic ion at the outer and inner Helmholtz planes (OHP, IHP) of the nucleus peak is, as will be shown in Eq. (15), expressed by the electrostatic potentials and the concentration overpotential in the electric double layer. The electrostatic potential fluctuation at the top of the nucleus $\phi_2\left(x,y,\zeta^a,t\right)^a$ in the diffuse layer is written by the potential fluctuation at the substrate $\phi_2\left(x,y,0,t\right)^a$ and the potential fluctuation varied by the nucleus $L_\phi^a\zeta\left(x,y,t\right)^a$,

$$\phi_2\left(x,y,\zeta^a,t\right)^a=\phi_2\left(x,y,0,t\right)^a+L_\phi^a\zeta\left(x,y,t\right)^a \tag{4a}$$

where ζ^a is the surface height fluctuation of the 2D nucleus, and L_ϕ^a is the average potential gradient in the diffuse layer, defined by (Aogaki, 1995)

$$L_\phi^a=-\frac{\langle\Phi_2\rangle}{\lambda} \tag{4b}$$

where λ is the Debye length, and $\langle\Phi_2\rangle$ is the average potential fluctuation in the diffuse layer. In the case of deposition at early stage, as shown in Figs. 10 and 12, due to cathodic polarization, the average diffuse layer overpotential $\langle\Phi_2\rangle$ takes a negative value $\langle\Phi_2\rangle<0$ for no specific adsorption or aniodic specific adsorption, and takes a positive value $\langle\Phi_2\rangle>0$ for cationic specific adsorption, so that the average potential gradient in the diffuse layer L_ϕ^a becomes positive and negative, respectively. From Eq. (4a), the difference of the potential fluctuation at the OHP between the top and bottom of the nucleus is thus given by

$$\Delta\phi_2\left(x,y,\zeta^a,t\right)^a=L_\phi^a\ \zeta\left(x,y,t\right)^a \tag{5}$$

where

$$\Delta\phi_2\left(x,y,\zeta^a,t\right)^a \equiv \phi_2\left(x,y,\zeta^a,t\right)^a - \phi_2\left(x,y,0,t\right)^a \tag{6}$$

In the same way as Eq. (5), the difference of the concentration fluctuation in the diffuse layer is expressed by

$$\Delta c_m\left(x,y,\zeta^a,t\right)^a = L_m^a \zeta\left(x,y,t\right)^a \tag{7a}$$

where L_m^a is the average concentration gradient in the diffuse layer, defined by (Aogaki, 1995)

$$L_m^a = -\frac{z_m F}{\lambda RT} C_m^*\left(0,t\right)\left\langle \Phi_2 \right\rangle \tag{7b}$$

where R is the universal gas constant, T is the absolute temperature, z_m is the charge number, F is Faraday constant, and

$$\Delta c_m\left(x,y,\zeta^a,t\right)^a \equiv c_m\left(x,y,\zeta^a,t\right)^a - c_m\left(x,y,0,t\right)^a \tag{8}$$

Since both fluctuations are in the Boltzmann equilibrium in the diffuse layer, from Eqs. (4b) and (7b), the following relationship between L_m^a and L_ϕ^a is obtained

$$L_m^a = -\frac{z_m F}{RT} C_m^*\left(0,t\right) L_\phi^a \tag{9}$$

On the other hand, the concentration overpotential is written by the Nernst equation.

$$H\left(x,y,\zeta^a,t\right) = \frac{RT}{z_m F} \ln\left\{\frac{C_m\left(x,y,\zeta^a,t\right)}{C_m^*\left(z=\infty\right)}\right\} \tag{10}$$

where $C_m^*\left(z=\infty\right)$ is the bulk concentration. From Eq. (2), the concentration at the top of the projection is written as

$$C_m\left(x,y,\zeta^a,t\right) = C_m^*\left(0,t\right) + c_m\left(x,y,\zeta^a,t\right)^a \tag{11}$$

Under the condition

$$\left|c_m\left(x,y,\zeta^a,t\right)^a\right| << C_m^*\left(0,t\right) \tag{12}$$

Eq. (10) leads to the concentration overpotential fluctuation

$$\delta H\left(x,y,\zeta^a,t\right)^a = \frac{RT}{z_m F}\frac{c_m\left(x,y,\zeta^a,t\right)^a}{C_m^*\left(0,t\right)} \tag{13}$$

where the approximation

$$C_m^*\left(x,y,\zeta^a,t\right) \approx C_m^*\left(0,t\right) \tag{14}$$

is used. Therefore, expanding the potential area to Helmholtz layer, we obtain the difference of the electrochemical potential fluctuation between the top and bottom of the nucleus.

$$\Delta\delta\overline{\mu}_m\left(x,y,\zeta^a,t\right)^a = z_m F\left\{\Delta\phi_1\left(x,y,t\right)^a + \Delta\phi_2\left(x,y,\zeta^a,t\right)^a\right\} + \frac{RT}{C_m^*\left(0,t\right)}\Delta c_m\left(x,y,\zeta^a,t\right)^a \tag{15}$$

$\phi_1\left(x,y,t\right)^a$ and $\phi_2\left(x,y,z,t\right)^a$ are the fluctuations of the electric potentials at the inner Helmholtz plane (IHP) (Helmholtz layer overpotential) and outer Helmholtz plane (OHP) (diffuse layer overpotential), respectively. Substitution of Eqs. (5) and (7a) into Eq. (15) with Eq. (9) leads to the cancellation of $\Delta\phi_2\left(x,y,\zeta^a,t\right)^a$ and $\Delta c_m\left(x,y,\zeta^a,t\right)^a$, so that only the term of the Helmholtz layer overpotential $\Delta\phi_1\left(x,y,t\right)^a$ survives. i.e.,

$$\Delta\delta\overline{\mu}_m\left(x,y,\zeta^a,t\right)^a = z_m F\Delta\phi_1\left(x,y,t\right)^a \tag{16}$$

$\phi_1\left(x,y,t\right)^a$ and $\phi_2\left(x,y,\zeta^a,t\right)^a$ are related by the differential double-layer potential coefficient $\left(\partial\langle\Phi_1\rangle/\partial\langle\Phi_2\rangle\right)_\mu$ (Aogaki, 1995).

$$\phi_1\left(x,y,t\right)^a = \left(\frac{\partial\langle\Phi_1\rangle}{\partial\langle\Phi_2\rangle}\right)_\mu \phi_2\left(x,y,\zeta^a,t\right)^a \tag{17}$$

where it should be noted that $\langle\Phi_1\rangle$ and $\langle\Phi_2\rangle$ denote the average values of the asymmetrical overpotential fluctuation of the Helmholtz and diffuse layers $\left\langle\phi_1\left(x,y,t\right)^a\right\rangle$ and $\left\langle\phi_2\left(x,y,\zeta^a,t\right)^a\right\rangle$, respectively. The subscript μ suggests that chemical potentials (activities) of the components are kept constant. Therefore, $\Delta\phi_1\left(x,y,t\right)^a$ is expressed by

$$\Delta\phi_1\left(x,y,t\right)^a = \left(\frac{\partial\langle\Phi_1\rangle}{\partial\langle\Phi_2\rangle}\right)_\mu \Delta\phi_2\left(x,y,\zeta^a,t\right)^a \tag{18}$$

Substituting Eq. (18) into Eq. (16), we have

$$\Delta\delta\overline{\mu}_m\left(x,y,\zeta^a,t\right)^a = z_m F\left(\frac{\partial\langle\Phi_1\rangle}{\partial\langle\Phi_2\rangle}\right)_\mu \Delta\phi_2\left(x,y,\zeta^a,t\right)^a \tag{19}$$

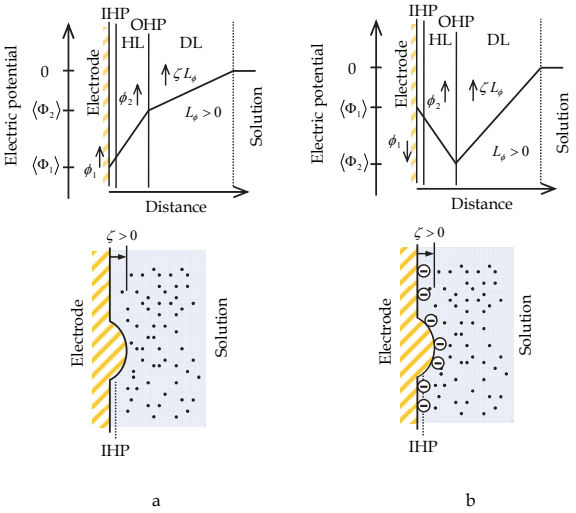

Fig. 10. Electrostatic potential distribution in the electric double layer. a; the case when specific adsorption is weak or absent, b; the case when anionic specific adsorption is strong. HL, Helmholtz layer; DL, diffuse layer.

The sign of the difference of the electrochemical potential fluctuation is determined by the difference of the potential fluctuation in the diffuse layer and the differential double-layer potential coefficient. As shown in Fig.10, in the case where no specific adsorption or anionic specific adsorption takes place, since the former is positive in the early stage of deposition (Eq. (5)), the sign of the electrochemical potential fluctuation depends on the latter value. When the specific adsorption of anion is absent or weak, i.e., $\left(\partial\langle\Phi_1\rangle/\partial\langle\Phi_2\rangle\right)_\mu > 0$ is fulfilled, $\Delta\delta\overline{\mu}_m\left(x,y,\zeta^a,t\right)^a$ becomes positive. In view of the cathodic negative polarization in the diffuse layer, this means that at the top of the peak, the reaction resistance decreases, so that the nucleation turns unstable. In the case of strong specific adsorption of anion, due to the minimum point of the potential at the OHP shown in Fig.10b, on the contrary, $\left(\partial\langle\Phi_1\rangle/\partial\langle\Phi_2\rangle\right)_\mu < 0$ is derived. As a result, the difference of the electrochemical-potential fluctuation in Eq. (19) becomes negative, which heightens the reaction resistance, leading to stable nucleation. When cationic specific adsorption occurs, as shown in Fig. 12b, due to negative potential gradient, . $\Delta\phi_2\left(x,y,\zeta^a,t\right)^a$. becomes negative (Eq. (5)). Since cation does not yield intense specific adsorption, the potential distribution does not have a maximum point, so that $\left(\partial\langle\Phi_1\rangle/\partial\langle\Phi_2\rangle\right)_\mu$ >0 is held. Therefore, $\Delta\delta\overline{\mu}_m\left(x,y,\zeta^a,t\right)^a < 0$ leads to stable nucleation. Namely, at early stage, specific adsorption always suppresses 2D nucleation.

Without strong adsorption of anion or cation, the deposition process is accelerated, so that the asymmetrical fluctuation turns unstable, finally the 2D nucleus is self-organized. It is concluded that the asymmetrical fluctuations control the total electrode reaction, and the total electrolytic current increases.

2.2 The second instability in 3D nucleation

As the reaction proceeds, outside the double layer; a diffusion layer is simultaneously formed, where the second instability occurs. According to the preceding paper (Aogaki et al., 1980), Fig. 11 shows the potential distribution in the diffusion layer, where an embryo of 3D nucleus is supposed to emerge. Since in the diffusion layer, due to metal deposition, the average concentration gradient of the metallic ion L_m becomes positive, the difference of the concentration fluctuation between the top and bottom of the embryo becomes positive.

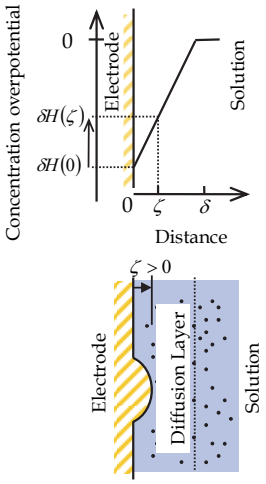

Fig. 11. Concentration distribution of metallic ion in the diffusion layer.

$$\Delta c_m\left(x,y,\zeta^s,t\right)^s = L_m\zeta\left(x,y,t\right)^s \ (>0) \tag{20}$$

where ζ^s is the surface height fluctuation of 3D nucleus. As will be discussed later, with the average thickness of the convective-diffusion layer $\langle\delta_c\rangle$ (> 0) and the concentration difference between the bulk and surface θ_∞^* (> 0), the average concentration gradient of the diffusion layer is written by

$$L_m \equiv \frac{\theta_\infty^*}{\langle\delta_c\rangle} \ (>0) \tag{21}$$

According to Eqs. (3) and (13), for the symmetrical fluctuations, it is held that the difference of the concentration overpotential is also positive in the following,

$$\Delta\delta H\left(x,y,\zeta^s,t\right)^s = \frac{RT}{z_m F\left\langle C_m\left(x,y,0,t\right)\right\rangle}\ \Delta c_m\left(x,y,\zeta^s,t\right)^s \ (>0) \tag{22}$$

where $\Delta\delta H^s$ is defined by the difference of the fluctuation between the top and the bottom of the nucleus

$$\Delta\delta H\left(x,y,\zeta^s,t\right)^s \equiv \delta H\left(x,y,\zeta^s,t\right)^s - \delta H\left(x,y,0,t\right)^s \tag{23}$$

Since the concentration overpotential takes a negative value for metal deposition, this means that at the top of the nucleus, the concentration overpotential decreases, accelerating instability, i.e., the following unstable condition is always fulfilled.

$$\Delta\delta H\left(x,y,\zeta^s,t\right)^s > 0 \tag{24}$$

Since the concentration gradient is positive, the top of the 3D nucleus contacts with higher concentration than other parts. Namely, the concentration overpotential decreases there, and mass transfer is enhanced. As a result, the symmetrical fluctuations always turn unstable, and the 3D nucleus is self-organized (Fig. 4a). However, in a magnetic field, since the micro-MHD flows interfere with the concentration fluctuation and disturb it, the 3D nucleation is resultantly suppressed together with not always the symmetrical concentration fluctuation but also the micro-MHD flow (1st micro-MHD effect)(Fig. 4b).

2.3 The third instability in secondary nodule formation

At the later stage of deposition, a grown 2D nucleus protrudes out of the double layer into the diffusion layer, which means that the nucleus develops under the same situation as that of 3D nucleation discussed above. At the same time, rate-determining step is changed from electron-transfer in the electric double layer to mass transfer in the diffusion layer, and expressed by the concentration overpotential; instability arises from the fluctuation of the concentration overpotential, δH^a around the 2D nucleus, and the difference of the fluctuation between the top and the bottom of the nucleus $\Delta\delta H^a$ is defined by

$$\Delta\delta H\left(x,y,\zeta^a,t\right)^a \equiv \delta H\left(x,y,\zeta^a,t\right)^a - \delta H\left(x,y,0,t\right)^a \tag{25}$$

Though $\Delta\delta H^a$ is expressed by Eq. (13), i.e.,

$$\Delta\delta H\left(x,y,\zeta^a,t\right)^a = \frac{RT}{z_m F C_m^*\left(0,t\right)}\Delta c_m\left(x,y,\zeta^a,t\right)^a \tag{26}$$

the difference of the concentration fluctuation is given not by L_m^a but by L_m.

$$\Delta c_m\left(x,y,\zeta^a\right)^a = L_m\zeta\left(x,y,t\right)^a \ (>0) \tag{27}$$

Due to the positive values of L_m and $\Delta c_m\left(x,y,\zeta^a\right)^a$, $\Delta\delta H\left(x,y,\zeta^a,t\right)^a$ in Eq. (26) becomes positive. Since cathodic polarization gives negative concentration overpotential, this indicates the decrease of the overpotential at the top of the 2D nucleus. Namely, from the same reason as the second instability, the unstable condition for 2D nucleation in the diffusion layer is always fulfilled. In view of the fact that the 2D nucleation arises from the electrode reaction process in the double layer, this unstable condition must be rewritten by the parameters of the double layer. With the ohmic drop disregarded, assuming that the total overpotential is kept constant, we can derive the following relationship between the fluctuations of the electrochemical potentials at the double layer and the diffusion layer.

$$\Delta\delta\overline{\mu}_m\left(x,y,\zeta^a,t\right)^a = -z_m F\Delta\delta H\left(x,y,\zeta^a,t\right)^a \tag{28}$$

As a result, it is concluded that $\Delta\delta\overline{\mu}_m\left(x,y,\zeta^a,t\right)^a < 0$ is the unstable condition for the secondary nodule formation from 2D nuclei in the diffusion layer. This condition also corresponds to the stable condition in the first instability of 2D nucleation. As shown in Fig. 12a, according to Eq. (19), for an anionic adsorbent, the positive difference $\Delta\phi_2^a$ (> 0) in Eq. (5) from the negative overpotential $\langle\Phi_2\rangle$, and the negative value of the differential double layer potential coefficient $\left(\partial\langle\Phi_1\rangle/\partial\langle\Phi_2\rangle\right)_\mu$ (< 0) due to strong specific adsorption give the unstable condition $\Delta\delta\overline{\mu}_m\left(x,y,\zeta^a,t\right)^a < 0$. For a cationic adsorbent, since usually cation does not yield strong specific adsorption, as shown in Fig. 12b, negative difference $\Delta\phi_2^a$ (< 0) in Eq. (5) from the positive overpotential $\langle\Phi_2\rangle$, and the positive value of $\left(\partial\langle\Phi_1\rangle/\partial\langle\Phi_2\rangle\right)_\mu$ (> 0) due to weak specific adsorption lead to the same unstable condition $\Delta\delta\overline{\mu}_m\left(x,y,\zeta^a,t\right)^a < 0$. Namely, after long-term deposition, whether adsorbent is anionic or cationic, specific adsorption induces unstable secondary nodule formation.

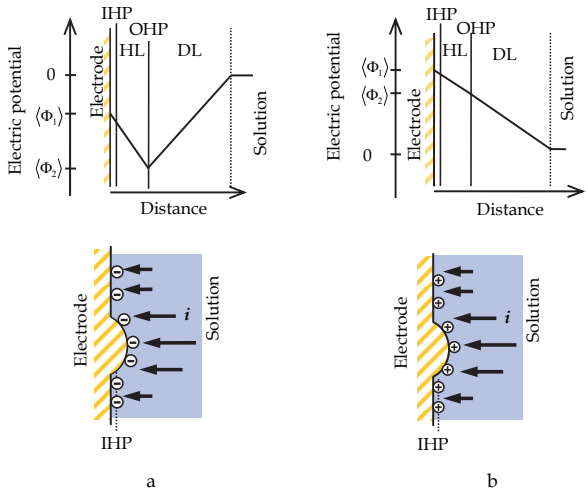

Fig. 12 Potential distribution in the electric double layer by specific adsorption. a, anionic adsorbent; b, cationic adsorbent.

3. First and second micro-MHD effects in a parallel magnetic field

Magnetic field affects the unstable processes of the nucleation, suppressing or enhancing them, so that the morphology of deposit is drastically changed. In a magnetic field, electrochemical reaction induces the fluid motion by Lorentz force called MHD flow, which enhances mass transfer (MHD effect). At the same time, the MHD flow generates minute

vortexes and convection cells called micro-MHD flows, which are the nonequilibrium fluctuations of MHD flow, often interacting with other nonequilibrium fluctuations, i.e., asymmetrical and symmetrical fluctuations accompanying nucleation; for 3D nucleation, the growth of symmetrical fluctuation is suppressed, and the sizes of 3D nuclei decrease (1st micro-MHD effect)(Fig. 4b). For 2D nucleation, asymmetrical fluctuations develop with secondary nodules (2nd micro-MHD effect)(Fig. 5b).

In Fig. 1, the magnetic flux density is applied in z-direction, and the current flows in y-direction, so that the resultant MHD main flow occurs in x-direction. In the boundary layer, micro-MHD flows arise from hydrodynamic and MHD interactions. The equations of the nonequilibrium fluctuations including micro MHD flows on the solution side under a parallel magnetic field have been established (Morimoto et al., in the course of submission-a). The equations are changed to the amplitude equations by Fourier transformation with respect to x- and y-directions. In view of the low electric conductivity and small representative length of electrochemical system, the effect of electromagnetic induction can be disregarded. For calculating the first and second micro-MHD effects, the amplitude equations are solved; the amplitude of the z-component of the velocity fluctuation w is

$$W^0(z,t) = A_2(t) z^2 e^{-kz} \tag{29}$$

and the amplitude of the z-component of the vorticity fluctuation ω_z is

$$\Omega^0(z,t) = -i4T^* \left(\frac{B_0}{\rho\nu}\right) \langle \delta_c \rangle^{-3/4} \left(\frac{k}{k_y}\right) A_2(t) z e^{-kz} \tag{30}$$

Then, at the electrode surface, the amplitude of the concentration fluctuation c_m is expressed by

$$\Theta^0(0,t) = -\frac{4k^3\left(32T^*\langle\delta_c\rangle^{1/4}k^5 + z_m F\theta_\infty^* k_y^2\right) - iB_x^*\langle\delta_c\rangle^{-3/4}k_x\left(16T^*\langle\delta_c\rangle^{1/4}k^5 + 5z_m F\theta_\infty^* k_y^2\right)}{2z_m F D_m \langle\delta_c\rangle k^4 k_y^2\left(8k^3 + iB_x^*\langle\delta_c\rangle^{-3/4}k_x\right)} A_2(t) \tag{31}$$

where k_x and k_y are the x- and y-components of the wave number k, respectively, and

$$T^* \equiv 1.6307\mu_0(\gamma z_m F D_m)^{3/4}\nu^{3/2}\rho^{5/4}L^{1/4}\theta_\infty^{*3/4}B_0^{-9/4} \tag{32}$$

$$B_x^* = 1.6307\left(\gamma z_m F D_m \rho^{-1}\right)^{3/4}\left(\frac{\nu}{D_m}\right)\nu^{-3/2}L^{1/4}\left(\theta_\infty^* B_0\right)^{3/4} \tag{33}$$

The amplitude of the concentration gradient fluctuation at the electrode surface is written by

$$D\Theta^0(0,t) = \frac{8T^*}{z_m F D_m \langle\delta_c\rangle^{3/4}}\left(\frac{k}{k_y}\right)^2 A_2(t) \tag{34}$$

where $D \equiv \partial/\partial z$, the coefficient $A_2(t)$ is an arbitrary function of time, and γ is the cell constant of MHD electrode. μ_0 is the magnetic permeability, ν is the kinematic viscosity,

ρ is the density, and D_m is the diffusion coefficient. B_0 is the magnetic flux density, L is the electrode length, and θ_∞^* is the concentration difference between the bulk and surface. Equations (31) and (34) are connected to calculate $A_2(t)$ with the amplitudes of the fluctuations on the electrode side. In the following sections, the amplitudes of the symmetrical and asymmetrical fluctuations on the electrode side are derived.

3.1 First micro-MHD effect

In electrodeposition, hydrated metallic ions are traveling from the bulk to the electric double layer through the diffusion layer. At the double layer, dehydration first takes place, and adsorption follows at the Helmholtz layer. Transferring electrons, the adsorbed ions become adatoms, and some of them take part in nucleation. Other adatoms, according to the difference of surface energy, transfer along the electrode surface, settling as lattice atoms. Since the rate of electron transfer is sufficiently high, the mass transfer processes in the solution phase and the crystal phase become rate-determining steps, so that the electron transfer process is assumed in quasi-equilibrium state.

The mass balance of adatoms consists of the mass flux density of metallic ions from solution phase and the mass flux densities of adatoms by surface diffusion and incorporation to crystal lattices, i.e., $\vec{j}^s_{flux}$, $\vec{j}^s_{surf}$ and $\vec{j}^s_{inc}$, respectively.

$$\frac{\partial}{\partial t} c_{ad}(x,y,t)^s + \nabla_\perp \cdot \vec{j}^s_{surf} = \vec{n} \cdot \vec{j}^s_{flux} - \vec{n} \cdot \vec{j}^s_{inc} \tag{35}$$

where $c_{ad}(x,y,t)^s$ is the symmetrical fluctuation of the adatom concentration, $\vec{n}$ is the unit normal vector of the electrode surface, and $\nabla_\perp \equiv (\partial/\partial x, \partial/\partial y)$. Equation (35) is explicitly described as (Morimoto et al., in the course of submission-b)

$$\frac{1}{\Omega_m}\frac{\partial}{\partial t}\zeta(x,y,t)^s = -\Omega_m \gamma^* \frac{D_{ad}}{RT} C^*_{ad} \nabla^4_\perp \zeta(x,y,t)^s + D_m \left\{ \vec{n} \cdot \nabla c_m(x,y,z,t)^s \right\} \tag{36}$$

where $\nabla^4_\perp \equiv \partial^4/\partial x^4 + \partial^4/\partial y^4$. Ω_m is the molar volume, γ^* is the surface energy, D_{ad} is the surface diffusion coefficient, and C^*_{ad} is the adatom concentration.

Fourier transformation of Eq. (36) allows us to derive the amplitude equation.

$$\frac{1}{\Omega_m}\frac{\partial}{\partial t} Z^0(t)^s = -\Omega_m \gamma^* \frac{D_{ad}}{RT} C^*_{ad} k^4 Z^0(t)^s + D_m D\Theta^0(0,t)^s \tag{37}$$

Substituting for $D\Theta^0(0,t)^s$ from Eq. (34) in Eq. (37), we finally have the amplitude equation of ζ^s

$$\frac{1}{Z^0(t)^s}\frac{d}{dt} Z(t)^s = p \tag{38}$$

Equation (38) is solved as

$$Z^0(t)^s = Z^0(0)^s \exp(pt) \tag{39a}$$

where p is the amplitude coefficient, i.e.,

$$p = -\Omega_m^2 \gamma^* \frac{D_{ad}}{RT} C_{ad}^* k^4 + \alpha_{mMHD} \Omega_m D_m k \left\{ L_m - \frac{\Omega_m \gamma^*}{RT} \left\langle C_m \left(x, y, 0, t \right) \right\rangle k^2 \right\} \tag{39b}$$

where α_{mMHD} is the micro-MHD coefficient describing the effect of the micro-MHD flow on 3D nucleation, being expressed by

$$\alpha_{mMHD} \equiv \frac{16 T^* \left\langle \delta_c \right\rangle^{1/4} k^5 \left(8k^3 + i B_x^* \left\langle \delta_c \right\rangle^{-3/4} k_x \right)}{4k^3 \left(32 T^* \left\langle \delta_c \right\rangle^{1/4} k^5 + z_m F \theta_\infty^* k_y^2 \right) - i B_x^* \left\langle \delta_c \right\rangle^{-3/4} k_x \left(16 T^* \left\langle \delta_c \right\rangle^{1/4} k^5 + 5 z_m F \theta_\infty^* k_y^2 \right)} \tag{39c}$$

As shown in Eq. (39c), α_{mMHD} is a complex number, acting as a spatial filter for the fluctuations, which controls the first micro-MHD effect, decreasing nucleus size. Actually, in the case of α_{mMHD} = 1, the amplitude coefficient p is consistent with that in zero magnetic field (Aogaki et al., 1980). However, in general, due to the complex number of α_{mMHD}, the amplitude coefficient p also becomes complex number; Eq. (39a) is rewritten as

$$\mathrm{Z}^0 \left(t \right)^s = \mathrm{Z}^0 \left(0 \right)^s \exp\left(\mathrm{Re} pt \right) \exp\left(i \, \mathrm{Im} pt \right) \tag{40a}$$

where $\mathrm{Re} p$ and $\mathrm{Im} p$ denote the real and imaginary parts of p. In Eq. (40a), the part of $\exp\left(i \, \mathrm{Im} pt \right)$ expresses oscillation with time. However, because of the smallness of the $\mathrm{Im} p$, in comparison with the representative time of 3D nucleation, the period of the oscillation is quite long, so that such oscillation can be neglected, i.e.,

$$\mathrm{Z}^0 \left(t \right)^s = \mathrm{Z}^0 \left(0 \right)^s \exp\left(\mathrm{Re} pt \right) \tag{40b}$$

In Eq. (39b), as long as L_m is positive $\mathrm{Re} p$ becomes positive for some wave number k, which leads to the unstable growth of 3D nuclei discussed in Section 2.2. The real part $\mathrm{Re} \alpha_{mMHD}$ is a spatial high-pass filter concerning the wave number of fluctuation. According to Eq. (40b), the component of fluctuation corresponding to the wave number region of $\mathrm{Re} p$ > 0 can unstably develops with time. In this process, since $\mathrm{Re} \alpha_{mMHD}$ restricts such unstable growth of 3D nucleus with smaller wave number (larger nucleus size), first micro-MHD effect emerges.

$\mathrm{Z}^0 \left(0 \right)^s$ is the initial amplitude of the symmetrical surface fluctuation. In view of the thermal motion in atomic scale, assuming an isotropic white noise with normalization, we obtain the equation of the initial amplitude,

$$\left| \mathrm{Z}^0 \left(0 \right)^s \right|^2 = \frac{XY}{\pi} \frac{\left\langle \zeta_{cr}^{s2} \right\rangle}{k_{\max}^2} \tag{41}$$

where $\left\langle \zeta_{cr}^{s2} \right\rangle$ is the mean square height of surface fluctuation in atomic scale at the initial state. X and Y are the x- and y-lengths of the electrode, respectively. $k_{\max}$ is the upper limit of the wave number. Inserting Eq. (40a) into Eq. (37), and using Eq. (39b), we obtain

$$D\Theta^0(0,t)^s = \alpha_{mMHD} k \left(L_m - \frac{\Omega_m \gamma^*}{RT} \left\langle C_m(x,y,0,t) \right\rangle k^2 \right) Z^0(0)^s \tag{42}$$

By using Fourier inversion, $\mathrm{Re}\, D\Theta^0(0,t)^s$ is converted to $\left\{ \partial c_m(x,y,z,t)^s / \partial z \right\}_{z=0}$, i.e.,

$$\left\{ \frac{\partial c_m(x,y,z,t)^s}{\partial z} \right\}_{z=0} = \frac{1}{2\pi} \int_{-\infty}^{\infty} \int_{-\infty}^{\infty} \mathrm{Re}\, D\Theta^0(0,t)^s \exp\left[-i\left(k_x x + k_y y \right) \right] dk_x dk_y \tag{43}$$

Then, the mass flux of the symmetrical fluctuation is given by

$$j_{flux}(x,y,0,t)^s = -D_m \left\{ \frac{\partial c_m(x,y,z,t)^s}{\partial z} \right\}_{z=0} \tag{44}$$

The effective surface heights of the 3D nuclei are also calculated in the following,

$$\zeta(x,y,t)^s = \frac{1}{\Omega_m} \int_0^t j_{flux}(x,y,0,t)^s dt \tag{45}$$

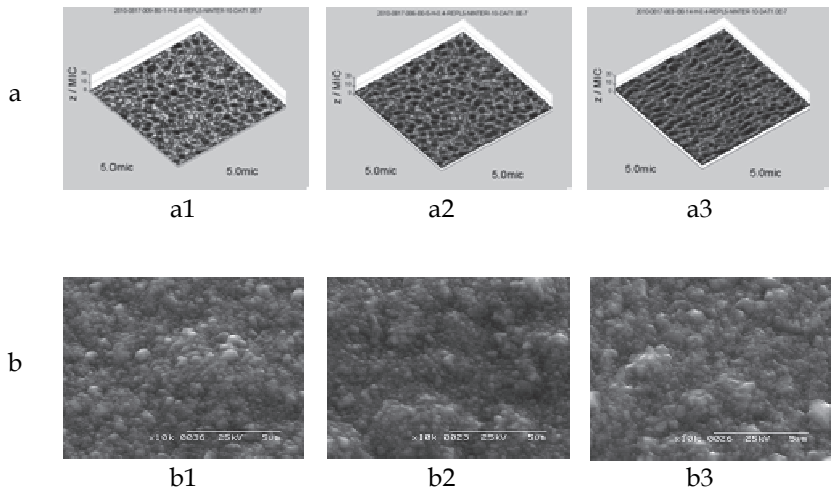

Fig. 13. First micro-MHD effect. a; calculation of the morphology of copper 3D nuclei. a, calculation: a1, B_0 = 0 T; a2, B_0 = 5 T; a3, B_0 = 14 T. b, SEM image: b1, B_0 = 0 T; b2, B_0 = 5 T; b3, B_0 = 14 T (Morimoto et al., in the course of submission-b).

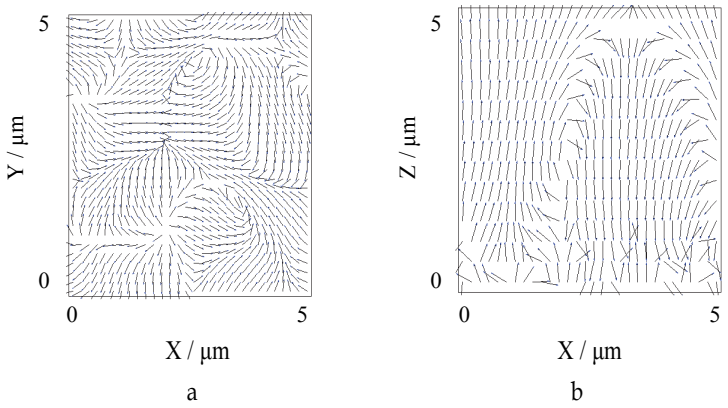

Fig. 14. Horizontal and cross-sectional distributions of micro-MHD flow. a, horizontal distribution; b, cross-sectional distribution. B_0 = 5 T (Morimoto et al., in the course of submission-b).

In Fig. 13, the theoretical calculation and experimental result of first micro-MHD effect are exhibited; as magnetic flux density increases, the size of 3D nucleus decreases. In Fig. 14, the micro-MHD flows corresponding to the 3D nucleation are exhibited.

3.2 Second micro-MHD effect

3.2.1 Instability equation

Due to large scale of length ($\approx$100 μm), the asymmetrical fluctuations controlling 2D nucleation result not from the nucleation process on the electrode surface but from the electrochemical reaction process in the electrical double layer and the micro-MHD flow in the convective diffusion layer; since the term with higher power of wave number is neglected, the equation corresponding to Eq. (37) is simply expressed by

$$\frac{1}{\Omega_m}\frac{\partial}{\partial t}\mathrm{Z}^0(t)^s = D_m D\Theta^0(0,t)^s \tag{46}$$

At the same time, from Eqs. (5), (19), (26) and (28), the following relationship is finally derived as

$$\Theta^0(0,t)^a = -\frac{z_m F}{RT}\left(\frac{\partial\langle\Phi_1\rangle}{\partial\langle\Phi_2\rangle}\right)_\mu L_\phi^a C_m^*(0,t) Z^0(t)^a \tag{47}$$

Since 2D nucleation is controlled by micro-MHD flow, not the surface height fluctuation but the concentration fluctuation determines the Gaussian power spectrum. The amplitude of the concentration fluctuation is thus expressed by

$$\left|\Theta^0(0,t)^a\right|^2 = \frac{XY}{\pi}\theta_\infty^{*2} a^{+2}\exp\left(-a^{+2}k^2\right) \tag{48a}$$

$$a^+ = \frac{\langle\delta_c\rangle}{m} \tag{48b}$$

where a^+ is the autocorrelation distance of the fluctuations, which is defined by the average thickness of the convective-diffusion layer $\langle \delta_c \rangle$ and the number of vortexes m vertically standing in a line between the electrode and the diffusion layer boundary, i.e., the a^+ is equal to the average size of the vortex.
Substituting Eq. (47) into Eq. (46), we obtain the evolution equation of the asymmetrical fluctuation.

$$\frac{\partial \Theta^0(0,t)^a}{\partial t} = A_\theta D \Theta^0(0,t)^a \tag{49a}$$

where

$$A_\theta \equiv \frac{z_m F D_m \Omega_m C_m^*(0,t)\langle \Phi_2 \rangle}{\lambda RT}\left(\frac{\partial \langle \Phi_1 \rangle}{\partial \langle \Phi_2 \rangle}\right)_\mu \tag{49b}$$

The unstable condition is therefore

$$A_\theta > 0 \tag{49c}$$

Namely, with Eq. (49c), the same instability analysis as discussed in Section 2.3 is also possible. Substituting for $\Theta^0(0,t)^a$ and $D\Theta^0(0,t)^a$ from Eqs. (31) and (34) in Eq. (49a), we obtain the equation of the coefficient $A_2(t)$ as follows,

$$\frac{dA_2(t)^a}{dt} = h\left(\langle \delta_c \rangle\right) A_2(t)^a \tag{50a}$$

where

$$h\left(\langle \delta_c \rangle\right) = -16T^* A_\theta k^6 h\left(\langle \delta_c \rangle\right)^+ \tag{50b}$$

The explicit form of $h\left(\langle \delta_c \rangle\right)^+$ is given by

$$h\left(\langle \delta_c \rangle\right)^+ \equiv \frac{\langle \delta_c \rangle^{1/4}\left(8k^3 + iB_x^* \langle \delta_c \rangle^{-3/4} k_x\right)}{4k^3\left(32T^* \langle \delta_c \rangle^{1/4} k^5 + z_m F \theta_\infty^* k_y^2\right) - iB_x^* \langle \delta_c \rangle^{-3/4} k_x \left(16T^* \langle \delta_c \rangle^{1/4} k^5 + 5 z_m F \theta_\infty^* k_y^2\right)} \tag{50c}$$

3.2.2 Calculation of the average thickness of diffusion layer $\langle \delta_c \rangle$

To calculate the coefficient $A_2(t)$ in Eq. (50a), as shown in Eq. (48b), it is necessary to determine the value of $\langle \delta_c \rangle$. After long-term deposition, it is thought that the asymmetrical concentration fluctuation has already developed to the maximum point, so that the secondary nodule formation fulfills the following condition concerning the mean square value of the asymmetrical concentration fluctuation over the electrode surface.

$$\frac{d}{dt}\left\langle \left| c_m\left(x,y,0,t\right)^a \right|^2 \right\rangle \approx 0 \tag{51a}$$

Here, the Rayleigh theorem suggests the relationship

$$\left\langle \left| c_m\left(x,y,0,t\right)^a \right|^2 \right\rangle = \frac{1}{XY}\int_{-\infty}^{\infty}\int_{-\infty}^{\infty} \left| \Theta^0\left(0,t\right)^a \right|^2 dk_x dk_y \tag{51b}$$

From Eq. (51b), more generally, it can be said that the mean square value of the fluctuation is calculated by the integration of that of the amplitude. Although the concentration fluctuation has already grown up to its ultimate state, the gradient of the fluctuation can still develop with new components of the fluctuation; this inevitable development of the micro-MHD convection leads to the decrease of the convective-diffusion layer thickness, promoting mass transfer process (Fig. 5). In terms of the mean square values of the concentration fluctuation and its gradient, the average thickness of the convective-diffusion layer is defined by

$$\left(\frac{\langle \delta_c \rangle}{m}\right)^2 \equiv \frac{\left\langle \left| c_m\left(x,y,0,t\right)^a \right|^2 \right\rangle}{\left\langle \left| \left(\frac{\partial c_m\left(x,y,z,t\right)}{\partial z} \right)_{z=0} \right|^2 \right\rangle} \tag{52}$$

From Eq. (48b), the term on the left hand side in Eq. (52) is equal to the square value of the autocorrelation distance of the fluctuation. By differentiating Eq. (52) with respect to time, the following nonlinear evolution equation is derived.

$$\frac{d\langle \delta_c \rangle}{dt} = -f\left(\langle \delta_c \rangle\right)\langle \delta_c \rangle \tag{53a}$$

where

$$f\left(\langle \delta_c \rangle\right) \equiv \frac{\dfrac{d}{dt}\left\langle \left| \left(\dfrac{\partial c_m\left(x,y,z,t\right)^a}{\partial z} \right)_{z=0} \right|^2 \right\rangle}{2\left\langle \left| \left(\dfrac{\partial c_m\left(x,y,z,t\right)^a}{\partial z} \right)_{z=0} \right|^2 \right\rangle} - \frac{\dfrac{d}{dt}\left\langle \left| c_m\left(x,y,0,t\right)^a \right|^2 \right\rangle}{2\left\langle \left| c_m\left(x,y,0,t\right)^a \right|^2 \right\rangle} \tag{53b}$$

After solving Eq. (53a), the average current density is calculated by

$$\left\langle j_z^a \right\rangle = -z_m F D_m \theta_\infty^* / \langle \delta_c \rangle \tag{54}$$

In the case of copper deposition from sulfuric acid solution, the condition $\left(\partial\langle \Phi_1 \rangle / \partial\langle \Phi_2 \rangle\right)_\mu > 0$ are generally fulfilled (Aogaki et al., 2010), so that from Eq. (49c), a positive diffuse layer overpotential $\langle \Phi_2 \rangle > 0$ is required for secondary nodule formation.

However, since copper deposition is a cathodic reaction, the diffuse layer overpotential is usually supposed negative, of which contradiction is, as discussed in Section 2.3, solved by the adsorption of cation such as proton in the double layer, where the positive charges of protons adsorbed on the Helmholtz layer shift the overpotential to positive side. Such discussion has been validated in Fig. 15 by the scanning electron microscope (SEM) images for the copper depositions with and without the adsorption of protons, i.e., the secondary nodules can be seen only in the case of proton adsorption.

Theoretical current-time curve was calculated by means of Eqs. (53a) and (53b). Figure 16 exhibits the comparison between theoretical calculation and experimental result of current-time curves for the copper deposition. Both curves are in good agreement, quite slowly increasing up to a steady state. From the calculation, it is estimated that the value of $\langle \Phi_2 \rangle$ is small, i.e., the order of 1 mV. To ascertain the above discussion, based on the theory, we calculated the surface morphology of secondary nodules and the velocity distribution of the micro-MHD flows. Figure 17 represents the surface morphology, and Fig. 18 represents the horizontal and vertical velocity distributions of the corresponding micro-MHD vortexes.

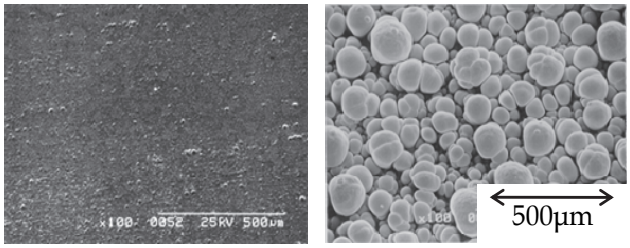

Fig. 15. SEM photos of secondary nodules. a, without the adsorption of H^+ ions; b, with the adsorption of H^+ ions (2nd micro-MHD effect) (Aogaki et al., 2010).

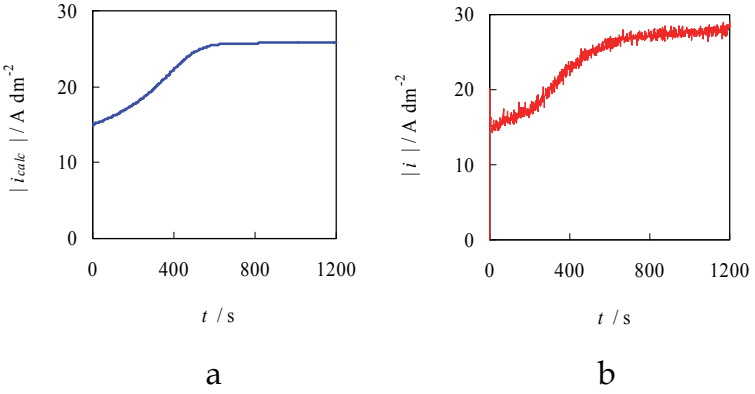

Fig. 16. Current-time curves for secondary nodule formation in copper deposition up to 1200 s. a; calculation, b; experimental result. Applied overpotential, -0.4 V; bulk concentration, 300 mol m^{-3}. B = 5 T (Aogaki et al., 2010).

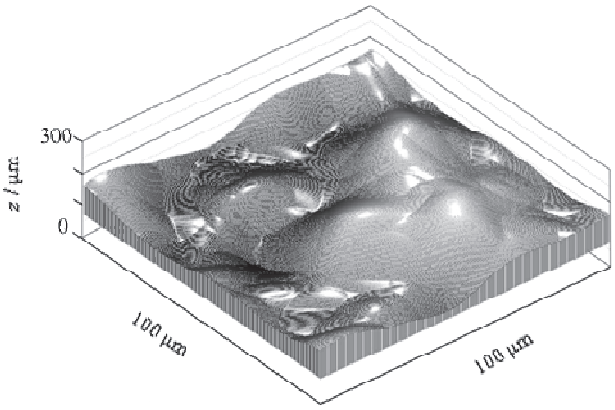

Fig. 17. Calculated surface morphology of copper secondary nodules. B = 5 T. Deposition time is 1000 s, and concentration is 300 mol m^{-3}. Nucleation takes place at the interval of 10 s (Aogaki et al., 2010).

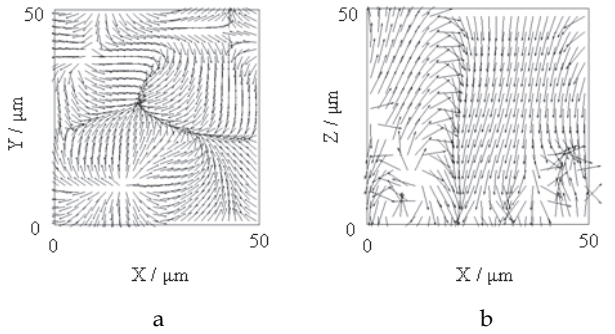

Fig. 18. 2nd micro-MHD flows in the formation of copper secondary nodules at 5 T.
a, horizontal motion at z = 30 μm; b, cross-sectional motion at y = 30 μm, where the xy-plane is taken as an electrode surface, and the z coordinate is used for deposition height.

4. Chirality appearance in a vertical magnetic field

In electrodeposition under a vertical magnetic field, as discussed in 1. Introduction, it is thought that instead of vortexes with chiral symmetry, vortexes having chirality emerge. The best way to make clear the process of the evolution of the chirality is to pursue how chiral symmetry is broken down from a perfectly symmetrical state. Instead of vertical MHD flow, as shown in Fig. 19, a more simple case is taken where an electrochemical system is rotating under a vertical uniform magnetic field, and also it is assumed that current density is uniform and the current lines are vertical everywhere. It should be noted that the whole system including the electrodes and solution rotates all in one body.

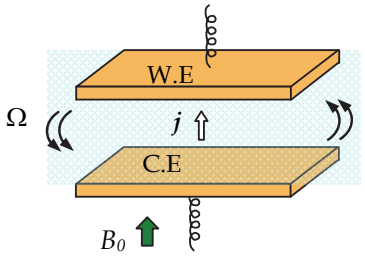

Fig. 19. Schematic of a rotating electrolysis system. W.E, working electrode; C.E., counter electrode; Ω, angular velocity; B_0, magnetic flux density (Aogaki et al., 2009d).

After starting electrodeposition, nonequilibrium fluctuations are introduced; asymmetrical fluctuations for 2D nucleation and symmetrical fluctuations for 3D nucleation. Then, the evolution of the fluctuations is calculated within MHD framework. In this case, whole system is rotating in an angular velocity Ω (> 0) clockwise when seeing the solution from electrode side. The rotating axis of this system is perpendicular, and the magnetic flux density B_0 (>0) is upward applied vertically to the electrodes. The nonequilibrium fluctuation equations to describe the micro-MHD flows and the concentration fluctuation are first derived, which are then transformed to the amplitude equations by Fourier transformation. The amplitude equations are solved under the boundary conditions concerning rigid and free surfaces. For a rigid surface under a downward flow w_r (z-component of the velocity) < 0, at the electrode surface, the amplitude of the concentration gradient fluctuation is expressed by

$$D\Theta_r^0(0,t) = \frac{12a_1}{5z_mFD_mS} \tag{55a}$$

The amplitude of the concentration fluctuation at the electrode surface is

$$\Theta_r^0(0,t) = -\frac{384k^5 + 9z_mFD_mST_rR^*}{160z_mFD_mS\ k^6}a_1 \tag{55b}$$

For a free surface under an upward flow w_f (z-component of the velocity) > 0, at the electrode surface, the amplitude of the concentration gradient fluctuation is

$$D\Theta_f^0(0,t) = \frac{12ka_0}{5z_mFD_mS} \tag{56a}$$

The amplitude of the concentration fluctuation at the electrode surface is

$$\Theta_f^0(0,t) = -\frac{96k^5 - 5z_mFD_mST_fR^*}{40z_mFD_mSk^5}a_0 \tag{56b}$$

where

$$S \equiv \frac{B_0}{\rho\nu} \tag{57}$$

$$T_j \equiv \pm \frac{2\Omega}{\nu} \quad \text{for j = r or f} \tag{58}$$

where as will be discussed later, subscripts 'r' and 'f' imply rigid and free surfaces, respectively. The signs '+' and '-' are taken for the clockwise and counterclockwise rotations corresponding to the signs of the z-component of the vorticity ω_{zj}, respectively when seeing the solution from electrode side. Then, it follows that

$$R^* \equiv \frac{L_m}{D_m} \tag{59}$$

a_0 and a_1 are arbitrary coefficients.

4.1 Formation of micro-mystery circle

4.1.1 Occurrence of chirality

As discussed initially, micro-mystery circle is treated as a 2D nucleus arising from asymmetrical fluctuations. For asymmetrical fluctuation, as discussed in the former sections, due to much larger scale of length of asymmetrical fluctuation than that of symmetrical fluctuation, not nucleation process on the electrode but electrochemical process in the electric double layer controls the total reaction. Therefore, the same amplitude equations as Eqs. (49a) and (49b) are derived. The unstable condition for the micro-mystery circle formation is also the same as Eq. (49c), which means that the micro-mystery circle formation in a vertical magnetic field follows the same unstable condition as the secondary nodule formation in a parallel magnetic field. Namely, when proton adsorption occurs, micro-mystery circle is self-organized.

However, the equations of the coefficients a_0 and a_1 are different from the same kind of equation Eq. (50a). Substituting for $D\Theta_r^0(0,t)$ and $\Theta_r^0(0,t)$ from Eqs. (55a) and (55b) in Eq. (49a), we have the coefficient equation for a rigid surface, i.e.,

$$\frac{da_1^a}{dt} = -A_\theta f_r^a(k) a_1^a \tag{60a}$$

and

$$f_r^a(k) = \frac{128k^6}{128k^5 + 3\alpha_r^{a*}} \tag{60b}$$

where

$$\alpha_r^{a*} = z_m F D_m S^a T_r^a R^* \tag{60c}$$

S^a, T_r^a and R^* are the parameters expressing magnetic field, rotation and mass transfer, respectively. Here, R^* is positive in Eq. (59). To avoid the singular point of k in Eq. (60b), the condition

$$S^a \; T_r^a > 0 \tag{61}$$

is required. For the external magnetic flux density defined by $B_0 > 0$, S^a is also positive in Eq. (57). In view of Eq. (58), T_r^a must be thus positive, being defined by

$$\mathrm{T}_r^a = +\frac{2\Omega}{\nu} \tag{62}$$

Since Ω is the angular velocity of the rotation of the system, and assumed to be positive, i.e., clockwise, the + sign indicates that the micro-MHD flow on a rigid surface rotates clockwise, i.e., in the same direction as that of the system, i.e., $w_r^a < 0$ and $\omega_{zr}^a > 0$.
For a free surface, substituting for $D\Theta_f^0(0,t)$ and $\Theta_f^0(0,t)$ from Eqs. (56a) and (56b) in Eq. (49a), we get

$$\frac{da_0^a}{dt} = -A_\theta f_f^a(k) a_0^a \tag{63a}$$

where

$$f_f^a(k) = \frac{96k^6}{96k^5 - 5\alpha_f^{a*}} \tag{63b}$$

where

$$\alpha_f^{a*} = z_m F D_m S^a T_f^a R^* \tag{63c}$$

Since R^* is, as discussed above, positive. In order to avoid the singular point of k in Eq. (63b), the condition

$$S^a \; T_f^a < 0 \tag{64}$$

is required. Since S^a is positive,

$$\mathrm{T}_f^a = -\frac{2\Omega}{\nu} < 0 \tag{65}$$

must be fulfilled. In comparison with Eq. (62), Eq. (65) indicates that the micro-MHD vortexes on a free surface rotates in the direction reverse to that of the vortexes on a rigid surface, i.e., $w_f^a > 0$ and $\omega_{zf}^a < 0$.

4.1.2 Formation of micro-mystery circle

To treat the two independent self-organization processes concerning rigid and free surfaces at one time, it is necessary to describe the amplitudes in complex numbers. In Fourier inversion, utilizing the characteristic nature of complex Fourier transform, where even and odd functions are simultaneously transformed in the real and imaginary parts, we treat the rigid surface and free surface components as even and odd functions, respectively.
In consideration of the stochastic process in multiple nucleus formation, the following unit complex number is introduced.

$$R_d^a = \cos\theta_{rand}^a + i\sin\theta_{rand}^a \tag{66}$$

where θ_{rand}^a is the uniform random number between 0 and 2π, which are assigned to all grid points defined in an electrolyte solution. From the amplitudes of the gradients of the concentration fluctuations, the actual concentration gradients are calculated by Fourier inversion as follows,

$$\left\{\frac{\partial c_{mj}(x,y,z,t)}{\partial z}\right\}_{z=0} = \frac{1}{2\pi}\int_{-\infty}^{\infty}\int_{-\infty}^{\infty} D\Theta_j^0(z,t)^a \exp\left[-i\left(k_x x + k_y y\right)\right] dk_x dk_y \quad \text{for j = r or f} \tag{67}$$

where

$$D\Theta_r^0(0,t)^a = \frac{12\beta_1^a f_r^a(k)a^+}{5z_m F D_m S_r^a}\exp\left(-\frac{a^{+2}k^2}{2}\right)R_d^a \tag{68a}$$

and

$$\beta_1^a = \frac{5}{12}\alpha_r^a\left(\frac{XY}{\pi}\right)^{1/2} z_m F D_m \theta_\infty^* S_r^a \tag{68b}$$

Then, we have

$$D\Theta_f^0(0,t)^a = \frac{12\beta_0^a f_f^a(k)a^+}{5z_m F D_m S_f^a}\exp\left(-\frac{a^{+2}k^2}{2}\right)R_d^a \tag{69a}$$

where

$$\beta_0^a = \frac{5}{12}\alpha_f^a\left(\frac{XY}{\pi}\right)^{1/2} z_m F D_m \theta_\infty^* S_f^a \tag{69b}$$

As discussed initially, to automatically determine the rigid and free areas, the signs of the z-components of the velocity w_j^a and vorticity ω_{zj}^a for j =r or f are important. The actual z-components of velocity and vorticity fluctuations are calculated by the Fourier inversions. For a clockwise rotating system, under the conditions $w_r^a < 0$ and $\omega_{zr}^a > 0$, the current density on the rigid surface is calculated by

$$j_{zr}(x,y,0,t)^a = -z_m F D_m \left\{\frac{\partial c_{mr}(x,y,z,t)}{\partial z}\right\}_{z=0} \tag{70a}$$

Under the conditions $w_f^a > 0$ and $\omega_{zf}^a < 0$, the current density on the free surface is given by

$$j_{zf}(x,y,0,t)^a = -z_m F D_m \left\{\frac{\partial c_{mf}(x,y,z,t)}{\partial z}\right\}_{z=0} \tag{70b}$$

The total current density $j_z(x,y,0,t)^a$ is thus expressed by

$$j_z(x,y,0,t)^a = j_{zr}(x,y,0,t)^a + j_{z_f}(x,y,0,t)^a \tag{70c}$$

As a result, the surface morphology of the 2D nucleation is effectively calculated by

$$\zeta(x,y,t)^a = -\frac{\Omega_m}{z_m F}\int_0^t j_z(x,y,0,t)^a dt \tag{71}$$

In this calculation, only 1/4th of the total fluctuations is used at one time. This inadequacy is solved by multiple nucleus formation randomly occurring in time axis.
In Fig. 20a, an example of the theoretical calculation is exhibited. Owing to multiple random nucleus formation, though nucleation takes place all over the surface, four regular micro-mystery circles emerge. Figure 20b represents the 3D SEM image of a micro-mystery circle formed in copper deposition, which was observed in a rotating electrode system under a vertical magnetic field.

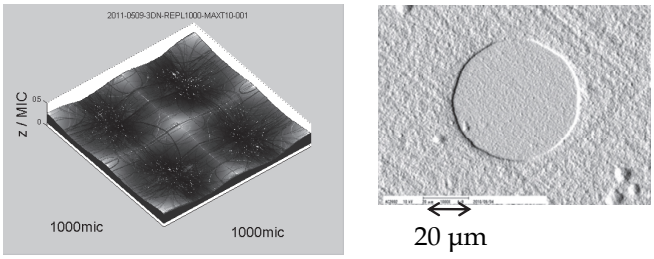

Fig. 20. Morphology of micro-mystery circle. a, theoretical calculated morphology;
b, SEM image of copper micro-mystery circle in copper deposition of the rotating system.

4.2 Formation of nano-mystery circle

As have been discussed in last section, at the boundary on a free surface of 2D nucleus covered with ionic vacancies, the frictionless rotation of vortex reverse to the rotating system yields a concentric circular pattern of micro-mystery circle, whereas at the boundary on the rigid surface, due to friction, the solution is kept stationary. 3D nucleus formation on a rigid surface of 2D nucleus also receives the same effects as 2D nuclei, i.e., the precession to micro-MHD flows and the selection of the direction of rotation. However, there are some differences; due to small scale of length, i.e., low Reynolds number, the effective viscosity that vortexes feel becomes too high to rotate, so that rotations themselves become impossible. To solve this problem, a new effect of ionic vacancy to decrease viscosity is required.
Considering that ionic vacancies are easy to coalesce from a nature of bubble, we propose a new effect called 'micro-hydroplaning'. Due to coalescence, ionic vacancies are supposed to act like a creamy lubricant. Let us imagine a coffee surface with cream, where due to the difference of viscosity, without mixing, the cream forms white stripes surrounding coffee vortexes. If these stripes are replaced with those of ionic vacancies, just like a wheel in the

well-known hydroplaning effect, a micro-vortex surrounded by the stripes of ionic vacancies can rotate freely. This phenomenon effectively decreases kinematic viscosity. Since ionic vacancies gather in an upward flow of a 3D nucleus, according to this effect, the local kinematic viscosity in the upward flow drastically decreases for rotation. As a result, in the downward flow without ionic vacancy, due to effectively high viscosity, the rotation itself is prohibited, remaining stationary, whereas in the upward flow containing the stripes of ionic viscosity, owing to effectively low viscosity, a vortex can rotate. In the same way as that of the micro-mystery circle formation, but quite different in size, a concentric circular pattern called nano-mystery circle with chirality is thus formed. At the center of the nano-mystery circle, a screw dislocation with chirality emerges. In Fig. 21a, the theoretical calculation of nano-mystery circle is represented. In spite of random multiple nucleus formation, nano-mystery circles can be seen. Figure 21b shows the SEM image of a copper deposit, where many shallow dimples in the same shape are observed.

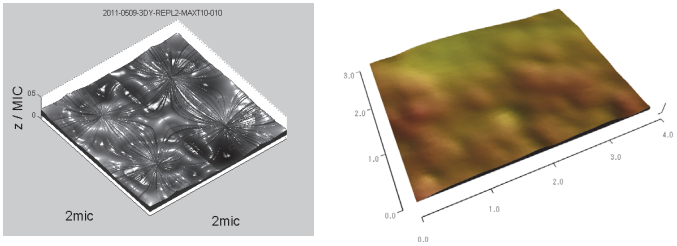

a b

Fig. 21. Morphology of nano-mystery circle. a, theoretical calculation (2 μm in full scale); b, SEM image ofcopper nano-mystery circle in copper deposition of the rotating system (4 μm in full scale).

5. Conclusion

In a parallel magnetic field, usually an electrode system called MHD electrode is used, which consists of a rectangular channel with two open ends (Fig. 1). Arriving through the inlet, the solution moves along the electrode surface, and leaves out of the outlet. As a result, generated vacancies are continuously swept away from the electrode surface. This is the reason why the vacancy does not affect the deposition process in a parallel magnetic field.

6. References

Aogaki, R., Fueki, K., & Mukaibo, T. (1975). Application of Magnetohydrodynamic Effect to the Analysis of Electrochemical Reactions –2. Diffusion Process in MHD Forced Flow of Electrolyte Solutions. *DENKI KAGAKU* (presently *Electrochemistry*), Vol. 43, No. 9, (August 1975), pp. 509-514, ISSN 1344-3542

Aogaki, R., Kitazawa, K., Kose, Y., & Fueki, K. (1980). Theory of Powdered Crystal Formation in Electrocrystallization -Occurrence of Morphological Instability at the Electrode Surface. *Electrochimica Acta,* Vol. 25, No. 7, (July 1980), pp. 965-972, ISSN 0013-4686

Aogaki, R. (1995). Instability of Nonequilibrium Fluctuation in Electrochemical Nucleation I. Occurrence of Instability. *Journal of Chemical Physics,* Vol. 103, No. 19, (November 1995), pp. 8602-8615, ISSN 0021-9606

Aogaki, R. (2001). Magnetic Field Effects in Electrochemistry. *Magnetohydrodynamics,* Vol. 37, No. 1/2, (August 2001), pp. 143-150, ISSN 0024-998X

Aogaki, R., Morimoto, R., Sugiyama, A., & Asanuma, M. (2008a). Self-organization of Copper Secondary Nodules by the Second Micro-MHD Effect. *ECS Transactions,* Vol. 13, No. 16, (December 2008), pp. 15-24, ISSN 1938-6737

Aogaki, R. (2008b). Theory of Stable Formation of Ionic Vacancy in a Liquid Solution. *Electrochemistry,* Vol. 76, No. 7, (June 2008), pp. 458-465, ISSN 1344-3542

Aogaki, R., Morimoto, R., Sugiyama, A., & Asanuma, M. (2009a). Double Layer Mechanism in Self-organization of Copper Secondary Nodules under a Parallel Magnetic Field. *Magnetohydrodynamics,* Vol. 45, No. 2, (April 2009), pp. 245-252, ISSN 0024-998X

Aogaki, R., Miura, M., & Oshikiri, Y. (2009b). Origin of Nanobubble-Formation of Stable Vacancy in Electrolyte Solution. *ECS Transactions,* Vol. 16, No. 25, (May 2009), pp. 181-189, ISSN 1938-6737

Aogaki, R., Morimoto, R., Sugiyama, A., & Asanuma, M. (2009c). Origin of chirality in magnetoelectrodeposition, *Proceedings of 6th International Conference Electromagnetic Processing of Materials*, pp. 439-442, ISBN 978-3-936104-65-3, Dresden, Germany, October 2009

Aogaki, R., Morimoto, R., & Asanuma, M. (2010). Nonequilibrium Fluctuations in Micro-MHD Effects on Electrodeposition. *Journal of Magnetism and Magnetic Materials,* Vol. 322, No. 9/12, (June 2010), pp. 1664-1668, ISSN 0304-8853

Mogi, I., & Watanabe, K. (2005). Chirality of magnetoelectropolymerized polyaniline electrodes. *Japan Journal of Applied Physics,* Vol. 44, No. 5, (January 2005), pp. L199-L201, ISSN 0021-4922

Mogi, I. (2008). Chiral Electrode Behaviors of Magnetoelecrodeposited Ag films for Amino Acids. *ECS Transactions,* Vol. 13, No. 16, (December 2008), pp. 45-52, ISSN 1938-6737

Sugiyama, A., Morimoto, R., Hashiride, M., Nagai, Y., & Aogaki, R. (2004). Application of Vertical Micro-disk MHD electrode to the Analysis of Heterogeneous Magneto-convection. *Electrochimica Acta,* Vol. 49, No. 28, (November 2004), pp. 5115-5124, ISSN 0013-4686

Morimoto, R., Sugiyama, A., & Aogaki, R. (2004). Nano-scale Crystal Formation in Copper Magneto-electrodeposition Under Parallel Magnetic Fields. *Electrochemistry,* Vol. 72, No. 6, (May 2004), pp. 421-423, ISSN 1344-3542

Morimoto, R., Aogaki, R., Sugiyama, A., & Asanuma, M. (n.d-a). Micro-MHD Effects in a Parallel Magnetic Fields -1. Equations of Micro-MHD Flows. in the course of submission to J. Chem. Phys.

Morimoto, R., Aogaki, R., Sugiyama, A., & Asanuma, M. (n.d-b). Micro-MHD Effects in a Parallel Magnetic Fields -2. 1st Micro-MHD Effect: Suppression of Three Dimensional (3D) Nucleation. in the course of submission to J. Chem. Phys.